THE HONG KONG POLYTECHNIC UNIVERSITY
DEPARTMENT OF MECHANICAL ENGINEERING

OPEN- AND CLOSED-LOOP CONTROL OF FLOW-STRUCTURE INTERACTION ON SQUARE CYLINDERS IN A CROSS FLOW

MING-MING ZHANG

A thesis submitted in partial fulfilment of the requirements for the Degree of Doctor of Philosophy

March, 2004

CERTIFICATE OF ORIGINALITY

I hereby declare that this thesis is my own work and that, to the best of my knowledge and belief, it reproduces no material previously published or written, nor material that has been accepted for the award of any other degree or diploma, except where due acknowledgement has been made in the text.

_____(Signed)

Zhang Ming Ming

March, 2004

ABSTRACT

The thesis deals with active control of fluid-structure interaction. Five inter-related subtopics are addressed.

1). A novel perturbation technique, creating a local perturbation on a cylinder surface using piezo-ceramic actuators, was presented to perturb fluid-structure interaction on the cylinder and subsequently to simultaneously control both vortex shedding and its induced vibration.

2). The open-loop control of resonant fluid-structure interaction was experimentally studied when the vortex shedding frequency f_s synchronized with the natural frequency, f_n, of the dynamic system. A square cylinder, flexibly supported at both ends, was allowed to vibrate only in the lift direction. Three actuators were embedded underneath one side, parallel to the flow, of the cylinder. They were simultaneously activated by a sinusoidal wave, thus causing the cylinder surface to oscillate. As the normalized perturbation frequency f_p^* lied outside the possible synchronization range ($f_p^* = 0.11 \sim 0.26$), structural vibration Y, vortex circulation (Γ) and mean drag coefficient ($\overline{C}_D$) were reduce effectively, especially at f_p^* of 0.1 while as f_p^* fell within the synchronization range, the three quantities were enhanced, especially at f_p^* of 0.13.

3). The same technique was extended to include closed-loop control. The control action of the actuators was controlled by a Proportional-Integral-Derivative (PID) controller. Three control schemes were investigated using different feedback signals, including flow velocity u, Y and a combination of both. It was observed that the

control scheme based on the feedback of the coupled Y and u led to the almost complete destruction of the Kármán vortex street and a significant reduction in Y, Γ and $\overline{C}_D$, outperforming by far an open-loop control as well as the other two closed-loop schemes. The alteration in the phase shift between Y and u (ϕ_{Yu}) from in phased to anti-phased, the impaired spectral coherence (Coh_{Yu}) and effective damping might be responsible for this.

4). Vortex shedding from a fix-supported rigid cylinder was manipulated by the perturbation technique, based on a feedback flow signal via a PID controller. It was observed that Γ, u, lift and drag coefficients and $\overline{C}_D$ may be effectively decreased or increased, corresponding to anti-phased or in-phased perturbation and flow, respectively. Similar effects were obtained as the Reynolds number varied. The relationship between the perturbation and force acting on fluid was also examined.

5). Experiments on the closed-loop control of the vortex-induced flexible cylinder vibration was finally conducted under resonance and non-resonance case. Five control schemes were investigated based on the feedback from either individual or combined responses of Y and u. For resonance case, f_s coincided with the first-mode natural frequency of the fluid-structure system. The best performance was achieved using the feedback signal from a combination of u and Y. Vortex shedding was almost completely destroyed, resulting in a great reduction in Γ, Y, and $\overline{C}_D$. Non-resonant cases were also briefly discussed, leading to similar observations in terms of control effects.

LIST OF PUBLICATIONS ALREADY PUBLISHED, ACCEPTED OR SUBMITTED

Referenced Journals:

Cheng, L., Zhou, Y. & **Zhang, M. M.** 2003 Perturbed interaction between vortex shedding and induced vibration. *Journal of Fluids and Structures*, **17**, 887-901.

Cheng, L., Zhou, Y. & **Zhang, M. M.** 2004 Controlled vortex-induced vibration on a fix-supported flexible cylinder in crossflow. *Journal of Sound and Vibration* (Submitted).

Zhang, M. M., Zhou, Y. & Cheng, L. 2003 Spring-supported cylinder wake control. *AIAA Journal*, **41**, 1500-1506.

Zhang, M. M., Cheng, L. & Zhou, Y. 2004 Closed-loop control of fluid-structure interactions on a flexibly supported cylinder. *European Journal of Mechanics B/Fluids*, **23**, 189-197.

Zhang, M. M., Cheng, L. & Zhou, Y. 2004 Closed- loop-controlled vortex shedding from a flexibly supported square cylinder under different schemes. *Physics of Fluids*, **16**, 1439-1448.

Zhang, M. M., Cheng, L. & Zhou, Y. 2004 Closed-loop manipulation of vortex shedding from a fixed-supported square cylinder. *Experiments in Fluids* (Submitted).

Referenced Conference Proceedings:

Cheng, L., Zhou, Y. & **Zhang, M. M.** 2002 A perturbation technique for flow-induced vibration control. *2002 ASME International Mechanical Engineering Congress & Exposition*, November 17-22, New Orleans, Louisiana, USA, No. IMECE2002-33569.

Cheng, L., **Zhang, M. M.** & Zhou, Y. 2003 Active control of vortex-induced vibration of a square cylinder in cross flow. *The 32nd International Congress and Exposition on Noise Control Engineering*, August 25-28, Jeju. International Convention Center, Seogwipo, Korea, 2462-2469.

Zhang, M. M., Zhou, Y. & Cheng, L. 2002 Vortex control in a flexible supported cylinder wake. *Proceedings of 3th. Bluff Body Wakes and Vortex-Induced Vibrations*, December 17-20, Port Douglas, Australia, 155-158.

Zhang, M. M., Cheng, L. & Zhou Y. 2003 *IUTAM Symposium On Integrated Modelling of Fully Coupled Fluid-Structure Interactions Using Analysis, Computations, and Experiments*, June 1-6, Rutgers University, New Brunswick, New Jersey, USA.

Zhang, M. M., Cheng, L. & Zhou, Y. 2003 Closed-loop control of the resonant flow-structure interaction using PID controller. *Third International Symposium on Turbulence and Shear Flow Phenomena-2003*, June 25-27, Sendai International Center, Sendai, Japan, 549-554.

Zhang, M. M., Cheng, L. & Zhou, Y. 2003 Closed-loop control of the wake of a flexibly supported cylinder. *Seventh Triennial International Symposium on*

Fluid Control, Measurement and Visualization , August 25-28, Sorrento, Italy, , No. ID-184.

Zhang, M. M., Zhou, Y. & Cheng, L. 2004 Closed-loop controlled vortex shedding from a square cylinder. *10th Euromech European Turbulence Conference*, 29 June-2 July, The Norwegian University of Science and Technology, Trondheim, Norway.

Zhang, M. M., Cheng, L. & Zhou, Y. 2004 Control of Vortex-induced vibration on a rigidly supported flexural Cylinder. 8th International Conference on Flow-Induced Vibrations. 5-9 July, Ecole Polytechnique, Paris, France, 345-350.

ACKNOWLEDGEMENT

I would first express my sincere gratitude and acknowledgements to my supervisors, Prof. L. Cheng and Dr. Y. Zhou for their creative ideas and insights throughout my study period and the preparation of this thesis. I have benefited a lot from their considerate and strict working attitudes in the past three years and I believe this will also deeply influence my future careers. At the same time, I would also express my great appreciation to Prof. R. M. C. So, the head of ME department, for giving me the opportunity to learn so much at Hong Kong PolyU.

Second, grateful acknowledgements are widely delivered to Dr. Y. Y. Li, H. J. Zhang, Z. J. Wang, S. J. Xu, G. Q. Xu, M. H. Liu and S. Z. Di, Prof. Z. Wei, Mr. X. W. Wang, Jeff Huang, J. C. Hu and Eric Yiu and Mrs. Carrie Ling for their useful suggestions and discussions during experiments. In addition, gratitude should also be expressed to Mr. K. Y. Ng, K. K. Lo and all the technicians in the Project Laboratory for their help during the construction of the experimental setups.

Third, I wish to acknowledge the funding support of the Central Research Grant of The Hong Kong Polytechnic University through Grant G-W108.

Fourth, I also appreciate Prof. S. Dong, Z. Q. Deng, Y. C. Liang and D. Li who were my previous supervisors when I studied in Harbin Institute of Technology. They contributed a lot to cultivate my fundamental and experimental abilities in the past.

Finally, I wish to say thanks to my family members, my wife, Z. Y. Yang, my parents, my sister, Ling Ling and my aunt, S. F. Liu. Their love and trust have provided so much spiritual and mental encouragement for me, which helped me go through the three years study period and keep the proper perspective on life.

CONTENTS

NOMENCLATURE

$\overline{C}_D$	Mean drag coefficient.
C_D, C_L	Fluctuating drag and lift coefficient. $C_D = F_D/(0.5\rho U_\infty^2 hl)$. $C_L = F_L/(0.5\rho U_\infty^2 hl)$.
$C_{D,rms}$, $C_{L,rms}$	Root mean square value of C_D and C_L.
Co_{Yu}	Cospectrum of Y and u.
Coh_{Yu}, Coh_{Yu_2}	Spectral coherence between Y and u.
D, D_Y, D_u	Differential gain.
E	Electric field (C).
E_Y, $E_u(E_{u_2})$	Power spectrum density function of Y and u, respectively.
E_{ε_y}	Power spectrum density function of ε_y.
E_{F_L}, E_{F_D}	Power spectrum density function of F_L and F_D, respectively.
$E_{Y,\Delta f}^{(n)}$, $E_{u,\Delta f}^{(n)}$	Energies of Y and u associated with f_s^* (n = 1), its second (n = 2) and third (n = 3) harmonics.
$E_{Y,\Delta f}^{(m)}$, $E_{\varepsilon_y,\Delta f}^{(m)}$	Energies in E_Y and E_{ε_y} associated with the vibration corresponding peaks at f_n^*, $2f_s$ and $f_n^{'''*}$, respectively. m = 1, 2, 3.
$E_{u_2,\Delta f}^{(n)}$	Energies in E_{u_2} associated with the vibration corresponding peaks at f_s, $2f_s$ and $3f_s$, respectively. n = 1, 2, 3.
f	Frequency (Hz).

f^*	Normalized f ($=fh / U_\infty$).
f_s	Vortex shedding frequency (Hz).
f_s^*	Normalized f_s ($=f_s h / U_\infty$).
$2f_s$	Second harmonic of f_s (Hz).
$2f_s^*$	Normalized $2f_s$ (Hz).
$3f_s$	Third harmonic of f_s (Hz).
$3f_s^*$	Normalized $3f_s$ (Hz).
f_n	First natural frequency of cylinder (Hz).
f_n'	First mode resonance frequency of cylinder/fluid system (Hz).
$f_n'^*$	Normalized f_n' ($=f_n' h / U_\infty$).
$f_n'''^*$	Third mode resonance frequency of cylinder/fluid system (Hz).
f_p	Perturbation frequency (Hz).
f_p^*	Normalized f_p ($=f_p h / U_\infty$).
F_L, F_D	Fluctuating lift and drag forces (N).
F_L'	Fluctuating force on fluid due to cylinder oscillation ($\overrightarrow{F_L'} = \overrightarrow{F_f} + \overrightarrow{F_p}$) (N).
F_f	Fluctuating force due to flow separation (N).
F_p	Fluctuating force due to perturbation (N).
F_x, F_y, F_z	Three components of a dynamic or quasi-static force (N).
h	Height of cylinder (m).
I, I_Y, I_u	Integral gain.
l	Cylinder length (m).

m	Mass per unit length of cylinder (kg/m).
n_f	Fibre refractive index.
p	Stress field (N).
P, P_Y, P_u	Proportional gain.
$\widetilde{P}, \widetilde{P}_q$	Gain coefficient in amplitude between the output and input of the controller.
$\widetilde{P}_{q,opt}$	Optimal $\widetilde{P}$.
$\widetilde{P}_{u_1}, \widetilde{P}_Y, \widetilde{P}_{\varepsilon_y}$	Gain coefficient using u_1, Y and ε_y for feedback signals.
Q_{Yu}	Quadrature spectrum of Y and u.
Re	Reynolds number $\equiv U_\infty h / \nu$.
u (u_1, u_2), v	Fluctuating flow velocities along x and y direction, respectively (m/s).
$u_{2,\,\mathrm{rms}}$	Root mean square value of u_2 (m/s)
u_{rms}, v_{rms}	Root mean square value of u and v (m/s).
u^*_{rms}	Normalized u_{rms} (= $u_{\mathrm{rms}} / U_\infty$).
$\overline{u^2}^*$, $\overline{v^2}^*$, $\overline{uv}^*$	Reynolds stress, normalized with U_∞^2.
$\overline{U}$, $\overline{V}$	Mean velocities along x and y direction, respectively (m/s).
$\overline{U}^*$	Normalized $\overline{U}$ (= $\overline{U} / U_\infty$).
U_r	Reduced velocity $\equiv U_\infty / f_n h$.
U_∞	Free stream velocity (m/s).
V_p	Perturbation voltage (volts).
$V_{p,\,\mathrm{rms}}$	Root mean square value of V_p (volts).

W	Control energy ($= V_p^2 / R$) (W). R represents the resistance of the actuators.
x, y, z	Coordinates in the stream-wise, lateral and span-wise directions, respectively.
Y	Displacement of cylinder oscillation (mm).
$\dot{Y}$	Cylinder oscillation velocity (m/s).
Y_{max}	Maximum Y (mm).
Y_{rms}	Root mean square value of Y (mm).
Y^*_{rms}	Normalized Y_{rms} ($=Y_{\text{rms}} / h$).
Y_p	Perturbation displacement (mm).
$Y_{p,\text{rms}}$	Root mean square value of Y_p (mm).
$\dot{Y}_p$	Perturbation velocity (m/s).

Greek Symbols

Γ	Vortex circulation (m^2/s).
Γ^*	Normalized Γ ($=\Gamma h / U_\infty$).
Λ	Bragg grating pitch (nm).
ε	Strain.
ε_y	Fluctuating strain of the cylinder along y direction.
$\varepsilon_{y,\text{rms}}$	Root mean square value of ε_y.
ϕ_{Yu}	Spectral phase between Y and u.
$\phi_{Y_p u_2}$	Spectral phase between Y_p and u_2.
$\phi_{Y_p C_L}$	Spectral phase between Y_p and C_L.

$\widetilde{\phi}$, $\widetilde{\phi}_q$	Phase shift between the output and input of the controller (deg).
$\widetilde{\phi}_{q,opt}$	Optimal $\widetilde{\phi}$.
$\widetilde{\phi}_{u_1}$, $\widetilde{\phi}_{\varepsilon_y}$, $\widetilde{\phi}_Y$	Phase shift using u_1, ε_y, Y for feedback signals.
λ_B	Bragg resonance wavelength (nm).
$\Delta\lambda_B$	Shift in λ_B (nm).
λ_{B0}	Bragg wavelength of the grating under strain-free condition (nm).
ν	The fluid kinematic viscosity (m^2/s).
ρ	Air density (kg/m^3).
ω_z	Spanwise vorticity (s^{-1}).
ω_z^*	Normalized ω_z (= $\omega_z h / U_\infty$).
$\lvert\omega_{z\max}^*\rvert$	Maximum ω_z^*.
$\lvert\omega_{zc}^*\rvert$	Cutoff level of ω_z^*.
ζ	Damping ratio.
ζ_e	Effective damping ratio.
$\zeta_{y,e}^{(k)}$	Effective damping ratio associated with $f_n^{'*}$ and $f_n^{''''*}$. $k = 1, 3$.
ζ_f	Fluid damping ratio.
$\zeta_{y,f}^{(k)}$	Fluid damping ratio associated with $f_n^{'*}$ and $f_n^{''''*}$. $k = 1, 3$.
ζ_s	Damping ratio of first mode structural vibration.
$\zeta_{y,s}^{(k)}$	Structural damping ratio associated with $f_n^{'*}$ and $f_n^{''''*}$. $k = 1, 3$.

CHAPTER 1

INTRODUCTION

1.1 Background

When a two-dimensional bluff body is subject to a cross flow, the boundary layer will separate from each side of the body beyond a critical Reynolds number Re (Re = $U_\infty h / \nu$, where U_∞ is the free-stream velocity, h is the characteristic height of structure, and ν is the kinematic viscosity), and continue on in the main flow as a free vortex layer which separates the fluid in the wake from the main flow. Under this unstable condition, the free vortex layer begins to roll up in such a way that a Kármán vortex is formed at its end. The vortex is then shed alternately with the one on the opposite side and continues its winding up motion as it moves downstream. This process is controlled by the dynamics in the negative base pressure region and feedback from the fluctuating wake (Gerrard, 1966; Bearman, 1967; Naudascher, 1987; and Unal & Rockwell, 1988a). The asymmetrical arrangement of vortices is accompanied by an alternating pressure which creates the fluid excitation forces, causing the structure to vibrate. The resultant structural motion alters the flow pattern, vortex strength, vortex shedding frequency or mean drag *et al.*, giving rise to highly nonlinear fluid-structure coupling. This kind of fluid-structure interaction has been

widely investigated in the past (e.g. Bishop & Hassan, 1964; Tanida *et al.* 1973; Griffin & Ramberg, 1975; Davies, 1976; Sarpkaya, 1979; Bearman, 1984; Ongoren & Rockwell, 1988; and Williamson & Roshko, 1988).

In practice, people often pursue desired changes in vortex shedding or vortex-induced structural vibration to satisfy the actual requirement of engineering. In most cases, vortex shedding needs to be impaired to control the vortex-induced structural vibration, noise, lift or drag force for the design of aircraft, automobile, bridge or high-rise building etc.; while in some other engineering applications, such as mixing, combustion or heat transfer, it needs to be enhanced to obtain a better performance (Ghoniem & Ng, 1987; Ottino, 1989; Viswanath, 1996; Wu & Perng, 1999; Gau *et al.* 1999; Morgenthal & McRobie, 2002; Valencia & Paredes, 2003; and Konstantinidis *et al.* 2003). By the same token, although the vortex-induced structural vibration may be utilized in some engineering applications such as offshore drilling, marine hydrodynamics or underwater acoustics, it should be suppressed in most cases, for example, civil and wind engineering, nuclear and conventional power generation, and electric power transmission, and so on. This is because the excessive vibration may cause the deformation, fatigue or even damage in engineering structures in the long run, which has become the research topics of some papers (Ware & Shah, 1988; Yamane & Orita, 1994; Guerout & Fisher, 1999; Taylor & Pettigrew, 2000; Goyder, 2002; and Pettigrew & Taylor, 2003). The impact will be intensified under resonance or synchronization since it is often accompanied by a relatively large vibration amplitude, large deformation and stress that may exceed the allowable safe values of design (Griffin & Hall, 1991). Typical examples include the collapse of the Tacoma Narrows Bridge due to a sustained steady wind producing vortex shedding at

resonance frequency of the bridge over a long period and the damage of piling during the construction of an oil terminal on the Humber estuary of England in 1960s (Griffin & Ramberg, 1976). These incidents fully justify the necessity of suppressing the occurrence of resonance and synchronization of structures in cross flow. As a result, the control of the vortex shedding and its induced structural vibration has always attracted the interests of many researchers for many years.

1.2 Literature Review

1.2.1 Mechanism of vortex shedding and wake

Understanding the mechanism of the vortex shedding from bluff bodies has attracted the attention of many researchers. Provansal *et al.* (1987) and others experimentally showed that vortex shedding was a result of an initially linear wake instability. The interest in considering the absolute and convective nature of instabilities in wakes originated from the concepts developed in the field of plasma physics, and has been applied to free shear flows by Huerre & Monkewitz (1985, 1990). It is now widely accepted that the observed Kámán vortex street is the nonlinear limit cycle of a self-excited global instability. The behavior has been related to the existence of a finite region of absolute instability in the near wake. Schumm (1991) presented some experimental evidence for this by showing that transient behavior closely follows the tendency predicted by the Landau equation.

Wakes in a stream of constant velocity are only asymptotically self-preserving. In addition they don't seem to reach a universal equilibrium state, developing instead in a way which depends on characteristics of the wake producing body: e.g. its shape

and solidity, as was shown by Wygnanski *et al.* (1979). Wake flow is characterized by periodicity (Berger & Wille, 1972), where typical (coherent) structures are similar to those in the jet, with a multitude of modal development in the axisymmetric case. In the two-dimensional case the two dominating modes-the sinusoidal and varicose-are of comparable strength and probability, showing a tendency towards early developing of three dimensionalities. Wakes can be both absolutely and convectively unstable, depending on the region under consideration. The near wake with its characteristic recirculation is clearly the producing body (Fuchs *et al.* 1979; and Strykowski, 1986). The far wake is convectively unstable, shown by Oster and Wygnanski (1982).

Wake behind a square cylinder and a circular cylinder has some fundamentally different behaviors in terms of flow separation and Re dependence. For example, a square cylinder wake is characterized by a fixed separation point. In contrast, the separation point on a circular cylinder varies. However, the physics associated with vortex-induced vibrations on a bluff body in a cross flow is in essence the same, irrespective of the cross-section shape of the bluff body, implying that a control technique applicable for one bluff body, say a circular cylinder, should be workable for another such as a square cylinder, or vice versa. This is perhaps why most of previous attempts for the control of vortex-induced vibrations were made based on a circular cylinder model.

1.2.2 Previous control methods review

A variety of control techniques have been developed in the past, which can be roughly classified as passive and active control methods (Dorf & Bishop, 1995; and Gad-el-Hak, 2001).

1.2.2.1 Passive control methods

A considerable amount of research has been conducted using passive control methods, which require no external energy input to the flow-structure system, to control flow and subsequently suppress the flow-induced vibration. Zdravkovich (1981), Every *et al.* (1982) and Wilson & Tinsley (1989) manipulated the vortex shedding and drag force by passively modifying the geometry of structures, resulting in an alteration of the pressure gradient around the structure. Another typical passive method was to place longitudinal grooves or riblets on the surface of structures. By doing so, irregularities were introduced into the shear wake of the structure, which inhibited the vortex shedding. This technique has proved successful particularly in offshore explorations and marine hydraulics (Hwang & Chao, 2000; and Owen *et al.* 2001). Other passive methods consist in controlling the flow separation behind cylinders by placing fixed mechanical vortex generators, such as another cylinder or a plate in the shear region. It was observed that by optimizing the position of the secondary structure, a reduction in vortex shedding was obtained (Unal & Rockwell, 1988b; Sakamoto, 1997; Bouak & Lemay, 1998; and Alam *et al.* 2002). The effectiveness of these passive techniques lies in its partially impeding the global mode instability of wake behind the structure. Provansal *et al.* (1987) demonstrated that von Kármán vortex shedding was a limit-cycle oscillation of the near wake, resulted from a global mode instability. Using passive methods, the zone of absolute convective instability in the near wake can be sufficiently shrunk and the phenomenon of Hopf bifurcation happens in the wake, thus causing the impairment of the global mode instability (Huerre & Monkewitz, 1985; and Chomaz *et al.* 1988). The passive control methods, drawing energies directly from the flow to be controlled, are often of

technical simplicity, practicability and reasonably cheap, which warrants their wide application in many kinds of nowadays engineering. However, these methods may not be properly described by the term 'flow control' but rather by 'flow management' because they only disturb the normal development of flow instead of flow itself. Thus it is not easy for the passive disturbance to obtain a significant effect on vortex shedding. In addition, adding surface protrusions to structural surface or modifying the cross section of structure may influence the stiffness and integrity of the structure, which may cause problems in some cases.

1.2.2.2 Open-loop control methods

In contrast, active control methods involve the input of energies via actuators to bring about desirable changes to the flow-structure system, using either independent external disturbance or feedback-signal controlled system. The former is often referred to as the open-loop control, whereas the latter is called the closed-loop control or feedback control. In both cases, one of the key points to ensure a successful control is that actuators used should create significant effects on physical parameters to be controlled. This is the problem of controllability, which is one of the most crucial issues to be addressed in designing a control system. In the case of flow-induced vibration control, a possible actuation mechanism should warrant significant effects on vortex shedding or structural vibration.

Most of the open-loop control methods reported in the literatures aimed at controlling the vortex shedding using different techniques. Blevins (1985) explored the influence of a transverse sound wave on vortex shedding from cylinders at Re from 20000 to 40000. The acoustic wave was given out from two loudspeakers

mounted on each side of the wind tunnel. He found that the sound introduced in this passive way could increase the coherence of vortex shedding along the cylinder axis and cause lock on to occur. In another word, the normal evolution of vortex shedding could be controlled under acoustic excitation. Inspired by this idea, Hsiao and Shyu (1991) and Fujisawa and Takeda (2003) used acoustic waves emitted continually from a slot on the surface of a cylinder and demonstrated that a local perturbation near the shear layer instability frequency and around the flow separation point caused an increase in lift but a reduction in drag and the vortex scale at Re from 420 to 34000 and at Re of 9000, respectively. Under this condition, the upper surface pressure of the cylinder was greatly reduced, especially near the slot, as compared to the lower surface pressure, resulting in the enhancement of the upward lift. At the same time, the destruction of Kármán vortices due to the break in the normal vortex shedding decreased the momentum loss and the drag on the cylinder was also reduced accordingly. Similarly, Bera *et al.* (2000) deployed a pulsed acoustic signal to obtain an enhancement of lift force and an impairment of flow separation and drag force (Re $= 1.33 \times 10^5$).

Another approach reported in the literatures is to disturb the flow field by blowing and sucking flow through the holes or slots on the surface of the cylinder, which is often called surface bleeding technique. Williams *et al.* (1992) introduced symmetric and anti-symmetric forcing into a water flow (Re = 470) at a frequency of about two times of vortex shedding frequency (f_s) through two rows of holes located at $\pm 45°$, respectively, away from the forward stagnation line of the cylinder. Like Hsiao and Shyu (1991), introducing disturbances into the boundary layer before separation proved to have a large effect on the vortex evolution. In their work, they

observed a modified behavior of f_s and the flow structure at high bleed coefficient. Here the bleed coefficient represents the momentum induced by the unsteady bleed jets relative to the momentum in the undisturbed free stream. Likewise, Ghee and Leishman (1992) blew the air periodically from a narrow spanwise slot of a cylinder and thus controlled the vortex circulation and improve the fluctuating lift force at Re of 3×10^6.

Koopmann (1967) affected the natural wake by transversely oscillating the cylinder at various driving frequencies. Above a determined threshold oscillation amplitude (about 10% of cylinder diameter), the transverse vibration of a cylinder driven at f_s induced coherence of the separation points along its span, causing a reduction in the lateral spacing of the vortices. By rotating a circular cylinder at a frequency of $5f_s$ and Re = 150, Protas and Wesfreid (2002) modified the distribution of Reynolds stresses and decreased their magnitudes, resulting in a 25% reduction in the mean drag. This was associated with control which drove the mean flow toward the unstable sysmmetric state (the basic flow).

Based on the electromagnet actuators, Henoch and Stace (1995) and Kim and Lee (2000) locally applied the Lorentz force on the structural surface in the range of 70-130° from the stagnation point along the cylinder circumference in both clockwise and counterclockwise directions. The results showed that under positive Lorentz force, the separation point was moved rearward in such a drastic manner that the vortex shedding process was almost diminished and the drag force was effectively reduced.

On the other hand, some people tried to directly control the vortex-induced structural vibration by setting the tuned mass dampers on the structures. The structural

damping could be changed by tuning the mass of the damper. Results from both numerical simulations and experiments indicated that the structural vibration was effectively attenuated when adding certain amount of mass to the damper and this technique has been successfully used to suppress the oscillation of some actual engineering structures, for example, bridge deck and chimney (Ricciardelli, 2001; and Strommen & Hjorth-Hansen, 2001).

1.2.2.3 Closed-loop control methods

Controls using either passive or open-loop method cannot always lead to satisfactory performance because the control signal is not directly related to the responses from fluid field or structural vibration and therefore cannot fully affect the nonlinear fluid-structure interaction. This problem maybe solved by utilizing closed-loop control methods, under which the input to the actuators for controlling fluid field or structural vibration is continuously adjusted based on the corresponding feedback signals acquired by sensors. A suitable choice of the feedback signal is crucial for ensuring the good performance of a closed-loop system. Two basic schemes are widely adopted in the literatures: feedback from flow measurement and feedback from structural vibration measurement.

Previous closed-loop techniques involving flow control mostly have their feedback signals from flow, typically hot wire signals. This scheme should work quite well provided only flow is to be controlled. Berger (1967) was probably the first to introduce the feedback control to suppress the wake instability. He used a hot wire signal obtained in the wake to actuate a bimorph cylinder transverse to the oncoming flow and reported the possibility of avoiding vortex shedding at a Re of 80. Compared

with the condition without control, the separation point of vortices was moved oppositely by the control, which attenuated the roll-up motion of the vortex shedding. Likewise, Warui and Fujisawa (1996) managed to reduce the vortex strength using electromagnetic actuators, installed at both ends of a circular cylinder, to create a lateral oscillation, which was controlled by a feedback hot wire signal from the turbulent wake (Re = 6700). Tokumaru and Dimotakis (1991) and Filler *et al.* (1991) created a rotary oscillation of a cylinder to produce regulated injection of circulation into the wake. The cylinder was activated by the hot wire feedback signal from fluctuating velocities in the wake. By doing so, they managed to attenuate both vortex strength and drag force at Re of 15000 and within Re range from 250 to 1200, respectively. Shiels and Leonard (2001) numerically investigated the underlying physics of the observation made by Tokumaru *et al.* and concluded that rotational oscillation triggered multiple vorticity structures, which led to a time-averaged separation delay and subsequent drag reduction.

Like open-loop methods, some researchers also deployed the acoustic excitation technique into the closed-loop system. Ffowcs-Williams and Zhao (1989) used a hot wire signal to provide a feedback control into a loudspeaker mounted on the wind tunnel wall. The acoustic excitation from the loudspeaker suppressed vortex shedding from a cylinder at Re = 400. Roussopoulos (1993) revisited the problem and concluded that the onset Reynolds number for vortex shedding could be increased by 20% as a result of the control. The transient instability mode of vortex shedding induced by the feedback actuation was responsible for the control effect, which only took effect within a downstream region of 9 diameters distance from the cylinder. This was because the transient instability mode was not global in the downstream

direction, in the sense of the mode strength at all locations being instantaneously correlated. Lewit (1992) used a feedback hot wire signal to activate sound waves inside a circular tube. The sound waves interacted with flow through two rows of holes, arranged at ± 90° away from the forward stagnation line of the tube, respectively, so that the sound waves through the two rows of holes were anti-phased, thus suppressing vortex shedding from the tube up to $Re = 10^4$, as observed by a hot wire probe at one point in the wake and by a remote microphone for the overall assessment. Huang (1996) also introduced sound, again generated inside a cylinder and activated by a feedback hot wire signal from the wake, into flow through a thin slit on the cylinder surface. The position of the slit was located near the separation point of vortices. He found that the vortex shedding on both sides of the cylinder could be suppressed up to a Re range between 4×10^3 and 1.3×10^4. This showed that the vortex shedding was not only a growing of initial perturbations but also a result of the instabilities involving two parallel shear flows. The effect of the feedback sound was probably to break the interaction between the two shear flows, and consequently stopped the vortex shedding. Recently, using a similar actuation mechanism as Huang, Wolfe and Ziada (2003) reduced the response of tandem cylinders, with one being located in the downstream of the other one. Meanwhile the lift force on the downstream cylinder was decreased down to 70%.

Gunzburger and Lee (1996) employed surface bleeding technique to investigate the feedback effect on vortex shedding from a cylinder at low Re (< 80). Two pressure transducers, placed at $\pm 7\pi / 32$ from the leading edge, were used as sensors. The position of the actuators could be adjusted. When fluid was sucked through two slots on the cylinder surface centered at $\pm 23\pi / 32$ and blown through another slot

centered at π, they obtained a maximum reduction in the vortex strength and the lift. The amount of fluid injected or sucked through orifices was determined through a simple feedback law from pressure measurements at stations along the surface of the cylinder. Min and Choi (1999) further developed a suboptimal feedback control algorithm for surface bleeding technique by numerical simulation at Re = 100 and 160. The location of feedback sensors was limited to the cylinder surface, and the control output from actuators was the blowing and suction on the cylinder surface. The mean drag and drag/lift fluctuations significantly decreased using the cost function defined as the square of the difference between the target pressure and real flow pressure on the cylinder surface. They attributed the reduction in drag to a decrease of pressure near the stagnation point and a significantly increase of base pressure.

Liepmann and Nosenchuck (1982) tested two heating cylinders in tandem and experimentally demonstrated that a delay of the transition of the instability waves on the downstream cylinder to turbulent motion was achieved if the relative phase shift between the two driving voltages for heating cylinders was properly tuned by the feedback controller.

The aforementioned existing work all concerns the impairment of vortex shedding. On the contrary, under closed-loop control, the vortex shedding can also be reinforced by surface bleeding or oscillating cylinder technique for transport enhancement in heat transfer or combustion (Tsutsui *et al.* 2001; and Wang *et al.* 2003).

A different kind of control scheme requires the structural vibration signal to be fed back to controllers for the control of vortex-induced structural vibration. Baz and

Ro (1991) used an electromagnetic actuator installed inside a rigid cantilevered cylinder to exert a force on the cylinder. The actuator was driven by a feedback velocity signal of structural vibration measured on the cylinder, thus increasing damping to the cylinder and effectively reducing the vortex-induced vibration at the occurrence of resonance (Re = 17160 ~ 26555), when the vortex shedding frequency, f_s, coincided with the natural frequency, f_n', of the system. Baz and Kim (1993) further investigated the same problem using a cantilevered flexible cylinder. Based on the information of the cylinder vibration and an independent finite element model controller, the piezoelectric actuators generated a control action to attenuate the vortex-induced first mode oscillation. As a result, the amplitude of vibration reached a 40% reduction over a Re range between 5500 and 7500. Using similar setup as Baz and Kim, Tani *et al.* (1999) developed a μ-synthesis theory based robust controller and also effectively suppressed the first mode oscillation by enlarging the damping of the structure. Bonding electromagnetic actuators on a plate surface to excite the structure, Sébastien *et al.* (2003) attempted to actively alter the modal damping of a flexible tube bundle in a cross flow using velocity feedback to attenuate the structural vibration at high flow velocities.

1.3 Motivations and Objectives

Previous literature review shows some commonalities among the existing work, which motivate the present research. 1). Most of existing work focused on a separate control of either fluid field or structural vibration. In fact, a large majority of them dealt with suppressing vortex shedding from rigid structures. A few papers which aimed at controlling structural vibration in a cross flow considered the flow only as a

disturbance, rather than a control target. Many engineering applications, however, require a simultaneous control of both flow and its induced vibration. A simultaneous control of both elements would probably be more effective. 2). Most of existing work used rigid cylinders, with either rigid or flexible supports. Controlling vibrations of flexible structures have seldom been considered. Flexural vibrations of the structure, however, are responsible for many engineering problems such as the fatigue, instability and noise generation. Considering the practical importance and the technical difficulties involved, the issue is worth investigating. 3). There is a lack of information on comparison among different sensing techniques for providing feedback signals. A simultaneous control of both vortex shedding and structural vibration certainly requires more advanced and sophisticated sensing schemes. 4). The rapid development in new intelligent materials, computing and control technology provides new possibilities and therefore sheds new light on this problem of particular importance. Research is needed to take advantages of the most up-to-date technologies.

The general objective of this work is to establish, implement and assess a novel technique using piezoceramic actuators of new generation to achieve a simultaneous control of flow and its induced structural vibration. In the pursuit of this general objective, the following issues are addressed:

1) To propose a so-called perturbation technique, together with implementation details.
2) To assess the effectiveness of the technique using different configurations and control schemes.

3) To reveal the underlying physics involved, via simultaneous measurement and analysis of both flow and vibration signals.

4) To assess the adaptivity of the controller.

1.4 Outline

The thesis is organized in seven chapters. Chapter 1 introduces the background of the present work. At the same time, some related previous work are reviewed. Motivations and objectives of this investigation are presented.

In Chapter 2, the concept of the perturbation technique is put forward. Characteristics of the THUNDER actuators used to implement the technique are described. Experimental setup is introduced. Major facilities, such as particle image velocimetry (PIV) and laser Doppler anemometer (LDA) are briefly described.

Using open-loop method, the perturbed interaction between vortex shedding from a flexibly supported rigid cylinder and vortex-induced resonant vibration on the cylinder is experimentally investigated in Chapter 3. The control effects on the fluid field and structural vibration are shown by the results from PIV, flow visualization, LDA, hot wire and laser vibrometer measurements. The preliminary mechanism is discussed by investigating the change in phase shift and spectral coherence between flow and cylinder oscillation.

In Chapter 4, results obtained in Chapter 3 are refined and improved using closed-loop control based on proportional-integral-derivative (PID) controllers. Three control schemes, utilizing feedback signals from flow, structural vibration or a combination of both, are considered and compared. The performances of the control schemes are assessed through measurements using a PIV, flow visualization, and

LDA. To understand the underlying physics, changes in spectral phase and coherence between flow and structural vibration due to the deployment of the control are investigated, along with the varying fluid damping of the fluid-structure system, evaluated from structural oscillation signals using an auto-regressive moving average (ARMA) technique.

In order to better understand the effect of the perturbation on the flow, Chapter 5 presents results obtained using a closed-loop control system with a simplified PID controller to control the vortex shedding from a fixed supported rigid cylinder. In addition, the adaptivity of the controller is also assessed when varying Re. The control effects on fluid field are shown with the results of PIV, flow visualization, LDA and single hot wire, respectively. The modification of lift and drag coefficients are assessed through the measurement of a load cell system. To understand the control mechanism, conversions in spectral phase shift between the perturbation signal and the fluctuating flow velocity signal or lift force simultaneously sampled with a laser vibrometer, the monitor hot wire and load cell, respectively, are discussed in detail.

The closed-loop control of the perturbed interaction between vortex shedding and vortex-induced vibration on a flexible cylinder is studied in Chapter 6. Five control schemes, utilizing feedback signals from streamwise flow velocity u measured by a single hot wire, structural vibration Y by a laser vibrometer and dynamic strain in the transverse direction ε_y by an optical fiber Bragg grating (FBG) sensor, and a combination of u and ε_y or u and Y, are conducted and compared. The control performances on the structural oscillation are evaluated in both time domain and frequency domain in terms of Y, ε_y and u, respectively. To understand the physics, the modification of fluid field is documented using PIV, flow visualization, and LDA. At

the same time, changes in spectral phase and coherence between u and Y, along with the varying fluid damping of the fluid-structure system calculated using ARMA technique, due to the deployment of the control, are also investigated.

Chapter 7 summarizes the conclusions drawn from the present work.

CHAPTER 2

PERTURBATION TECHNIQUE AND MAJOR EXPERIMENTAL FACILITIES

2.1 Introduction

As stated in Section 1.3, although quite a number of techniques have been successfully applied to control vortex shedding or its induced structural vibration, there is a lack of methods addressing simultaneous control of both elements. In practice, however, when a bluff body is subject to a cross flow, the generation of the vortex shedding from the body and structural vibration are dependent on each other, which has been extensively demonstrated in many occasions. Thus controlling one target without considering the other cannot always satisfy the actual requirement of engineering. In order to solve the problem, the present work aims at establishing a novel technique to break the fluid-structure interaction using a local structural surface perturbation with a view to alter both vortex shedding and its induced structural vibration at the same time. The perturbation generation is implemented using actuators made of smart materials.

In the last decade, technologies using smart materials have become the enabler that cuts across traditional boundaries in material science and engineering. Smart

technology has given rise to a broad spectrum of research and applications. The perturbation technique proposed in the present work is based on the use of an advanced pizeoceramic actuator, called THUNDER (THin layer composite UNimorph piezoelectric Driver and sEnsoR), which is newly developed by NASA Langley research center. THUNDER actuator is superior to traditional pizeoceramic actuators in many aspects, such as large displacement and reasonably good load-bearing capacity.

The main aim of this chapter is to introduce the characteristic of THUNDER and investigate the possibility of applying the perturbation technique into flow and flow-induced vibration control. To this end, the idea which motivates the perturbation technique is firstly explained. Then characteristics of THUNDER and its installation method are described. Based on these, the embodiment of the perturbation technique, including the design of mechanical configuration and control system, is introduced. In addition, major experimental facilities used, such as particle image velocimetry (PIV) and laser Doppler anemometer (LDA), are briefly described for those unfamiliar.

2.2 Perturbation Technique

Steady flow incident on a bluff body is a common occurrence. When the Reynolds number exceeds a critical value, the boundary layer on each side of the body will separate from the body to form an unsteady flow pattern, that is, a staggered vortex street. Periodic forces on the structures are generated as the vortices alternately shed from each side of the structure, which causes the structure to vibrate. The resultant structural vibrations may in turn influence the flow field, giving rise to fluid-structure coupling and even resonance. The frequency of the forces/vortex shedding

can be appreciably modified and the structural vibration can be grossly amplified. The coupling is in general a highly non-linear function of both structural motion and flow velocity.

In fact, steady flow incident on bluff bodies is usually unstable and develops into an unsteady wake. Vortex shedding is a result of the initially linear wake instability. Thus the mature vortex structure depends on its infant form. On the other hand, small local perturbations into flow will grow exponentially when they are small enough to conform to the linear theory (Provansal, 1987). This implies that very small local perturbations to the flow may exert significant influence on the unsteady Kármán vortex structure. Although the physics involved is not fully known, there is strong evidence that weak perturbations do influence the normal vortex shedding in the highly non-linear unsteady wake, and that influence can sometimes be dramatic. Some examples on vortex shedding impaired by small local perturbation have been mentioned in Section 1.2 (Hsiao & Shyu, 1991; Williams *et al.* 1992; and Huang, 1996). On the top of that, Den Hartog (1947) and Parker (1966) introduced small local perturbation to flow by transversely oscillating cylinder and emitting acoustic waves inside the cylinder, respectively. By doing so, they all discovered the enhancement of vortex shedding.

The fact that vortex shedding is sensitive to local perturbation may also indirectly influence the vortex-induced structural vibration since the former is the excitation source of the latter. A direct alteration on both or either element may change the nature of fluid-structure interaction. In other words, if an appropriate local perturbation is created to modify the fluid-structure interaction, both vortex shedding and its induced vibration may be affected at the same time. Based on this idea, a novel

technique, referred to as the perturbation technique, is conceived to provide a possible control of both flow and structural vibration. The local perturbation is imposed on the structural surface using piezoelectric actuators.

2.3 Piezoelectric Effect and Piezoceramic Actuator

The piezoelectric phenomenon was first discovered in 1880 by Pierre and Jacques Curie who demonstrated that when a stress field (p) was applied to certain crystalline materials, an electrical charge was produced on the material surface (Jaffe *et al.* 1971). It was subsequently demonstrated that the converse effect was also true; when an electric field (E) was applied to a piezoelectric material it changed its shape and size. This effect was found to be due to the electrical dipoles of the material spontaneously aligning in the electric field. Figure 2-1 shows a schematic graph illustrating the process.

Due to the internal stiffness of the material, piezoelectric elements were further found to generate displacement and force to some extent when their natural expansion was constrained. This observation ultimately led to their use as actuators in many engineering applications. The actuator made of Lead Zirconate Titanate (PZT) is a typical example. The piezoelectric actuator has many advantages, for instance, relative temperature insensitivity, linear response at low excitation levels, lightweight, flexibility and broadband frequency response, and so on. Traditional piezoelectric actuators, however, suffer from some inherent drawbacks. First, they have very limited displacement and load capacity. As mentioned in Yoon *et al.* (2002), monolithic piezoelectric actuators can generate massive stress (~ tons/in^2) but only nimiscale strain (~ 10^{-3}). A proper design of mechanical amplification system is

usually needed to increase the displacement generation at the expense of reducing the loading capacity. Second, they have significant hysteresis and creep at large electric field level. Third, piezoelectric effect generated through poling may decay, thus leading to aging effects and performance degradations.

2.4 THUNDER Actuator and its Installation

The perturbation technique proposed in the present work is based on the use of a type of advanced pizeoceramic actuators, called THUNDER (THin layer composite UNimorph piezoelectric Driver and sEnsoR), which overcome the aforementioned drawbacks related to conventional piezoelectric actuators. THUNDER was developed by NASA Langley research center. It can provide larger displacement and load capacity, smaller dimensions, more reliability, strength and flexibility than the traditional ones. This owes to a particular fabrication process (Copeland *et al.* 1999). THUNDER is a layered composite in which individual materials are layered on top of each other to form a "sandwich", comprising a metal base layer, a piezoelectric layer at the middle and an aluminum foil on the top; LaRC^{TM}-SI adhesive is applied between the layers (Figure 2-2(a)). The entire assembly is placed into an autoclave for processing. During the autoclave cycle, the "sandwich" is heated and squeezed, allowed to cook and then cooled to room temperature. During the cool down cycle, the mismatch in coefficients of thermal expansion causes the metal and ceramic layers to contract at different rates, and they begin to work against one another, putting the ceramic in compression at room temperature. However, the strength of the adhesive bond holds everything together. The result is a "pre-stress" internal to the individual layers, which results in the characteristic bend or curvature of the finished product

(Figure 2-2(b)). As illustrated in Figure 2-2(c), under an applied voltage, the actuator deforms out of plane. To our knowledge, various applications using THUNDERs have been explored by several researchers. Typical examples include vibration isolation (Marouzé & Cheng, 2002), precision positioning (Horner & Taleghani, 2001), airfoil shaping (Pinkerton & Moses, 1997) and active noise control (Jayachandran *et al.* 1999), etc.

Two appealing features motivate the choice of THUNDER actuators in the present work. The first is its high displacement and high load capacity within a wide range of frequency. This feature may ensure the actuator to impose sufficient effect to the flow-structure system. The second is its small size, which makes it possible to be placed inside a structure in a much easier and less intrusive way than many conventional actuators such as loudspeakers and electromagnet actuators. THUNDERs (model TH 8-R) manufactured by Face International Co. were selected as the actuator in this work. Specifically, without any loading, this actuator may vibrate at a maximum displacement of about 2 mm and a frequency up to 2 kHz. It has small dimensions, with a length, width and height of 63.5 mm, 12.7 mm and 3.83 mm, respectively, and has a maximum force capacity of 67 N.

A proper installation of the THUNDER actuators is a key factor to fully explore its high displacement feature. Various experiments were conducted to find the most suitable installation method of the actuator inside a structure. In all tests, a THUNDER, without any loading, was driven by a sinusoidal signal generated by a signal generator (HP-DS345) and amplified by a dual-channel piezo driver amplifier (Trek PZD700-2). The excitation voltage and frequency of the signal were adjusted within the range from 0 to 200 volts (root mean square value) and from 0 to 2 kHz,

respectively, during experiments. The apex displacement of the THUNDER in the vertical direction was measured using a Polytec Series 3000 Dual Beam Laser Vibrometer (Polytec Series 3000) and the output was analyzed using a personal computer with a 12-bit A/D board at a sampling frequency of 3.5 kHz per channel.

The ideal working condition for a THUNDER is to have both ends free, since the vertical displacement at the midpoint of the apex is generated by a change in the radius of curvature. However, practical consideration requires at least one rigid supported end, that is, the displacement as well as the slope should be fixed at the end. Then there are three possible methods for installing a THUNDER into a structure as illustrated in Figure 2-3: (1) cantilevered; (2) rigid supported at one end and free at the other end; (3) rigid supported at both ends. Experimental results showed that, under the excitation frequency and voltage, the apex displacements of the actuator were similar using the first two mounting cases, which were much larger than case (3). Considering the practical aspects, the second method was finally used in this work. There were different ways to implement a rigid support at one end of the actuator, such as screw, clamp or silicone-glue, as discussed by Marouzé and Cheng (2002). In the present work, an adhesive tape was used to fix the actuator at one end whilst the other end could move freely along the structural surface (Figure 2-4).

2.5 Embodiment of Perturbation Technique

The mechanical configuration of the preferred embodiment of the technique can be described by way of a schematic, shown by Figure 2-5. A structure with a rectangular cross section being subject to cross flow represents a typical bluff body. Under normal operating conditions and normal installation, one structural surface is

activated and controlled by a plurality of actuators embedded underneath the surface to move generally and substantially orthogonal to the direction of cross flow. By this way, a local perturbation is created to counteract the fluid excitation induced by the flow and subsequently its induced vibration. Note the movement of the movable structural surface is independent of the structure, particularly represented as Y_p.

Specifically, a square cylinder of a height of h with various stiffness and boundary conditions is selected as test model in this work. Figure 2-6 shows one typical design used in this work. Three THUNDERs are embedded in series in a slot on one side of the cylinder to support a thin plastic plate, which is installed flush with the cylinder surface. The length of the plastic plate is 493 mm, 2 / 3 of the cylinder length. One end of each actuator is adhesive tape-fixed on the bottom side of the slot, while the other is free. The actuators and the walls of the slot around the actuators are well lubricated to reduce contact friction. To minimize the asymmetry of the dynamic system, the opposite side of the cylinder is identically constructed. Driven by the actuators, this plate will oscillate to create the local perturbation of the cylinder surface. This experimental setup is implemented in a wind tunnel. The root mean square (r.m.s.) value of Y_p, i.e. $Y_{p,\mathrm{rms}}$, measured using a laser vibrometer, is the same at different spanwise locations along the cylinder, suggesting a uniform oscillation of the surface. Furthermore, the movement of the surface in the streamwise or spanwise direction is essentially negligible. Thus, the perturbation is unlikely to cause any significant three-dimensionality of the flow.

The actuator is a dynamically nonlinear component. Its dynamic response may vary with the activating frequency, even though the imposed voltage is maintained at a constant. In order to demonstrate this, a test using the structure shown in Figure 2-6

was conducted under no-flow conditions and the root mean square value of activating voltage (V_p), i.e. $V_{p,\ rms}$ (= 141.4 volts) on the actuators. The cylinder was fix-supported at both ends and could be approximately considered to be rigid as a whole. The deformation of the activated actuators caused a displacement Y_p on the plastic plate. The $Y_{p,rms}$ varied with the perturbation frequency f_p (Figure 2-7), showing a maximum of $0.021h$. The actuators have been designed such that the peak in $Y_{p,rms}$ occurred around the region of interest.

A control system is needed to control the motion of the actuators. Two methods can be deployed: open-loop and closed-loop. For open-loop control, the actuators are directly excited using a signal with controllable frequency and amplitude generated by a signal generator, while for closed-loop control, they are activated by the signal from a feedback system. The feedback control system takes the instantaneous signals from structural vibration or/and the flow velocity behind the structure as its input. The structural vibration may be detected by vibration sensing means disposed on appropriate parts of the structure and the flow velocity may be measured using the flow velocity sensing means. Based on the feedback signals measured by the two sensing means, the controller of the feedback control system generates the excitation signals to drive the actuators and thus control the movement of the movable structural surface along Y_p direction.

To further illustrate the closed-loop scheme, Figure 2-8 supplies a schematic block diagram of a typical feedback control system used in the present work. It can be seen that the vibration characteristics of the structure are detected by a laser vibrometer as input to a conditioner. The conditioned signal is used either as input to the feedback controller or to monitor the modification of structural vibration. The

flow velocity is detected by a first and a second detection means which can be, for example, tungsten hot wires. In the present example, the first detection means (hot wire ①) is for monitoring the downstream flow velocity when the flow passes the structure and the second detection means (hot wire ②) is for acquiring the feedback signal of the vortex shedding. The two flow information are fed into a CTA (Constant Temperature Anemometer), which is an amplifier used for amplifying the flow velocity signal. The structural vibration and flow velocity can be used as feedback signals either separately or simultaneously. After that they are fed into a low-pass filter and then are input into an analogue-to-digital converter (ADC) for processing by a controller. In the present work, a digital Proportional-Integral-Derivative (PID) controller is used. Proportional gain (P), integral gain (I) and derivative gain (D) of the PID controller can be tuned to generate an output signal, which is converted by a digital-to-analogue converter (DAC) into an analogue stream of signals. The analog signals are low-pass filtered again before they are amplified to activate the actuators. The signals monitoring structural vibration and flow velocity can be recorded by a PC for further analyses.

The controller used in this work is developed and implemented based on a dSPACE system installed in a computer, which is an open software platform and has a real-time system for rapid control prototyping, production code generation and hardware-in-the-loop tests. Specifically, the model of the controller is first designed using SIMULINK function of MATLAB 6.0 and simulated off-line. The accessory software (ControlDesk 2.0) of dSPACE system is run to activate the Real-Time Interface (RTI) file. The RTI is the link between dSPACE's real-time systems and the MATLAB/SIMULINK. It extends Real-Time Workshop (C code generator) for the

seamless and automatic implementation of SIMULINK models on the present dSPACE real-time hardware, digital signal processor (DSP) system. The DSP system performs mathematical operations to digitally represent signals and used for sampling and processing feedback signals. In addition, the parameters of the controller can be conveniently tuned using the virtual instruments editor within ControlDesk software providing friendly dialog and property pages that customize the instrument's common properties. As an example, Figure 2-9 displays the interface of a PID controller used in this work (the upper window). A SIMULINK model is shown in the lower window.

2.6 Major Experimental Facilities

In the present work, all experiments were conducted in a closed circuit wind tunnel with a square working section (0.6 m × 0.6 m) of 2.4 m in length. Using an axial fan and an AC power (380 vlots, 60 Hz, 3ϕ, 60 Hp), the contraction ratio is 9:1. The wind speed of the working section is up to 50 m/s, which is controlled by a Dynagen inverter (S36-4060-686 90Amps) with a resolution of 0.3 rpm/60 Hz. The streamwise mean velocity uniformity is about 0.1% and the turbulence intensity is less than 0.4%. Some advanced experimental facilities, such as particle image velocimetry (PIV) for the measurements of iso-contours of spanwise vorticity and flow visualization and laser Doppler anemometer (LDA) for the measurement of flow velocity profiles as well as some conventional facilities, such as laser vibrometer and hot wire, etc, were thoroughly used in the measurements of this thesis.

The velocity field is measured using a Dantec standard PIV2100 system. Figure 2-10 illustrates a PIV system. Flow is seeded by smoke, which is generated from Paraffin oil, of a particle size around 1 μm in diameter. Flow is illuminated in the

plane of mean shear by two New wave standard pulsed laser sources of a wavelength of 532 nm, each having a maximum energy output of 120 mJ. Digital particle images were taken using one CCD camera (HiSense type 13, gain × 4, double frames, 1280 × 1024 pixels). The CCD used is 1k by 1.3k cooled one with 12 bits and 9 Hz. A Dantec FlowMap Processor (PIV2100 type) is used to synchronize image taking and illumination. The processor, with a capacity of 32 GB and a bandwidth of 133 MB/s, has 4 channels plug and play camera kits. Using 100 Mbit Ethernet and optional Gigabit Ethernet under TCP/IP protocol, the processor may communicate with application PC. In addition, the processor has 4 BNC channels for analogue reference, 4 25-pin D-sub channels for TTL output, 3 BNC channels for Triggers and Trigger enable and one laser synchronization cable for laser trigger. A wide-angle lens is used so that each image covered enough area for observation. An optical filter is used to allow only the green light (the wavelength = 532 nm) generated by a laser source to pass.

The flow visualization measurement is conducted using the flow visualization function of the PIV system. The same smoke as used in the PIV measurement is introduced through eight injection pinholes (diameter = 1 mm), symmetrically distributed at the mid-span of the leading side (normal to the flow direction) of the cylinder. The CCD camera is used on the single-exposure mode. A wide-angle lens is also used to enlarge the view-field.

The mean velocities, $\overline{U}$ and $\overline{V}$, and fluctuating velocities, u and v, along longitudinal and lateral direction, respectively, in the wake are measured using a two-component laser Doppler anemometer (LDA) system (Dantec Model 58N40 with an enhanced Flow Velocity Analyzer signal processor), shown by the photo in Figure 2-

11. The laser is SP2017 argon ion with 5 W power output. The measuring volume has a minor axis of 1.18 mm and a major axis of 2.48 mm. Thus, the measured mean velocity is estimated to have an error of less than 3% and the corresponding error for the measured r.m.s. values, u_{rms} and v_{rms}, is less than 10%. The maximum velocity of measurement is close to velocity of sound and the measurement distance ranges from 10 millimeters to several meters. The frequency response range is from 2.23 Hz to 100 MHz. The seeding is provided by smoke, the same as used in the PIV and flow visualization measurements. The focus of the optics system, being placed horizontally or vertically, may be flexibly adjusted and the length of its optical fiber may extend up to more than 20 meters. In addition, the software and hardware of the LDA system are controlled by an advanced FVA system control platform, for result display.

2.7 Conclusions

The concept of the so-called perturbation technique is introduced in this chapter. Practical means are also provided to implement the technique using piezoceramic actuators, i.e., THUNDER. Major facilities that will be used in the following chapters are briefed. It is shown that

1) The essence of the proposed perturbation technique is to generate a local perturbation on the cylinder surface to perturb the interaction between the flow and structural vibration. Both open- or closed-loop control methods should be investigated.
2) Due to its superior characteristics over conventional actuators, such as high displacement range, high loading capacity and small dimensions, THUNDER is a promising candidate and is selected to implement the technique. Details

regarding its installation are important to ensure a maximum performance of the actuators.

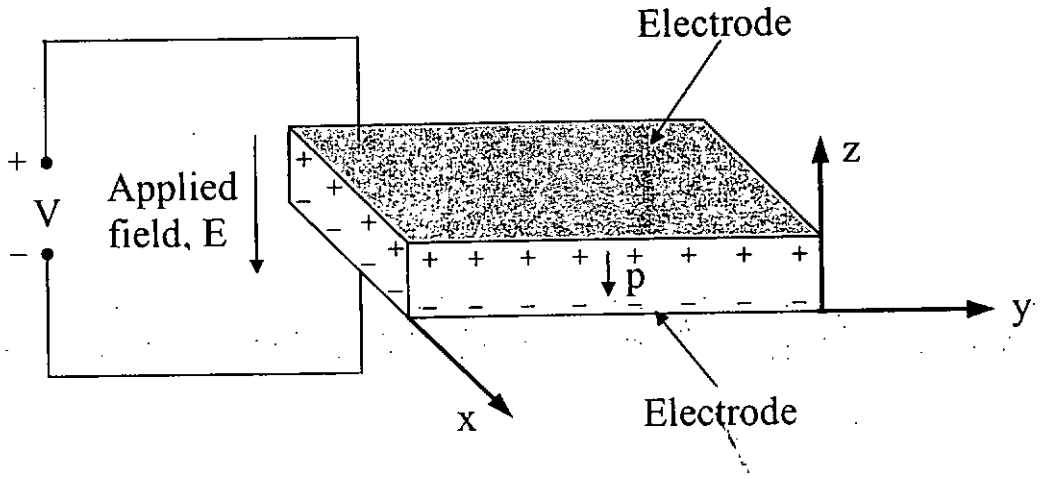

Figure 2-1 Principle of piezoelectricity

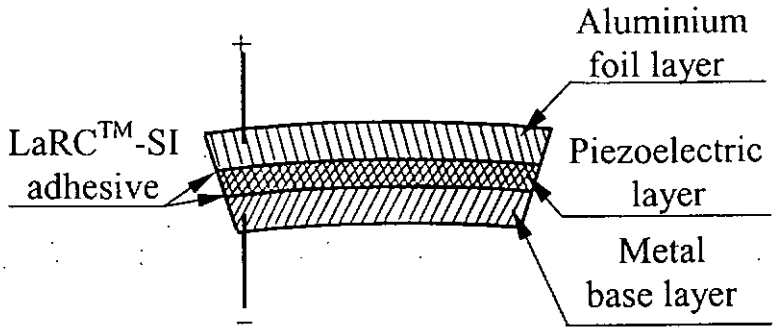

(a)

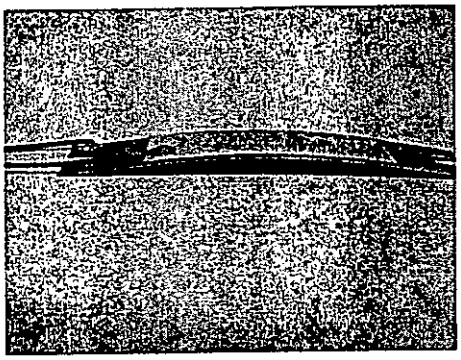

(b)

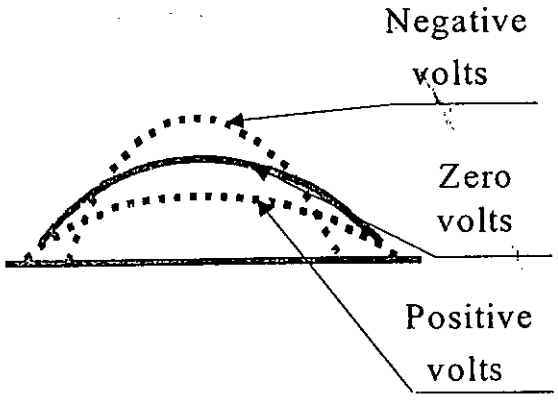

(c)

Figure 2-2 Description of THUNDER actuators: (a) cross sectional view; (b) photo of THUNDER; (c) typical deformation vs. applied voltage.

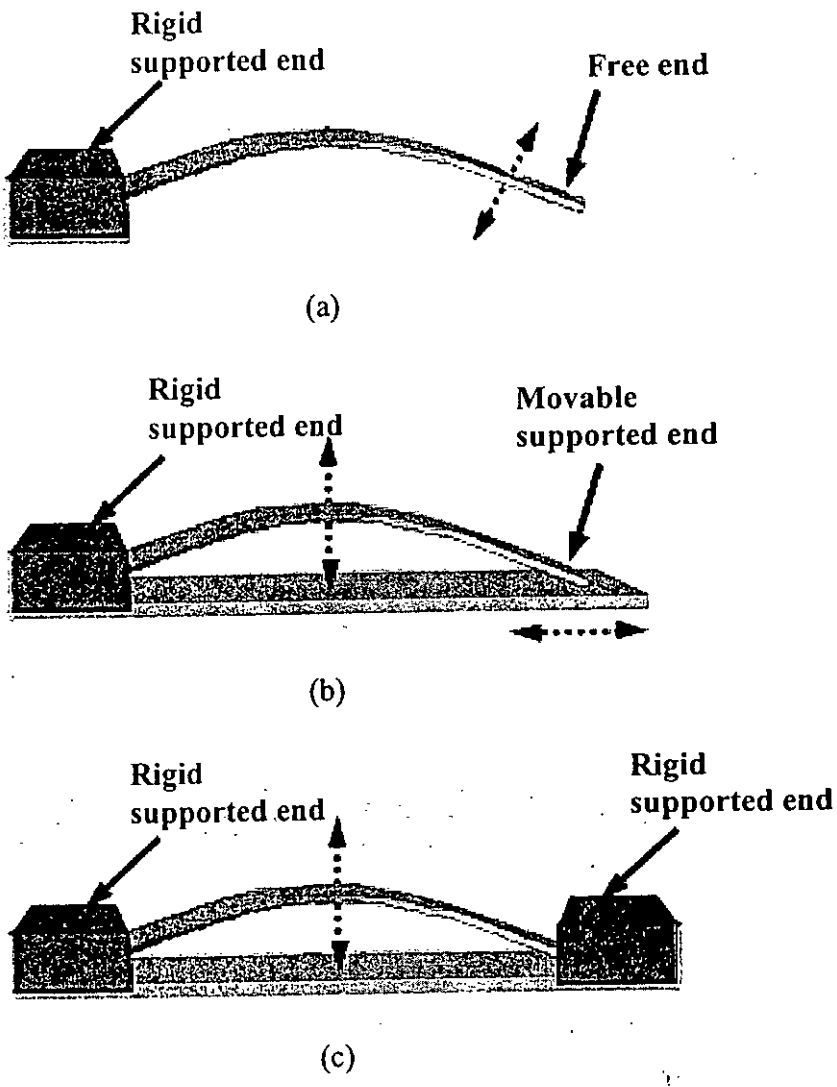

Figure 2-3 Schematic of THUNDER installment methods: (a) cantilevered; (b) rigid supported at one end and movable supported at the other end; (c) rigid supported at both ends.

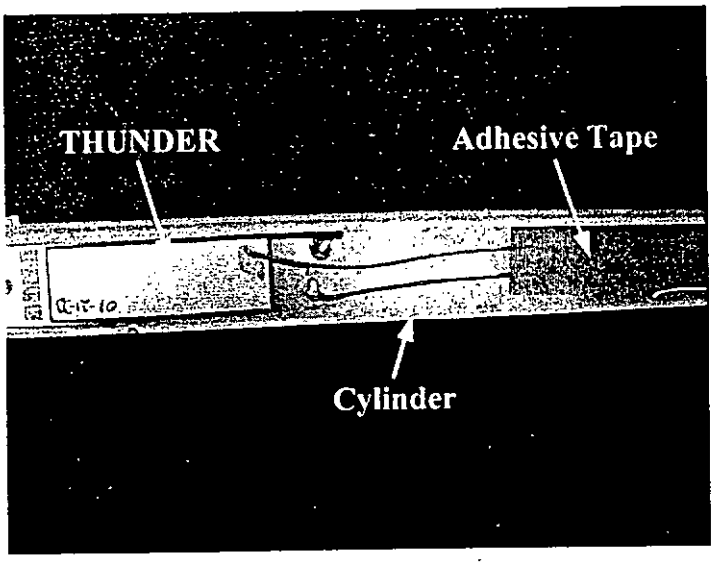

Figure 2-4 Photo of THUNDER using adhesive tape to fix one end.

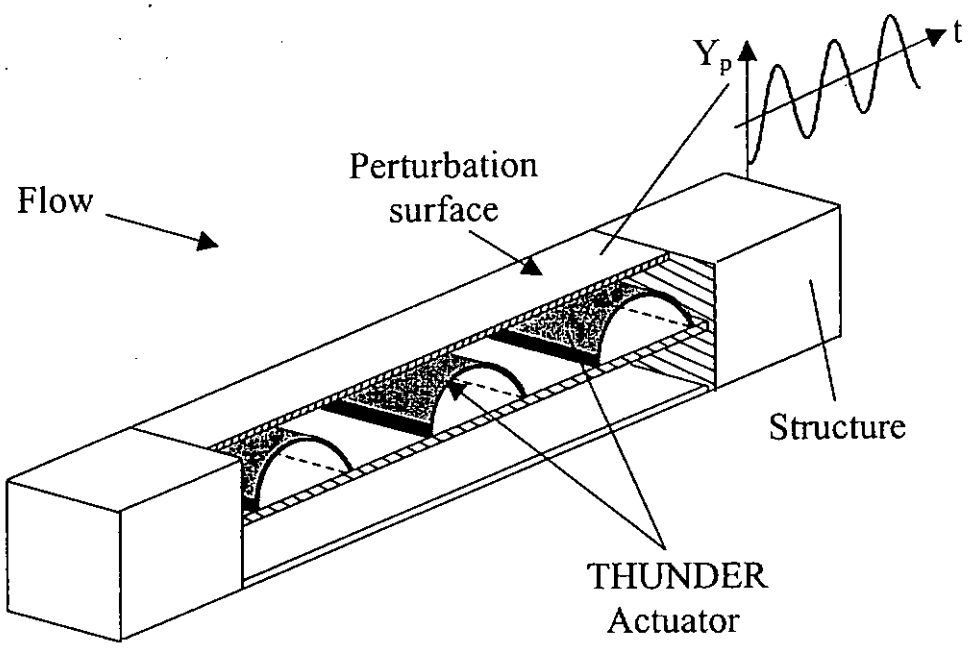

Figure 2-5 A partially exploded view of a structure under cross flow.

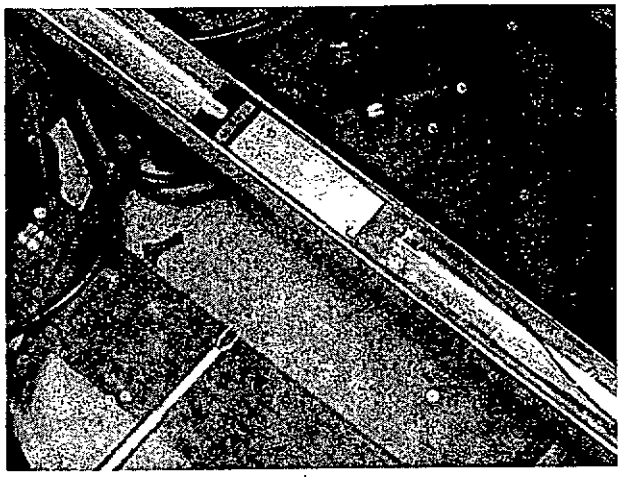

(a)

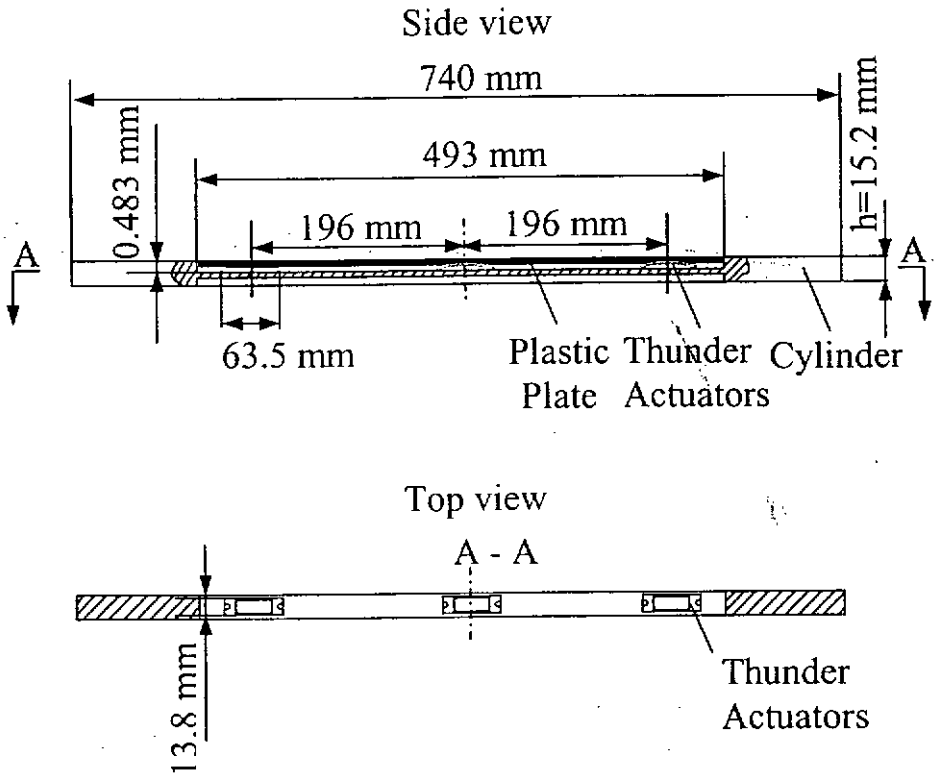

(b)

Figure 2-6 Photograph (a) and schematic arrangement (b) of THUNDERs installed in the square cylinder.

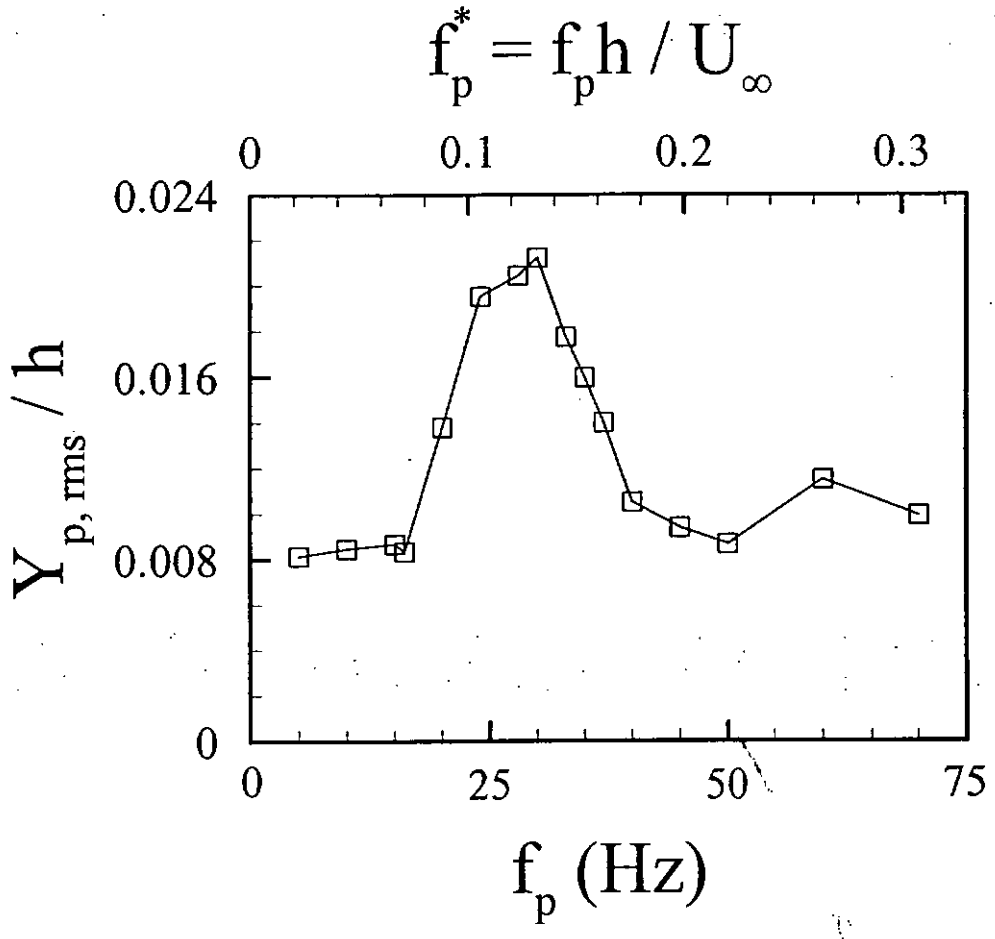

Figure 2-7 Dependence of the perturbation amplitude on the perturbation frequency under a constant voltage (no flow).

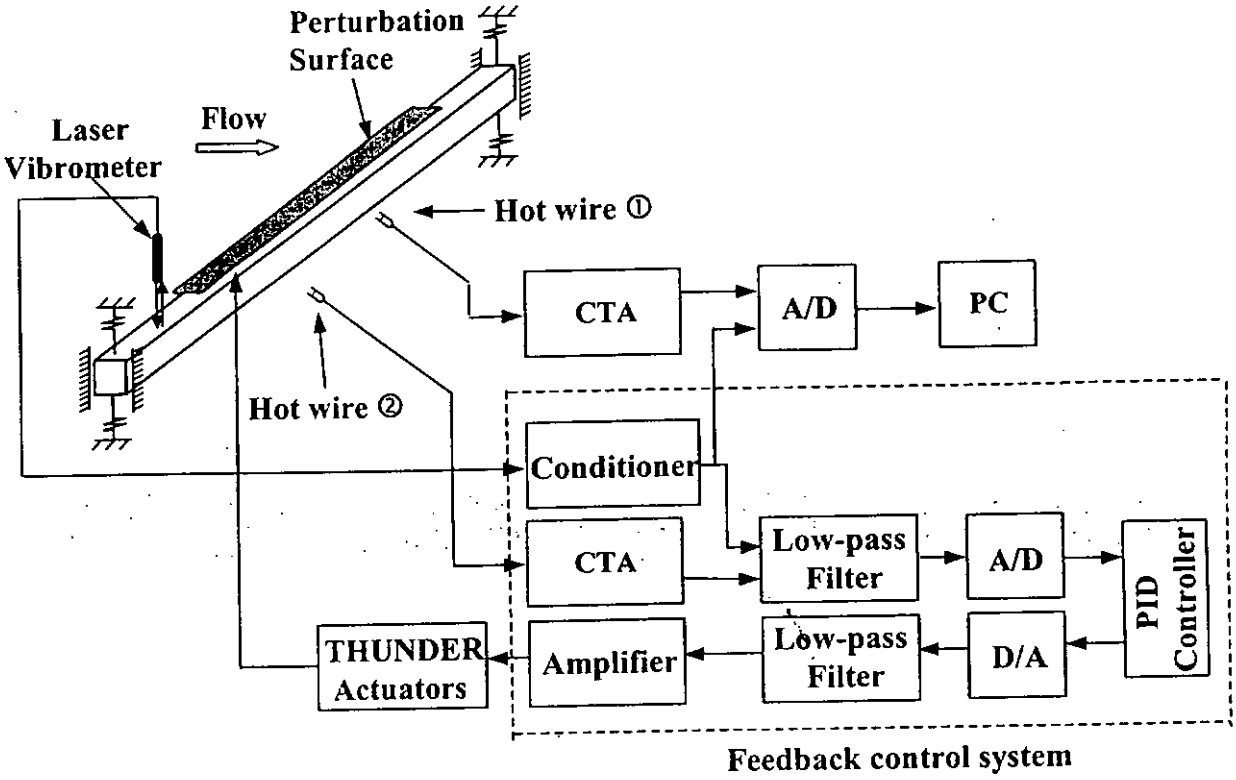

Figure 2-8 Schematic block diagram showing an exemplary feedback control means of perturbation technique.

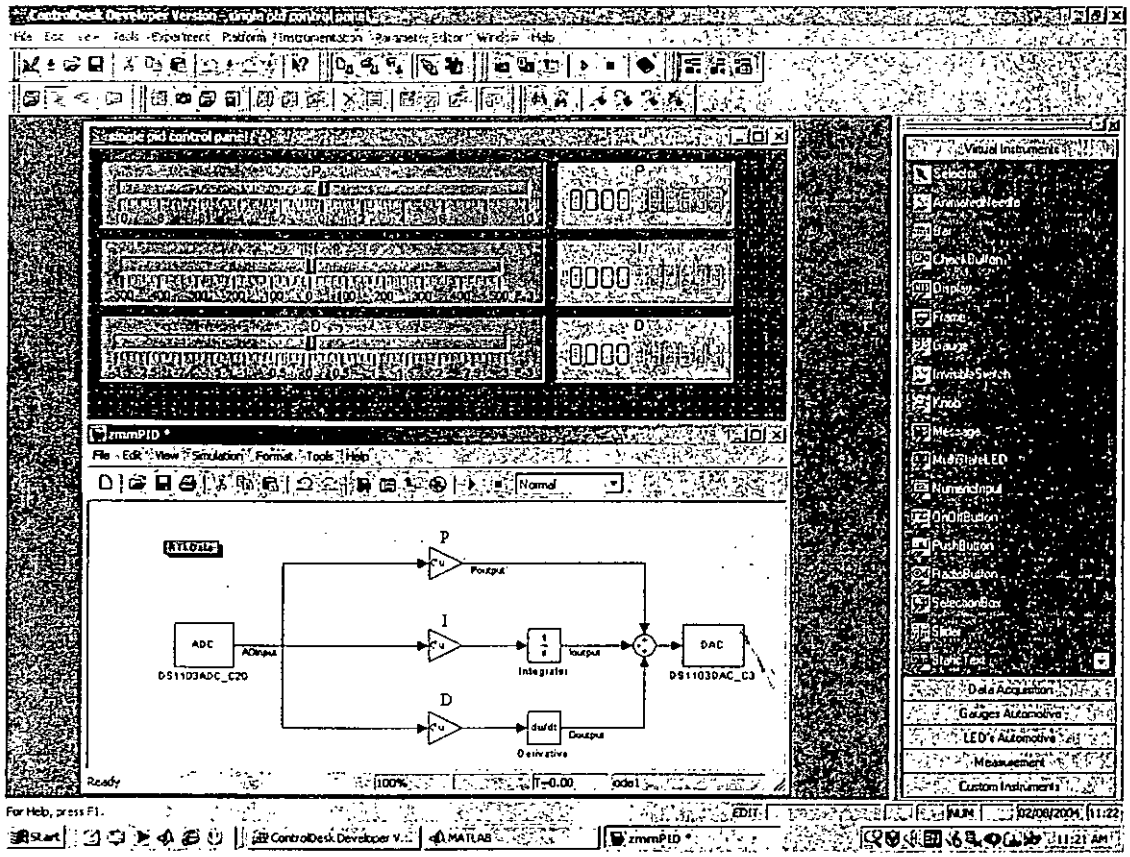

Figure 2-9 Typical interface of PID controller used in this work.

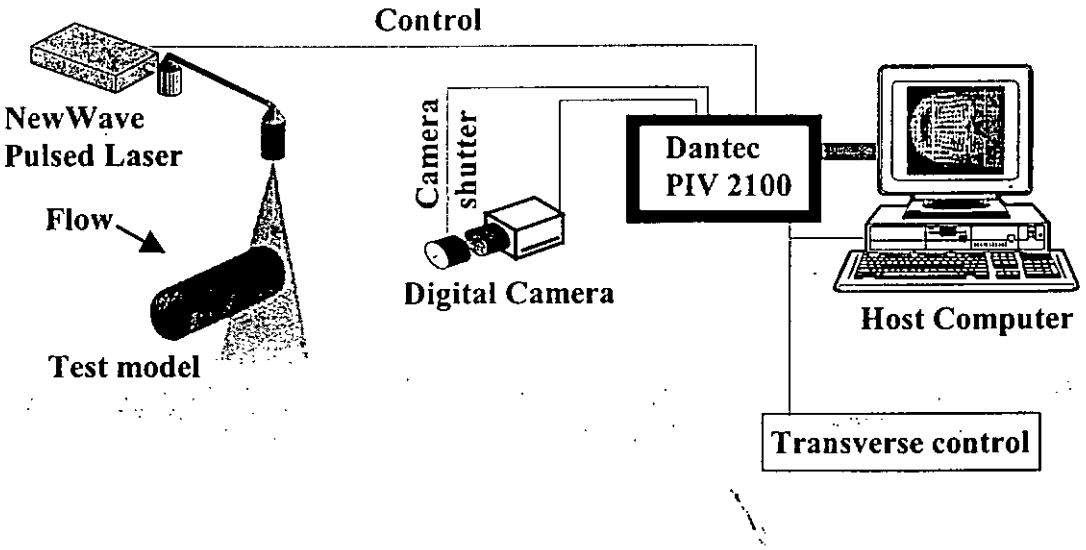

Figure 2-10 Typical PIV measurement using Dantec standard PIV2100 system.

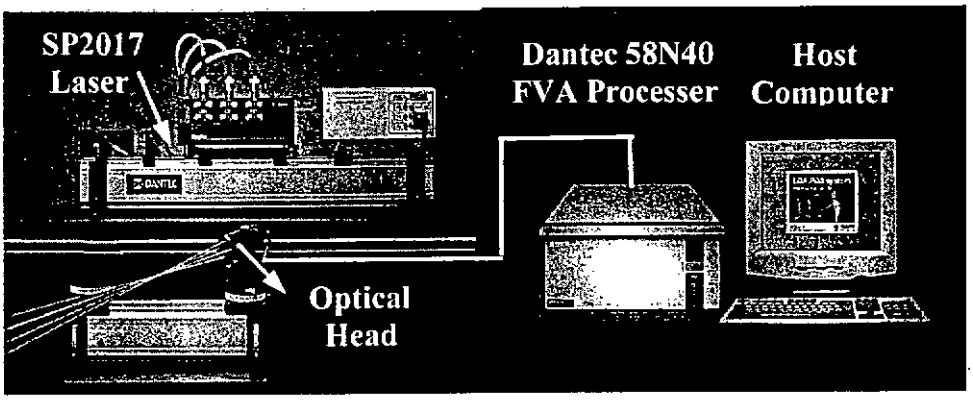

Figure 2-11 Typical LDA measurement using Dantec standard 58N40 FVA system.

CHAPTER 3

OPEN-LOOP CONTROL OF FLUID-STRUCTURE INTERACTION ON A FLEXIBLE-SUPPORTED CYLINDER

3.1 Introduction

Fluid flowing over a bluff body is often seen in engineering. Examples include flow past heat exchangers, offshore structures, power transmission lines, and high-rise buildings. Beyond a critical Re, a pair of staggered vortex streets forms and subsequently their alternating shedding happens behind the body. When the vortex shedding frequency is near to the natural frequency of the body, resonance or synchronization will occur (Griffin and Hall, 1991). Under resonance, the vortex shedding and its induced structural vibration will be greatly enhanced. The resonant structural vibration could have significant impact on the fatigue life of structures, even leading to disastrous consequences. The painful lessons include the collapse of the Tacoma Narrows Bridge due to a sustained steady wind producing vortex shedding at resonance frequency of the bridge over a long period and the damage of piling during the construction of an oil terminal on the Humber estuary of England in 1960s (Griffin & Ramberg, 1976). So this kind of vibration should be effectively

suppressed. On the other hand, the enhancement of vortex shedding is desired for some engineering applications, such as combustion and heat transfer (Gau *et al.* 1999; and Konstantinidis *et al.* 2003). As mentioned in Section 1.3, in order to obtain the satisfactory results for these engineering problems, both vortex shedding and structural vibration should be controlled simultaneously by modifying the resonant fluid-structure interaction using control methods. This issue is discussed in this Chapter using a flexibly-supported cylinder undergoing resonance in a cross flow. The perturbation technique described in Chapter 2, together with an open-loop control scheme, is applied. Both impaired and enhanced cases are considered.

Experiments use techniques such as flow visualization, PIV, laser vibrometer and hot wire, to measure the perturbation effect on structural vibration and vortex strength. Furthermore, to discuss the preliminary mechanism, the perturbed fluid-structure interaction is investigated by a simultaneous measurement of flow and structural vibration using laser vibrometer and hot wire. Additionally, the variation in the cross-flow distribution of Reynolds stresses is also measured using a two-component LDA system.

3.2 Experimental Setup

Experiments were conducted in a closed circuit wind tunnel. See the corresponding part in Section 2.6 for more information. An aluminum alloy square cylinder of side h = 0.0152 m was mounted horizontally in the midplane, 0.2 m downstream of the exit plane of the contraction, and spanned the full width of the working section, resulting in a blockage of about 2.53%. The cylinder, supported on springs at both ends, was allowed to vibrate laterally (Figure 3-1). The spring system

is outside the wind tunnel. Each spring is supported by a wide base which has the same length as the cylinder height and connects the spring with the cylinder. During experiments, when the cylinder is subject to the rocking vibration excited by the flow, the four springs may exert an opposite moments to the cylinder by the spring base. Then the rocking vibration may be constrained automatically. Therefore the rocking vibration was negligible, which was checked using laser vibrometer. On the other hand, using laser vibrometer, the along-wind movement was measured to be less than 0.1 mm, much less than the structural displacement in the transverse direction (≈ 1.2 mm). Thus the along-wind movement was also found to be negligible. Measurements were carried out on the resonant condition of the fluid-structure system when the vortex shedding frequency (f_s) was very near to the natural frequency (f_n = 30 Hz) of the cylinder. By tuning the stiffness of the springs, the natural frequency of the cylinder could be set to be 30 Hz, which was determined from the frequency response of the cylinder vibration when excited with an electromechanical shaker under no flow condition. The corresponding reduced velocity, $U_r (\equiv U_\infty / f_n h)$, was about 7.8, Re was 3500.

Using the half-power technique, the structural damping ratio, ζ, was estimated to be 0.034, giving a reduced damping or Scruton number, $2m(2\pi\zeta)/\rho h^2$, of 15.2 in the synchronization range, where m is the mass per unit length of cylinder; ζ the damping factor and ρ the air density. The Scruton number is a very important parameter, which governs the synchronization between vortex shedding and induced vibration. This number is in this case well below the critical value, i.e. 64, as proposed by Blevins (1990), implying an oscillation of significant amplitude. The

normalized root mean square value (r.m.s.), Y_{rms}/h, of Y versus the reduced velocity U_r ($U_\infty / f_n h$) is given in Figure 3-2. Y_{rms}/h shows its maximum, about 0.055, at $U_r \approx$ 7.8 (Re = 3500), where the resonance occurs. The corresponding maximum displacement of the cylinder was about 1.2 mm, or $0.08h$. The correspondence between the measured Y / h and the Scruton number at resonance is in good agreement with the data given in Figure 3-21 of Blevins (1990).

Three THUNDER actuators were embedded in series in a slot on one side of the cylinder to support a thin plastic plate of 3 mm thick which was installed flush with the top cylinder surface. The actuators were activated by a signal generated from a signal generator (HP-DS345) and amplified by a dual channel piezo driver amplifier (Trek PZD 700-2). Driven by the actuators, this plate would oscillate to create the local perturbation of the cylinder surface. The detailed installation arrangement and geometry dimension of the actuators were described in Figure 2-6.

A Dantec standard PIV2100 system introduced in Section 2.6 was used to measure the perturbation effect on velocity field. Digital particle images were taken using one CCD camera (HiSense type 13, gain × 4, double frames, 1280 × 1024 pixels). A wide-angle lens was used so that each image covered an area of 150 mm × 120 mm of the flow field, i.e., $x / h \approx 0.8 \sim 10.8$ and $y / h \approx -2.7 \sim 5.2$; the x and y coordinates and their origin are defined in Figure 3-1. The longitudinal and lateral image magnifications were identical, i.e., 0.12 mm/pixel. Each laser pulse lasted 0.01 μs. The interval between two successive pulses was typically 50 μs. Thus, a particle would only travel 0.179 mm (1.53 pixels or $0.0118h$) at U_∞ = 3.576 m/s, which was used for measurements. In the image processing, 32 × 32 rectangular interrogation

areas were used. According to the PIV manual, the optimal pixel distance corresponds to 1 / 4 interrogation length for good two-dimensional PIV measurement. Specifically, 1 / 4 interrogation length, i.e. 8 pixels distance, seems to be optimal in the present work. However, optimal pixel distance, adjusted by the time between two successive pulses, is enslaved to two factors: orientation precision and the number of effective particles. The large optimal pixel distance corresponds to high orientation precision and small effective particles and vise versa. To balance the two factors and subsequently obtain good PIV results, the interval between two successive pulses was set to be 50 μs, corresponding to a 1.53 pixels distance at U_∞ = 3.58 m/s. In addition, each interrogation area included 32 pixels ($\approx 0.25h$) with 25% overlap with other areas in either the longitudinal or lateral direction. The ensuing in-plane velocity vector field consisted of 53 × 42 vectors. Spanwise vorticity component, ω_z, was approximately obtained based on particle velocities using a central difference scheme. The spatial resolution of vorticity estimate depends on grid spacing, about 2.9 mm or $0.19h$.

The control effect on flow pattern was conducted using the flow visualization function of the PIV system. The same smoke as used in the PIV measurement was introduced through eight injection pinholes (diameter = 1 mm), symmetrically distributed at the mid-span of the leading side (normal to the flow direction) of the cylinder. The CCD camera was used on the single-exposure mode. A wide-angle lens was also used to enlarge the view-field so that each image covered an area of approximately 165 mm × 125 mm or $x / h \approx 0.33 \sim 11.2$ and $y / h \approx -4.1 \sim 4.1$ in the flow field. The recording interval between successive images was 0.143 s. Other configuration parameters were similar with the PIV measurement.

In order to investigate the underlying physics of the perturbation technique, a Polytec Series 3000 Dual Beam Laser Vibrometer (Zhou *et al.* 1999) and a 5 μm tungsten hot wire were used to measure simultaneously the structural displacement and flow velocity, respectively. The hot wire, placed at $x / h = 2$ and $y / h = 1.5$, was operated at an overheat ratio of 1.8 with a constant temperature anemometer. Signals from both the laser vibrometer and the hot wire were conditioned and digitized using a 12-bit A/D board at a sampling frequency of 3.5 kHz per channel. The duration of each record was about 20 s.

In addition, the mean flow velocities, $\overline{U}$ and $\overline{V}$, and fluctuating velocities, u and v, along the x and y direction, respectively, in the wake ($x / h = 3 \sim 25$) was measured before and after perturbation using a LDA system described in Section 2.6.

3.3 Tuning of Perturbation Amplitude and Frequency

Tests were conducted to document the tuning of perturbation amplitude and frequency, Y_p and f_p, on the resonance. The aim of parameters tuning is to find the appropriate values for the perturbation voltage ($V_{p,\mathrm{rms}}$) or Y_p and f_p, under which the structural vibration Y and fluctuating flow velocity u can be effectively controlled. To this end, experiments were first carried out to determine the optimal $V_{p,\mathrm{rms}}$ by keeping f_p constant. It was found that a higher $V_{p,\mathrm{rms}}$ necessarily leads to a better result. Since the amplitude voltage exerted on the actuator must be less than 200 volts, the $V_{p,\mathrm{rms}}$ is set to be 141 volts. Figure 3-3 presents the variation of the r.m.s. displacement, Y_{rms}, of the cylinder and the r.m.s. streamwise velocity, u_{rms}, with f_p. A constant voltage, whose r.m.s. value was 141volts, was applied on the actuators as f_p varied. The broken lines indicate Y_{rms} and u_{rms} without perturbation. Y_{rms} and u_{rms} exhibit similar variation

with f_p. The maximum attenuation occurs at $f_p^* = f_p h / U_\infty = 0.1$, resulting in $Y_{rms} = 0.014h$ and $u_{rms} = 0.12\,U_\infty$. Unless otherwise stated, the asterisk in this chapter denotes normalization by h and U_∞. For $f_p^* < 0.1$, both Y_{rms} and u_{rms} are smaller than those without perturbation, but appreciably larger than those at $f_p^* = 0.1$. It is worthwhile recalling that $Y_{p,rms}$ displays a broad peak between $f_p^* = 0.1$ and 0.13, and reduces substantially for $f_p^* < 0.1$ or $f_p^* > 0.13$ (Figure 2-7). The variation in $Y_{p,rms}$ will have an impact on Y_{rms}. Figure 3-4 shows the variation in Y_{rms} with r.m.s. voltage ($V_{p,rms}$), imposed on the actuators, at a fixed f_p^* (= 0.1). The voltage and $Y_{p,rms}$ are correlated, though not linearly (Wilson & Tinsely, 1989). As the $V_{p,rms}$ increases from 0 to 141 volts, $Y_{p,rms}$ should increase and hence Y_{rms} decreases from $0.056h$ to $0.014h$. Therefore, the small $Y_{p,rms}$ for $f_p^* \leq 0.08$, as compared with that at $f_p^* = 0.1$ (Figure 2-7), may partially account for the less effective attenuation in Y_{rms} and also u_{rms} (Figure 3-3).

A pronounced peak in Y_{rms} and u_{rms} occurs at $f_p^* = 0.13$, coinciding with the frequency of vortex shedding from a square cylinder (Vickery, 1966; Lyn & Rodi, 1994; and Zhou & Antonia, 1995), namely, $f_p^* = f_s^* = f_n^*$. Both Y_{rms} and u_{rms} are doubled, compared with the unperturbed one. Apparently, perturbation leads to a much more violent resonance, acting as an 'amplifier'. As $f_p^* > f_s^* = f_n^*$, the resonance is less 'amplified', but in general more violent than that without perturbation. Again, the decreased $Y_{p,rms}$ for $f_p^* > 0.13$ may be partially responsible for the less effective amplification than that at $f_p^* = 0.13$.

Note that both Y_{rms} and u_{rms} exhibit local peaks at $f^* = 0.065$ and 0.26, namely at the sub-harmonic and the second harmonic of $f_n^* = 0.13$. This is probably due to a partial synchronization between f_p^* and f_n^*. The observation suggests that, in order to avoid violent resonance, perturbation should be avoided at a sub-harmonic or harmonic frequencies of the system natural frequency.

3.4 Perturbation Effects on Flow and Structural Vibration

3.4.1 Impaired effect

In Figure 3-3, it is obvious that when the synchronising flow excitation and structural vibration were perturbed at $f_p^* = 0.1$ ($Y_{p,rms} = 0.02h$) and $f_p^* = 0.13$ ($Y_{p,rms} = 0.021h$), Y_{rms} and u_{rms} reached the minimum and maximum value, respectively. Here $V_{p,rms}$ is about 141 volts. The results were examined and compared with those without perturbation. So in order to exhibit the most significant effect of the perturbation technique on Y and u, experiments were first carried out under the two cases.

Figure 3-5 shows the photograph taken using the flow visualization technique when the fluid-structure system was under the resonance condition, i.e., $f_s^* = f_n^* = 0.13$ (Re = 3500, $U_r = 7.8$), without any external perturbation. The solid square in the figure indicates the cylinder position. The Kármán vortex street is evident. The iso-contour (Figure 3-6) of the normalized spanwise vorticity, $\omega_z^* = \omega_z h / U_\infty$, from the PIV measurement show similar flow pattern. The uncertainty of the vorticity measurement was estimated to be about 9%. The flow visualization and PIV results presented in this thesis are all instantaneous instead of phase-averaged. Two reasons

may explain this. First, the maximum rate of the present PIV2100 system for flow visualization and PIV measurement is about 4 photos/sec and subsequently it is impossible to capture photos at almost the same phase within each cycle. Second, in each chapter, many results like time histories, power spectra and LDA measurement, and so on, are enough to verify the effectiveness of the control. Thus flow visualization and PIV measurements are only used to provide additional evidence instead of very accurate quantitative measure. During experiment, hundreds of flow visualization and PIV photos were taken before and after control and the results were found to be repetitive to some extent. Finally, the typical one with averaged vorticity value and flow pattern was selected to represent the corresponding control case.

Once a perturbation was introduced at $f_p^* = 0.1$, however, the flow structure changed drastically, as shown in Figure 3-7. The quantitative information on the impaired vortex street may be gained from the contour of ω_z^* (Figure 3-8). The magnitude, $\left|\omega_{z\max}^*\right|$, of the maximum ω_z^* drops by about 50%. Furthermore, the size of vortices also shrinks significantly. The circulation around a vortex may be estimated by the following numerical integration (Cantwell & Coles, 1983):

$$\frac{\Gamma}{U_\infty h} = \sum_{i,j} (\omega_z^*)_{ij} \frac{\Delta A}{h^2}, \tag{3-1}$$

where $(\omega_z^*)_{ij}$ is spanwise vorticity over area $\Delta A = \Delta x \Delta y$ with Δx and Δy being the integral step along x and y directions, respectively. Integration was conducted over an area enclosed by the cutoff level $\left|\omega_{zc}^*\right| = 0.4$, about 10% of $\left|\omega_{z\max}^*\right|$, as used by Sumner *et al.* (2000). The error associated with the estimation of Γ is about 15%. Evidently,

the estimation error of Γ mainly attributes to the measurement uncertainty of spanwise vorticity ($(\omega_z^*)_{ij}$). In Sumner *et al.* (2000), a uniform rotation was applied to one digital image taken by the PIV system to create another digital image. Then based on this image pair, a cross-correlation PIV algorithm was used to compute the vorticity field. Since the applied rotation was known, the theoretical vorticity was easy to be calculated. Thus the measurement uncertainty could be estimated by comparing the experimental and theoretical vorticity value. In addition, this approach only estimates the error in the cross-correlation and subsequent calculations. Errors due to particle seeding, number of particles, particle image size, light sheet thickness, etc., had to be assessed and accounted for separately. The decrease in Γ exceeds 50%, compared with the case without perturbation (Figure 3-6).

Figure 3-9 shows the typical time histories of the perturbed and unperturbed signal Y. Before the cylinder was perturbed, its vibration amplitude Y along the y direction was 1.2 mm or $0.08h$. There is a drastic change; Y drops from a maximum of $0.08h$ in the absence of the perturbation to about $0.02h$ after being perturbed, about 75% attenuation. Furthermore, the perturbed signal is significantly less periodical than that without perturbation. A similar observation is made of the u signal. The fluctuating velocity amplitude was reduced due to perturbation by about 68%, suggesting a substantial decline in the strength of fluid excitation (Figure 3-10).

3.4.2 Enhanced effect

As the perturbation frequency was increased to $f_p^* = 0.13$, which coincided with the natural frequency of the fluid-cylinder system, the vortex shedding (Figure 3-11) was enhanced. The vortices appear better organized and larger in size when compared

with that without perturbation (Figure 3-5). This is more evident in the contour of ω_z^* (Figure 3-12). The magnitude of the maximum ω_z^* experiences a jump of 38%; the size enclosed by $|\omega_{zc}^*| = 0.4$ increases drastically (c.f., Figure 3-6). Accordingly, a conservative estimate of Γ (part of the area enclosed by $|\omega_{zc}^*| = 0.4$ was outside the PIV image) doubles that in Figure 3-6. Considering a relatively small perturbation amplitude, $Y_{p,\mathrm{rms}} / h$ = 2.1% (Y_{max} / h = 8%), the variation in the vortex street is astonishing, implying a great change in fluid-structure interactions during the vortex shedding process.

It is noteworthy that the surface perturbation was imposed only on the upper side of the square cylinder, but both sides of the wake centerline (Figures 3-5 to 3-8 and Figures 3-11 to 3-12) appear equally affected. The observation suggests that the local perturbation has changed the global interaction between fluid and structure.

3.5 Perturbed Fluid-structure Interaction

It has been seen from Section 3.4 that f_p^* is crucial in how the perturbation would influence the near-wake and implicitly on the fluid-structure interaction. In order to thoroughly understand the f_p^* effect on fluid-structure interactions when synchronization ($f_s^* = f_n^*$) occurs, the structural oscillation and streamwise fluctuating flow velocity were simultaneously measured using the laser vibrometer and a single hot-wire (the hot-wire was located at x / h = 2 and y / h = 1.5), respectively, as f_p^* varied from 0 to 0.34.

Figure 3-13(a) and Figure 3-13(b) display the power spectral density functions, E_Y and E_u, of Y and u, respectively. The spectrum of fluctuation α (α represents either Y or u) has been normalized so that $\int_0^\infty E_\alpha(f)df = 1$. At $f_p^* = 0$, a pronounced peak occurs at $f_s^* = 0.13$ in both E_Y and E_u, the number (0.91 in E_Y and 0.59 in E_u) near the peak indicating the peak magnitude at f_s^*. The second harmonic is also evident at $f^* = 0.26$. Once the perturbation is introduced, both E_Y and E_u show an additional spike at f_p^*. For $f_p^* \leq 0.1$, the peak value at f_s^* is attenuated for both E_Y and E_u. The attenuation effect is the most significant at $f_p^* = 0.1$ where the peak value in E_Y and E_u is only 25% and 40%, respectively, of its counter part at $f_p^* = 0$. The result is consistent with the flow visualization and PIV measurements (Figure 3-7 and Figure 3-8). Note that the peak at the second harmonic is also appreciably reduced. As f_p^* exceeds 0.13 but not beyond the second harmonic, 0.26, of f_s^*, the peak at f_s^* in E_Y and E_u is more pronounced than at $f_p^* = 0$; the maximum occurs at $f_p^* = 0.13$, where $f_p^* = f_s^* = f_n^*$ and the peak value in both E_Y and E_u is more than twice the value at $f_p^* = 0$, agreeable with the flow visualization and PIV data (Figure 3-11 and Figure 3-12). But once f_p^* reaches 0.3 and beyond, the peak value drops below that at $f_p^* = 0$. Evidently, the influence of the perturbation depends on the interrelationship between f_p^* and f_s^* or f_n^*.

The spectral coherence between Y and u, calculated by

$$Coh_{Yu} = \frac{Co_{Yu}^2 + Q_{Yu}^2}{E_Y E_u}, \tag{3-2}$$

provides a measure of the degree of correlation between the Fourier components of Y and u, where Co_{Yu} and Q_{Yu} are the cospectrum and quadrature spectrum of Y and u, respectively. Here, the cross-spectrum is computed from the Fourier transform of the correlation $\overline{Y(t+\tau)u(t)}$. See Zhang *et al.* (2000) for more details. Figure 3-14 presents Coh_{Yu} at f_s as f_p^* varies. The perturbation causes an increase in Coh_{Yu} at f_s, compared with that at $f_p^* = 0$, for $0.1 < f_p^* \leq 0.26$ and otherwise a decrease. The enhanced Coh_{Yu} range may result from synchronization between vortex shedding and induced vibration. Based on experimental data, Gowda (1975) suggested that for bluff bodies with fixed separation points the synchronization phenomenon began at $f_s \approx 0.8 f_n$ and ended when $f_s \approx 2 f_n$. This corresponds presently to a frequency range of $f_p^* = 0.11 \sim 0.26$, coinciding well with the range of enhanced Coh_{Yu}.

To gain a better insight into the relationship between the Y and u signals, Co_{Yu} is examined in Figure 3-15. A strong peak occurs at f_s^*, which is negative for $0 < f_p^* \leq 0.1$, positive for $0.1 < f_p^* \leq 0.26$, and negative again for $f_p^* > 0.26$. The peak indicates a good correlation between Y and u at f_s^*, while the positive and negative sign correspond to in-phased and anti-phased Y and u at f_s^*, respectively. The average phase shift between Y and u may be quantified by the spectral phase angle (Figure 3-16), defined by

$$\phi_{Yu} (\equiv \tan^{-1} \frac{Q_{Yu}}{Co_{Yu}}). \tag{3-3}$$

This angle is zero at $f_p^* = 0$, close to -π for $0 < f_p^* \leq 0.1$ and fluctuating about zero for $f_p^* > 0.1$. In a turbulent near-wake, vortices are highly coherent. As a matter of fact, the phase lag at f_s between lateral velocity signals is approximately zero across the wake even at $x / d = 10$ (Zhou *et al.* 2002). Speculatively, the phase at f_s of the measured streamwise velocity, u, at $x / h = 2$ and $y / h = 1.5$ could be the same as that of u at $x / h = 0$ because of the strong coherence of the shear-layer separating from the cylinder. Note that the lateral velocity component, v, leads u within the Kármán vortex by about $\pi / 2$ for $y / d > 0$ (Zhou & Antonia, 1993). This implies that the measured u could be about $\pi / 2$ lagging behind that of v at $x / h = 0$. On the other hand, given the cylinder oscillates harmonically, the measured Y is $\pi / 2$ lagging behind the cylinder velocity $\dot{Y}$. Therefore, the phase relationship between u and Y could represent that between v and $\dot{Y}$; which couldn't be directly measured due to the present experimental condition. At zero phase, v and $\dot{Y}$ synchronize, re-enforcing each other, causing the enhancement of the vortex strength (Figure 3-11 and Figure 3-12). At the phase of -π, v and $\dot{Y}$ are opposite in direction, implying that the flow and structural vibration now act against each other, thus resulting in the drastically reduced vibration amplitude and vortex strength (Figures 3-7 to 3-10). A better understanding of physics behind the observation perhaps requires the knowledge of the 3-D aspects of the flow, which are not measured presently.

An interpretation is now proposed for the enhancement and impairment of vortex shedding. As f_p^* falls within the possible synchronization range, the perturbation will not break the synchronization between vortex shedding and structural vibration; instead, the perturbation is more likely to increase the strength of

synchronization or resonance. Notably, at $f_p^* = 0.13$ where $f_n = f_s = f_p$, Coh_{Yu} at f_s reaches the maximum, 0.90. However, when f_p^* is beyond the synchronization range, the perturbation changes the phase relationship between synchronizing structural oscillation and vortex shedding from zero to near $\pm\pi$. This implies an alteration in the nature of fluid-structure interactions, the in-phased fluid excitation and structural oscillation turning into anti-phased interactions against each other, which dissipates each other in energy and results in drastic weakening vortex shedding and structural oscillation.

It is pertinent to comment that Coh_{Yu} at f_s drops to the minimum at $f_p^* = 0.1$ and reaches the maximum at $f_p^* = 0.13$. The perturbation effect is dependent on $Y_{p,\mathrm{rms}}$ as well as f_p^*. The $Y_{p,\mathrm{rms}}$ peak is presently set at $f_p^* = 0.1 \sim 0.13$ (Figure 2-7). This may explain why the perturbation effect is particularly eminent in this f_p^* range. The small $Y_{p,\mathrm{rms}}$ for $f_p^* = 0.02 \sim 0.07$ and $f_p^* \geq 0.26$ is at least partially responsible for the relatively weak perturbation effect over these frequencies (Figure 3-14).

3.6 Downstream Evolution of Perturbed Flow

It may be of fundamental interest to estimate how far downstream of the cylinder the perturbation effect could persist. This is investigated by examining the cross-flow distribution of mean velocity $\overline{U}^*$ and Reynolds stresses $\overline{u^2}^*$, $\overline{v^2}^*$ and $\overline{uv}^*$, obtained from the LDA measurement. Figure 3-17 presents a comparison in $\overline{U}^*$, $\overline{u^2}^*$, $\overline{v^2}^*$ and $\overline{uv}^*$ at $x / h = 3$ between the cases without perturbation and the impaired

($f_p^* = 0.1$) or enhanced vortex street ($f_p^* = 0.13$). For $f_p^* = 0.1$, the maximum of $\overline{U}^*$, $\overline{u^2}^*$, $\overline{v^2}^*$ and $\overline{uv}^*$ at $x/h = 3$ shows a considerable decrease, down to 85%, 85%, 88% and 78% of that unperturbed, respectively. On the other hand, for $f_p^* = 0.13$, the four quantities increase by 16%, 13%, 10% and 22%, respectively. The results are in line with the flow visualization and PIV measurements. Note that the perturbation on the upper side of the cylinder has the equal effect on either side of the wake centerline, as qualitatively seen from the vortex street (Figures 3-5 to 3-8 and Figures 3-11 to 3-12). The difference is still discernible at $x/h = 20$ but vanishes at $x/h = 25$, shown by Figures 3-18 to 3-20.

One remark is due to the perturbation effect on the drag coefficient, $\overline{C}_D$, which may be estimated based on $\overline{U}^*$, $\overline{u^2}^*$ and $\overline{v^2}^*$ (Antonia & Rajagopalan, 1990), viz.

$$\overline{C}_D = 2\int_{-\infty}^{\infty} \frac{\overline{U}}{U_\infty}\left(\frac{U_\infty - \overline{U}}{U_\infty}\right) d\left(\frac{y}{h}\right) + 2\int_{-\infty}^{\infty} \left(\frac{\overline{v^2} - \overline{u^2}}{U_\infty^2}\right) d\left(\frac{y}{h}\right). \qquad (3\text{-}4)$$

Without perturbation, $\overline{C}_D$ is 1.88, falling in the range (1.7 ~ 2.0) reported previously (Knisely, 1990; Zhou & Antonia, 2002; and Lee, 1975). $\overline{C}_D$ dropped about 21.0%, for the case of impaired vortex shedding ($f_p^* = 0.1$), but jumped by 35.1% when vortex shedding was enhanced ($f_p^* = 0.13$).

3.7 Conclusions

The proposed perturbation technique using THUNDER actuators in an open-loop scheme was deployed to generate a periodic perturbation of controllable

frequency and amplitude on the surface of a flexible-supported square cylinder in a cross flow. This perturbation altered the interaction between synchronising cylinder motion and vortex shedding. Subsequently, both vortex shedding and its induced vibration were modified. The following conclusions can be drawn.

1) When the perturbation frequency f_p^* is outside the possible synchronization range of the fluid-cylinder system (0.11 ~ 0.26 or $0.8 f_n^* \sim 2 f_n^*$), the fluid-structure interaction has been altered so that vortex shedding and structural oscillation are anti-phased. The maximum attenuation occurs at a perturbation frequency of $f_p^* = 0.1$, where the perturbation amplitude is very large (Figure 2-7). The spectral coherence at f_s drops from 0.66 ($f_p^* = 0$) to 0.15 ($f_p^* = 0.1$). Correspondingly, it is observed that, with a perturbation at amplitude of $0.028h$, the maximum structural displacement at resonance was reduced from $0.08h$ to $0.02h$. Meanwhile, the vortex strength (circulation) reduces by 50%. The drag coefficient $\overline{C}_D$ decreases 21.0%.

2) When f_p^* falls within the synchronization range of the fluid-cylinder system where $f_n^* = f_s^*$, perturbation could not break the bond in the synchronization between structural displacement and vortex shedding; rather it tends to reinforce the resonance. The spectral coherence at f_s increases substantially from 0.66 at $f_p^* = 0$ to 0.90 at $f_p^* = 0.13$. As a result, the vortex strength exceeds twice that at $f_p^* = 0$. There is an increase of 35.1% in $\overline{C}_D$. Two factors are probably responsible for the performance at $f_p^* = 0.13$. First, at this f_p^*, f_n^* is identical to the natural vortex shedding frequency; the resonance

without perturbation is likely to be strong. Second, the perturbation amplitude is largest (Figure 2-7).

3) The perturbation also alters considerably the cross-flow distribution of $\overline{U}^*$, $\overline{u^2}^*$, $\overline{v^2}^*$ and $\overline{uv}^*$. The maximum $\overline{U}^*$, $\overline{u^2}^*$, $\overline{v^2}^*$ and $\overline{uv}^*$ values at $x / h = 3$ drop by 14.6%, 15.2%, 12.1% and 22.0% respectively, in the attenuated vortex shedding case, and increase by 16.2%, 13.0%, 9.46% and 21.7%, respectively, in the enhanced vortex shedding case. The perturbation effect persists up to $x / h \approx 25$.

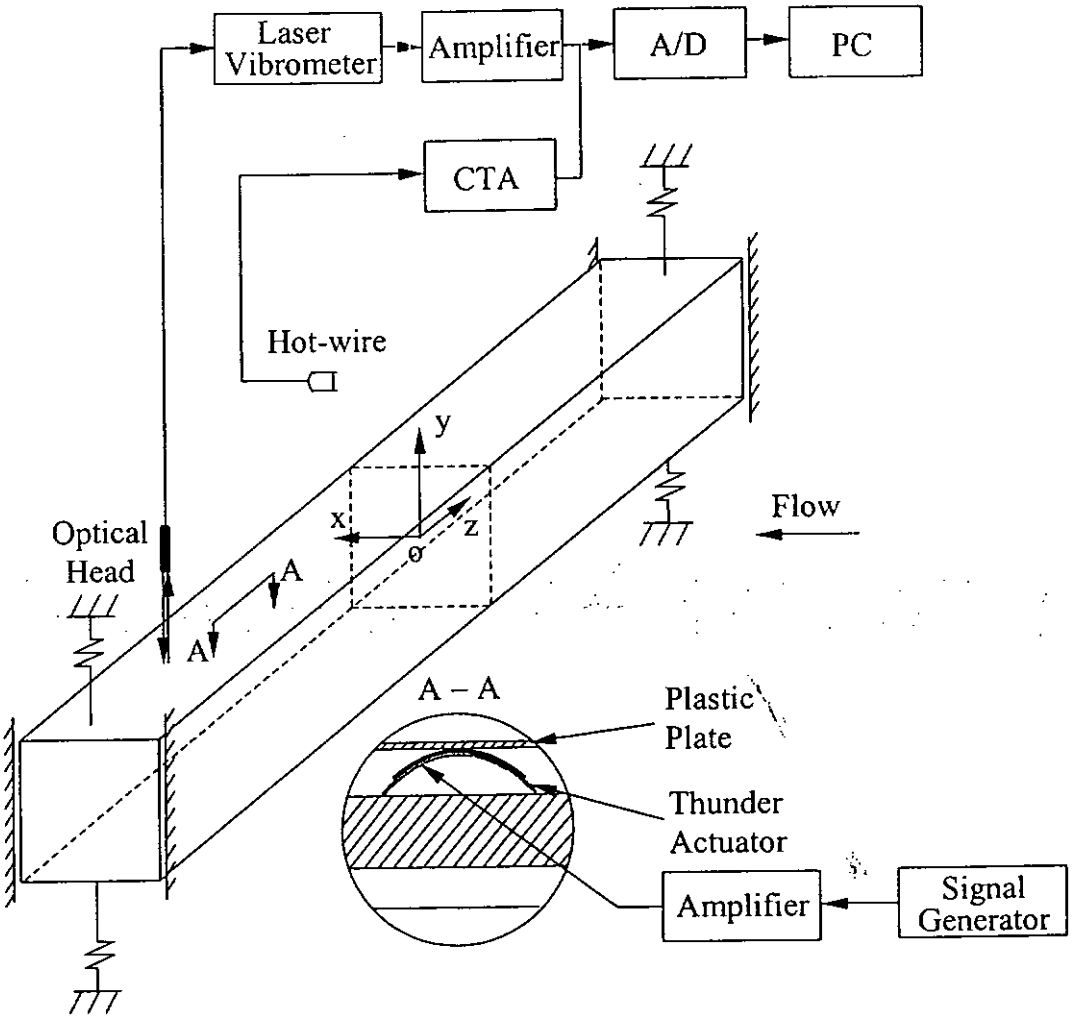

Figure 3-1 Experimental Setup.

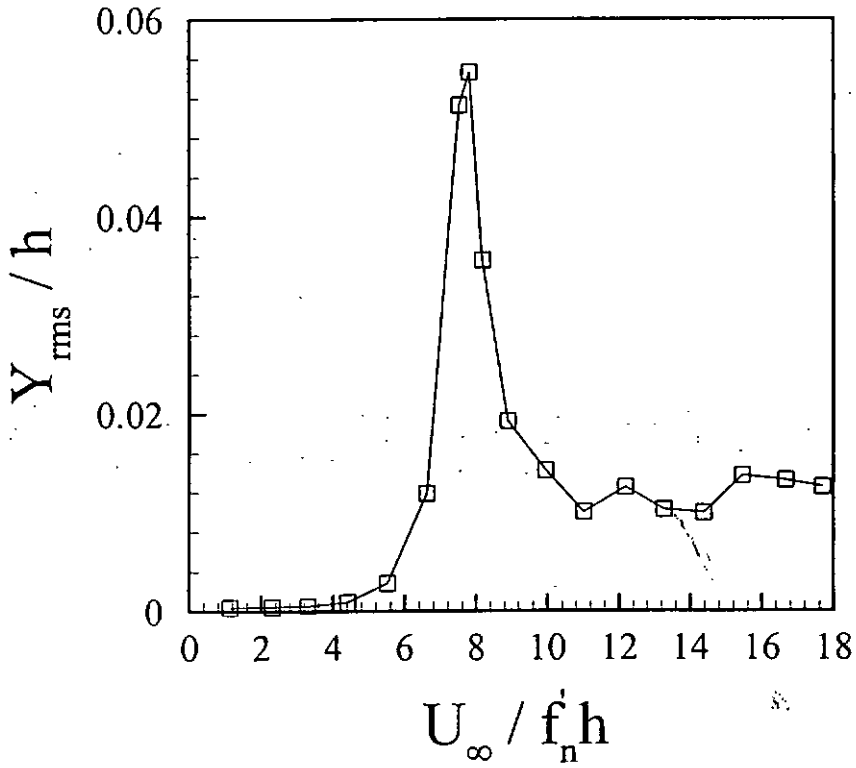

Figure 3-2 The rms displacement, Y_{rms}/h, of the cylinder versus the reduced velocity, $U_r = U_\infty / f_n h$.

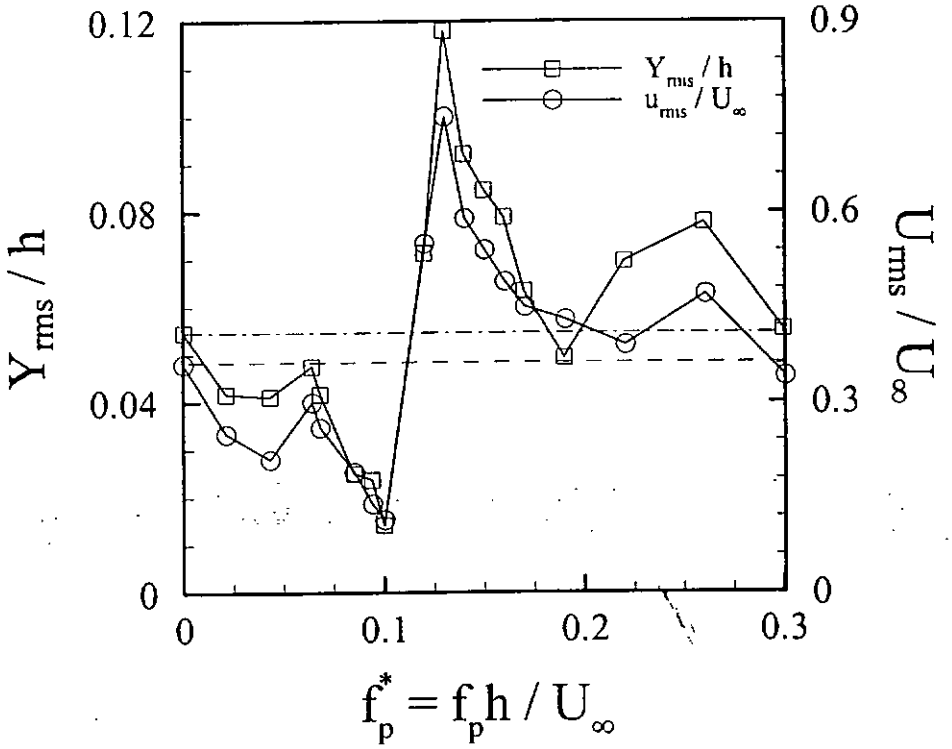

Figure 3-3 The effect of the perturbation frequency on the cylinder displacement and the flow velocity (a constant voltage was applied). The broken lines indicate the level without perturbation.

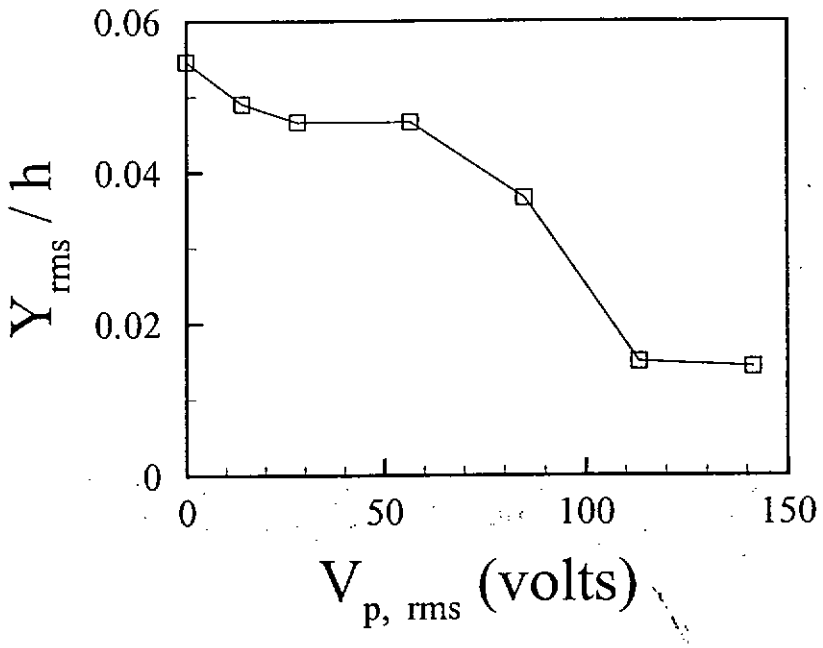

Figure 3-4 Variation of the cylinder displacement with voltage applied on actuators.

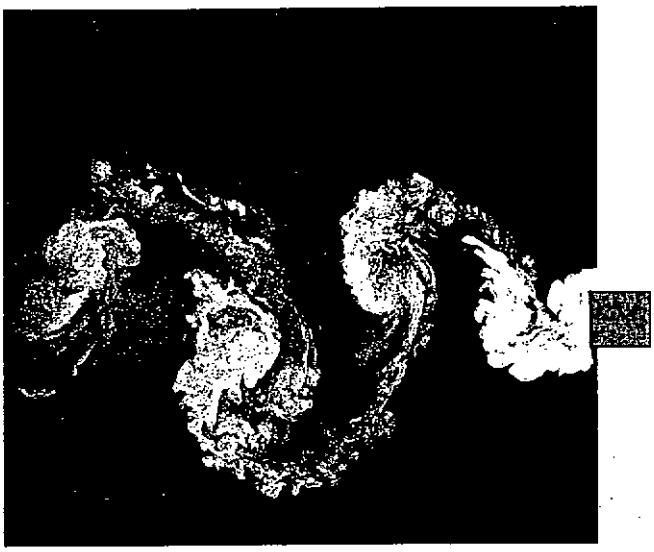

Figure 3-5 Typical photograph from flow visualization measurements of unperturbed vortex shedding ($f_p^* = 0$, $U_r = 7.8$, Re = 3500). Flow is right to left.

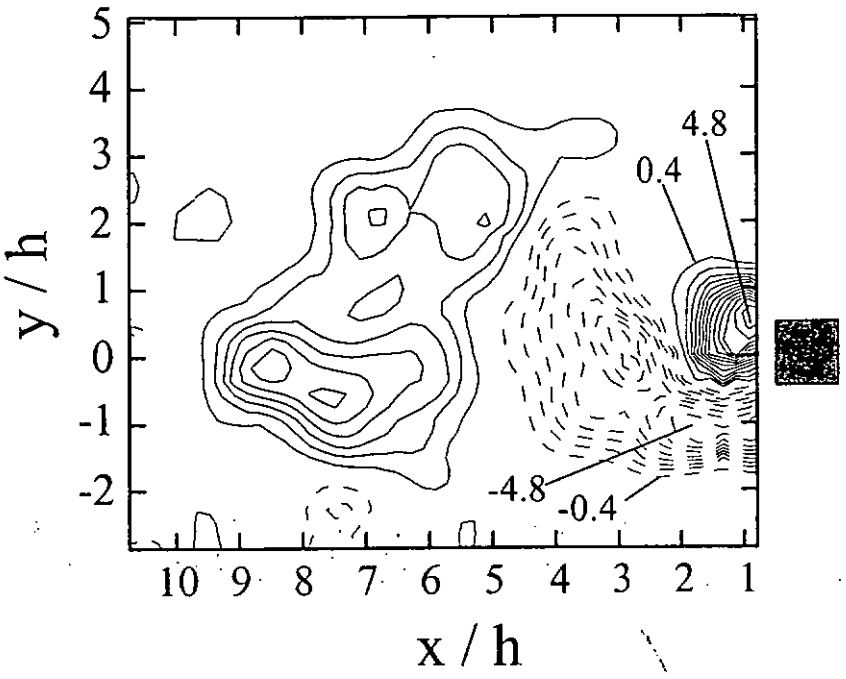

Figure 3-6 The iso-contour of spanwise vorticity $\omega_z^* = \omega_z h / U_\infty$ from PIV measurements of unperturbed vortex shedding (f_p^* = 0, U_r = 7.8, Re = 3500): the contour increment $\Delta\omega_z^* = 0.4$, the cutoff level $|\omega_{zc}^*| = 0.4$. Flow is right to left.

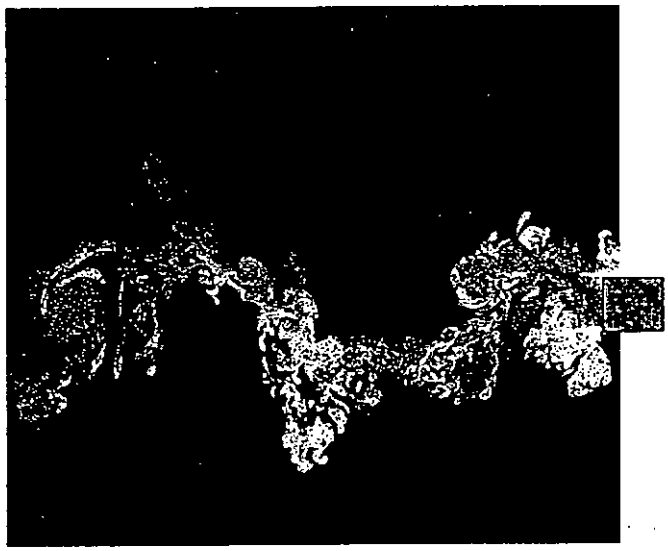

Figure 3-7 Typical photograph from flow visualization measurements of impaired vortex shedding ($f_p^* = 0.1$ is beyond the synchronization range, $U_r = 7.8$, Re = 3500). Flow is right to left.

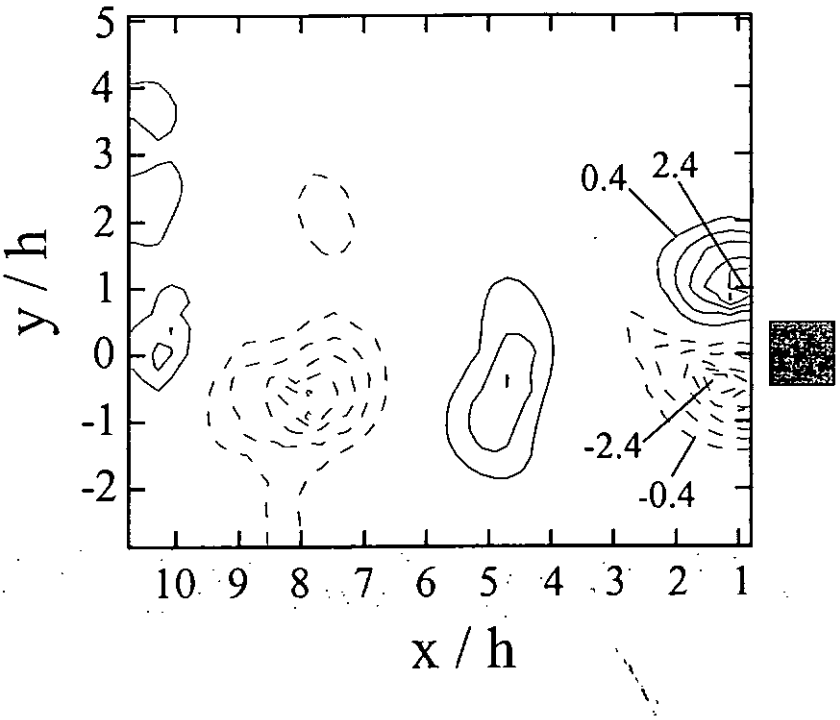

Figure 3-8 The iso-contour of spanwise vorticity $\omega_z^* = \omega_z h / U_\infty$ from PIV measurements of impaired vortex shedding (f_p^* = 0.1 is beyond the synchronization range, U_r = 7.8, Re = 3500): the contour increment $\Delta\omega_z^*$ = 0.4, the cutoff level $|\omega_{zc}^*|$ = 0.4 . Flow is right to left.

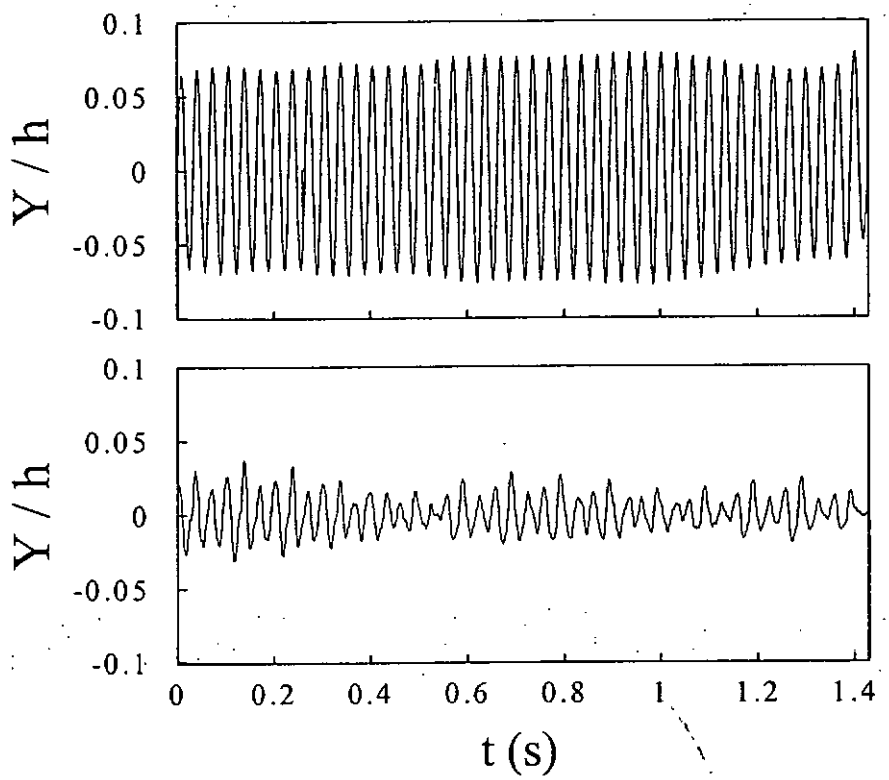

Figure 3-9 Typical time histories of the cylinder displacement Y with (lower trace) and without (upper trace) perturbation. The time origin is arbitrary.

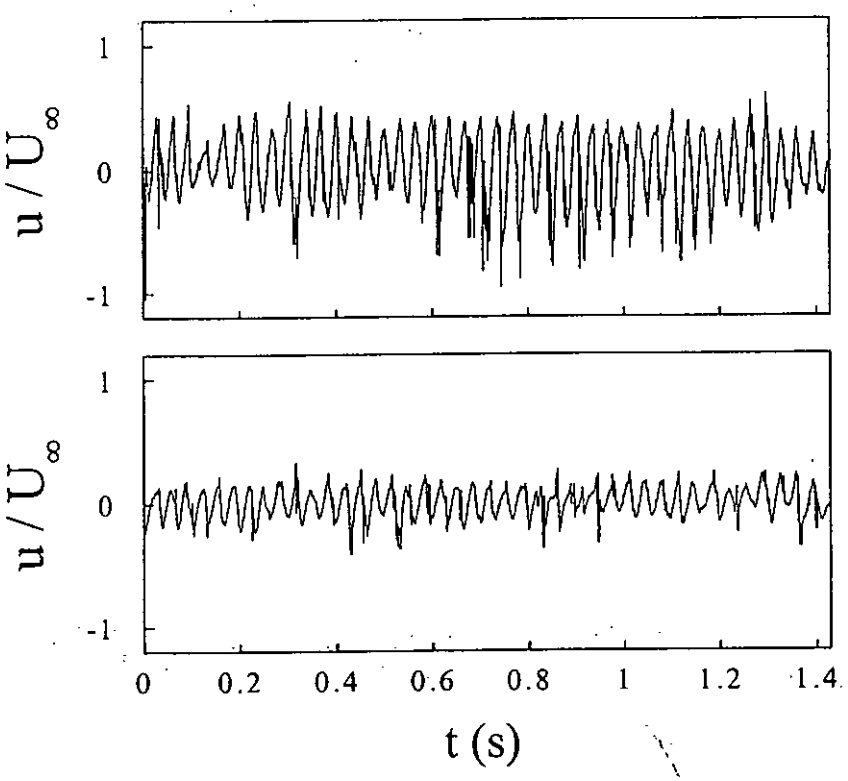

Figure 3-10 Typical time histories of the streamwise flow velocity u with (lower trace) and without (upper trace) perturbation. The time origin is arbitrary.

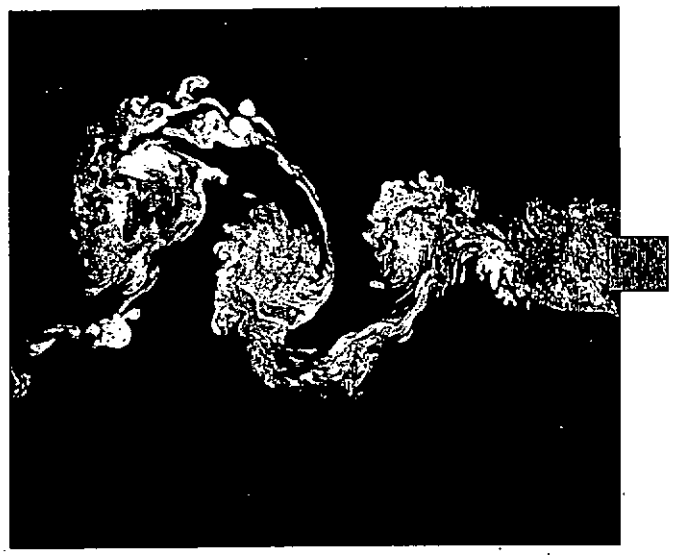

Figure 3-11 Typical photograph from flow visualization measurements of enhanced vortex shedding ($f_p^* = 0.13$ is within the synchronization range, U_r = 7.8, Re = 3500). Flow is right to left.

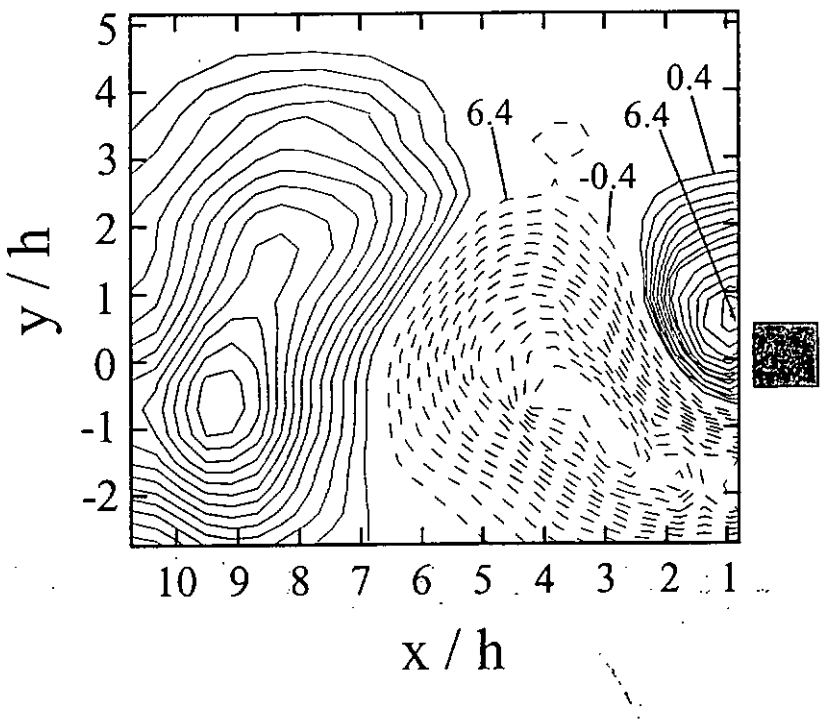

Figure 3-12 The iso-contour of spanwise vorticity $\omega_z^* = \omega_z h / U_\infty$ from the PIV measurements of enhanced vortex shedding (f_p^* = 0.13 is within the synchronization range, U_r = 7.8, Re = 3500): the contour increment $\Delta\omega_z^* = 0.4$, the cutoff level $|\omega_{zc}^*| = 0.4$. Flow is right to left.

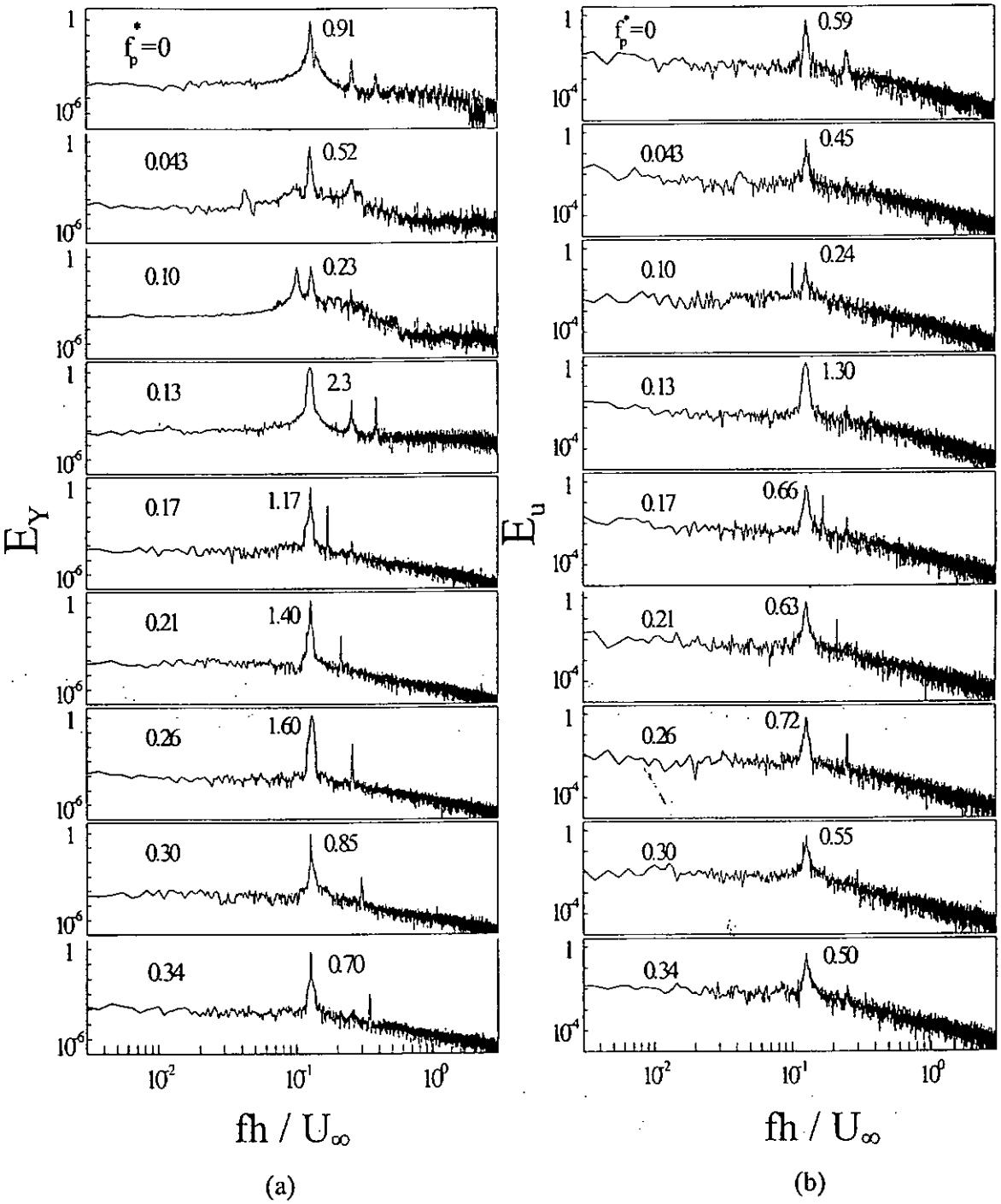

Figure 3-13 Power spectra of cylinder displacement Y (a) and fluctuating flow velocity u (b) at various perturbation frequency (f_p^*).

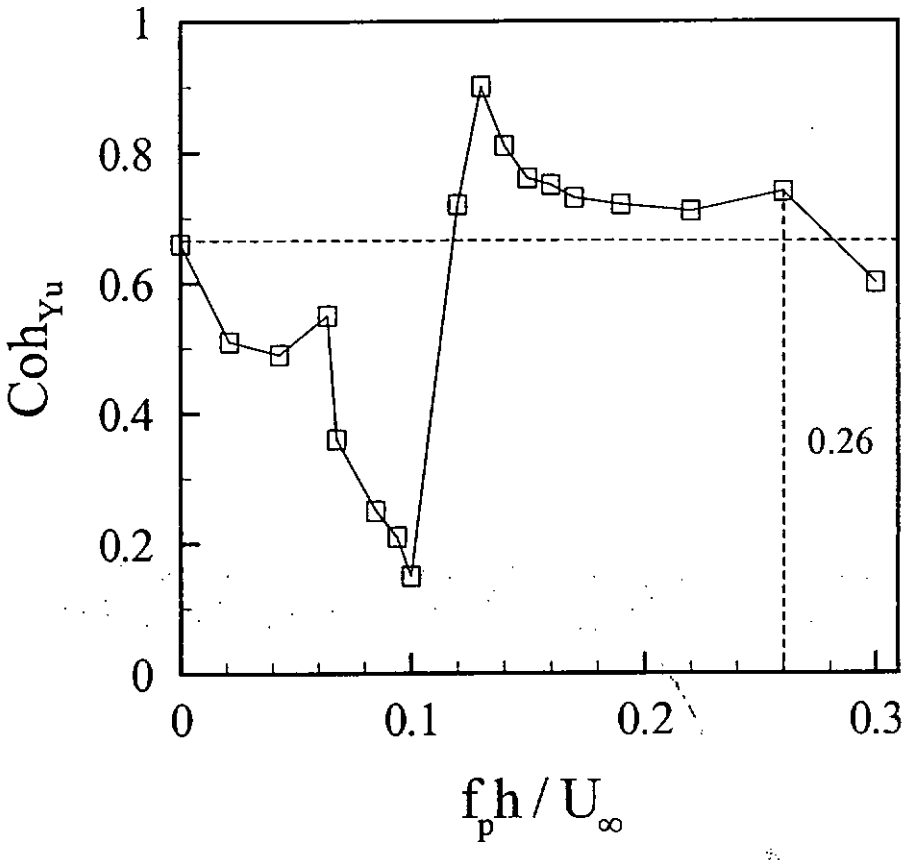

Figure 3-14 The effect of the perturbation frequency on the spectral coherence Coh_{Yu} at $f_s^* \approx 0.13$ between the Y and u signals.

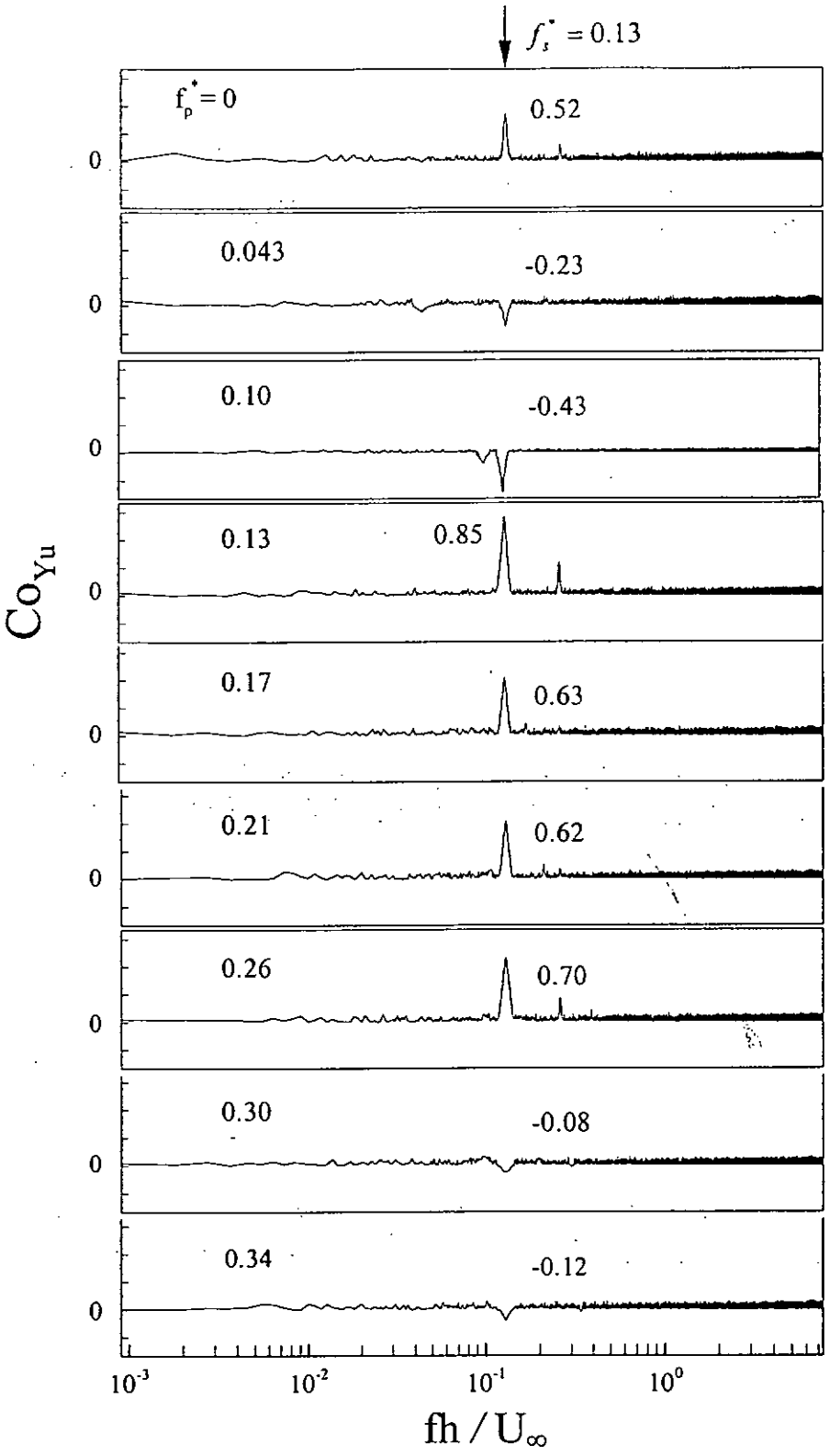

Figure 3-15 Cospectrum between the Y and u signals at various perturbation frequency (f_p^*).

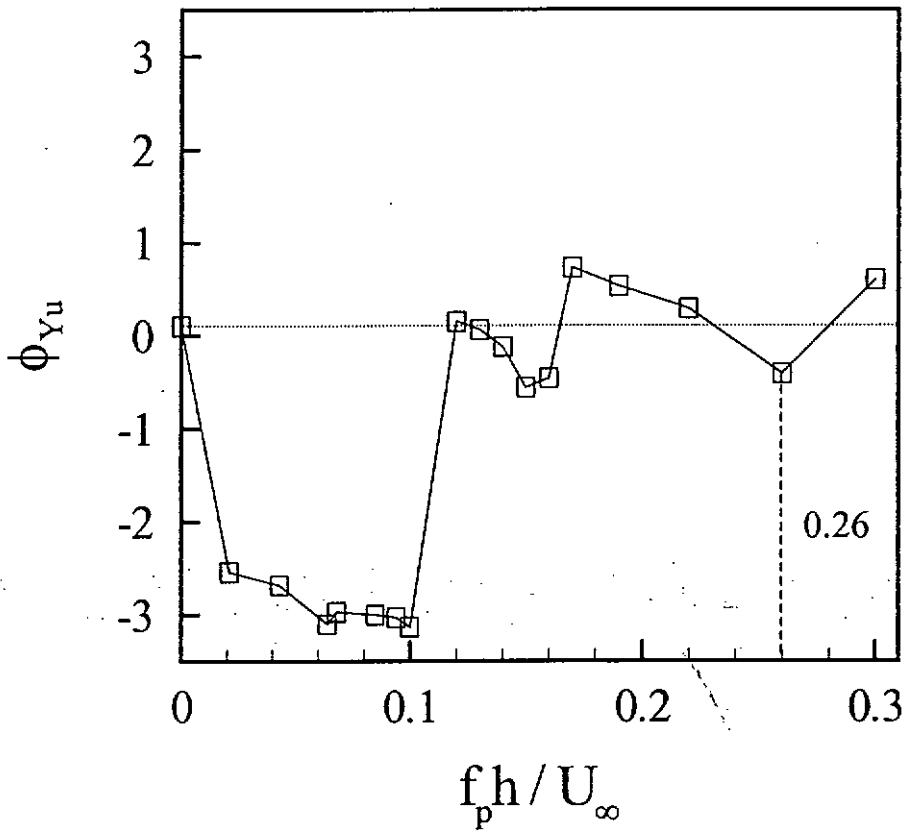

Figure 3-16 The effect of the perturbation frequency on the phase shift ϕ_{Yu} at $f_s^* \approx$ 0.13 between the Y and u signals.

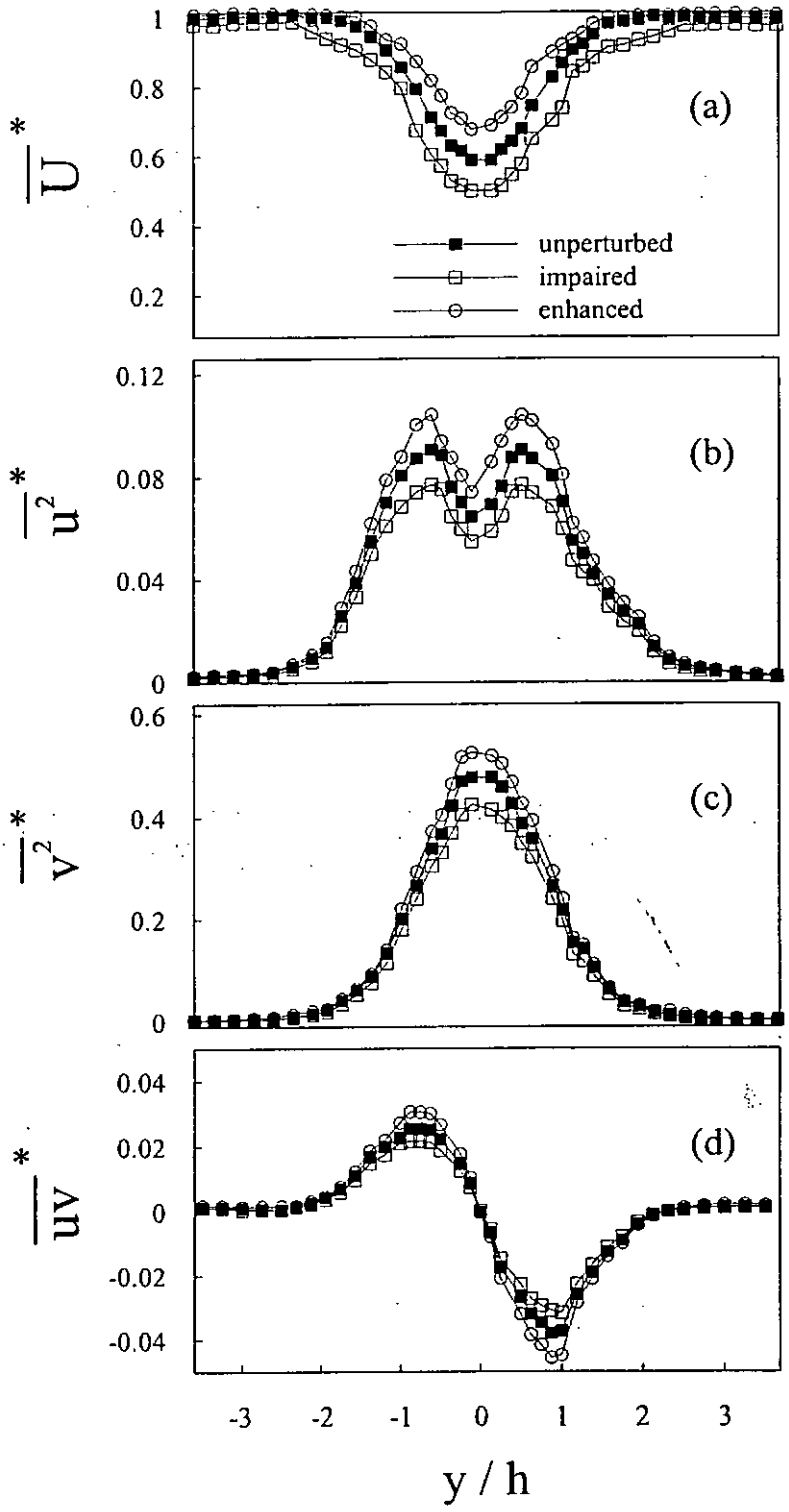

Figure 3-17 Cross-flow distribution of mean velocity, Reynolds stresses at $x/h = 3$: (a) $\overline{U}^*$, (b) $\overline{u^2}^*$, (c) $\overline{v^2}^*$, (d) $\overline{uv}^*$.

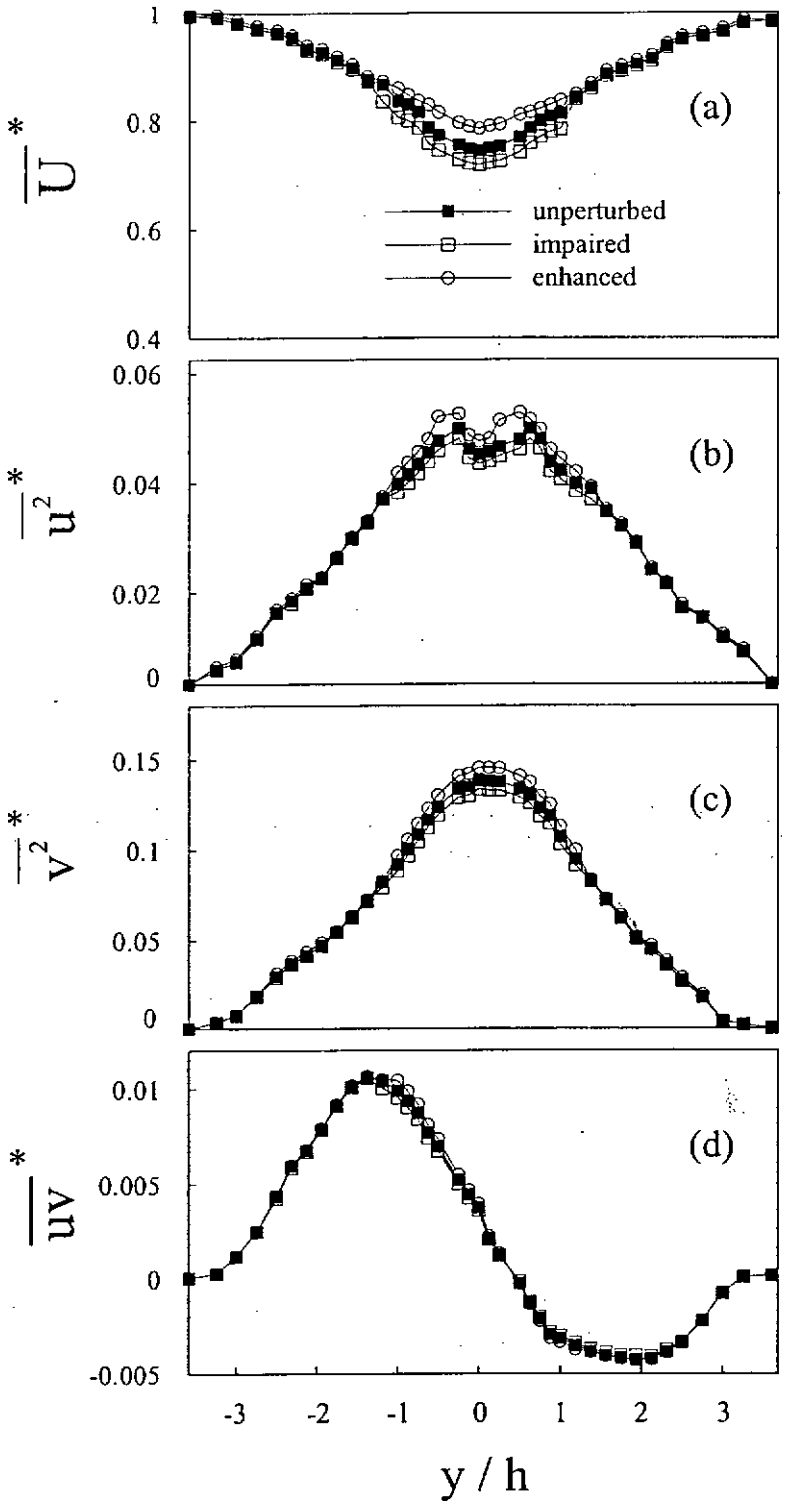

Figure 3-18 Cross-flow distribution of mean velocity, Reynolds stresses at $x/h = 10$: (a) $\overline{U}^*$, (b) $\overline{u^2}^*$, (c) $\overline{v^2}^*$, (d) $\overline{uv}^*$.

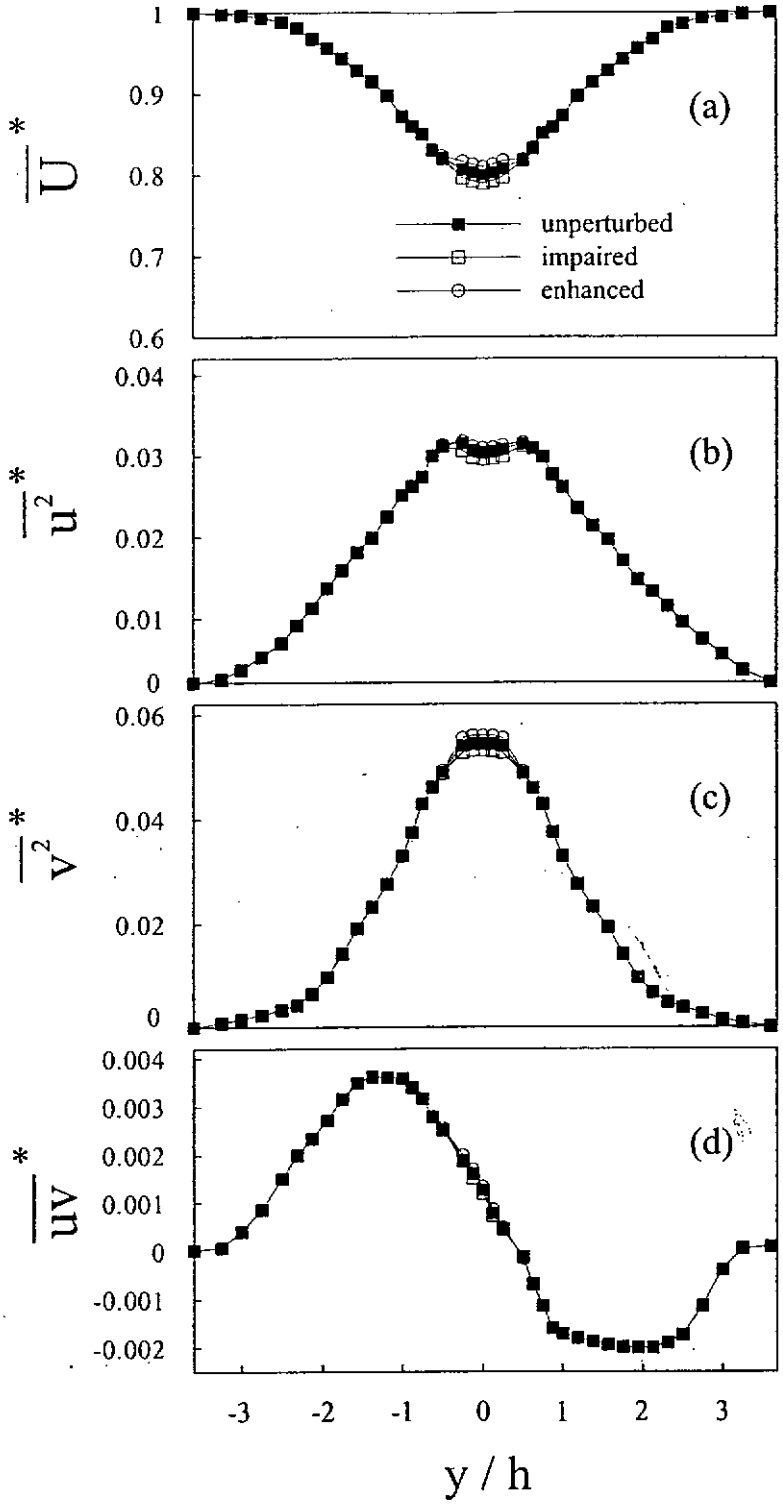

Figure 3-19 Cross-flow distribution of mean velocity, Reynolds stresses at $x / h = 20$: (a) $\overline{U}^*$, (b) $\overline{u^2}^*$, (c) $\overline{v^2}^*$, (d) $\overline{uv}^*$.

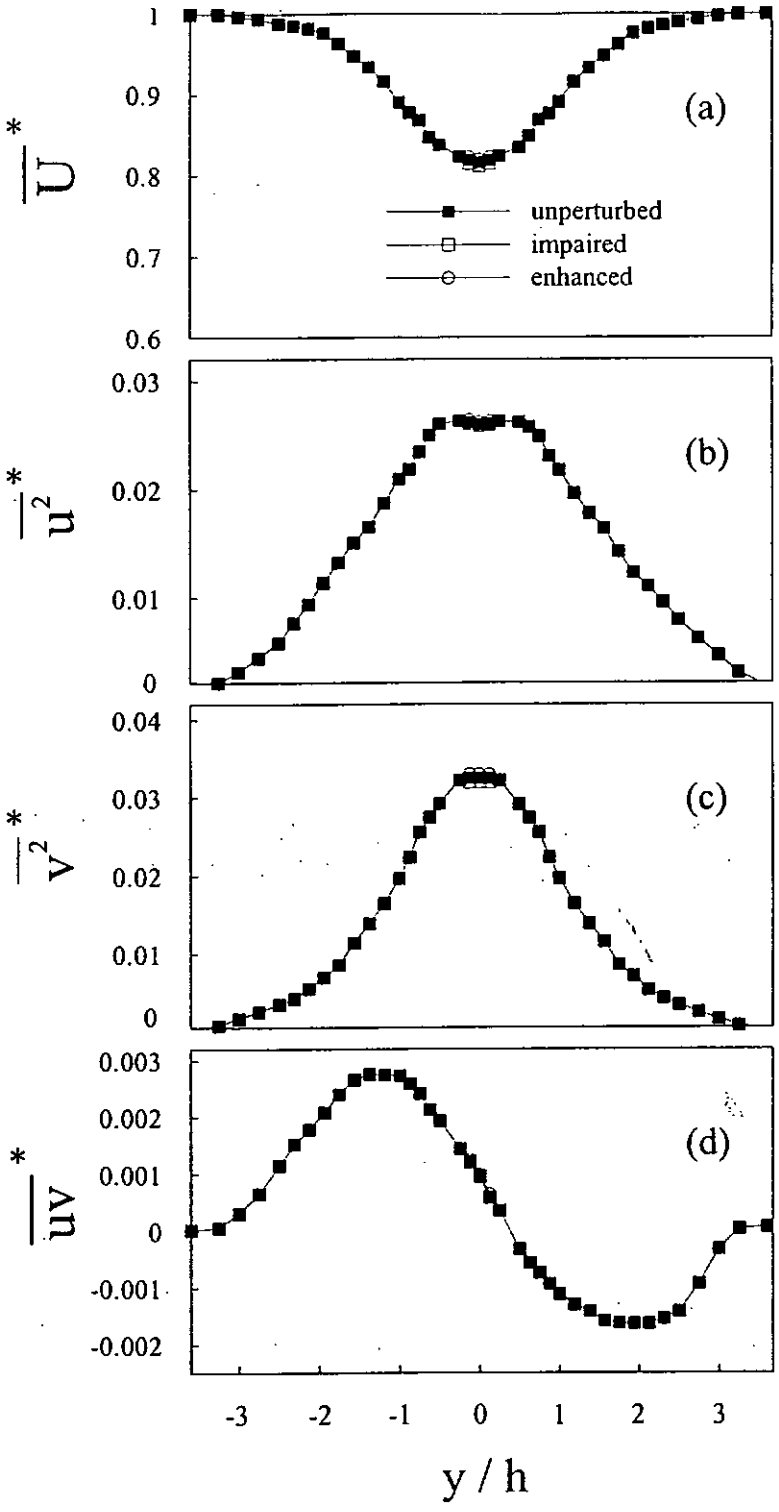

Figure 3-20 Cross-flow distribution of mean velocity, Reynolds stresses at $x/h = 25$: (a) $\overline{U}^*$, (b) $\overline{u^2}^*$, (c) $\overline{v^2}^*$, (d) $\overline{uv}^*$.

CHAPTER 4

CLOSED-LOOP CONTROL OF FLUID-STRUCTURE INTERACTION ON A FLEXIBLE-SUPPORTED CYLINDER

4.1 Introduction

As stated in Chapter 3, under open-loop method, a novel perturbation technique using THUNDER actuators embedded underneath the surface of a square cylinder to alter interactions between a flexibly supported cylinder and cross flow was established. Given a properly set perturbation frequency, both vortex shedding and vortex-induced vibration were significantly reduced as a result of perturbation. However, the open-loop control, without the feedback of either flow or structural vibration information, suffered from two major drawbacks. First, the perturbation frequency range to achieve desired performance was relatively narrow. Second, the required perturbation amplitude was rather large, about 2.8% of the cylinder height or 25% of the vibration amplitude of the cylinder. These problems may be resolved if a closed-loop system is developed.

The choice of the feedback signal is crucial for the performance of a closed-loop system. Previous closed-loop techniques involving flow or flow-induced vibration

control mostly have their feedback signals from flow, typically hot wire signals. See Ffowcs Williams *et al.* (1992), Roussopoulos (1993), Huang (1996), Berger (1967), Warui and Fujisawa (1996), Tokumaru and Dimotakis (1991) and Filler *et al.* (1991) for examples. This scheme should work quite well provided only flow is to be controlled. By the same token, one may consider the structural vibration signal to be ideal for the only control of structural vibration. Two examples are Baz and Ro (1991) and Tani *et al.* (1999). This begs the question: which is the best feedback signal, flow or structural vibration or something else?

The present chapter pursues two objectives: first, to improve the performance of the previous open-loop control system using closed-loop control system and find an optimum scheme to control fluid-structure interactions; second, to shed light upon the underlying physics of flow-structure interaction under external perturbation. Three control schemes, utilizing feedback signals from flow measured with a single hot wire, structural vibration measured with a laser vibrometer or a combination of both, are considered and compared. The performances of the control schemes were assessed through measurements using PIV, flow visualization, LDA, single hot wire and laser vibrometer. To understand the underlying physics, changes in spectral phase and coherence between flow and structural vibration due to the deployment of the control were again investigated, along with the varying fluid damping of the fluid-structure system, which was evaluated from structural oscillation signals using an auto-regressive moving average (ARMA) technique.

4.2 Experimental Details

All experiments were performed in a closed-circuit wind tunnel with a square

working section of 0.6 m × 0.6 m and 2.4 m long. More details of the tunnel were described in Section 2.6. The unperturbed condition was kept the same as that in Chapter 3. The previously used square cylinder of height h = 15.2 mm, flexibly supported on springs at both ends, was placed 0.2 m downstream of the exit plane of the tunnel contraction and allowed to vibrate laterally, as shown in Figure 4-1. The free-stream velocity (U_∞) was adjusted to be about 3.58 m/s, corresponding to a Re = 3500. At this Re, resonance occurred, that is, the vortex shedding frequency f_s coincided with the natural frequency f_n (= 30 Hz) of the fluid-cylinder system, the maximum cylinder displacement, Y_{max}, being still about 1.2 mm or 0.08h.

Details about the installation of the cylinder and characteristics of the actuators were introduced in Section 2.5. As shown in Figure 4-1, three THUNDER actuators were embedded in series in a slot underneath the plate. Under an applied voltage, the actuator deformed out of plane, driving the thin plate up and down and generating the desired surface perturbation.

The lateral structural displacement (Y) was measured by a laser vibrometer, which has a measurement uncertainty of about 0.5%. The laser beam was split into two, one monitoring the control performance and the other providing the feedback signal. The streamwise fluctuating velocity (u) was measured by two 5 μm tungsten hot wires, placed at $x/h = 2$, $y/h = 1.5$, $z/h = 0$ (hot wire ① in Figure 4-1) and $x/h = 1.6$, $y/h = -2.5$ and $z/h = 0$ (hot wire ② in Figure 4-1), respectively. The x, y and z coordinates and their origin are defined in Figure 4-1. Hot wires ① and ② were used to monitor the control performance and feedback signals, respectively. The choice of the feedback hot wire location may impact on the control performance. The fluctuating flow velocity measured with hot wire for feedback signal is required to be

highly coherent with vortex shedding and has little noise. Specifically, different locations along the streamwise and transwise directions were tested in the near wake. Locations near $x / h = 1.6$, $y / h = \pm 2.5$ and $z / h = 0$ were found to be the most appropriate. To avoid the monitor hot wire placed at $x / h = 2$, $y / h = 1.5$ and $z / h = 0$, the feedback hot wire was finally put at $x / h = 1.6$, $y / h = -2.5$ and $z / h = 0$. The constant temperature circuit was used for the operation of the hot wires at an overheat ratio of 1.8. The feedback signals were low-pass filtered at a cut-off frequency of 200 Hz and then sent to a proportional-integral-derivative (PID) controller built in with a 16 bit AD and DA converter. The signals were low-pass filtered again to remove the high frequency electronic noise (cut-off frequency = 200 Hz) and amplified by two dual channel piezo driver amplifiers (Trek PZD 700-2) in order to drive the THUNDERs. The signals, be they used for monitoring or feedback purposes, were conditioned and digitized using a 12-bit AD board at a sampling frequency of 3.5 kHz per channel. The duration of each record was about 20 s.

The flow visualization and PIV measurements were conducted using a Dantec standard PIV2100 system. A wide-angle lens was used so that each image covered an area of 165 mm × 125 mm or $x / h \approx 0.33 \sim 11.2$ and $y / h \approx -4.1 \sim 4.1$ of the flow field for flow visualization and 155 mm × 140 mm, i.e., $x / h \approx 0.6 \sim 10.8$, $y / h \approx -4.8 \sim 4.4$, for PIV measurements. The profiles of mean velocities in the x direction and Reynolds stresses along y direction in the wake ($x / h = 3$) were measured using a two-component LDA system. The detailed information about these techniques could be found in Section 2.6.

4.3 Control Scheme and Controller Design

Three control schemes were considered depending on feedback signals used, namely, PID-*Y*, PID-*u* and PID-*Yu*, referring to PID control using the *Y* signal measured by laser vibrometer, the *u* signal measured by hot wire ② and the combination of the two signals, respectively. The controller was developed and implemented based on a dSPACE system (see Section 2.5 for more details).

As illustrated in Figure 4-2, the output of a PID controller is proportional to the sum of the input signal, its integral and its derivative. The proportional gain (*P*), integral gain (*I*) and differential gain (*D*) of a PID controller can be individually or simultaneously adjusted. Each combination of the three quantities results in a different type of control. P control deploys a proportionally amplified input signal and has a limited success in obtaining a good performance in terms of steady-state errors, disturbance rejection and transit response. PI controller includes the integral of the input signal, and the steady-state error is eliminated at the expense of a larger transient overshoot and thus a further deterioration of the dynamic response. Once the derivative of the input signal is added, forming PID controller, the system is able to provide an acceptable degree of error reduction along with an acceptable stability (Franklin *et al.* 1998). Note that the time delay caused by the control loop can be apprehended by properly tuning the controller parameters. For each control scheme of PID-*Y*, PID-*u* or PID-*Yu*, gain coefficients should be adjusted during experiments to achieve a maximum reduction in the amplitudes of *Y* and *u*. The tuning procedure was first to keep $I = D = 0$ and vary *P* until the r.m.s. values, Y_{rms} and u_{rms}, of *Y* and *u* reached the minimum. Then *I* and *D* were successively added and adjusted until the

optimal performance was achieved. The same procedure was followed for the three schemes, i.e. PID-Y, PID-u and PID-Yu. Figure 4-3 shows the control performance versus each gain coefficient under different schemes. In the figure, the dash line and dotted line corresponded to unperturbed u_{rms}/U_∞ and Y_{rms}/h, respectively. Note that, for Yu-control, two sets of coefficients, (P_Y, I_Y, D_Y) and (P_u, I_u, D_u), are involved. It is evident that the PID controller outperforms the P and PI controllers. For all controllers, the Yu-control has the best performance in terms of the reduction in Y_{rms} and u_{rms}, followed by the u-control and then the Y-control. The difference in the control performance using different schemes is linked to the physical effect of each scheme on the fluid-structure system, which will be discussed in Section 4.5. It can also be seen that, irrespective of control schemes, P is much more effective than I or D in controlling vortex shedding and vortex-induced vibration. That is, compared with P control, the reduction in Y and u cannot be effectively improved after successively adding I and D to the controller. P control generates a control action that is proportional to structural oscillation velocity ($\dot{Y}$) or flow velocity, thus physically causing a change in the system damping. Theoretically, the resonant flow-structure system was surely very sensitive to any damping variations. On the other hand, I and D controls are physically linked to displacement and acceleration feedback, respectively. The former has an impact upon the system stiffness, whereas the latter influences the effective mass. Both may in principle alter the natural frequency, f_n, of the system to some extent. However, this slight change in f_n is probably not enough to generate any considerable effect on the strongly coupled vortex and structure synchronization, which occurs over the lock-on frequency range (Gowda, 1975).

The tuning process led to an optimal configuration for each scheme (PID control in Figure 4-3) with the following parameters: P_Y = 1.2, I_Y = -0.3, D_Y = -0.0004 for PID-Y, P_u = 3.5, I_u = 0.2, D_u = 0.0001 for PID-u and P_Y = 1.2, P_u = 0.4, I_Y = 0.2, I_u = 0.2, D_Y = 0.001, D_u = 0.0001 for PID-Yu. Unless otherwise stated, these parameters were used in experiments discussed hereinafter.

4.4 Performance of Various Control Schemes

Figure 4-4 compares the control performances of the three control schemes in terms of Y^*_{rms} and u^*_{rms}. Unless otherwise stated, the asterisk denotes the normalization by h and U_∞ in this work. Compared to the unperturbed case, Y^*_{rms} and u^*_{rms} were reduced respectively by 40% and 17% using PID-Y, 53% and 32% using PID-u and 82% and 70% using PID-Yu. Evidently, synchronizing vortex shedding and cylinder oscillation was greatly weakened in all cases. Nevertheless, PID-Yu overwhelms the other two schemes in performance, and PID-u considerably exceeds PID-Y. Remember the work in Chapter 3 ever attempted to manipulate the same fluid-structure system using an open-loop control system. In that case, whether the flow or structural vibration was enhanced or impaired depended on the perturbation frequency (f_p). Both Y_{rms} / h and $u_{\text{rms}} / U_\infty$ were reduced outside the synchronization range, i.e. $f_p^* = 0.11 \sim 0.26$, but increased within the range. Furthermore, the maximum reduction was 75% in Y_{rms} / h and 68% in $u_{\text{rms}} / U_\infty$, appreciably less than what was achieved by PID-Yu.

Typical photographs from flow visualization are presented in Figure 4-5. The solid square in the figure denotes the cylinder position. The case without any external

perturbation is given in Figure 4-5(a) as a baseline for comparison. The best performed open-loop controlled case when $f_p^* = 0.1$ and $f_s^* = f_n^* = 0.13$ is also included. Figure 4-6 presents the iso-contours of the normalized spanwise vorticity, $\omega_z^* = \omega_z h / U_\infty$, from the PIV measurement, which provide quantitative information on the performance of different control schemes, thus complementing flow visualization results. The experimental uncertainty of the vorticity measurement was estimated to be about 9%, close to the value of 10% reported by Sumner *et al.* (2000). The unperturbed flow (Figure 4-5(a) and Figure 4-6(a)) displays the familiar Kármán vortex street. In the case of the open-loop control, the Kármán vortex street in Figure 4-5(b) appears breaking up and the maximum vorticity level, $|\omega_{z\max}^*|$, in Figure 4-6(b) drops by about 47%, compared with the unperturbed flow (Figure 4-6(a)). For the closed-loop control of PID-*Y* and PID-*u* schemes, the vortex street (Figures 4-5(c) to 4-5(d) and Figures 4-6(c) to 4-6(d)) is again breaking up, and the maximum vorticity level is not any lower than the open-loop case. In fact, the vorticity contours in the PID-*Y* and PID-*u* control scheme displays higher level than that of the open-loop control. Once the PID-*Yu* scheme is applied, the control effect is strikingly enhanced; the flow visualization photograph in Figure 4-5(e) shows a radish-like wake, instead of the Kármán vortex street. The magnitude of $|\omega_{z\max}^*|$ is reduced by 71% (Figure 4-6(e)). Note that the surface perturbation was imposed only on the upper side of the square cylinder. However, the wake below the centerline appears equally affected (Figure 4-5 and Figure 4-6), similarly to Hsiao and Shyu (1991) and Huang (1996). The observation suggests that the present local perturbation has changed global interactions between fluid and structure.

Figure 4-7 presents the transition of the Y and u signals when the control action was switched on, which is evident from the variation of the actuating voltage (V_p). In all cases, there is a drastic reduction in the magnitude of Y or u once V_p was introduced. The most significant attenuation is obtained using PID-Yu (Figure 4-7(c)), compared with the unperturbed case. It is of interest to compare the magnitudes of the actuating voltage in volt used in different schemes. The V_p magnitude is only 27 volts for PID-Yu, but reaches 84 volts and 47 volts in PID-Y and PID-u, respectively. Evidently, PID-Yu requires a lower actuating voltage and hence smaller perturbation amplitude than the other two schemes yet achieves a markedly better performance.

Figures 4-8(a) to 4-8(b) show the power spectral density functions, E_Y and E_u, of Y and u, respectively, with and without control. The spectrum of fluctuation α (α represents either Y or u) has been normalized such that $\int_0^\infty E_\alpha(f)df = 1$. Without control, a pronounced peak occurs at $f_s^* = 0.13$ in both E_Y and E_u, the number, 0.91 in E_Y and 0.59 in E_u, near the peak indicating the peak magnitude at f_s^*. Under the open-loop control ($f_p^* = 0.1$), the peak magnitude at $f_s^* = 0.13$ recedes by 75% in E_Y and 61% in E_u, compared with the unperturbed case. With the PID controllers applied, the peak magnitude in E_Y and E_u at f_s^* also retreats greatly, by 31% in E_Y and 19% in E_u for PID-Y and by 57% in E_Y and 44% in E_u for PID-u. Yet, the retreat is less than that achieved by the open-loop system. However, the PID-Yu scheme manages to reduce the peak magnitude by 87% in E_Y and 81% in E_u, showing a performance significantly superior to the open-loop system and other closed-loop schemes. Table 4-1 compares reductions in $E_{Y,\Delta f}^{(n)}$ and $E_{u,\Delta f}^{(n)}$ between different control schemes.

$E_{Y,\Delta f}^{(n)}$ and $E_{u,\Delta f}^{(n)}$ (n = 1, 2, 3) represent the energies of Y and u associated with the fundamental frequency (f_s^*, n = 1), its second (n = 2) and third (n = 3) harmonics, respectively. $E_{Y,\Delta f}^{(n)}$ and $E_{u,\Delta f}^{(n)}$ were calculated by integrating their respective power spectrum density functions over -3dB bandwidth with respect to the peak value. The open-loop control may reduce some harmonics more than PID-Y or PID-u does, and the PID-Yu control has the best performance of all, including the open-loop control. The difference in the control performance is attributed to different control signals. In the open-loop case, the control signal is independent of vortex shedding; in the closed-loop schemes the feedback signals from the fluid-structure interaction system are deployed. The observation indicates that the closed-loop control may not necessarily achieve a performance better than the open-loop control; the proper choice of the feedback signal is crucial. It is the combination of Y and u signals, not individual Y or u, which contains the information on fluid-structure interaction physics and thus warrants the best performance.

The overall performances of the three closed-loop control schemes, together with open-loop control case ($f_p^* = 0.1$), are summarized in Table 4-2 for comparison. Note that the control voltage, V_p, is a good indicator for the input control energy W (= V_p^2 / R, where R represents the resistance of the actuators). Irrespective of the control schemes, R remains constant. Therefore, a lower control voltage means a low energy requirement. The circulation (Γ) around a vortex is estimated by Eq.(3-1). Integration was conducted over an area enclosed by the cutoff level $\left|\omega_{zc}^*\right| = 0.3$, about 7% of $\left|\omega_{z\max}^*\right|$, which is the same as Brian and Donald (1983) used. Errors associated with

the Γ estimate was about 15%. It can be seen that PID-u control outperforms PID-Y control in every category, resulting in a higher reduction percentage in Y_{rms}/h, u_{rms}/U_∞ and Γ despite smaller perturbation voltage amplitude. Among all control methods listed in Table 4-2, PID-Yu has unequivocally the best performance in minimizing Y^*_{rms}, u^*_{rms} and Γ^*. Its required actuating voltage V_p or the perturbation amplitude Y_p is only about 50%, 30% and 20% of that used for PID-Y, PID-u and the open-loop control ($f^*_p = 0.1$), respectively. The result indicates one great advantage of the closed-loop control system over the open-loop one, i.e., the possibility to develop a more compact, self-contained and low energy control system, in particular, if the PID-Yu scheme is applied.

Figure 4-9 compares the cross-flow distributions of mean velocity $\overline{U}^*$ and Reynolds stresses $\overline{u^2}^*$, $\overline{v^2}^*$ and $\overline{uv}^*$ measured by LDA at $x/h = 3$ of the flows with and without perturbation. The closed-loop control using the PID-Y and PID-u schemes is not included since their performance is not any better than the open-loop control. For the open-loop control ($f^*_p = 0.1$), the minimum $\overline{U}^*$ and maximum $\overline{u^2}^*$, $\overline{v^2}^*$ and $\overline{uv}^*$ show a considerable decrease, down to 85%, 85%, 88% and 78% of that unperturbed, respectively. This was further reduced to 73%, 77%, 75% and 71% of unperturbed case, respectively, for the closed-loop control using the PID-Yu scheme. The increased mean velocity deficit when the flow is perturbed is consistent with the decreased entrainment of high speed fluid from the free-stream due to the weakened vortex strength (Warui & Fujisawa, 1996). The reduced maximum $\overline{u^2}^*$, $\overline{v^2}^*$ and $\overline{uv}^*$ may be ascribed to the impaired vortex strength. It is pertinent to comment that $\overline{U}^*$,

$\overline{u^2}^*$, $\overline{v^2}^*$ and $\overline{uv}^*$ are reasonably symmetric or anti-symmetric about the centerline although the perturbation was imposed on the upper side only of the cylinder, internally consistent with the flow visualization and PIV measured vortex street (Figure 4-5 and Figure 4-6).

The drag coefficient, $\overline{C}_D$, was calculated based on the cross-flow distributions of $\overline{U}^*$, $\overline{u^2}^*$ and $\overline{v^2}^*$ in Figure 4-9, viz Eq.(3-4). Without perturbation, $\overline{C}_D$ was 1.88, falling in the range of 1.7 ~ 2.0, as previously reported by, e.g., Lee (1975), Knisely (1990) and Zhou and Antonia (1994a). $\overline{C}_D$ drops by 21.0% for the open-loop control and by 35.1% for the PID-*Yu* control. Hsiao and Shyu (1991) observed a reduced $\overline{C}_D$ in an acoustically excited circular cylinder wake. The observation was linked with a narrower wake and the smaller defect of mean velocity profile. The cross-flow distribution of $\overline{U}^*$ in Figure 4-9(a) suggests an increasing wake width due to the perturbation on the cylinder. However, the maximum $\overline{u^2}^*$ and $\overline{v^2}^*$ are reduced because of the perturbation. It is therefore proposed that the perturbation leads to greatly weakened flow separation or vortex shedding and subsequently an increased backpressure. Consequently, $\overline{C}_D$ decreases.

4.5 Discussions

To understand the physics behind impaired vortex shedding and structural vibration, the spectral phase shift (ϕ_{Yu}) and coherence (Coh_{Yu}) between vortex shedding and structural vibration are calculated from simultaneously measured Y and u using Eqs.(3-3) and (3-2), respectively. The analysis in Section 3.5 indicated that

ϕ_{Yu} at f_s^* approximately described the phase relationship between the coherent lateral velocity, v, of the flow around the cylinder and the lateral structural oscillating velocity, $\dot{Y}$, its zero and -π (π) values corresponding to synchronization and the opposite movement between $\dot{Y}$ and v, respectively. Without perturbation, ϕ_{Yu} is zero near f_s^* = 0.13 (Figure 4-10(a)), consistent with synchronizing vortex shedding and structural vibration. The plateau about f_s^* indicates the synchronizing Y and u signals over a range of frequencies. Once perturbed using the open-loop control (f_p^* = 0.1), ϕ_{Yu} was changed from 0 to π in a narrow frequency range about f_s^* (Figure 4-10(b)). This implies a change in the nature of the fluid-structure interaction, that is, the synchronizing v and $\dot{Y}$ turn into anti-phased interactions against each other. As a result, Coh_{Yu} at f_s^* recedes from 0.65 to 0.15 (Figure 4-11(a) and Figure 4-11(b)). The drastic reduction in Coh_{Yu} means a decoupled correlation between vortex shedding and structural vibration. With closed-loop controls deployed, ϕ_{Yu} about f_s^* again shifts from 0 to π, which is evident in Figures 4-10(c) to 4-10(e). It is noteworthy that the frequency range over which ϕ_{Yu} = π exceeds markedly that in the open-loop control. This frequency range is largest for PID-*Yu*, from 0.11 to 0.27 (Figure 4-10(e)), essentially covering the entire frequency range (0.11 ~ 0.26) of synchronization between vortex shedding and induced vibration for bluff bodies with fixed separation points (Gowda, 1975). Any excitation force falls in this frequency range may lead to the synchronization phenomenon. The observation suggests that PID-*Yu* has completely altered the phase relationship between v and $\dot{Y}$ from in-phase to anti-phase, whereas other schemes have done it over a small range of frequencies

about f_s^*. In correspondence to the changing phase between vortex shedding and structural vibration, the peak at f_s^* in Coh_{Yu} (Figures 4-11(c) to 4-11(e)) retreats, compared with the unperturbed flow, and in effect completely vanishes when PID-*Yu* is deployed.

The jump in ϕ_{Yu} from 0 to π is associated with greatly impaired vortex shedding and structural vibration. It may be inferred that the fluid-structure system damping must have been changed. Damping models the energy dissipation of the system during vibrations and plays an important role in the stability of a structure and its vibration amplitude. The synchronizing vortex shedding and structural oscillation will be effectively attenuated if the damping ratio of the system is increased. It is therefore worthwhile examining how the system damping ratio has been altered due to the introduction of control. In this work, we define the effective damping, representing the energy dissipation of a system, as the sum of structural damping and fluid damping. The former may be generated by material, friction, impacting and the rubbing of two surfaces in contact, while the latter results from skin friction and viscous dissipation, i.e., viscous shearing of a fluid at the surface of the structure and flow separation (Blevins, 1990). Fluid damping is motion-dependent and is difficult to estimate. Zhou *et al.* (2001) and Zhang *et al.* (2003) used an auto-regressive moving average (ARMA) technique to calculate the effective damping ratios from measured displacement time series. Interested readers may refer to their papers for more details of the technique. This technique is used presently to estimate the effective damping ratio ζ_e from the measured Y signal. In the present work, a program developed in Zhou *et al.* (2001) is used for the estimation of ζ_e. The accuracy of the calculation

depends on two factors: calculation order and the number of sampling points. During experiments, an order of 190 and 70000 data points were used for calculation, which was found to be sufficient to produce converged ζ_e. Figure 4-12 shows ζ_e for different schemes. The structural damping ratio ζ_s of the first mode motion, indicated by a dash line in the figure, was measured under no flow condition with the cylinder excited by an electromechanical shaker. Without perturbation, vortex shedding synchronizes with structural vibration, and ζ_e is less than ζ_s, albeit slightly. This suggests a negative fluid damping ratio ζ_f since $\zeta_e = \zeta_s + \zeta_f$. The negative ζ_f simply means that vortex shedding enhances the structural vibration (Zhou *et al.* 2001; and Zhang *et al.* 2003). For the open-loop control ($f_p^* = 0.1$), ζ_e increases by 163.2%, compared with the unperturbed case. Similarly, the closed-loop control using PID-*Y*, PID-*u* and PID-*Yu* leads to an increase in ζ_e by 37.9%, 97.7% and 271.4%, respectively.

Vortex-induced vibrations originate from fluid excitation forces, which are created by vortex shedding from a bluff body. The forces cause the structure to vibrate. The resultant structural vibrations may in turn influence the flow field, giving rise to fluid-structure coupling and even resonance when the frequency of the forces/vortex shedding can be appreciably modified (Zhou *et al.* 2001) and the structural vibration can be grossly amplified. The coupling is in general a highly non-linear function of both structural motion and flow velocity. In the open-loop control, the control signal is a periodic signal, which is independent of fluid-structure interactions. However, when the control signal frequency is outside the

synchronization range, i.e. $f_p^* = 0.11 \sim 0.26$, the control effect may alter the nature of the fluid-structure coupling, changing the in-phased fluid-structure synchronization into anti-phased interactions between fluid and structure. Meanwhile, the effective damping ratio of the system increases significantly, enhancing the dissipation of both vortex shedding and structural vibration energies. As such, the nature of fluid and structure interactions has been changed from reinforcing each other into moving against each other. This change in the physical interaction causes drastically weakened vortex shedding and hence structural vibration. For the PID-*u* closed-loop scheme, the feedback signal is from flow, which is the excitation source. Therefore, the effect of the control action is to modify directly the flow excitation and subsequently or indirectly the structural vibration. This control system allows the phase relationship between vortex shedding and structural vibration to be varied, either in-phased or anti-phased, or something between. In the anti-phased case, the control effect again alters the in-phased fluid-structure synchronization into anti-phased interactions between fluid and structure, thus reducing effectively vortex strength and structural vibration. Nevertheless, with an input energy of one third (Table 4-2) of that applied in the open-loop case, its performance is not necessarily better than the open-loop control. Similarly, the PID-*Y* control can reduce effectively the vortex strength and structural vibration. However, this scheme uses the structural vibration signal as the feedback signal, that is, the feedback information reflects the passive response of fluid-structure interactions, instead of the excitation source. Consequently, the control performance is less effective than the PID-*u* scheme, even though the input energy has nearly doubled that of the PID-*u* scheme. For the PID-*Yu* scheme, the feedback signal is a combination of both *Y* and *u* signals and reflects both

excitation consequence and source, and perhaps more importantly reflects the interaction/coupling between flow excitation and structural vibration, addressing the essence that amplifies both structural vibration and vortex shedding. As a result, this scheme has a superior performance to all other schemes, even with an input energy of 19%, 32% and 57% of those applied in the open-loop, PID-u and PID-Y schemes, respectively.

4.6 Conclusions

The closed-loop control using PID controllers is developed to suppress vortex shedding and vortex-induced vibration on a flexibly supported square cylinder. The control is made possible using THUNDER actuators to perturb one surface of the cylinder. Three control schemes are investigated, including PID-Y, -u and -Yu, each deploying one different feedback signal. The investigation leads to the following conclusions.

1) The presently developed flow control effectively turns the in-phased vortex shedding and structural vibration into the anti-phased. This is associated with a significant increase in the effective damping ratio of the flow-structure system, implying an enhanced dissipation of vortex shedding and structural vibration energies. As a result, both vortex strength and structural vibration amplitude are remarkably reduced, and their correlation appears diminishing. The drag coefficient is also greatly reduced.
2) The PID-Yu scheme, with the least input energy required, has the best performance of all, including the open-loop control; the visualized wake appears radish-like, suggesting an almost complete destruction of the Kármán

vortex street. Such a performance is attributed to its control signal, which is the combination of flow excitation and structural vibration, thus reflecting the non-linear interactions between fluid and structure. The PID-u control scheme outperforms the PID-Y strategy. While the latter targets the control of passive structural vibration, the former directly tackles the fluctuating flow, which is the origin of the excitation forces on structural vibration, thus being more effective. However, with a small input energy, compared with that applied in the open-loop system, the performance of the two closed-loop schemes is not necessarily better than that of the open-loop control. The observation points to the crucial role the feedback signal plays in the closed-loop control of flow or flow-induced vibrations.

3) The closed-loop control has many advantages over an open-loop system. The open-loop control depends on the perturbation frequency f_p^*; it can only suppress vortex shedding or structural vibration if f_p^* is outside the synchronization range. Within the synchronization range, the open-loop control enhances vortex shedding or structural vibration. On the other hand, with the feedback signal from flow, structural vibration or a combination of both, the closed-loop control can always suppress both vortex shedding and structural vibration. Furthermore, with the deployment of a closed-loop control, the required perturbation amplitude or voltage can be greatly reduced, pointing to the possibility of developing a more compact and self-contained control system.

Table 4-1 Reductions in $E_{Y,\Delta f}^{(n)}$ and $E_{u,\Delta f}^{(n)}$ associated with the first three harmonics of the vortex shedding frequency

Control Schemes		Open-loop $f_p^* = 0.1$	PID-Y	PID-u	PID-Yu
$E_{Y,\Delta f}^{(n)}$	$E_{Y,\Delta f}^{(1)}$	77%↓	38%↓	68%↓	92%↓
	$E_{Y,\Delta f}^{(2)}$	57%↓	80%↓	82%↓	86%↓
	$E_{Y,\Delta f}^{(3)}$	49%↓	62%↓	69%↓	83%↓
$E_{u,\Delta f}^{(n)}$	$E_{u,\Delta f}^{(1)}$	65%↓	37%↓	64%↓	84%↓
	$E_{u,\Delta f}^{(2)}$	76%↓	59%↓	68%↓	83%↓
	$E_{u,\Delta f}^{(3)}$	72%↓	48%↓	67%↓	81%↓

Table 4-2 Control performance of various control schemes

Control Schemes	Open-loop $f_p^* = 0.1$	PID-Y	PID-u	PID-Yu
Y_{rms}	75%↓	40%↓	53%↓	82%↓
u_{rms}	68%↓	17%↓	32%↓	70%↓
Γ	50% ↓	22% ↓	34% ↓	65% ↓
V_p	141.4 volts	83.7 volts	47.4 volts	27.1 volts
Y_p/Y_{max}	35.1%	20.5%	14.7%	7.0%

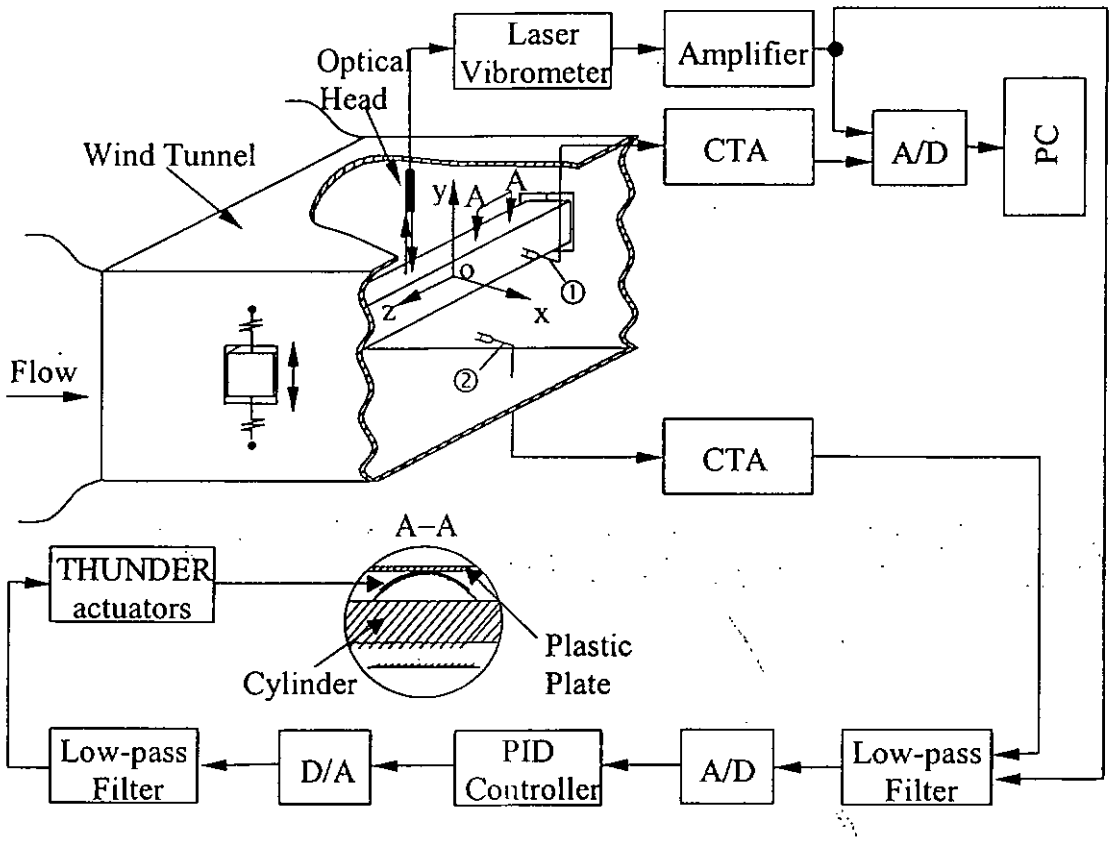

Figure 4-1 Experimental Setup. ① Monitor hot wire was located at $x = 2h$, $y = 1.5h$, $z = 0$; ② Feedback hot wire was located at $x = 1.6h$, $y = -2.5h$, $z = 0$.

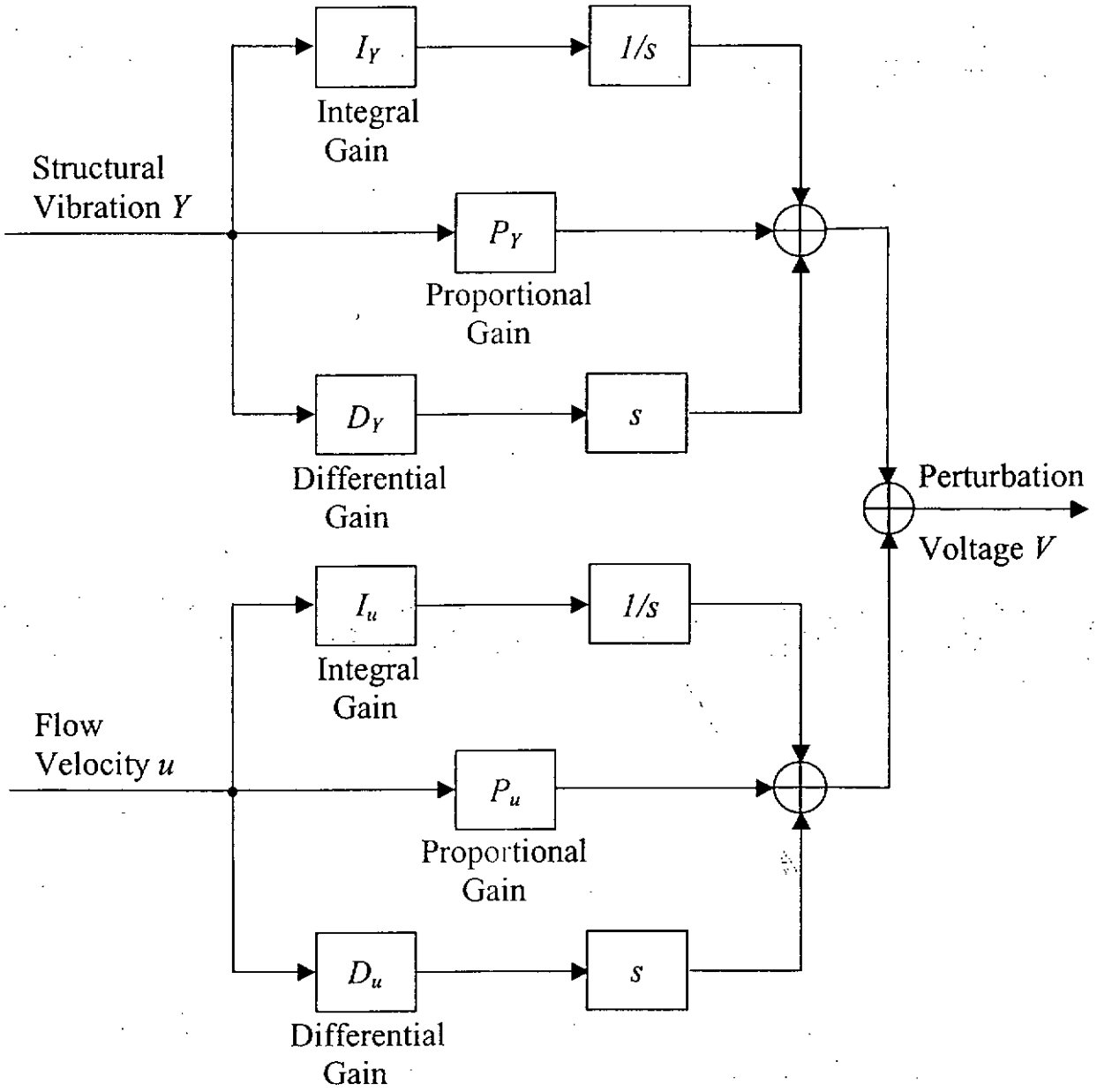

Figure 4-2 Block diagram of PID control schemes.

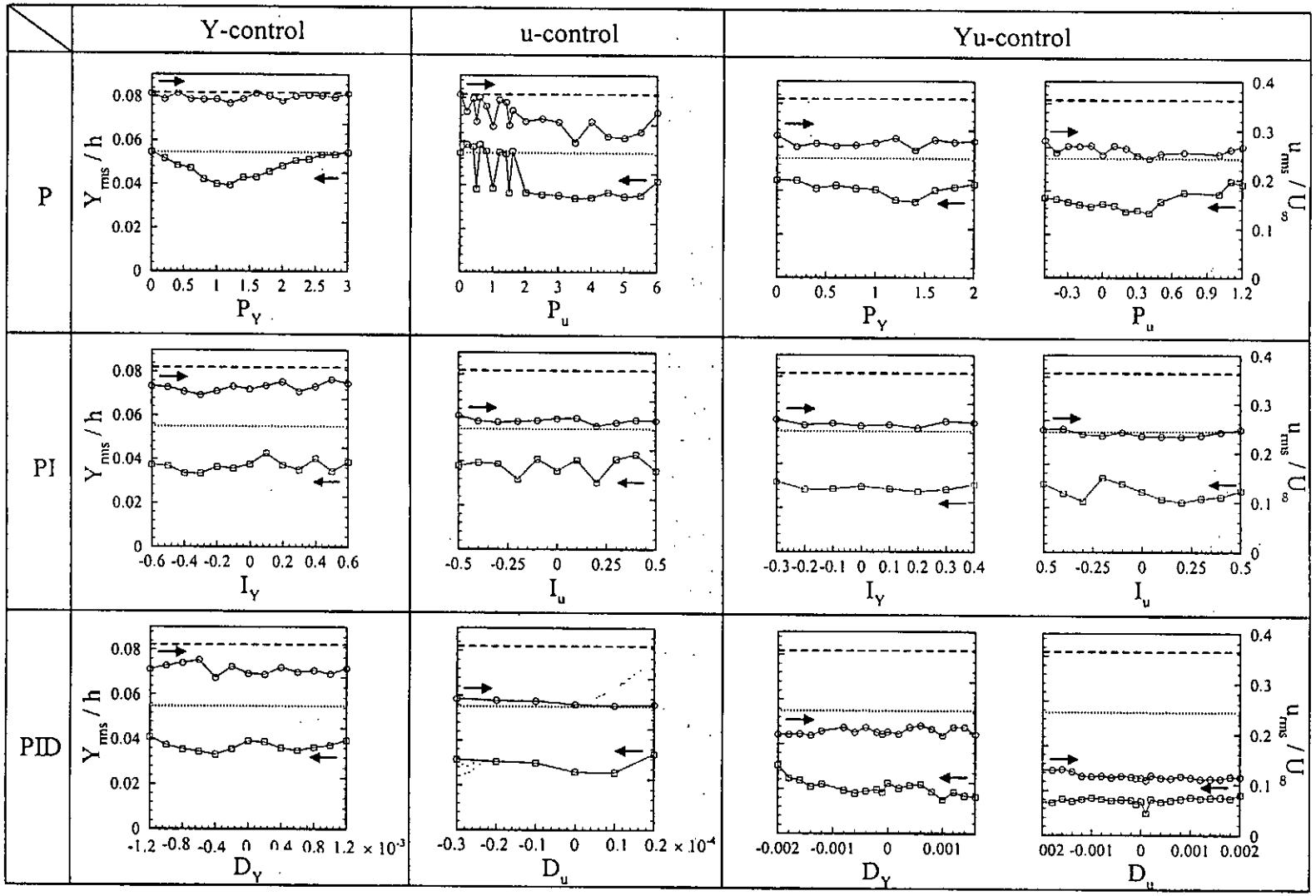

Figure 4-3 Variation of Y_{rms}/h and u_{rms}/U_∞ with the proportional gain (P), integral gain (I) and differential gain (D) under different control schemes. ..... : Unperturbed Y_{rms}/h; ---: Unperturbed u_{rms}/U_∞.

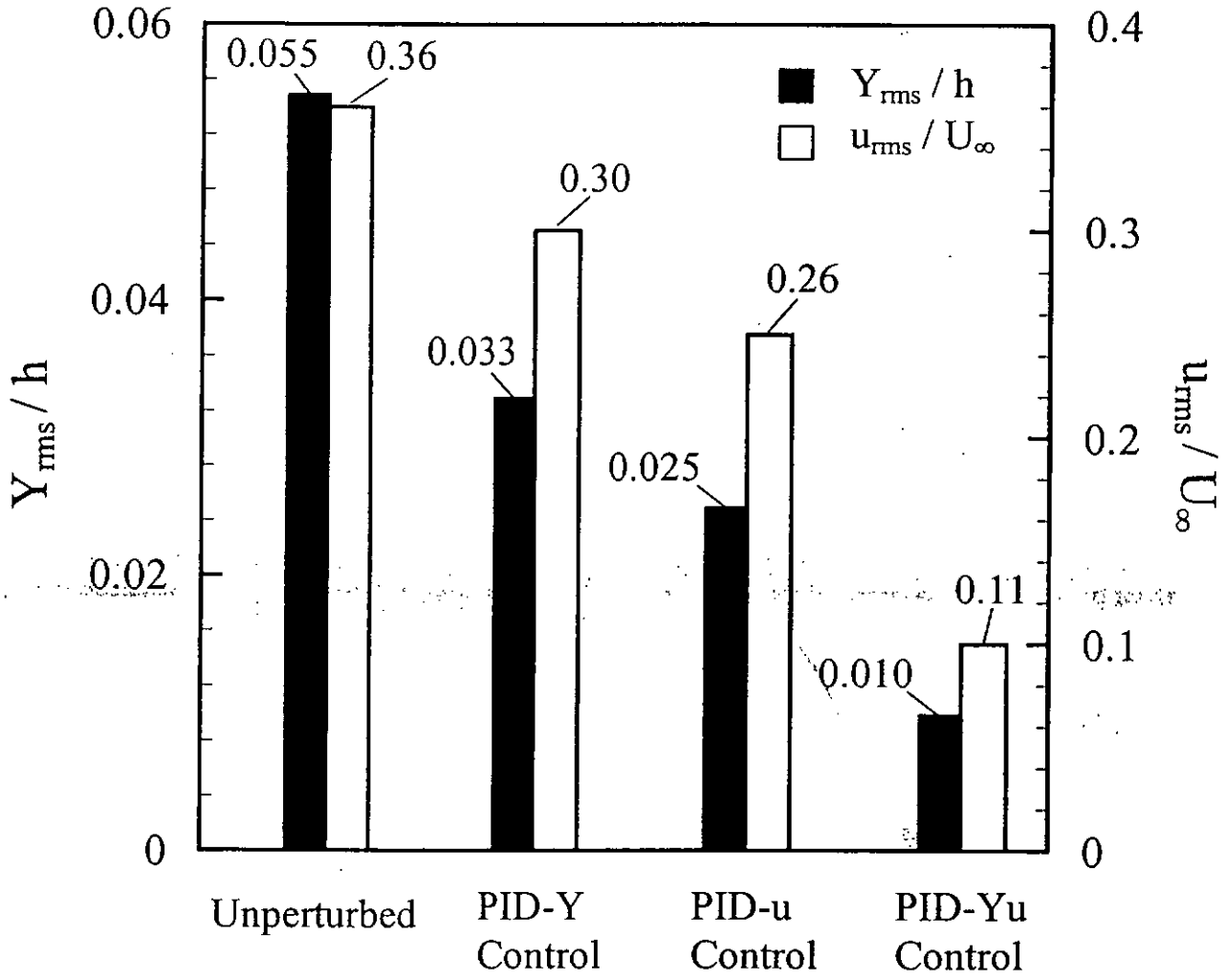

Figure 4-4 Comparison in u_{rms} and Y_{rms} among various control schemes. The feedback and monitor hot wires were located at $x / h = 1.6$, $y / h = -2.5$ and $x / h = 2$, $y / h = 1.5$, respectively.

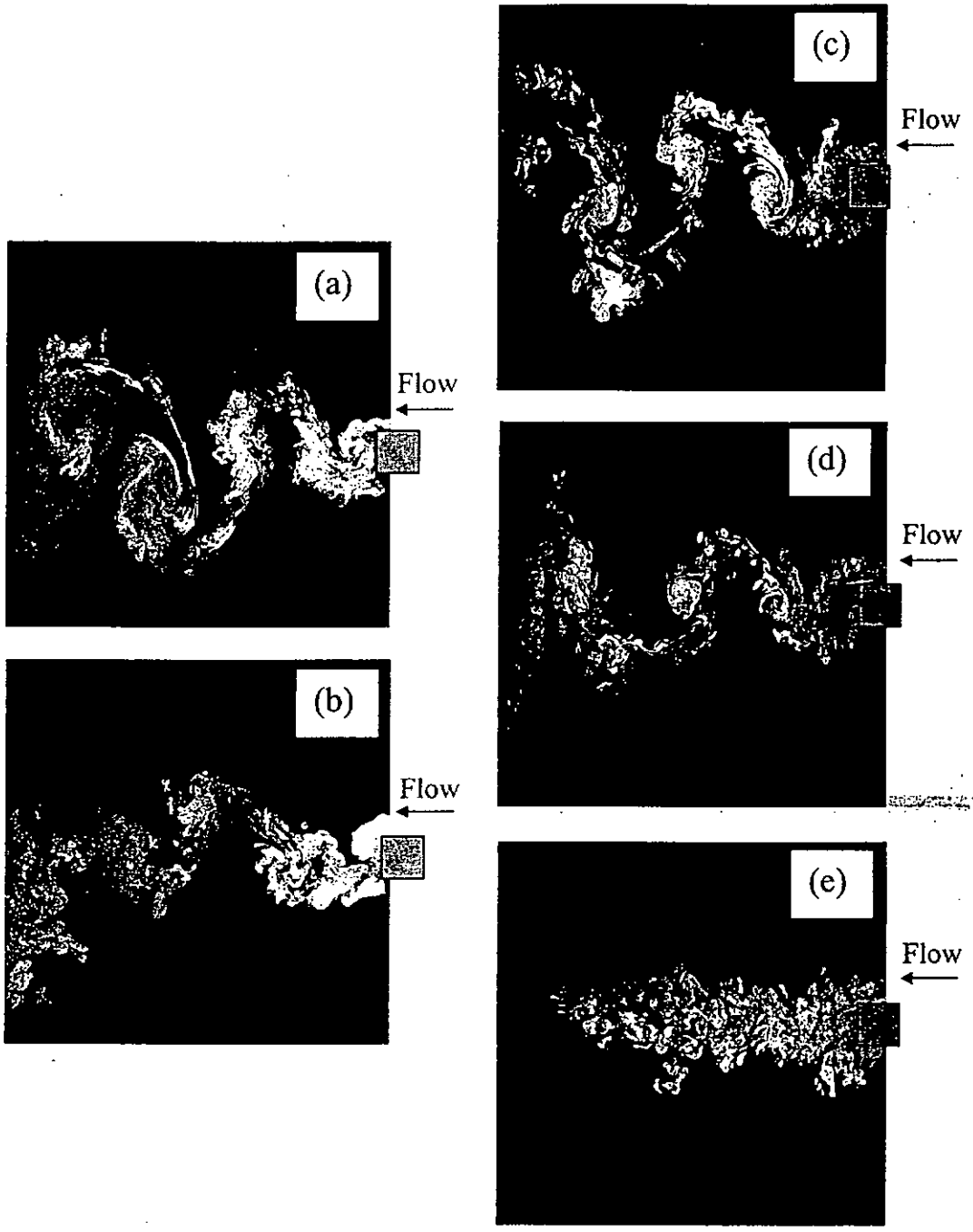

Figure 4-5 Typical photographs from flow visualization with and without control: (a) unperturbed; (b) open-loop control, $f_p^* = 0.1$ (c) PID-*Y*; (d) PID-*u*; (e) PID-*Yu*. The feedback and monitor hot wires were located at $x/h = 1.6$, $y/h = -2.5$ and $x/h = 2$, $y/h = 1.5$, respectively.

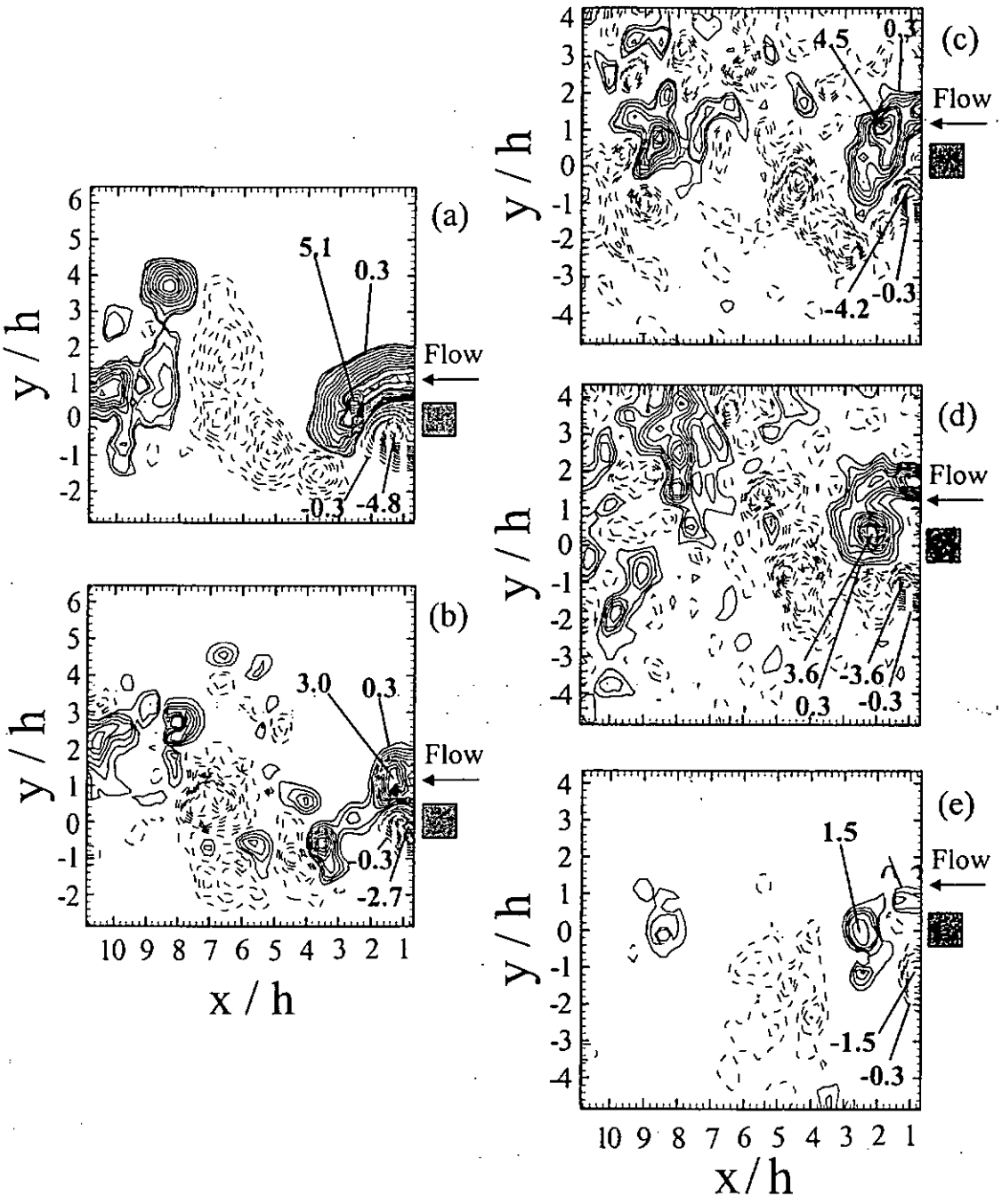

Figure 4-6 PIV measured iso-contours of spanwise vorticity $\omega_z^* = \omega_z h / U_\infty$ with and without control: (a) unperturbed; (b) open-loop control, $f_p^* = 0.1$; (c) PID-*Y*; (d) PID-*u*; (e) PID-*Yu*. The feedback and monitor hot wires were located at $x/h = 1.6$, $y/h = -2.5$ and $x/h = 2$, $y/h = 1.5$, respectively.

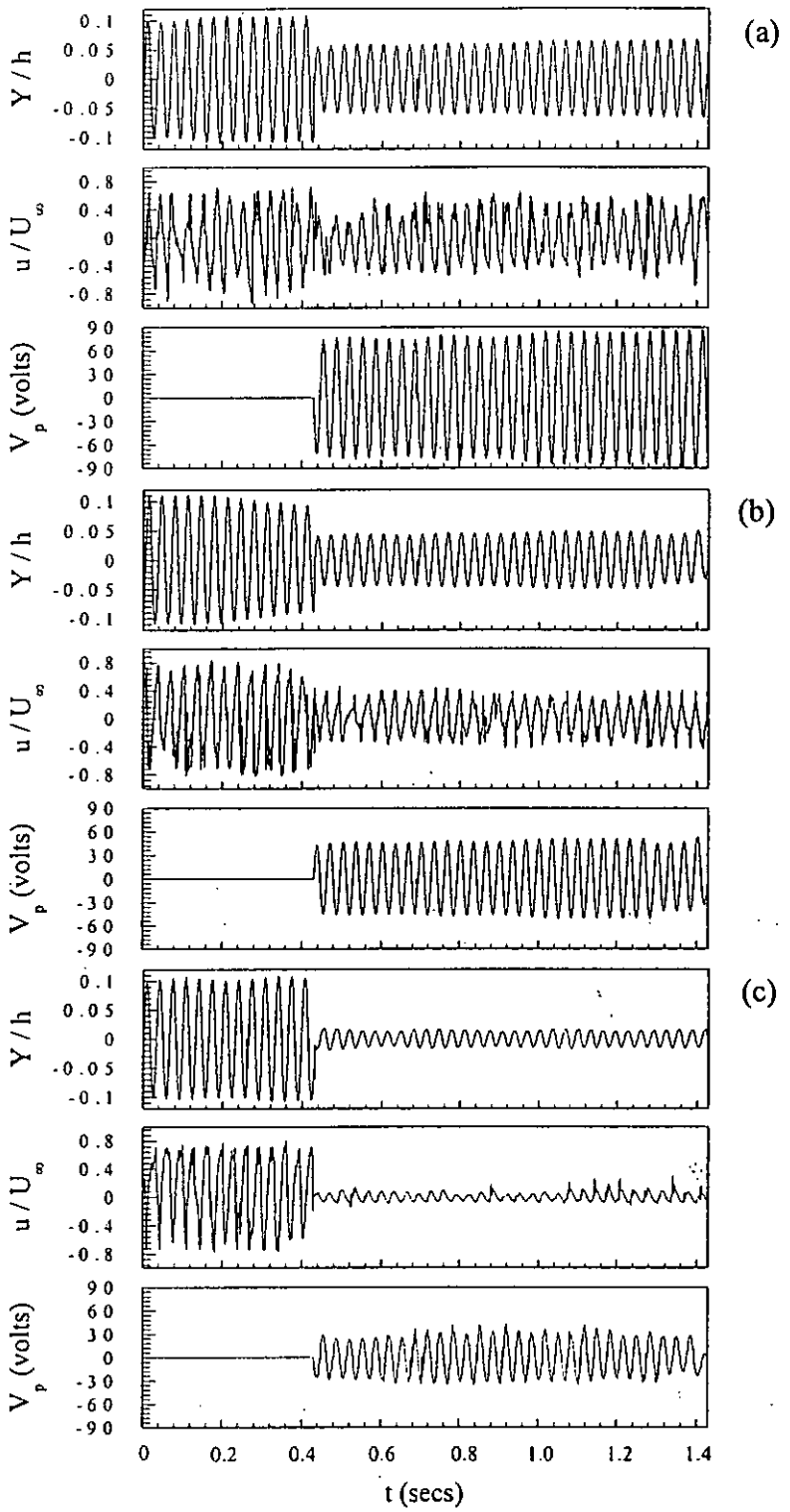

Figure 4-7 Typical transition of structural vibration (Y), flow velocity (u) and perturbation voltage (V_p) signals when PID controller was switched on. (a) PID-Y; (b) PID-u; (c) PID-Yu. The feedback and monitor hot wires were located at x / h = 1.6, y / h = -2.5 and x / h = 2, y / h = 1.5, respectively.

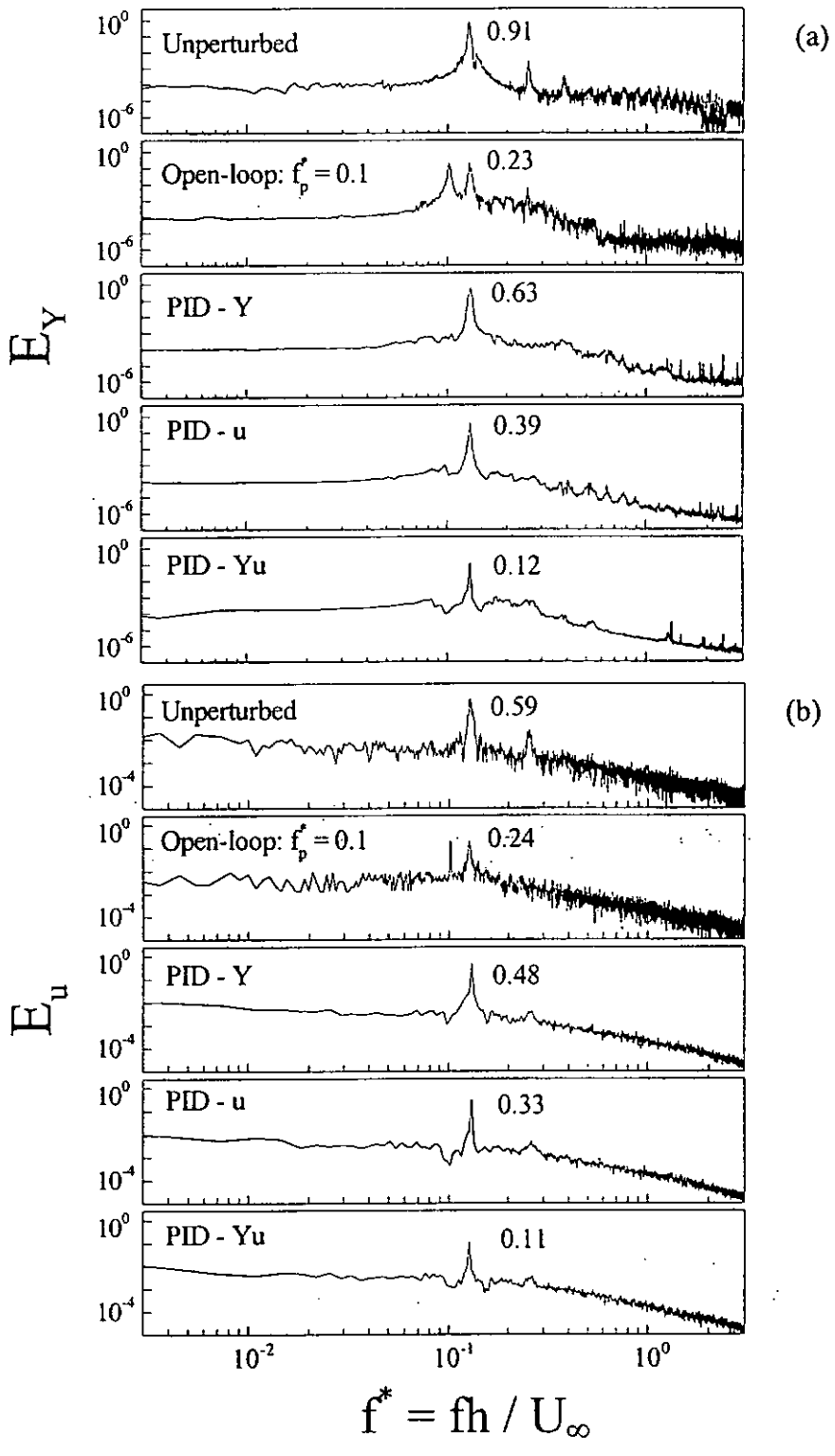

Figure 4-8 Power spectra of structural vibration (Y), flow velocity (u) with and without control: (a) E_Y, (b) E_u. The feedback and monitor hot wires were located at $x/h = 1.6$, $y/h = -2.5$ and $x/h = 2$, $y/h = 1.5$, respectively.

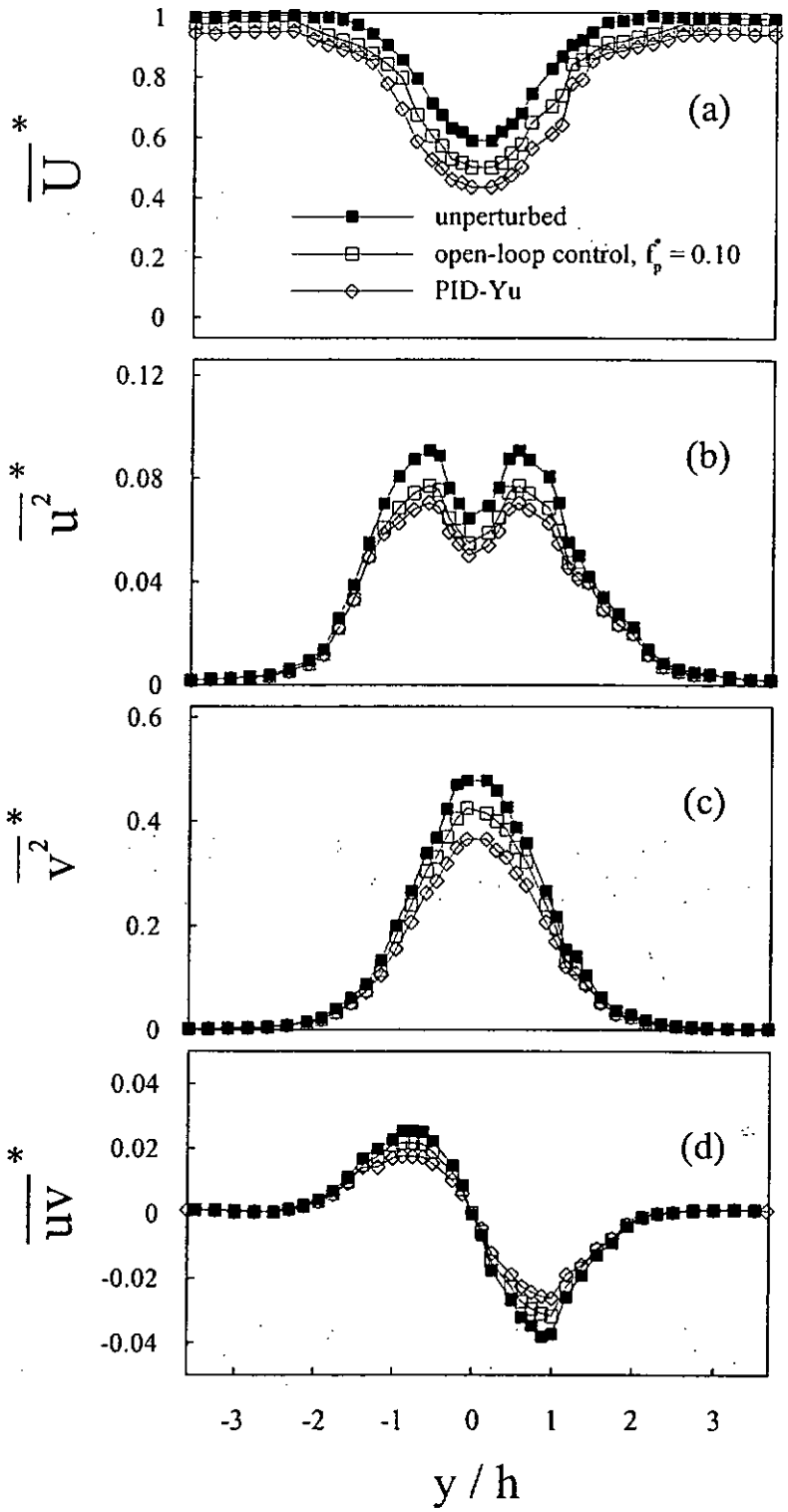

Figure 4-9 Cross-flow distribution of mean velocity and Reynolds stresses at $x/h = 3$ with and without control: (a) $\overline{U}^*$, (b) $\overline{u^2}^*$, (c) $\overline{v^2}^*$, (d) $\overline{uv}^*$. The feedback and monitor hot wires were located at x/h = 1.6, y/h = -2.5 and $x/h = 2$, y/h = 1.5, respectively.

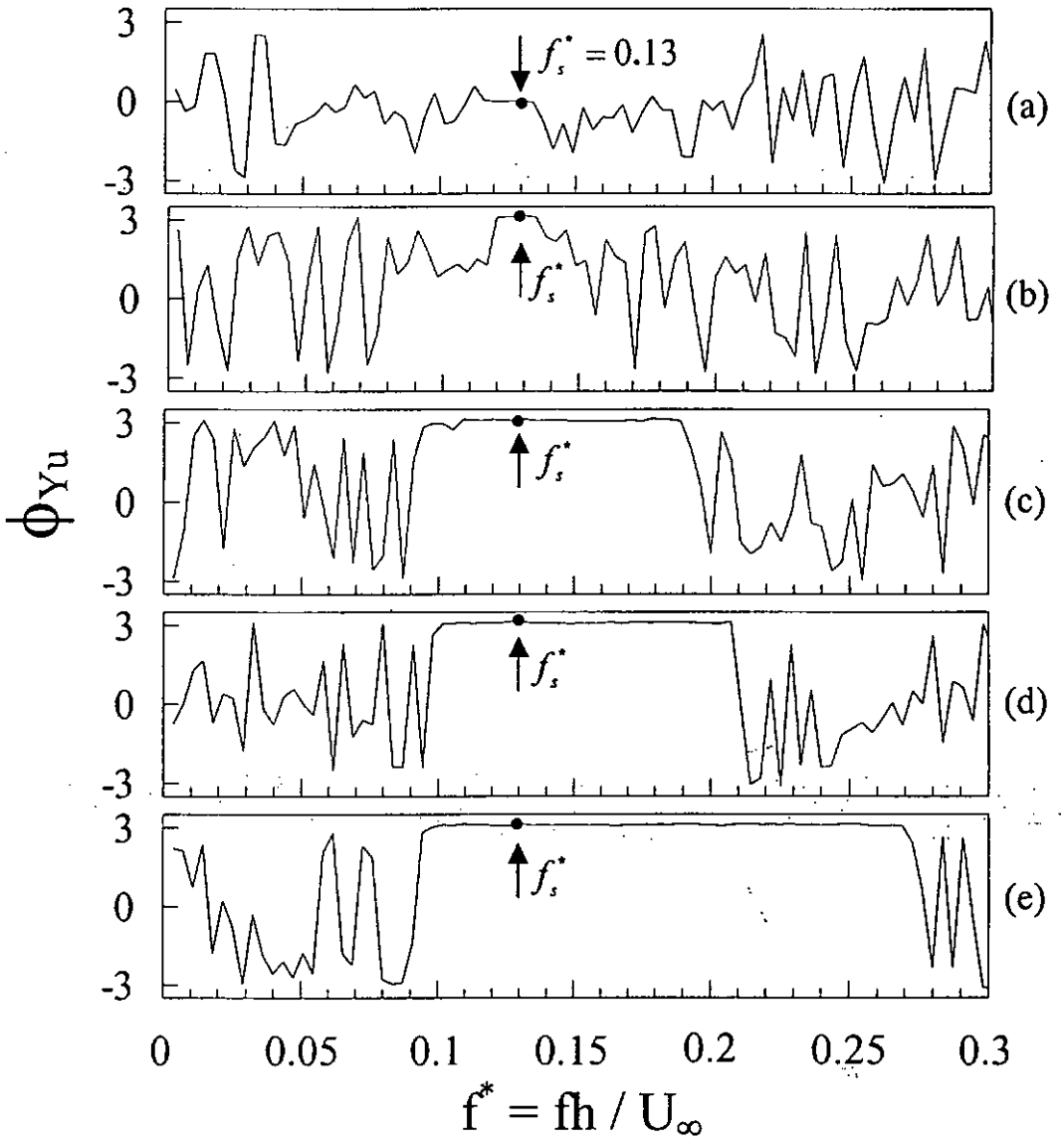

Figure 4-10 Phase shift ϕ_{Yu} between structural displacement Y and fluctuating streamwise flow velocity u with and without control: (a) unperturbed; (b) open-loop control, $f_p^* = 0.1$; (c) PID-Y; (d) PID-u; (e) PID-Yu. The feedback and monitor hot wires were located at $x / h = 1.6$, $y / h = -2.5$ and $x / h = 2$, $y / h = 1.5$, respectively.

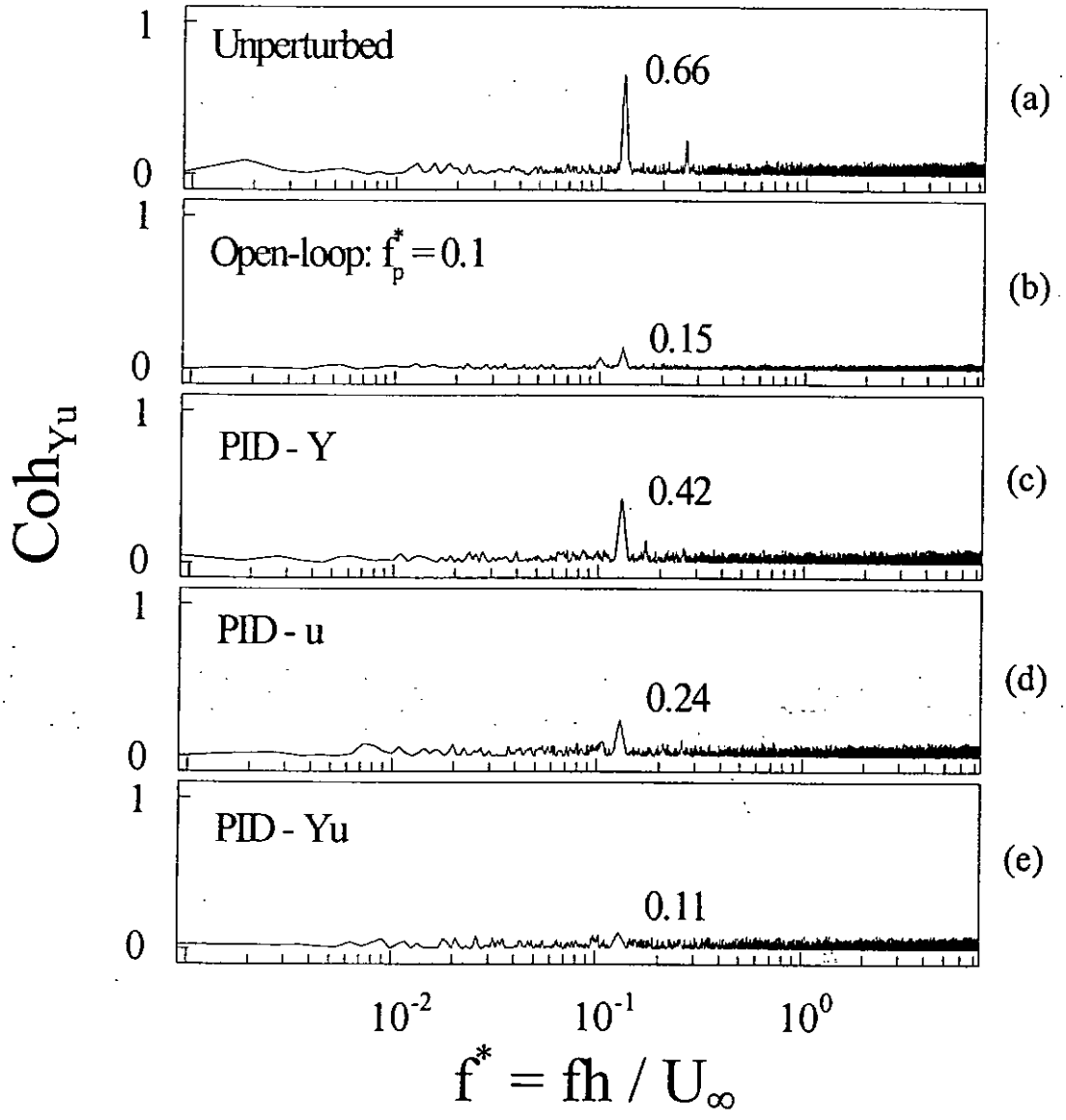

Figure 4-11 Spectral coherence Coh_{Yu} between structural displacement Y and fluctuating streamwise flow velocity u with and without control. The feedback and monitor hot wires were located at $x / h = 1.6$, $y / h = -2.5$ and $x / h = 2$, $y / h = 1.5$, respectively.

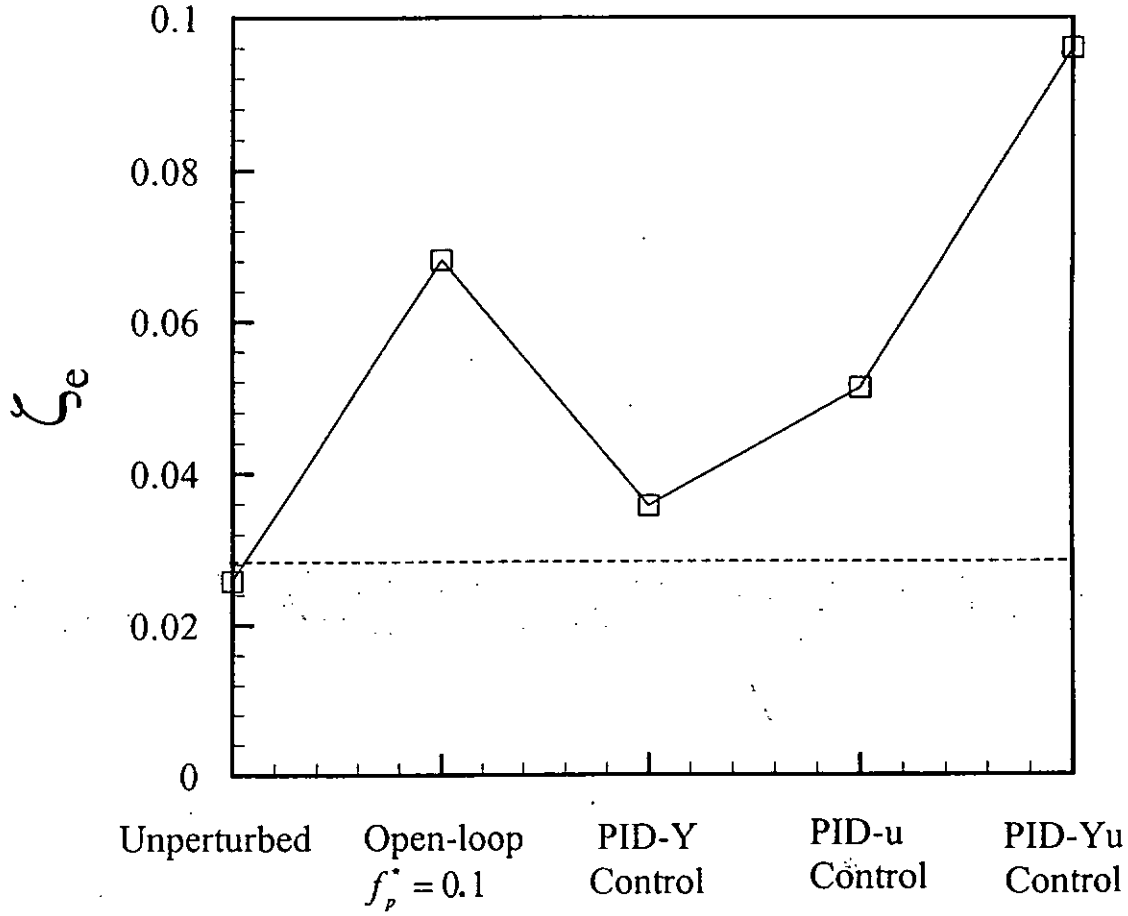

Figure 4-12 Effect of open- and closed-loop control on cross flow effective damping ratios, ζ_e . The dash line denotes the structural damping ratio ζ_s measured without flow.

CHAPTER 5

CLOSED-LOOP-MANIPULATED WAKE OF A STATIONARY CYLINDER

5.1 Introduction

The work presented in Chapter 3 and Chapter 4 was based on perturbing the cylinder surface and was all conducted in the context of a flexibly supported cylinder. As such, the vortex-induced structural oscillation was rather significant, up to $0.08h$ at the occurrence of resonance, where the frequency of vortex shedding coincided with the natural frequency of the fluid-structure system. It has been seen that the oscillation, especially under the closed-loop controlled perturbation, was turned into anti-phase with vortex shedding, and accordingly almost completely destroyed the vortex street. Since the surface perturbation amplitude used was typically 7% of the structural oscillation, it was technically difficult to disassociate the perturbation from the oscillation of the whole structure in terms of the role played in modifying the flow so as to extract the intrinsic relationship between the perturbation and the flow field. This relationship is believed to be crucial in fully understanding the control mechanism. Furthermore, in the absence of significant structural oscillation, one

wonders whether such a surface perturbation technique is still effective in the flow control.

This Chapter aims to address the aforementioned two issues. A fix-supported rigid square cylinder was used. The test model was built with pizeo-ceramic actuators to perturb the cylinder surface, along with a closed-loop control system deploying a simplified Proportional-Integral-Derivative (PID) controller. Tuned at one Re, the effectiveness of the controller was assessed in a range of Re to examine its robustness. The flow behind the cylinder was documented using a number of techniques, including a particle image velocimetry (PIV), flow visualization, laser Doppler anemometer (LDA) and hot wire velocimetry. The fluctuating lift and drag forces on the cylinder were measured using load cells. The cylinder surface perturbation was monitored using a laser vibrometer simultaneously with the forces or flow, thus allowing the relationship between the perturbation and flow modification to be examined in detail.

5.2 Experimental Condition

Experiments were conducted in the same closed circuit wind tunnel as described in Section 2.6. A square cylinder made of aluminum alloy, with a height h = 16.1 mm, was horizontally fix-mounted at both ends on the sidewalls of the wind tunnel (Figure 5-1). Three THUNDER actuators were embedded in series on the upper side of the cylinder and covered with a plastic plate, which was flush with the remaining part of the cylinder surface. Driven by the actuators, this plate may oscillate up and down to create a perturbation on the cylinder surface. The properties and detailed installation arrangement of the actuators were described in Section 2.5.

Hot wire ①, made of a 5 μm tungsten wire, measured streamwise fluctuating velocity (u), which was used as the feedback signal of the control system. The wire was placed at $x / h = 0$, $y / h = 1.6$ and $z / h = 0$, where a clean signal of vortex shedding was detected and the system delay due to the dislocation between the sensor and actuators was reduced to a minimum. After amplification, the feedback signal was processed through a low-pass filter at a cutoff frequency of 200 Hz to a Digital Signal Processor (DSP) controller fitted with 16-bit AD and DA converter. The converted analog signal was low-pass filtered again at a cutoff frequency of 200 Hz and amplified by two dual channel piezo-driver amplifiers (Trek PZD 700) to activate the actuators. The use of the two low-pass filters for both the feedforward and feedback passages was to remove high frequency noises from turbulence and electronic components.

Experiments were carried out at wind velocities of $U_\infty = 3$ m/s, 7 m/s and 9 m/s, corresponding to Re = 3200, 7400 and 9500, respectively. The control performance was monitored using various measurement techniques. The flow visualization and PIV measurements were conducted using a Dantec standard PIV2100 system. Each image covered an area of 213 mm × 161 mm or $x / h \approx 0 \sim 13.2$ and $y / h \approx -5 \sim 5$ of the flow field for flow visualization and 113 mm × 105 mm, i.e., $x / h \approx 1 \sim 8$, $y / h \approx -2.9 \sim 3.6$, for PIV measurements. A two-component LDA system was used to measure the cross-flow distributions of fluctuating velocities and Reynolds shear stress at $x / h = 3$. The detailed information about PIV and LDA measurements could be found in Section 2.6.

The fluctuating lift and drag forces, F_L and F_D, were measured using two 3-component load cells (Kistler 9251A), which is a kind of quartz force sensor for

measuring the three orthogonal components of a dynamic or quasi-static force acting in an arbitrary direction, shown by Figure 5-2(a). This force sensor contains 3 pairs of quartz rings which were mounted between two steel plates in the sensor housing. Two quartz pairs were sensitive to shear and measure the force components F_x and F_y, while one quartz pair sensitive to pressure measured the component F_z of a force acting on the sensor. The direction of x, y and z is defined in Figure 5-1. The electrical charges proportional to the three components were led via electrodes to the corresponding connectors. In addition, the quartz packet was protected by the stainless, tightly welded sensor housing. The latter had two fine-machined reference faces parallel to y. These faces can be used to position the sensor and consequently the coordinate system. This configuration warrants many advantages of the load cell, such as extended measuring range, high rigidity and minimal cross talk, etc. The force capacity and sensitivity of the load cell used in this work is 5 kN and 8 pC/N, respectively. The output of the load cell needs to be amplified using a charge amplifier (Kistler 5011). Figure 5-2(b) illustrates the installation of the load cells in the present experimental setup. The two load cells were mounted at the two ends of the cylinder using fixtures connected to the sidewalls of the wind tunnel.

Hot wire ②, made of 5 μm tungsten wire, was placed at $x / h = 2$, $y / h = 1.5$ and $z / h = 4$ to monitor the change in flow velocity (u_2) under the control effect. The perturbation displacement (Y_p) was measured by a laser vibrometer, simultaneously with u_2 or F_L and F_D. The measurement uncertainty of the laser vibrometer was about 0.5%. The Y_p and u_2 signals, along with F_L and F_D, were conditioned and digitized using a 12-bit A/D board at a sampling frequency of 3.5 kHz per channel. The duration of each record was 20 s.

5.3 Controller Design and Parameter Tuning

As mentioned in Chapter 4, by properly tuning the proportional gain (P), integral gain (I) and differential gain (D) of the PID controller, the control action was successfully applied to the system for the control of the resonant fluid-structure interaction. The development and implementation of the PID controller was performed using dSPACE system introduced in Section 2.5. The tuning process was, however, tedious and time-consuming because of the multitudinous combinations of P, I and D. In order to simplify the whole process, a two-parameter controller was developed through introducing a gain coefficient in amplitude $\tilde{P}$ and a phase shift $\tilde{\phi}$ between the output and input of the controller. Based on the transfer function of the PID controller (Franklin *et al.* 1991), the simplified controller and the conventional PID controller are related by the following equations:

$$\tilde{P} = \sqrt{P^2 + \left(\frac{4\pi^2 D f_s^2 - I}{2\pi f_s}\right)^2} \tag{5-1}$$

$$\tilde{\phi} = \sqrt{\frac{4\pi^2 f_s^2 D - I}{2\pi f_s P}} \tag{5-2}$$

where f_s is the vortex shedding frequency. Both $\tilde{P}$ and $\tilde{\phi}$ should be adjusted during tuning. The tuning procedure was first to keep $\tilde{\phi} = 0^\circ$ and vary $\tilde{P}$ until u_{rms} reached the minimum at $\tilde{P}_1$ and the maximum at $\tilde{P}_2$ ($\tilde{P}_1 < \tilde{P}_2$). Second, $\tilde{P}$ was successively increased within the range from $\tilde{P}_1$ to $\tilde{P}_2$ and each time $\tilde{\phi}$ was adjusted within a cycle. By doing so, two $\tilde{\phi}$, $\tilde{\phi}_1$ and $\tilde{\phi}_2$, could be obtained, under which u_{rms} reached

minimum and maximum, respectively. Finally, fixing $\tilde{\phi}$ at $\tilde{\phi}_1$ and $\tilde{\phi}_2$, respectively, $\tilde{P}$ was tuned again to find $\tilde{P}_3$ and $\tilde{P}_4$, corresponding to minimum and maximum case of u_{rms}, respectively. Then the tuning process may lead to two optimal configurations with the parameters: $\tilde{\phi} = \tilde{\phi}_1$ and $\tilde{P} = \tilde{P}_3$ for the impaired case, $\tilde{\phi} = \tilde{\phi}_2$ and $\tilde{P} = \tilde{P}_4$ for the enhanced case.

Tuning the controller parameters was carried out for U_∞ = 7 m/s (Re = 7400). Figure 5-3(a) shows the variation in the root mean square (rms) value, $u_{2,\,rms}$, of u_2 from hot wire ② within one cycle of $\tilde{\phi}$ as $\tilde{P}$ is kept constant at 0.3, 1 and 3, respectively. U_∞ is used to normalize $u_{2,\,rms}$. It is noted that, for all $\tilde{P}$ values, $u_{2,\,rms}$ displays its minimum at $\tilde{\phi} = 108^\circ$ and reaches the maximum at $\tilde{\phi} = 288^\circ$, suggesting a 180° phase shift between the two extremes. Figure 5-3(b) shows $u_{2,\,rms}$ at $\tilde{\phi} = 108^\circ$ and 288°, measured as $\tilde{P}$ varies from 0 to 9. At $\tilde{\phi} = 108^\circ$, $u_{2,\,rms}$ exhibits a dip at $\tilde{P}$ = 0.3, a 40% fall compared with the unperturbed case (the dash line). On the other hand, $u_{2,\,rms}$ is persistently enhanced at $\tilde{\phi} = 288^\circ$ and achieves a 90% amplification at $\tilde{P} = 9$ compared with the unperturbed condition. In following discussions, the two extremes, i.e. with the combinations of $\tilde{P} = 0.3$, $\tilde{\phi} = 108^\circ$ and $\tilde{P} = 9$, $\tilde{\phi} = 288^\circ$, are referred to as the impaired and the enhanced cases, respectively.

5.4 Performance of the Closed-loop Control

5.4.1 Flow modifications

Investigation was first conducted at Re = 7400. Figure 5-4 illustrates the typical signals of u_2, fluctuating lift and drag coefficients (C_L and C_D) when the closed-loop control was switched on and off. C_L and C_D are given by $F_L/(0.5\rho U_\infty^2 hl)$ and $F_D/(0.5\rho U_\infty^2 hl)$, respectively, where ρ and l stand for air density and cylinder length, respectively. Without perturbation, the rms values of C_L and C_D are about 1.41 and 0.132, respectively, which are consistent with Sakamoto *et al.*'s (1989) report. Evidently, the closed-loop controlled perturbation has a great influence on all the signals, drastically reducing at $\widetilde{P} = 0.3$ and $\widetilde{\phi} = 108^\circ$ (Figure 5-4(a)) or amplifying at $\widetilde{P} = 9$ and $\widetilde{\phi} = 288^\circ$ (Figure 5-4(b)) their amplitudes. The variation is well reflected in the power spectral density functions, E_{u_2}, E_{F_L} and E_{F_D}, of u_2, F_L and F_D (Figure 5-5). The spectrum has been normalized so that $\int_0^\infty E_\alpha(f)df = 1$ (α stands for u_2, F_L or F_D). In the absence of perturbation, both E_{u_2} and E_{F_L} display a pronounced peak at $f_s^* = 0.132$, which is agreeable with previous measurements (e.g. Vickery, 1966; Lyn & Rodi, 1994; and Zhou & Antonia, 1994a). As expected, the most prominent peak in E_{F_D} occurs at $2f_s^*$. The number near the most pronounced peak indicates the peak magnitude. This magnitude decreases by 33% in E_{u_2}, 33% in E_{F_L} and 28% in E_{F_D} for the impaired case and increases by 73% in E_{u_2}, 60% in E_{F_L} and 52% in E_{F_D} for the enhanced case. Correspondingly, the rms values of C_L and C_D shrink by 51% and

42%, respectively, for the former but go up by 60% and 67%, respectively, for the latter.

Figures 5-6 and 5-7 show the flow visualization photos and iso-contours of the normalized spanwise vorticity, $\omega_z^* = \omega_z h / U_\infty$, from the PIV measurement, respectively, for the unperturbed, impaired and enhanced cases. The square in the figures denotes the cylinder position. The maximum concentration of ω_z^* is given in Figure 5-7, so is the cutoff level (0.3). The experimental uncertainty of ω_z^* was estimated to be about 9%. The Kármán vortex street is evident in Figure 5-6(a) and Figure 5-7(a) when perturbation is absent. This street is greatly impaired in Figures 5-6(b) and 5-7(b) and enhanced in Figures 5-6(c) and 5-7(c). The circulation (Γ) around a vortex is estimated by Eq.(3-1). The $|\omega_{z\max}^*|$ and Γ drop by 50% and 71% for the impaired case and rise by 100% and 152% for the enhanced case, respectively, compared with the unperturbed flow. The results suggest an effective modification for vortex shedding.

Figure 5-8 presents the cross-flow distributions of the mean velocity $\overline{U}^*$ and Reynolds stresses $\overline{u^2}^*$, $\overline{v^2}^*$ and $\overline{uv}^*$ obtained from LDA measurements at $x / h = 3$. For the impaired case, the maximum $\overline{U}^*$, $\overline{u^2}^*$, $\overline{v^2}^*$ and $\overline{uv}^*$ exhibit a considerable decrease, down to 80%, 55%, 65% and 78% of their unperturbed counterparts, respectively. For the enhanced case, the quantities grow by 112%, 135%, 137% and 140%, respectively, compared with the unperturbed flow. The variations are expected in view of the significantly modified vortex strength. For instance, the impaired vortex strength is expected to reduce the entrainment of high-speed fluid from the

free-stream to the wake, thus causing an increased maximum velocity deficit and decreased fluctuating velocities (Warui & Fujisawa, 1996; and Williams *et al.* 1992). Interestingly, $\overline{uv}^*$ declines only marginally. In contrast, there is a considerable increase in $\overline{uv}^*$ as vortex shedding is enhanced (Figure 5-8(d)). It is well established that the coherent structures in a turbulent near wake contribute little to the Reynolds shear stress; it is those relatively small-scale structures residing mostly in the saddle region between spanwise vortices that are responsible for the generation of the Reynolds shear stress (Zhou & Antonia, 1994b). It will be shown later that the control mainly alters relatively large-scale structures in the wake for the impaired case but also affect flow structures across a wide range of frequencies, including those of relatively small scales. This explains the observation in regarding to $\overline{uv}^*$. From a different perspective, the vortex strength is doubled for the enhanced case. Subsequently, the straining motion of vortices is considerably enhanced in the saddle region, causing the appreciable rise in $\overline{uv}^*$ (Hussain & Hayakawa, 1987).

The time-averaged drag coefficient, $\overline{C}_D$, may be estimated based on $\overline{U}^*$, $\overline{u^2}^*$ and $\overline{v^2}^*$ using Eq.(3-4). $\overline{C}_D$ thus determined is 2.05, falling in the range, 1.7 ~ 2.1, of previously reports (Lee, 1975; Shimada & Ishihara, 2002; and Zhou & Antonia, 1994a). The value retreats by 20% for the impaired case but jumps by 37% for the enhanced case. Fujisawa and Nakabayashi (2002), reduced $\overline{C}_D$ by 16% using a rotating cylinder to control vortex shedding and attributed the effect to a diminished $\overline{u^2}^*$, which seems to be corroborated by the present data. A change in the near-wake

fluctuation, as evidenced in $\overline{u^2}^*$ and $\overline{v^2}^*$, may have an impact upon flow separation and hence the backpressure, leading to a modified $\overline{C}_D$.

5.4.2 Robustness of the closed-loop control

The controller used above was tuned to provide the optimum performance under the designed condition, i.e. at Re = 7400. Unlike an open-loop control system, the closed-loop control is expected to possess a certain degree of robustness when the working conditions change. This feature is confirmed by applying the controller tuned at Re = 7400 to Re = 3200 and 9500, respectively. The signals of u_2 / U_∞, C_L and C_D are similarly manipulated under these two Res as those at Re of 7400 shown in Figures 5-4 and 5-5 under the closed-loop control, but with lower efficiency, as shown by the typical transition (Figures 5-9 and 5-10) and the power spectrum (Figures 5-11 and 5-12), respectively. The modified flow is also verified by the flow visualization photos (Figures 5-13 and 5-14) and PIV data (Figures 5-15 and 5-16). Like Re = 7400, the vortex shedding behind the cylinder can either be destroyed (Figures 5-13(b) ~ 5-16(b)) or strengthened (Figures 5-13(c) ~ 5-16(c)). Table 5-1 tabulates the variation in Γ, $u_{2,\mathrm{rms}}$, the rms values of C_L and C_D, i.e. $C_{L,rms}$ and $C_{D,rms}$ for both impaired and enhanced cases for the three Reynolds numbers. In general, the flow is similarly modified by the closed-loop perturbation. It is not surprising to see that the best performance is obtained at Re = 7400. At Re = 3200 and 9500, Γ reduces by 42% and 58%, respectively, for the impaired case but rises by 92% and 120%, respectively, for the enhanced case, compared with the uncontrolled condition.

5.5 Discussions

Using a closed-loop control technique similar to the present one, an almost complete annihilation of the vortex street behind resonating cylinder and vortex shedding was observed in Chapter 4. The observation was ascribed to the opposite movement between the cylinder and the lateral flow velocity associated with vortex shedding under the controlled perturbation. However, the present cylinder was rigid and fix-supported at both ends.

In order to explore the underlying physics of present observation, the perturbation signal (Y_p) and the streamwise fluctuating velocity (u_2) from hot wire ② were simultaneously measured. So were the fluctuating lift (C_L) and Y_p. The spectral phase shift, $\phi_{\alpha_1\alpha_2}$ between α_1 and α_2 was calculated using Eq.(3-3).

Figure 5-17 presents $\phi_{Y_p u_2}$ as f^* varies for the three Res. At Re = 7400, $\phi_{Y_p u_2}$ is about $-\pi$ over a small range of frequencies around f_s^* for the impaired case but zero across the whole range of frequencies for the enhanced case (Figure 5-17(a)). An analysis similar to that in Section 3.5 points to that $\phi_{Y_p u_2}$ is equivalent to the phase shift between the perturbation velocity $\dot{Y}_p$ of the cylinder surface and the lateral flow velocity component, v, around the cylinder. Therefore, $\phi_{Y_p u_2} = -\pi$ means anti-phased $\dot{Y}_p$ and v, that is, the surface perturbation created by actuators actually moves against the lateral flow velocity. This opposite movement between $\dot{Y}_p$ and v is responsible for the greatly impaired vortex shedding (Figures 5-6(b) and 5-7(b)). Similarly, $\phi_{Y_p u_2} = 0$ corresponds to the in-phased $\dot{Y}_p$ and v, which promotes the roll-up motion of the

vortices (Figures 5-6(c) and 5-7(c)). The interrelationship between $\dot{Y}_p$ and v mimics the cylinder and fluid motions in Chapter 3 and Chapter 4. Nonetheless, since the cylinder displacement in the investigation of the two Chapters grossly exceeds Y_p, the opposite motion between cylinder and fluid produced a more dramatic effect, resulting in an almost complete destruction of the vortex street.

Interestingly, the perturbation results in the anti-phased $\dot{Y}_p$ and v over a small range of frequencies around f_s^* for the impaired case but the synchronized $\dot{Y}_p$ and v across almost the entire frequency range for the enhanced case (Figure 5-17(a)). This explains why the enhancement impact appears overwhelming that of the impaired case (Figures 5-3 ~ 5-8). It may be inferred that the present control technique well suits the applications where it is desirable to enhance vortex shedding such as vortex generators.

Note that the perturbation was imposed only on the upper surface of the square cylinder. However, the vortices shed from both sides of the cylinder appear equally impaired or enhanced under the perturbation (Figures 5-6 and 5-7). Vortex shedding is a result of initial wake instability (Provansal *et al.* 1987). In order to form a stable vortex street, it is essential for the two oppositely signed vortices separating from the cylinder to have approximately the same strength through interactions (Sakamoto *et al.* 1991). In other words, if the vortex strength on one side decreases or increases, it will do so on the other side to counterbalance and vice versa. Therefore, vortex shedding from both sides of the cylinder appears equally affected, notwithstanding the perturbation only on one side.

As Re is varied, the interrelationship between $\dot{Y}_p$ and v largely remains unchanged. Nevertheless, the frequency range over which $\dot{Y}_p$ and v are anti-phased narrows slightly for the impaired case (Figures 5-17(b) and 5-17(c)) or $\phi_{Y_p u_2}$ may slightly deviate from zero or fluctuate about zero at some frequencies for the enhanced case.

Insight into the physics of the present flow control may be better gained by investigating the force interaction between the perturbed surface and the flow. The behaviour of $\phi_{Y_p C_L}$ (Figure 5-18) is rather similar to $\phi_{Y_p u_2}$: $\phi_{Y_p C_L}$ is about zero for the enhanced case but - π for the impaired case, and undergoes changes similar to $\phi_{Y_p u_2}$ for different Re. The fluctuating lift force F_L on the cylinder, measured by the load cell, is largely attributed to the alternate separation of the boundary layer from the cylinder. This force is equal in magnitude and opposite in direction or anti-phased to the force, F_L', of the cylinder acting on fluid. The latter may be divided into two parts: force, F_f, linked to flow separation and force, F_p, due to the introduction of the perturbation. The three force vectors satisfy the relation $\overrightarrow{F_L'} = \overrightarrow{F_f} + \overrightarrow{F_p}$. F_p is directly proportional to the acceleration of fluid or the perturbed surface, which is anti-phased to Y_p. The same phase shift (π) from F_L (or C_L) to F_L' as from Y_p to F_p implies that $\phi_{Y_p C_L}$ reflects the phase relation between F_p and F_L'. Note that F_f overwhelms F_p in view of the very small perturbation amplitude, that is, F_f and F_L' are approximately in-phase. Therefore, the phase relation between F_p and F_L' in fact reflects that between F_p and F_f. We may now piece together the picture of the perturbed flow. The relation

$\phi_{Y_p C_L} = 0$ corresponds to in-phased F_f and F_p, leading to an amplified F_L' and enhancing vortex shedding. On the other hand, $\phi_{Y_p C_L} = -\pi$ corresponds to anti-phased F_f and F_p, resulting in a reduced F_L' and impaired vortex shedding.

5.6 Conclusions

Experimental investigation has been conducted to control the turbulent wake of a fix-supported square cylinder. The control was made possible by perturbing one cylinder surface using piezo-ceramic actuators, which are activated on feedback fluctuating flow velocity. The investigation leads to following conclusions:

1) The proposed technique is effective in either suppressing or enhancing the vortex street behind the cylinder. The interrelationship is crucial between the surface perturbation force, F_p, and the force, F_f, of the cylinder acting on fluid that is associated with vortex shedding. When the two forces are anti-phased, vortex shedding is greatly weakened. The vortex strength, fluctuating lift and drag coefficients drops by 71%, 51% and 42%, respectively. The mean drag coefficient decreases by 20%. When in-phased, F_p and F_f re-enforce each other, which enhances significantly vortex shedding. Consequently, the vortex strength increases by 152%, the fluctuating lift and drag coefficients experience a great jump, and the mean drag coefficient rises by 37%.
2) Tuned under one Re, the proposed technique is demonstrated to be effective over a range of Re.

3) The present one-sided perturbation has the same effect on vortices shed from both sides of the cylinder, thus producing a reasonably symmetrical wake about the centerline.

Table 5-1 Control performance at different Re: variation in Γ, $u_{2,\mathrm{rms}}/U_\infty$, $C_{L,rms}$ and $C_{D,rms}$ compared with the unperturbed flow. ↓ and ↑ denote a decrease and increase, respectively.

Re	7400		3200		9500	
Γ	71%↓	152%↑	42%↓	92%↑	58%↓	120%↑
$u_{2,\mathrm{rms}}/U_\infty$	40%↓	90%↑	26%↓	55%↑	31%↓	56%↑
$C_{L,rms}$	51%↓	60%↑	33%↓	30%↑	37%↓	51%↑
$C_{D,rms}$	42%↓	67%↑	20%↓	13%↑	37%↓	48%↑

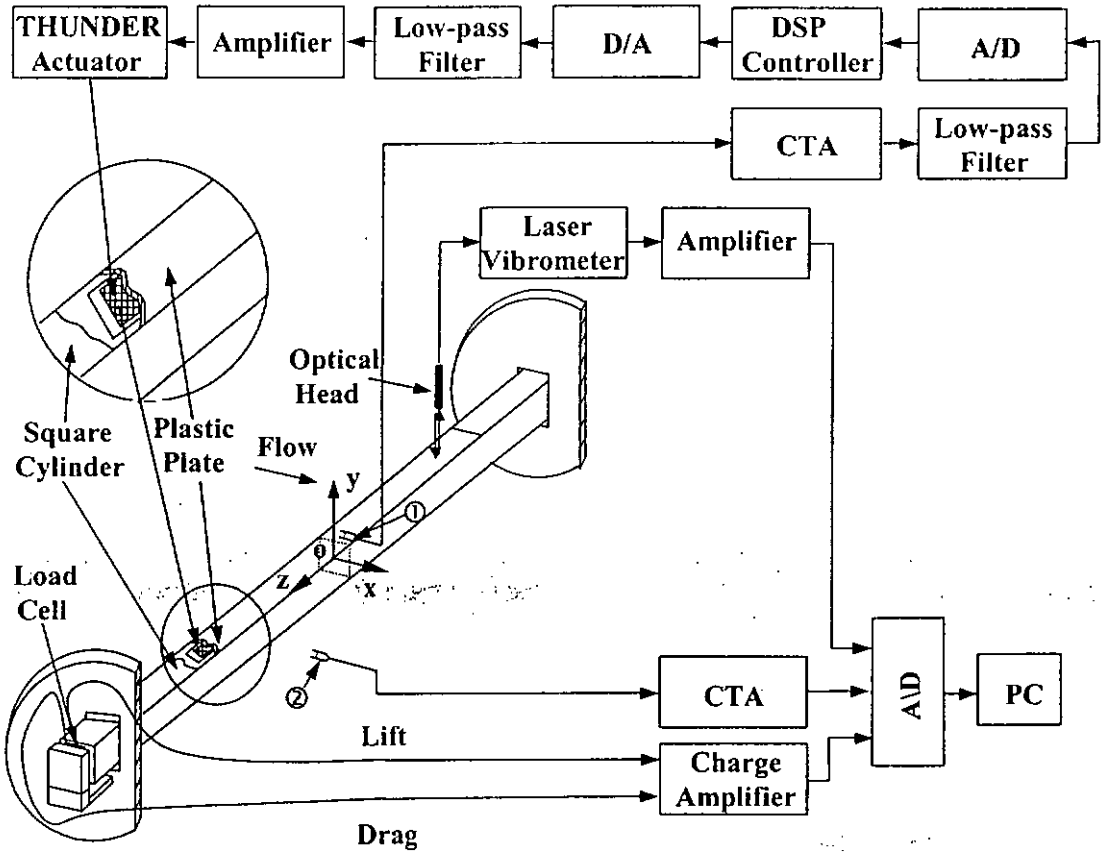

Figure 5-1 Experimental Setup. Feedback and monitoring hot wires ① and ② were placed at $x/h = 0, y/h = 1.6, z/h = 0$ and at $x/h = 2, y/h = 1.5, z/h = 4$, respectively.

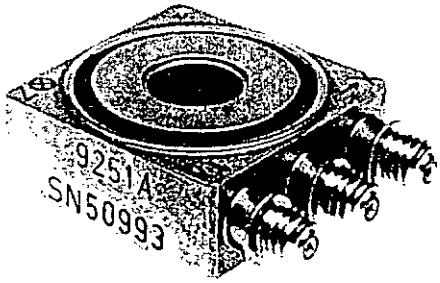

(a)

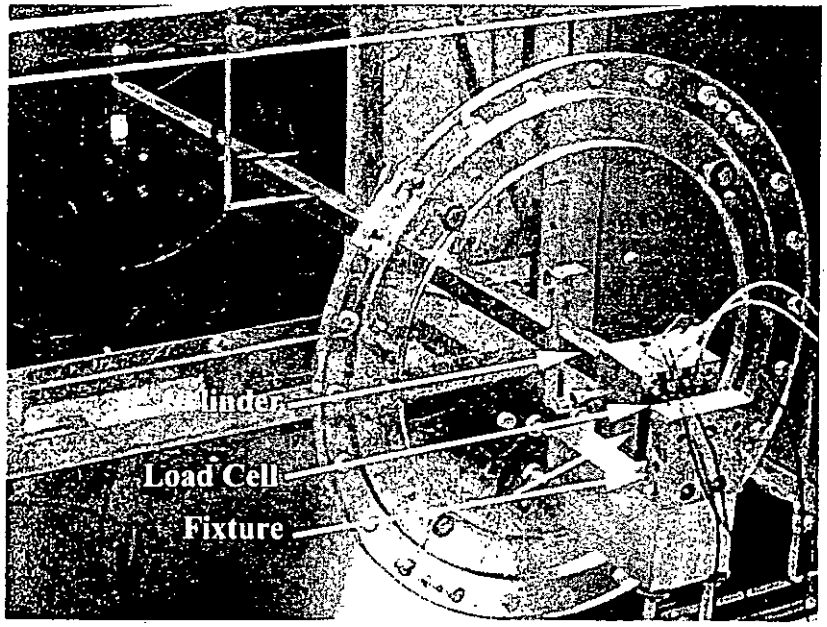

(b)

Figure 5-2 Load cell (a) and its installation (b).

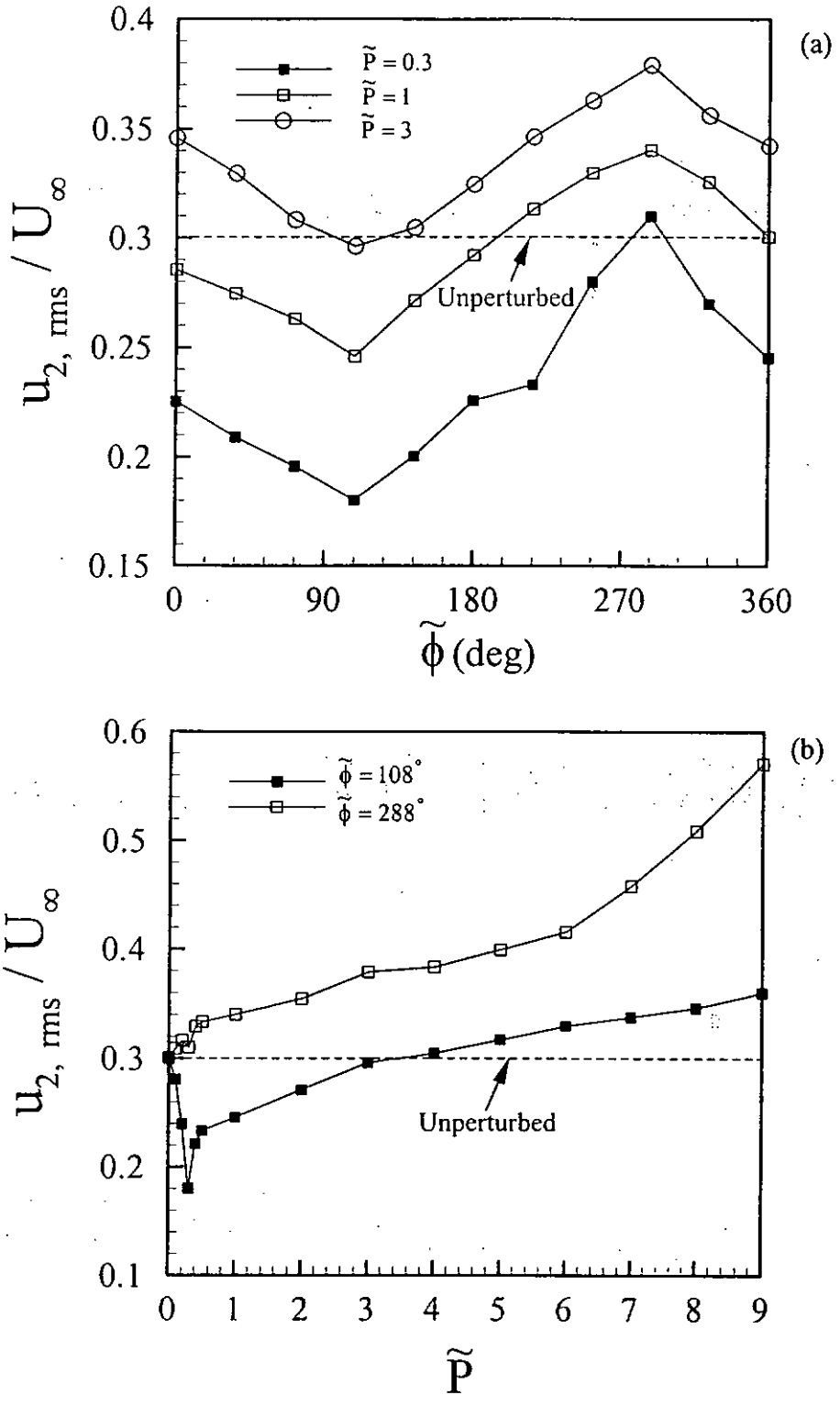

Figure 5-3 Dependence of $u_{2,\,rms}$ on (a) phase shift ($\tilde{\phi}$) and (b) gain ($\tilde{P}$), Re = 7400.

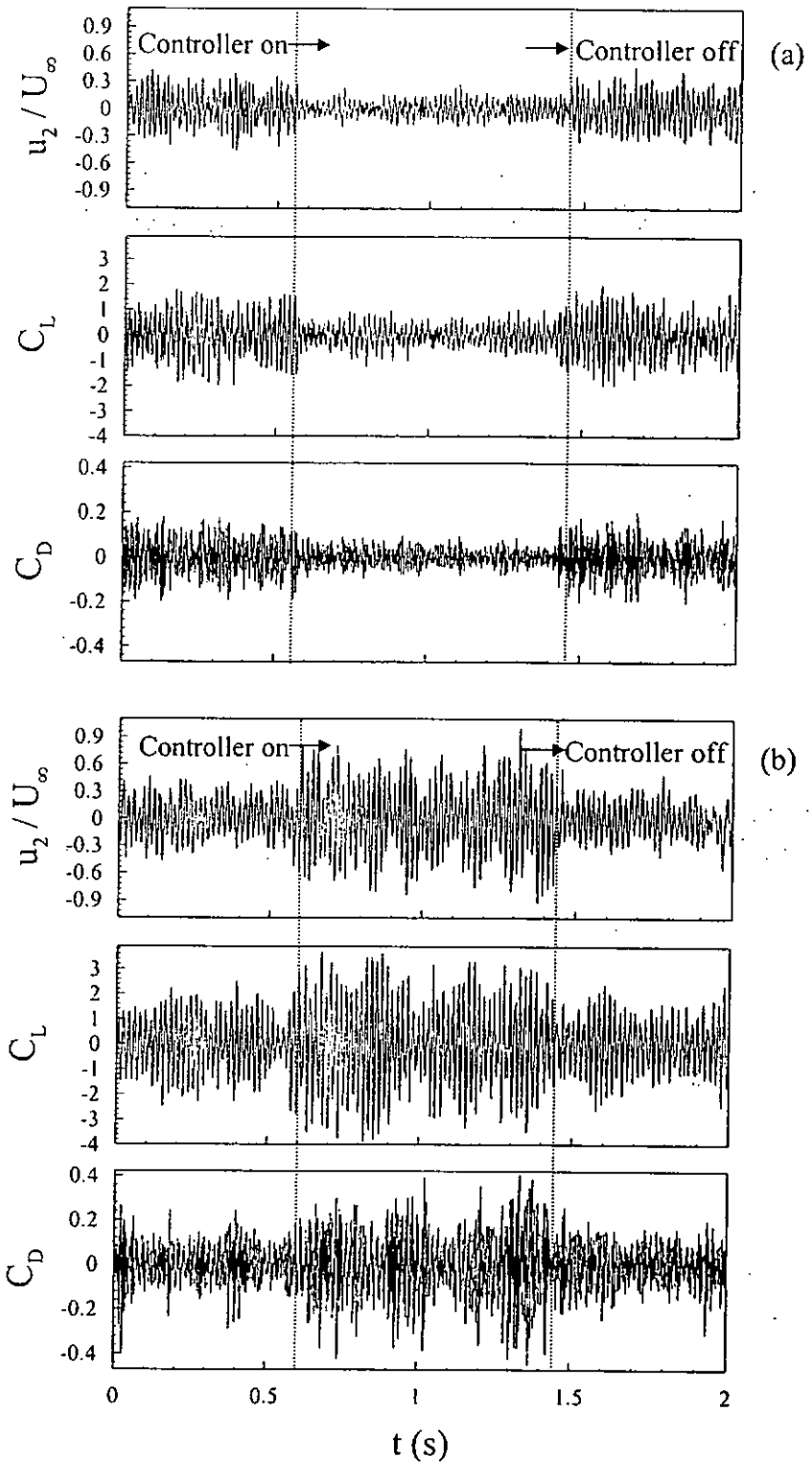

Figure 5-4 Typical time histories of normalized fluctuating flow velocity (u_2), lift coefficient (C_L) and drag coefficient (C_D) when the controller was switched on and off: (a) impaired, (b) enhanced. Re = 7400. Time is arbitrary.

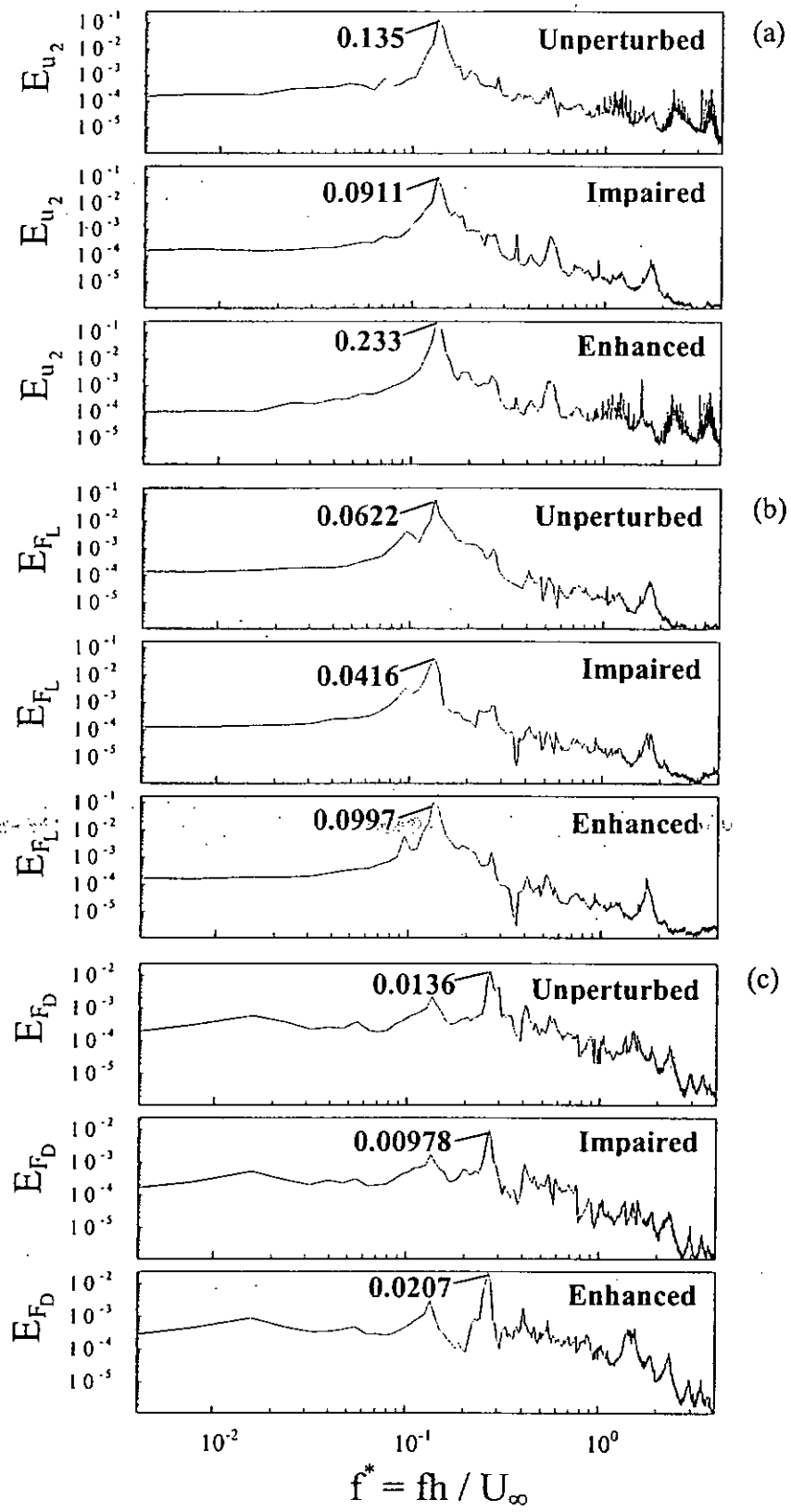

Figure 5-5 The u_2-, F_L- and F_D-spectra: (a) E_{u_2}; (b) E_{F_L}; (c) E_{F_D}. Re = 7400.

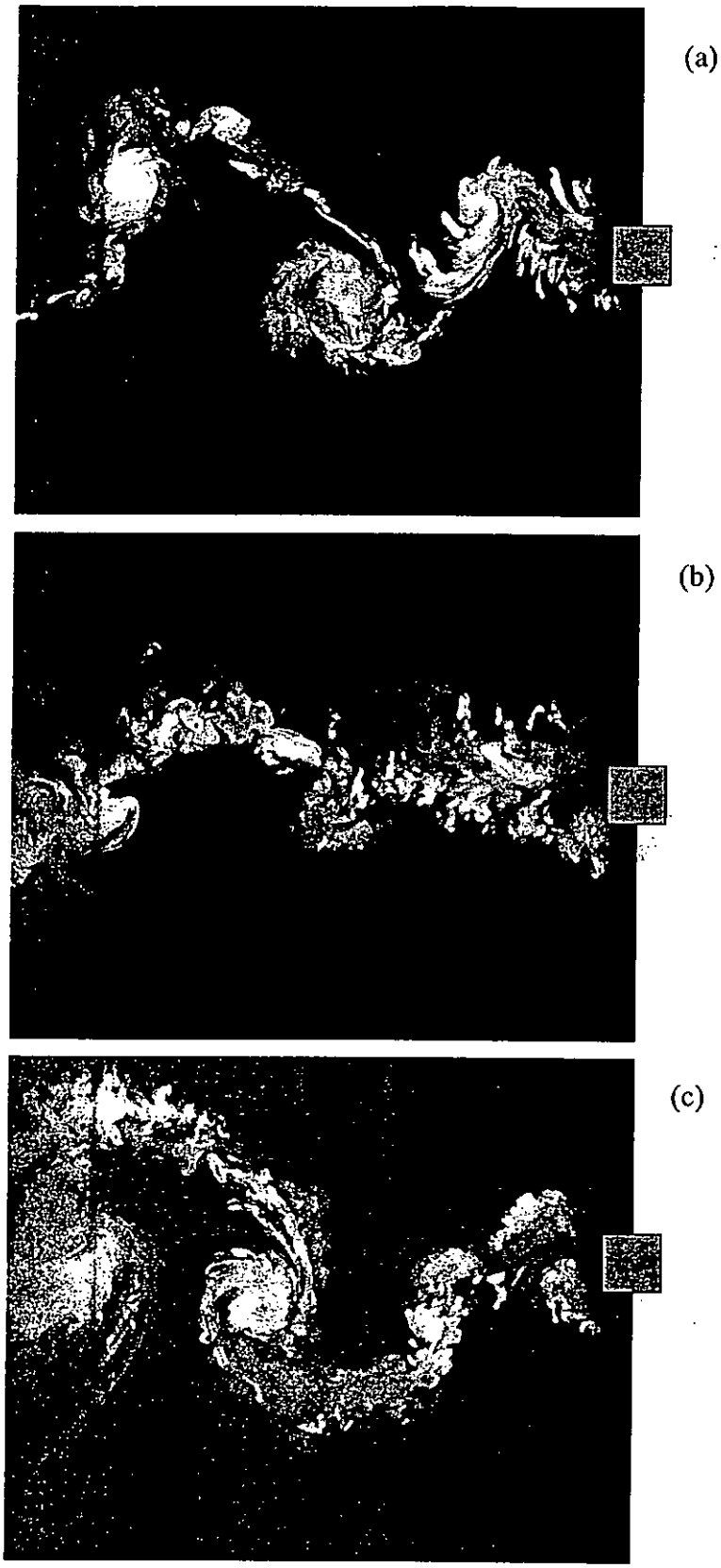

Figure 5-6 Typical flow visualization photos: (a) unperturbed flow, (b) impaired, (c) enhanced. Re = 7400.

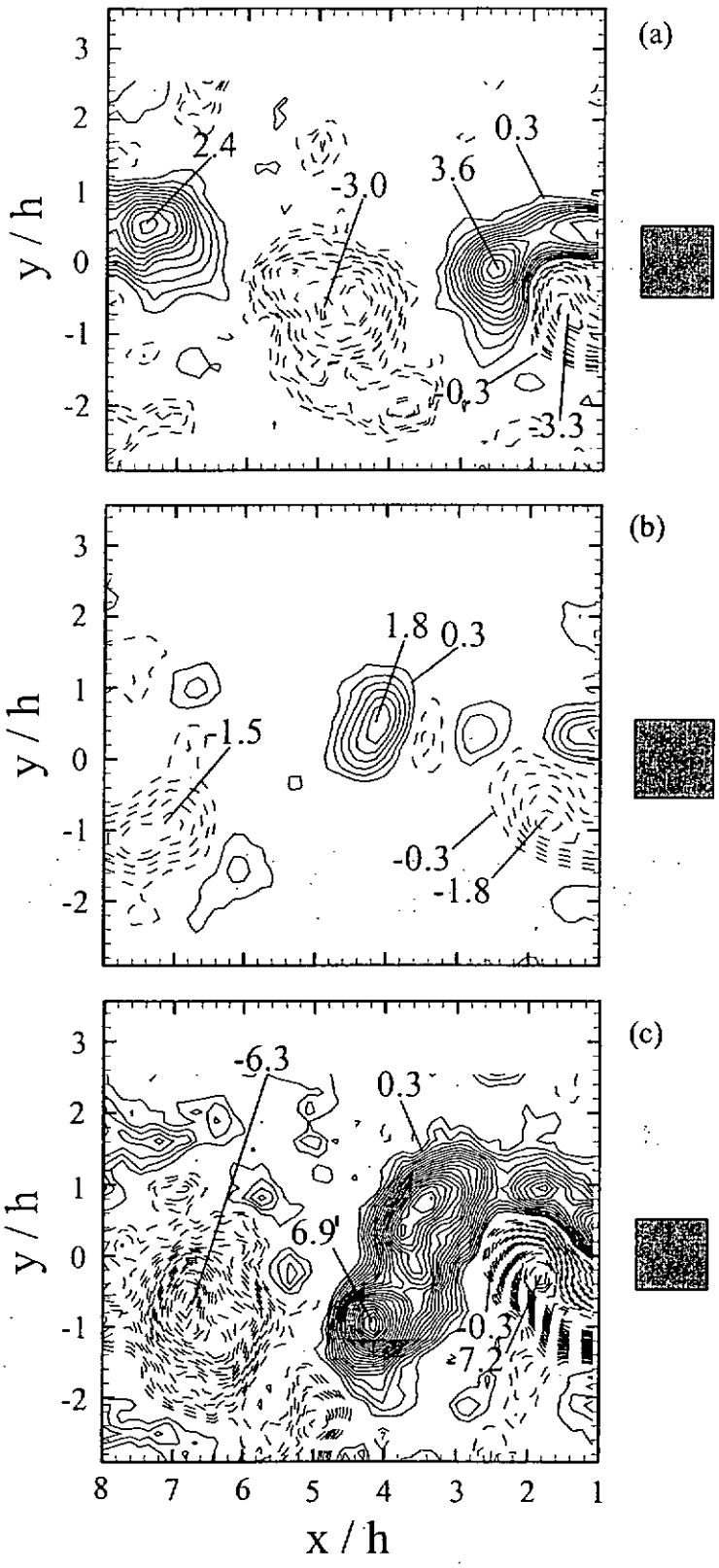

Figure 5-7 Typical iso-contour of spanwise vorticity $\omega_z^* = \omega_z h / U_\infty$ from the PIV measurements: (a) unperturbed flow, (b) impaired, (c) enhanced. Re = 7400.

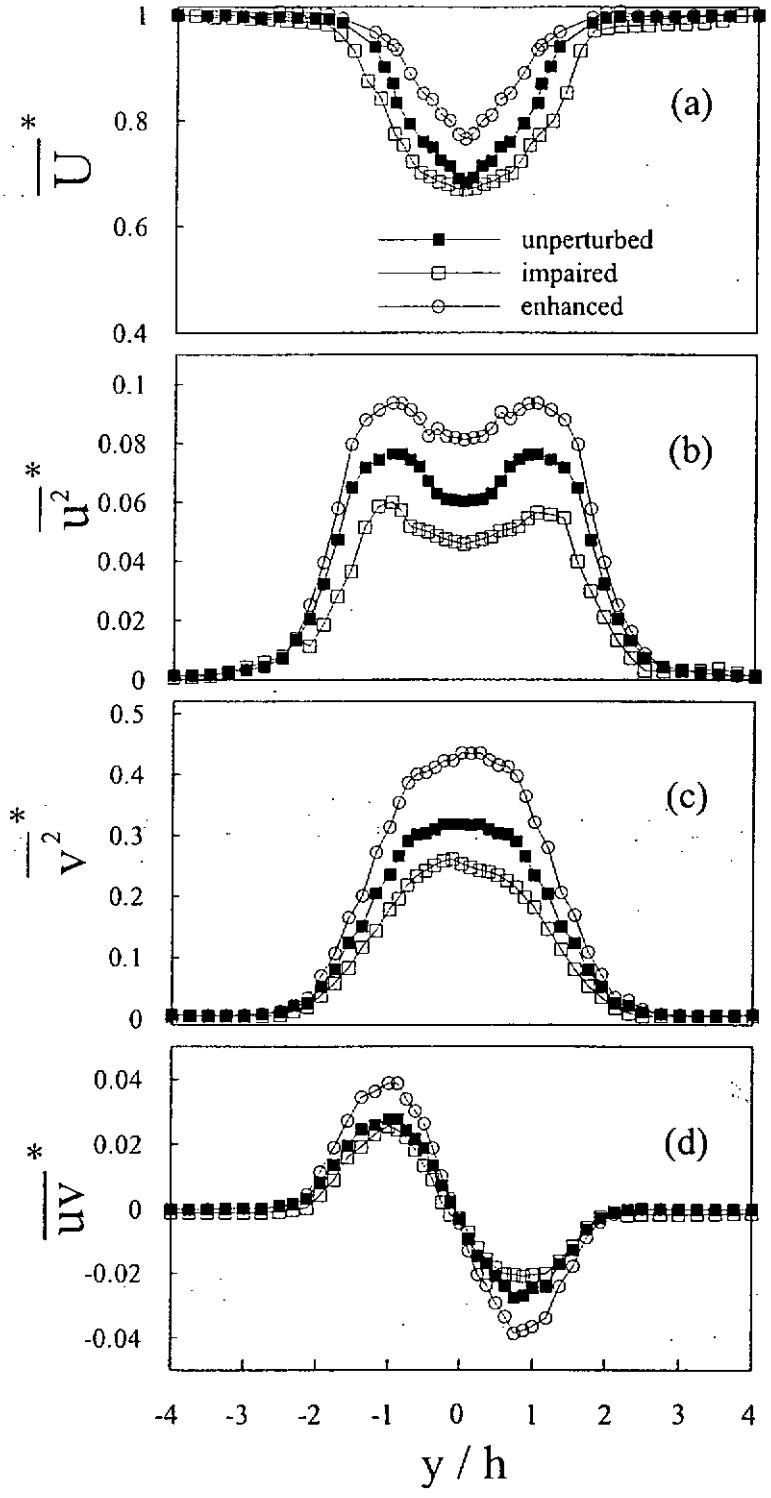

Figure 5-8 Cross-flow distributions of mean velocity and Reynolds stresses at $x/h = 3$: (a) $\overline{U}^*$, (b) $\overline{u^2}^*$, (c) $\overline{v^2}^*$, (d) $\overline{uv}^*$. Re = 7400.

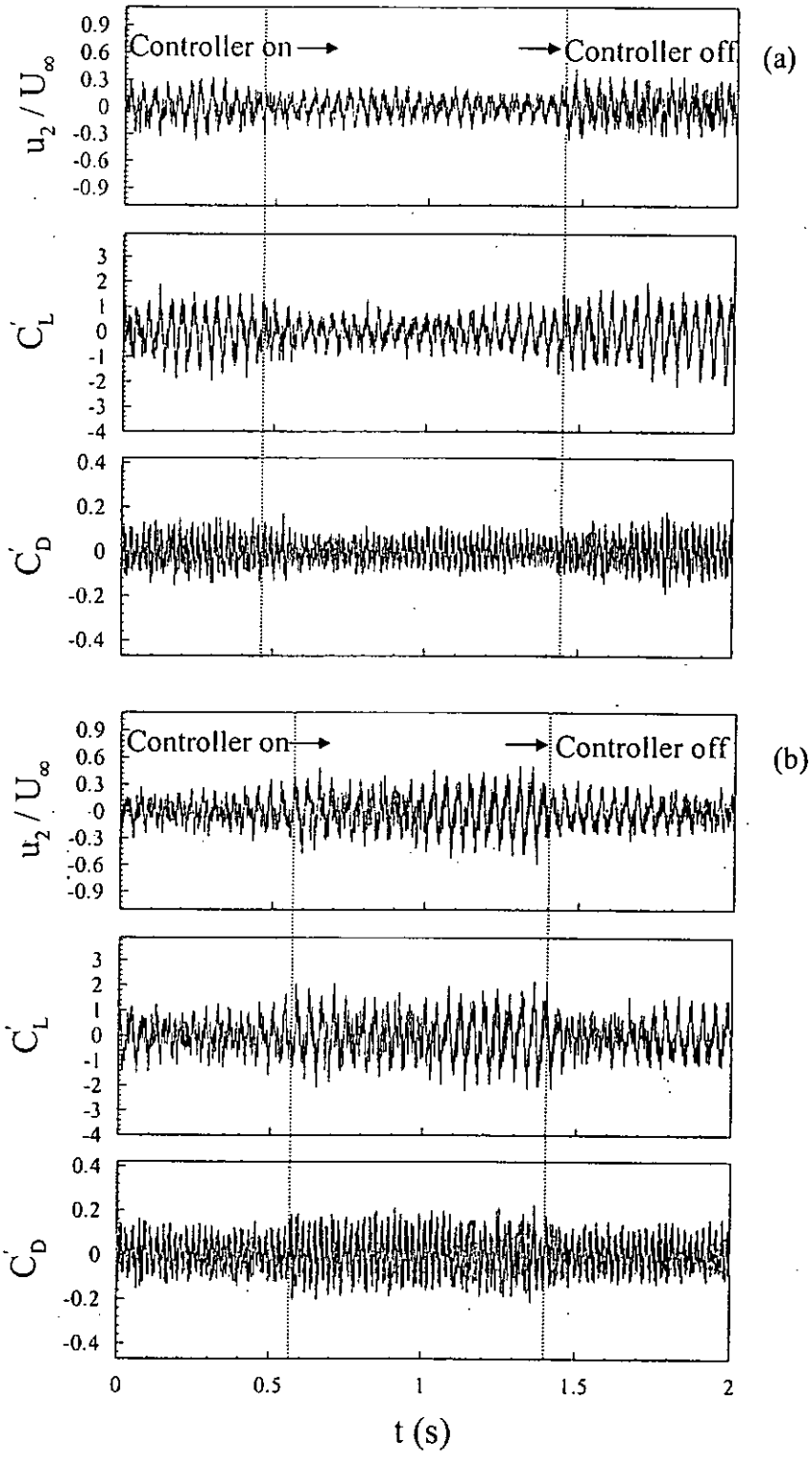

Figure 5-9 Typical time histories of normalized fluctuating flow velocity (u_2), lift coefficient (C_L) and drag coefficient (C_D) when the controller was switched on and off: (a) impaired, (b) enhanced. Re = 3200. The time origin is arbitrary.

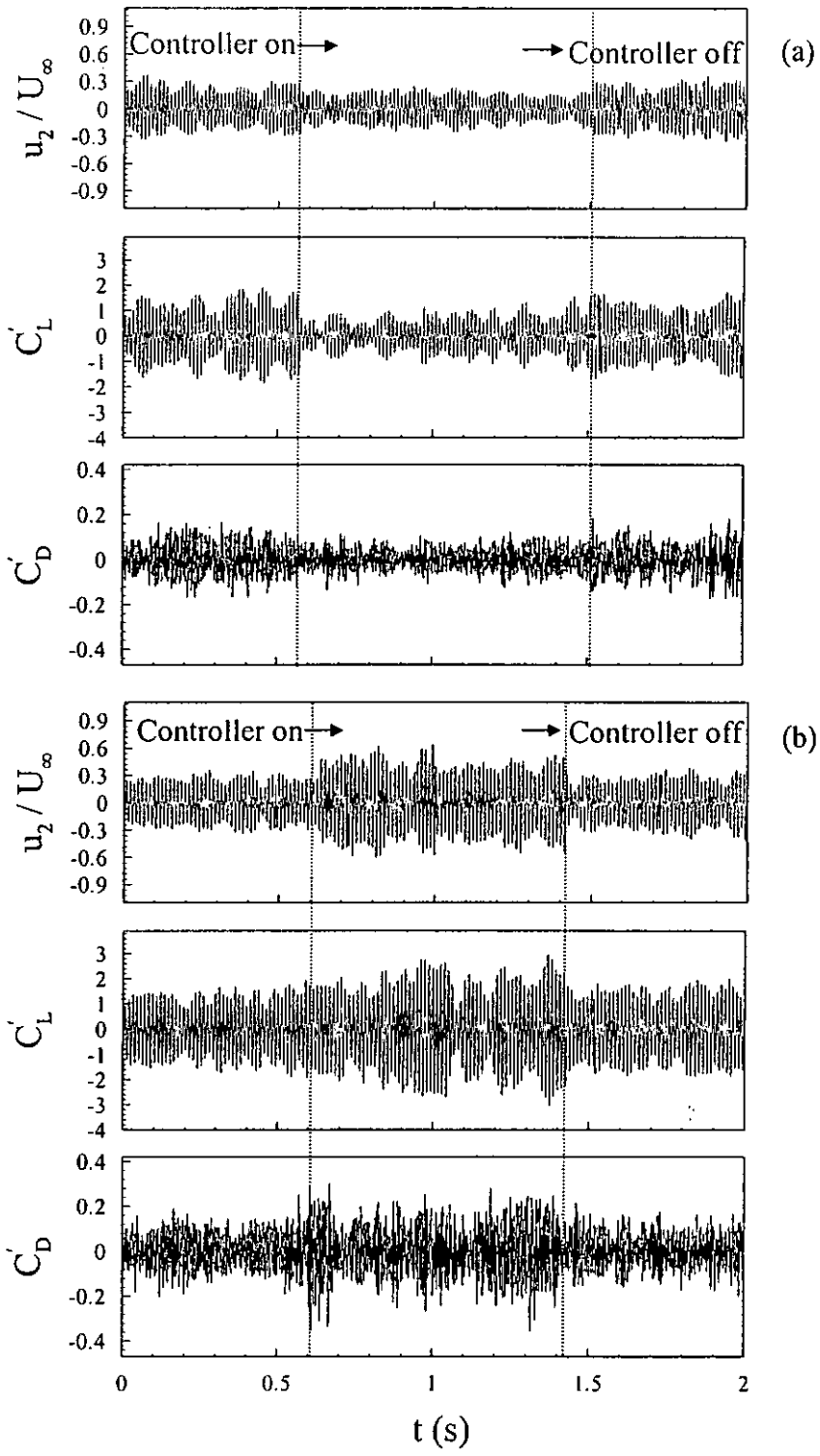

Figure 5-10 Typical time histories of normalized fluctuating flow velocity (u_2), lift coefficient (C_L) and drag coefficient (C_D) when the controller was switched on and off: (a) impaired, (b) enhanced. Re = 9500. The time origin is arbitrary.

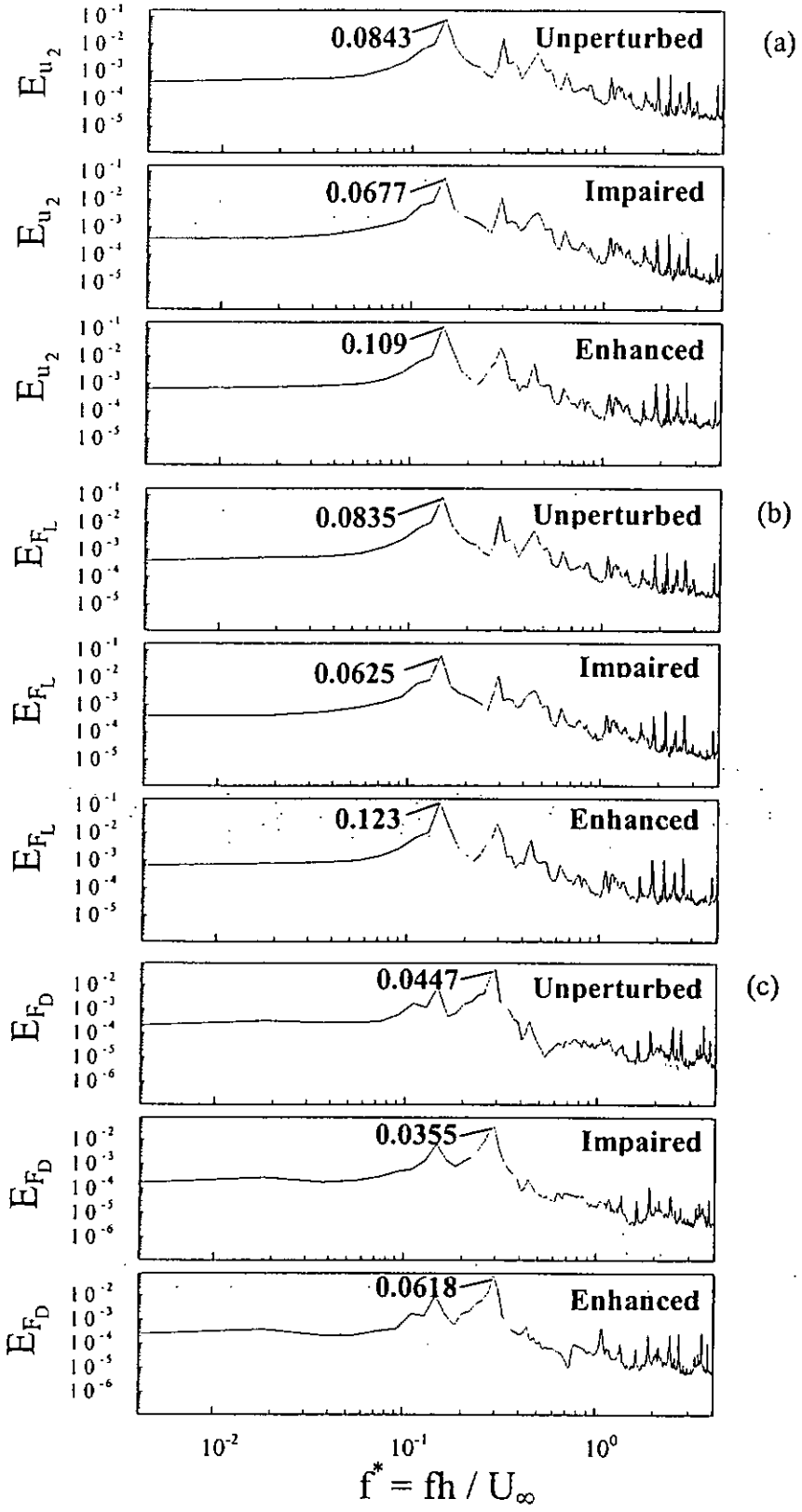

Figure 5-11 The u_2-, F_L- and F_D-spectra: (a) E_{u_2}; (b) E_{F_L}; (c) E_{F_D}. Re = 3200.

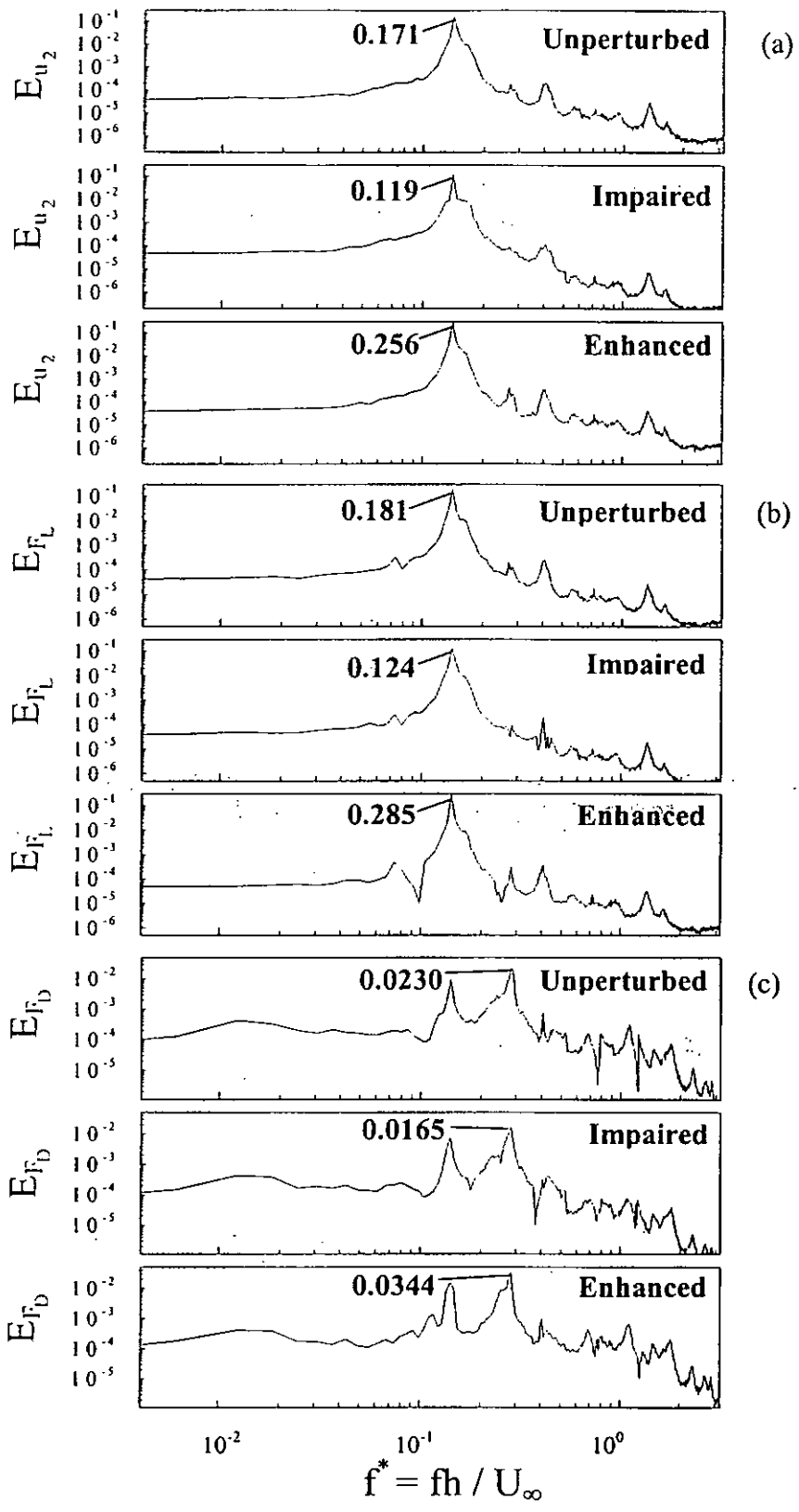

Figure 5-12 The u_2-, F_L- and F_D-spectra: (a) E_{u_2}; (b) E_{F_L}; (c) E_{F_D}. Re = 9500.

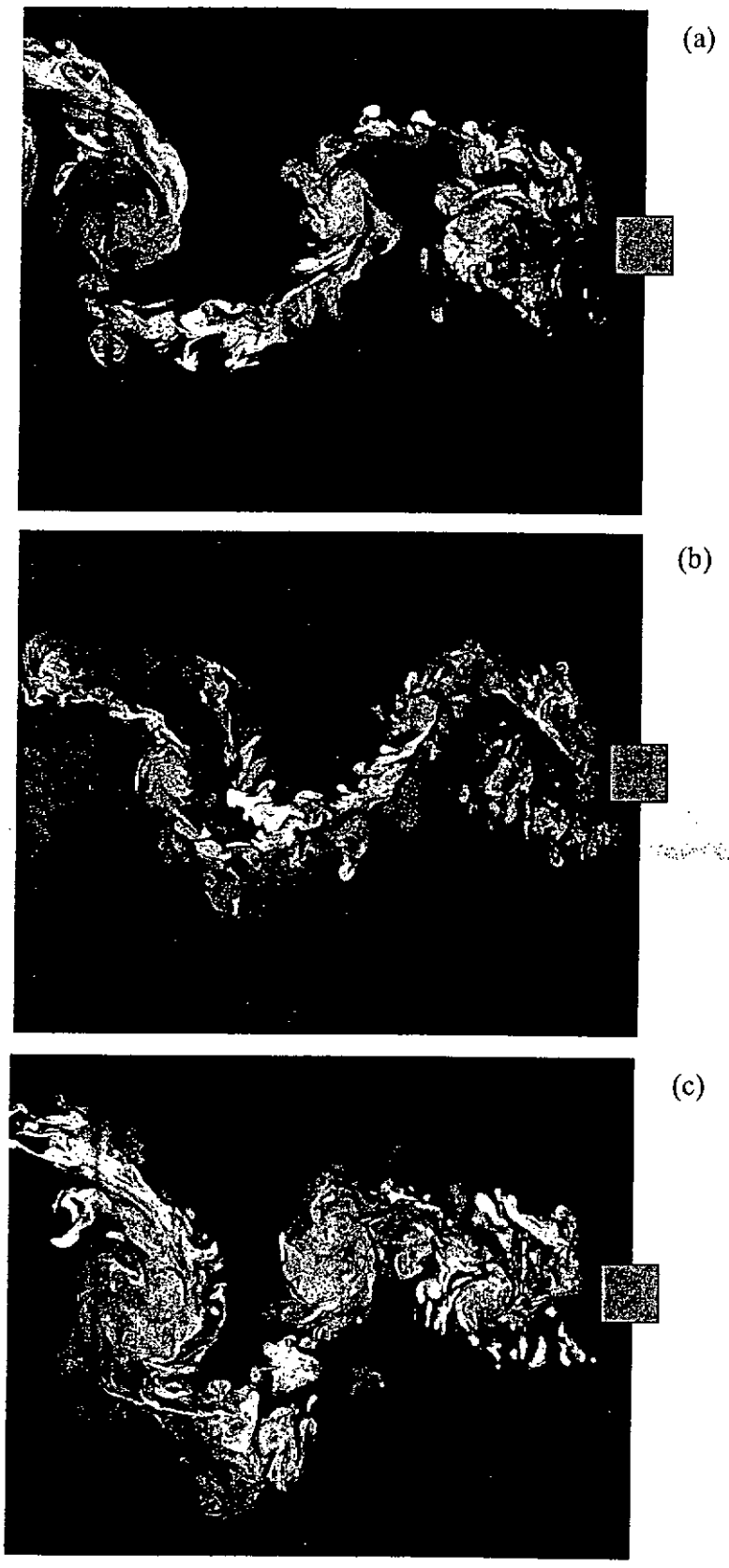

Figure 5-13 Typical flow visualization photos: (a) unperturbed flow, (b) impaired, (c) enhanced. Re = 3200.

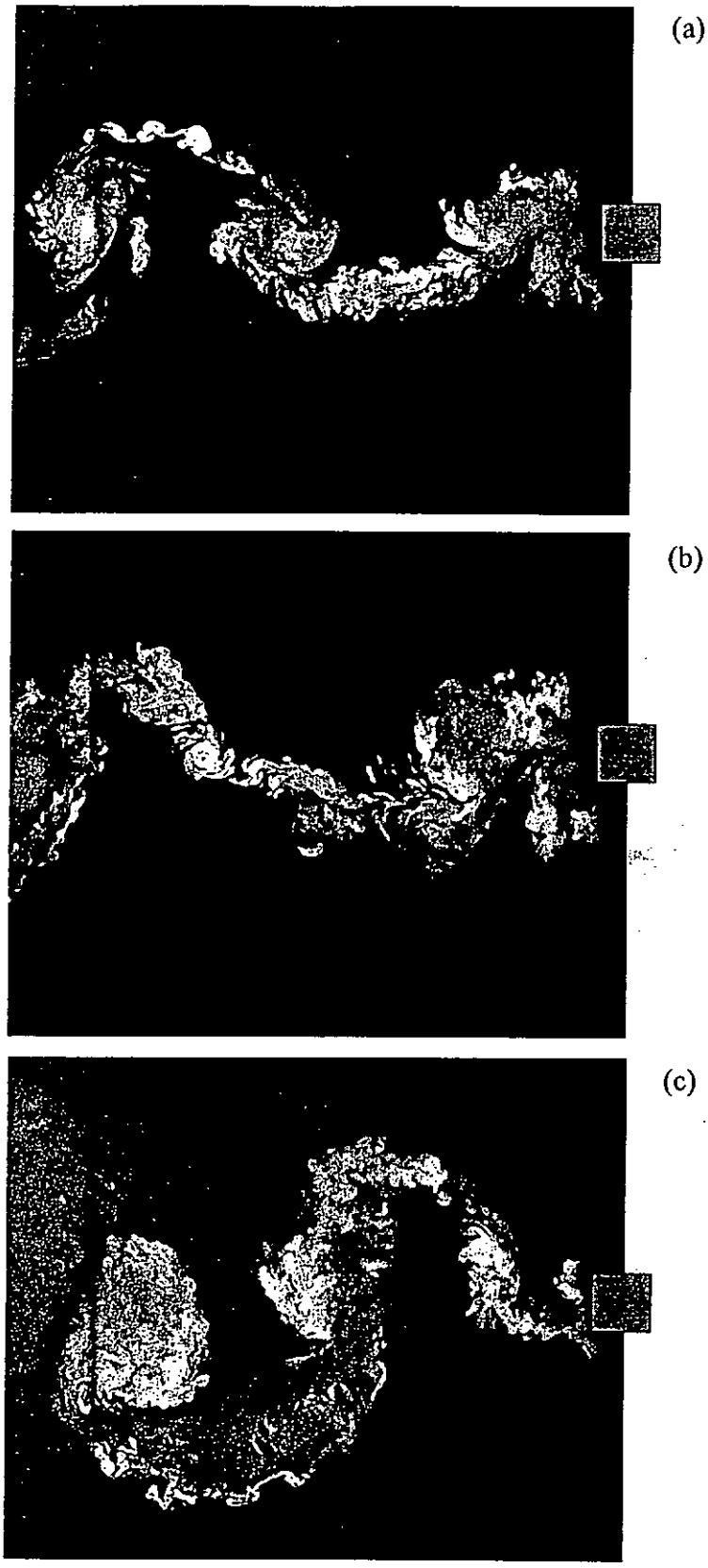

Figure 5-14 Typical flow visualization photos: (a) unperturbed flow, (b) impaired, (c) enhanced. Re = 9500.

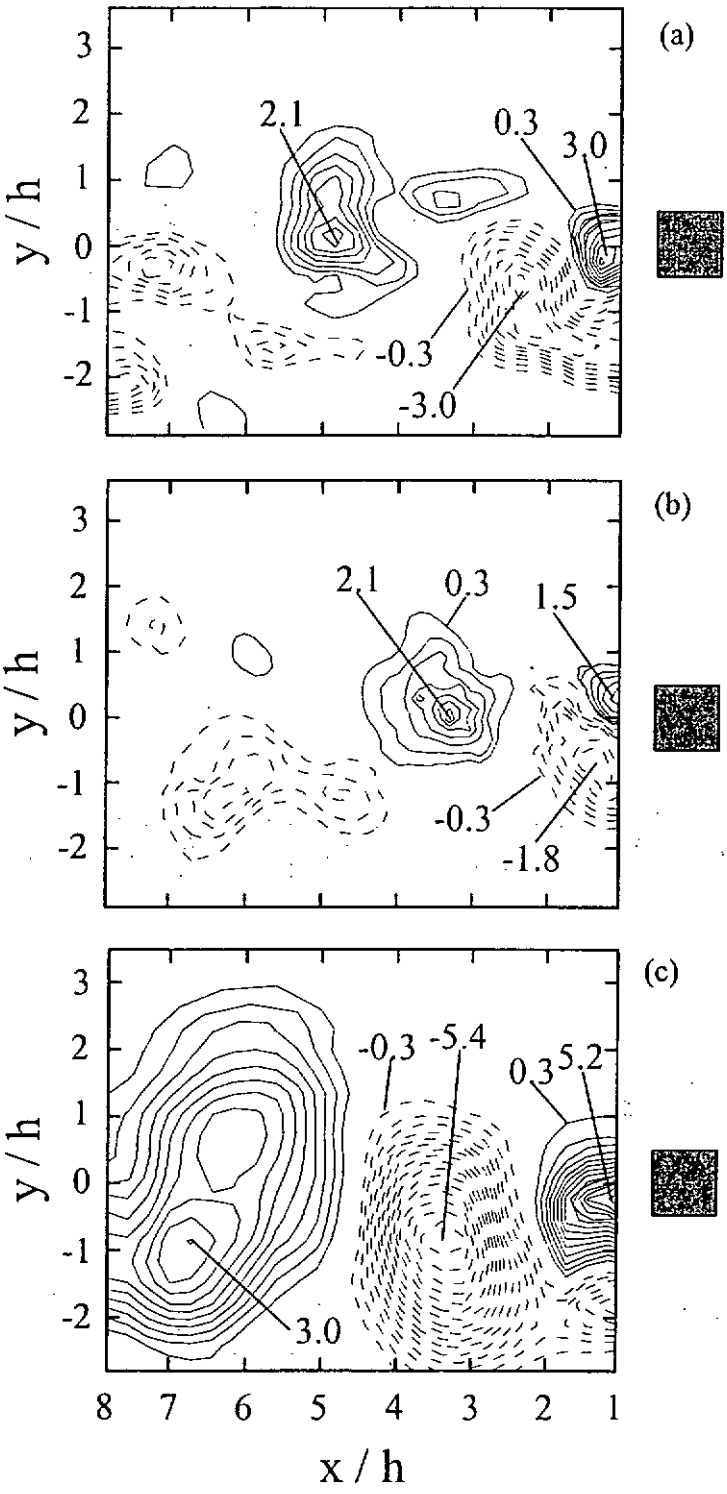

Figure 5-15 Typical iso-contour of spanwise vorticity $\omega_z^* = \omega_z h / U_\infty$ from the PIV measurements: (a) unperturbed flow, (b) impaired, (c) enhanced. Re = 3200.

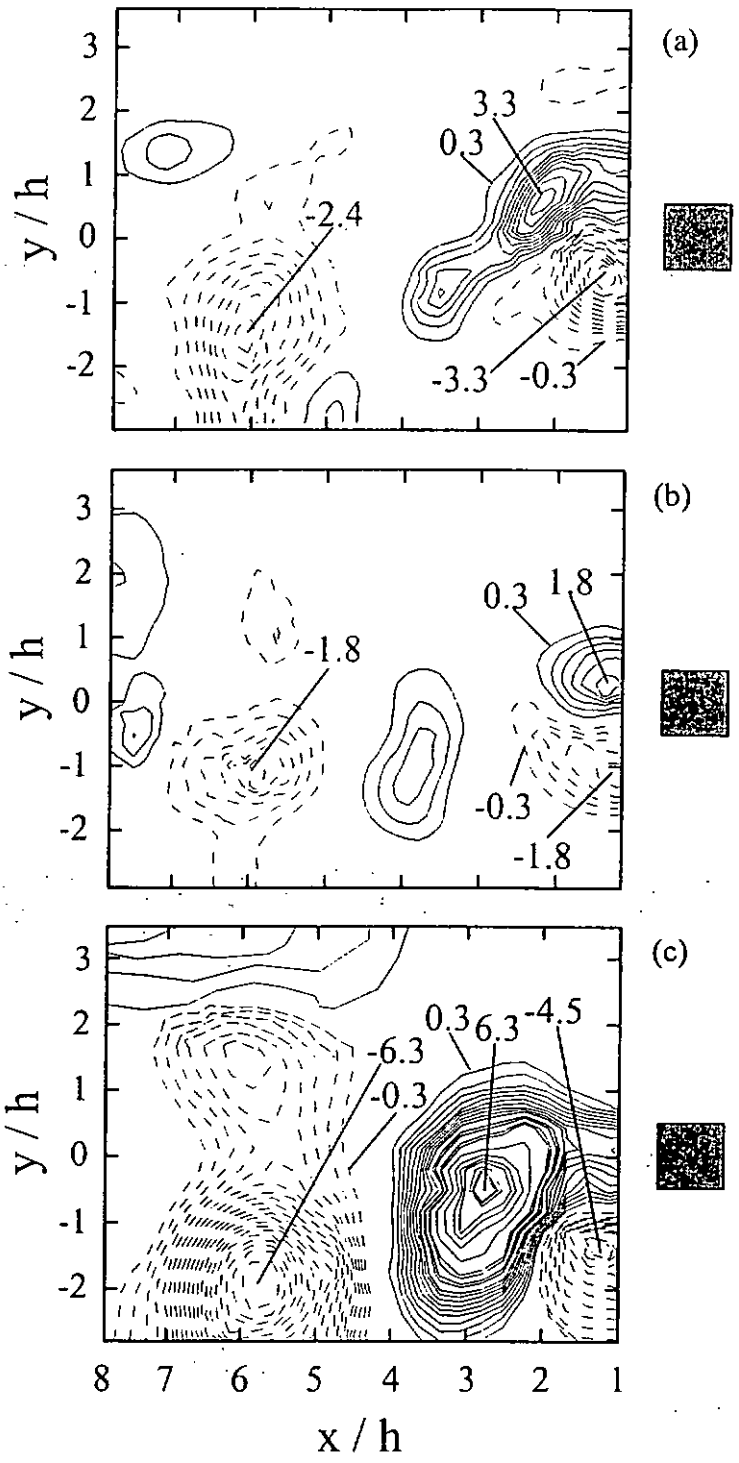

Figure 5-16 Typical iso-contour of spanwise vorticity $\omega_z^* = \omega_z h / U_\infty$ from the PIV measurements: (a) unperturbed flow, (b) impaired, (c) enhanced. Re = 9500.

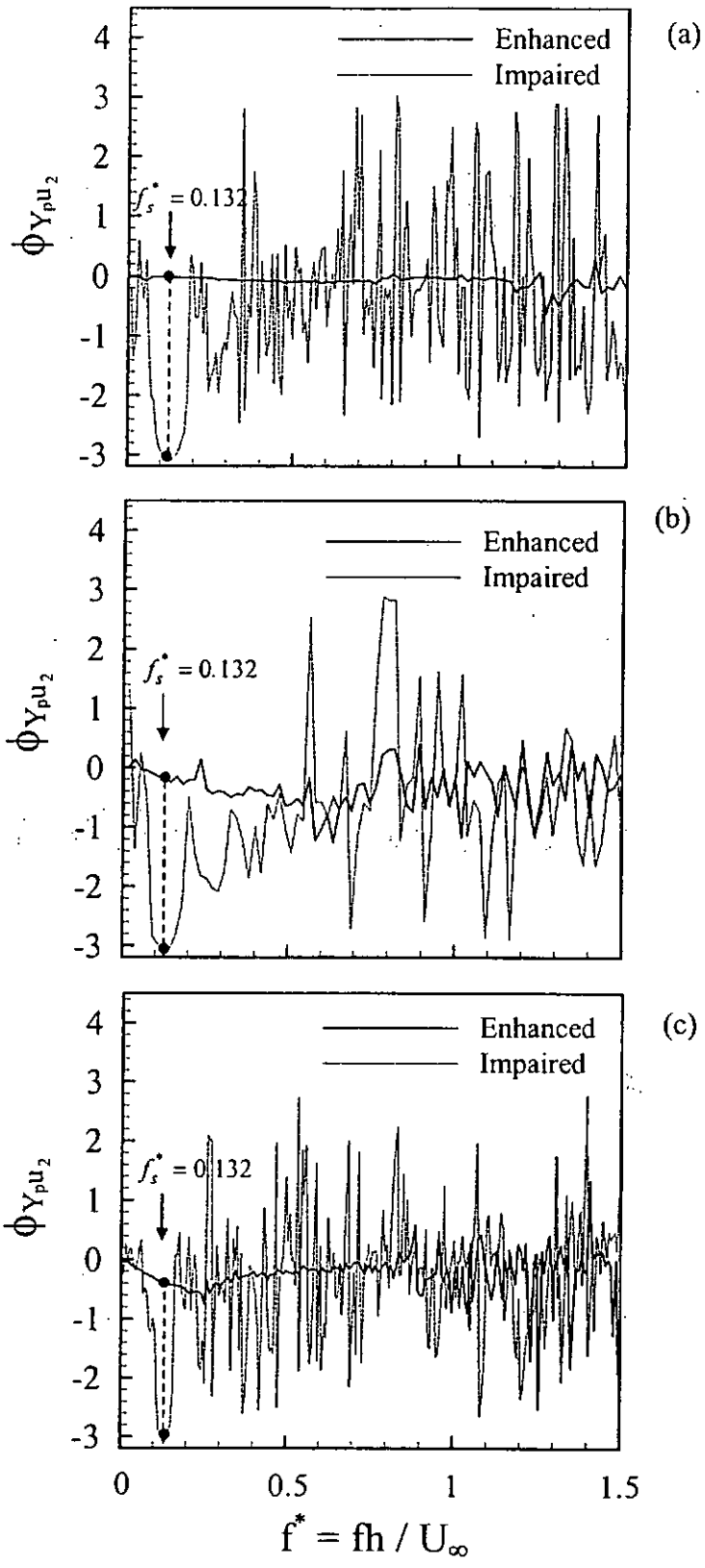

Figure 5-17 Phase shift $\phi_{Y_p u_2}$ between Y_p and u_2: (a) Re = 7400; (b) 3200; (c) 9500.

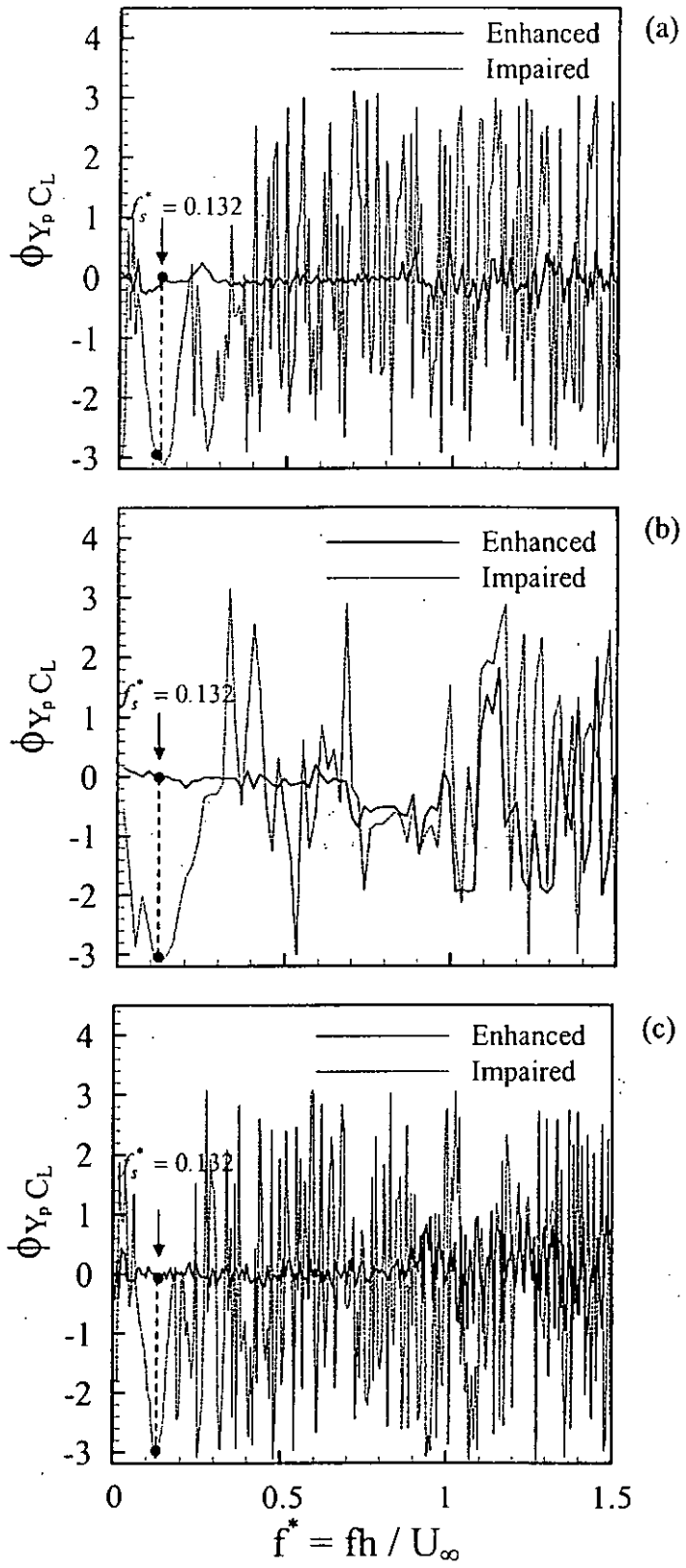

Figure 5-18 Phase shift $\phi_{Y_p C_L}$ between perturbation signal (Y_p) and the fluctuating lift coefficient signal (C_L): (a) Re = 7400; (b) 3200; (c) 9500.

CHAPTER 6

CLOSED-LOOP CONTROL OF VORTEX-INDUCED VIBRATION ON A FLEXIBLE CYLINDER

6.1 Introduction

Previous investigations examined rigid cylinders, either fixedly or flexibly supported. In practice, however, engineering structures are frequently flexible. Problems related to fatigue or noise radiation are mainly related to the flexural vibration of these structures, especially at the occurrence of resonances, when the vortex shedding frequency coincided with one of the natural frequencies of the system. The study of the structural resonances of lower modes (the 1^{st} mode in particular) is of particular importance due to the large vibration amplitude involved. As illustrated in Chapter 3-5, the proposed perturbation technique owes its effectiveness to a spanwise uniform perturbation created by actuators. Since flexible structures undergo non-uniform flexural vibrations along the spanwise direction, the effectiveness of this technique needs re-assessing. Meanwhile, the best control scheme has to be identified among the multitudinous combinations of feedback signals.

This work in the present chapter aims to address the issues raised above. Closed-loop control of vortex shedding and vortex-induced vibration of a fix-supported flexible cylinder under the resonance and non-resonance conditions was experimentally investigated. Five control schemes were considered and compared, which utilized feedback signals from streamwise fluctuating flow velocity u, lateral structural vibration Y, dynamic strain ε_y caused by the vibration, or a combination of these responses. These signals were measured using a hot wire, a laser vibrometer and an optical fiber Bragg grating (FBG) sensor, respectively. The control performances on the structural oscillation were evaluated in both time and frequency domain of Y, ε_y and u. In order to understand the underlying physics, the flow behind the cylinder was documented using a number of techniques, including PIV, flow visualization and a two-component LDA. The spectral phase and coherence between u and Y, along with the varying damping of the fluid-structure system under the control, were discussed in detail.

6.2 Experimental Details

6.2.1 Dynamic strain measurement

The fluctuating strain of the cylinder along y direction, ε_y, was measured using a Fiber Bragg grating (FBG) sensor. Figure 6-1(a) shows the generic concept of strain sensing using a FBG sensor. The FBG is photo-inscribed into an optical fibre using a high power UV laser beam and is associated with a small periodic refractive index variation in the fibre core. When the light of a broadband spectrum is guided through

the optical fibre to the FBG, a narrow band component as indicated by the spike in the reflection spectrum is reflected back at the Bragg resonance wavelength λ_B, given by:

$$\lambda_B = 2n_f \Lambda, \tag{6-1}$$

where Λ is the grating pitch and n_f is the fibre refractive index. The Bragg wavelength is strain-dependent through physical elongation of the sensor and through the change in the fibre refractive index due to photoelastic effects (Mizrahi & Sipe, 1993). An applied strain (ε) would cause a shift $\Delta\lambda_B$ in λ_B. For a standard single mode silica fibre, the relationship between ε and $\Delta\lambda_B$ is given by (Kersey *et al.* 1997):

$$\Delta\lambda_B = 0.78\lambda_{B0}\varepsilon, \tag{6-2}$$

where λ_{B0} is the Bragg wavelength of the grating under strain-free condition. Based on Eq.(6-2), for a nominal Bragg wavelength of λ_{B0} = 1556 nm as used in the present study, a strain of 1 μ will result in a shift of $\Delta\lambda_B$ = 1.2 pm. The wavelength shift $\Delta\lambda_B$ can be detected by a number of techniques (Morey *et al.* 1996; and Kersey *et al.* 1997). A tunable Fabry-Perot optical filter (F-P Filter) is used in the present study to convert the wavelength shift to a light intensity variation. The intensity signal is converted, through a photodetector, to a voltage signal which is amplified, sampled and processed to recover the applied strain signal. A detailed description of the FBG sensor system can be found in Jin *et al.* (2000) and James *et al.* (1999).

FBG sensors are unique in several aspects, which make them ideal tools for flow-induced vibration measurement. First, they are small in size (the diameter can be

as small as 80 μm) and light in weight. Their attachment onto a structure should cause a negligible effect on the vibration characteristics of structures. Second, as light is guided by optical fibers which are flexible (can be bent), the FBG sensors may be used to measure fluctuating strain at any point on a structure even when it is positioned within an array, overcoming the drawback of the laser vibrometer. Using wavelength division multiplexing and/or other multiplexing techniques, the FBG sensors have the potential to be used for simultaneous multi-point measurement on a single structure, or simultaneous measurement of many structures. These measurements may be of significance in determining the instantaneous operational mode shape of a structure in cross flow and in studying flow-structure interactions.

Specifically, in the present work, an optical silica fibers of diameter 125 μm built with FBG sensor was used to measure ε_y, due to lift, buried in a groove located at mid span of the lower cylinder surface, to measure the dynamic strain ε_y of the cylinder associated with Y and flushed with the surface using nail polish (Figure 6-1(b)). Since the sensor grating has a finite length of about 10 mm, the measurement represents the average strain over this length. A major contribution to error comes from the non-linearity effect when calibrating the relationship between output voltage and strain (Jin *et al.* 2000; and Zhou *et al.* 1999). The experimental uncertainty in ε_y was estimated to be about 16%. Like Figure 6-1(a), the FBG sensing systems were built in-house (Zhou *et al.* 2000).

6.2.2 Experimental setup

Experiments were carried out in the closed-circuit wind tunnel described in Section 2.6. A flexible square cylinder, made of nylon, of a height h = 17.3 mm was

fix-supported at both ends and placed 0.2 m downstream of the exit plane of the tunnel contraction, as shown in Figure 6-2. The arrangement of the actuators was the same as before, with details given in Figure 2-6. At the free-stream velocity (U_∞) of 5.85 m/s, the cylinder underwent its first-mode resonance at the natural frequency f_n = 47.9 Hz of the structure, which was determined from the frequency response of the cylinder vibration when excited with an electromechanical shaker under no flow condition. Due to the light mass loading of the fluid, f_n was very close to the resonance frequency of the cylinder/fluid system f_n'. The corresponding Re and the reduced velocity ($U_r = U_\infty / f_n' h$) were 6700 and 7.07, respectively. The maximum cylinder displacement, Y_{max}, was about 0.91 mm or 0.05h.

A 5 μm tungsten hot wire (hot wire ①) was placed at $x/h = 0$, $y/h = 1.5$ and $z/h = 5$ to measure the streamwise fluctuating velocity (u_1) of the flow. The cylinder vibration (Y) was measured using a laser vibrometer (Polytec OFV3100). Flexural deformation, ε_y, of the cylinder was monitored by a FBG sensor. The coordinates x, y and z correspond to streamwise, transverse and spanwise directions, respectively, as indicated in Figure 6-2.

The above measured signals can be used as feedback signals either individually or in combination. After amplification, all feedback signals were low-pass filtered at a cut-off frequency of 200 Hz and then input into a Digital Signal Processor (DSP) fitted with 16-bit AD and DA converter. The converted analog signals were low-pass filtered again (cut-off frequency = 200 Hz) and amplified by two dual channel piezo driver amplifiers (Trek PZD 700) before activating the actuators. The use of the two low-pass filters in the feed-forward and feedback passages was to remove high

frequency noises from turbulence and electronic components.

To monitor and analyze the control performance, a second 5 μm tungsten hot wire (hot wire ②) was placed at $x / h = 2$, $y / h = 1.5$, $z = 0$, where typical vortex shedding signal was highly coherent. The measured fluctuating velocity (u_2) signal was amplified and recorded by a personal computer simultaneously with other sensors through a 12-bit AD board at a sampling frequency of 3.5 kHz per channel. The duration of each record was 20 s.

The flow visualization and PIV measurements were conducted using a Dantec standard PIV2100 system, including a CCD camera for digital particle images and two New Wave standard pulsed laser sources for illumination. See Section 2.6 for more detailed information. Each image covered an area of 176 mm × 141 mm or $x / h \approx 0.5 \sim 10.8$ and $y / h \approx -4.1 \sim 4.1$ of the flow field for both flow visualization and PIV measurements. In addition, the cross flow distributions of flow velocities and Reynolds stresses at $x / h = 3$ were measured using a two-component LDA system.

6.3 Controller Design and Parameter Optimization

Based on the feedback signals, i.e. u_1, ε_y and Y, five different control schemes were investigated, which are divided into two categories. One is called one-element control scheme using a single signal from either flow field or cylinder vibration, referred to as u_Control, ε_y_Control and Y_Control, respectively. The other category is called two-element control scheme, which uses a combination of two signals from both cylinder vibration and flow, namely, $u + \varepsilon_y$_Control and $u + Y$_Control.

For each control scheme, a simple feedback controller was designed, which involves a gain coefficient in amplitude ($\widetilde{P}_q$) and a phase shift ($\widetilde{\phi}_q$) between the output and input of the controller q, representing u_1, ε_y or Y. Both $\widetilde{P}_q$ and $\widetilde{\phi}_q$ were manually tuned during experiments to ensure a maximum reduction in the root mean square (r.m.s.) value of Y, i.e., Y_{rms}. Following are the procedures for tuning: for the one-element scheme, first vary $\widetilde{P}_q$ by keeping $\widetilde{\phi}_q = 0^\circ$ to find a $\widetilde{P}_q$, i.e., $\widetilde{P}_{q,opt}$, leading to the smallest Y_{rms}; then given $\widetilde{P}_{q,opt}$ vary $\widetilde{\phi}_q$ within a cycle to determine the $\widetilde{\phi}_{q,opt}$, under which Y_{rms} reaches the minimum. The $\widetilde{P}_{q,opt}$ and $\widetilde{\phi}_{q,opt}$ values were used as the optimal parameters of the controller. For the two-element scheme, the same tuning process as the one-element scheme was first carried out for each feedback signal to obtain an initial configuration. Then apply simultaneously the two signals selected using the initial configuration as a starting point for fine tuning, in which both $\widetilde{P}_q$ and $\widetilde{\phi}_q$ were adjusted again for each signal. Several iterations were needed to reach the final configuration, giving the maximum reduction in Y_{rms}. The whole controller design process was carried out using the dSPACE system described in Section 2.5.

Figure 6-3 shows two typical examples of parameter tuning for u_Control (Figure 6-3(a)) and u + Y_Control (Figure 6-3(b)). The r.m.s. value of u_2 ($u_{2,\,rms}$), normalized by U_∞, and ε_y ($\varepsilon_{y,\,rms}$) were simultaneously measured during tuning. Before control, the Y_{rms} / h, $\varepsilon_{y,\,rms}$ and $u_{2,\,rms}$ / U_∞ are 0.041, 297μ and 0.24, respectively. For u_Control (Figure 6-3(a)), all three quantities show a dip at $\widetilde{P}_{u_1} = 2$ when $\widetilde{\phi}_{u_1} = 0$. Varying $\widetilde{\phi}_{u_1}$ within a cycle by keeping $\widetilde{P}_{u_1} = 2$ further reduces their

amplitude to a minimum at $\tilde{\phi}_{u_1} = 108^\circ$ before they reach a local maximum at $\tilde{\phi}_{u_1} = 288^\circ$, suggesting a 180° phase shift between the two extremes. The u + Y_Control requires tuning two sets of parameters, ($\tilde{P}_{u_1}$, $\tilde{\phi}_{u_1}$) and ($\tilde{P}_Y$, $\tilde{\phi}_Y$). Figure 6-3(b) shows the variation of the three physical quantities with respect to one set of parameter, while the other set is set to be optimal. It is clear that, when changing parameters in the controller, all three quantities undergo similar changes, pointing to the possibility to achieve the simultaneous control of both vortex shedding and the structural vibration using the same controller. The tuning process led to an optimal configuration for each scheme with parameters tabulated in Table 6-1. Unless otherwise stated, these parameters were used in experiments discussed hereinafter.

6.4 Control Performance

Figures 6-4 to 6-6 compare with the un-controlled case the control performances of the five control schemes in terms of the power spectra, E_Y, E_{ε_y} and E_{u_2}, of Y, ε_y and u_2. The spectrum of fluctuation α, representing Y, ε_y or u_2, has been normalized such that $\int_0^\infty E_\alpha(f)df = 1$. The frequency f was again normalized with h and U_∞ ($f^* = fh/U_\infty$). The effects of different control schemes on the cylinder vibration are illustrated by Figure 6-4 and Figure 6-5. Three pronounced peaks appear in the spectra at different frequencies. The first peak corresponds to the first-mode natural frequency, $f_n^{'*}$, of the fluid-structure system, which coincides with the shedding frequency f_s^* ($f_n^{'*} = f_s^* = 0.141$). The second one at $2f_s^*$ is the second harmonic of

f_s^* and the third one at $f_n'''^* = 0.49$ is the third-mode natural frequency of the system. Given the second-mode vibration anti-symmetrical about the mid span of the cylinder, no peak is expected at the second-mode natural frequency of the system. When the one-element control is deployed (Figures 6-4 to 6-5, (b)-(d)), there is a systematic reduction in both E_Y and E_{ε_y} compared to their un-controlled counterparts. *Y*_Control is best performed to suppress the resonant peaks at $f_n'^*$ and $f_n''''^*$, which drop from 0.21 and 0.13 to 0.096 and 0.066 at $f_n'^*$ in E_Y and E_{ε_y}, respectively, and from 0.14 and 0.06 to 0.016 and 0.019 at $f_n''''^*$, respectively. Note that *u*_Control may perform better in suppressing the peak at $2f_s^*$ in E_Y than *Y*_Control (Figure 6-4(b)). This is reasonable since structural vibration at $2f_s^*$ is mainly due to the second harmonic of the shedding frequency. The use of fluid sensor therefore brings more relevant information on flow into the controller. The two-element control schemes in general improve the control performance of the one-element scheme (Figures 6-4 to 6-5, (e)-(f)). The best result is achieved using *u* + *Y*_Control, with the peak amplitude at $f_n'^*$ reduced by 79% and 68% or by 94% and 75% at $f_n''''^*$ in E_Y and E_{ε_y}, respectively.

Figure 6-6 shows the corresponding u_2-spectrem. In the un-perturbed case, E_{u_2} displays three harmonics of the shedding frequency. The peak at $3f_s^*$ is completely eliminated for all five control schemes, while those at f_s^* and $2f_s^*$ are suppressed to different degrees. Among the three one-element control schemes, *u*_Control is best performed due to the direct feedback from the flow. Again, the two-element control schemes outperform the one-element control schemes in suppressing these peaks.

Figure 6-7 presents the reduction, compared with the unperturbed case, in energies in E_Y and E_{ε_y} associated with the vibration of different peaks, i.e., $E^{(m)}_{Y,\Delta f}$ and $E^{(m)}_{\varepsilon_y,\Delta f}$ (m = 1, 2, 3), or in energies in E_{u_2} associated with the harmonics of f_s^*, i.e., $E^{(n)}_{u_2,\Delta f}$ (n = 1, 2, 3). These energies were calculated by integrating the power spectral density functions over –3 dB bandwidth centered about the peaks. As evident in Figure 6-7(a) and Figure 6-7(b), the two-element schemes obviously perform better than the one-element schemes in terms of suppressing structural vibration, especially the first-mode resonance. In the best case, u + Y_Control reduces $E^{(1)}_{Y,\Delta f}$, $E^{(2)}_{Y,\Delta f}$ and $E^{(3)}_{Y,\Delta f}$ by 81.5%, 85.2% and 98.2%, and $E^{(1)}_{\varepsilon_y,\Delta f}$, $E^{(2)}_{\varepsilon_y,\Delta f}$ and $E^{(3)}_{\varepsilon_y,\Delta f}$ by 77.4%, 79.5% and 96.2%, respectively. On the other hand, u_Control (Figure 6-7(c)) greatly impairs vortex shedding, and the performance is further improved if the feedback consists of a combination of u and Y (or ε_y). The best performance is given by u + Y_Control, which reduces $E^{(1)}_{u_2,\Delta f}$, $E^{(2)}_{u_2,\Delta f}$ and $E^{(3)}_{u_2,\Delta f}$ by 80.3%, 86.5% and 96.4%, respectively. It is interesting to note that all control schemes are effective to suppress not only the vibration of the first-mode but also, even to a larger extent, that of the third-mode.

Figures 6-8 to 6-10 show the time histories of Y, ε_y and u_2. The two-element controllers reduce drastically the amplitudes of u_2, ε_y and Y in all cases. The effectiveness of the schemes is improved following the ladder of u_, ε_y_, Y_, u + ε_y_ and u + Y_Control. Interestingly, the control voltage required by each scheme is gradually decreased following the same order, as indicated by the r.m.s value, $V_{p,\,rms}$, of the control voltage (Table 6-2). Since the resistance of the actuators remains

constant irrespective of the control schemes, a lower control voltage means a lower energy input. Evidently, u + Y_Control requires the lowest actuating voltage and hence the smallest perturbation amplitude than other four schemes yet achieves the best performance of all (71% reduction in Y_{rms}, 65% in $\varepsilon_{y,rms}$ and 63% in $u_{2,\,rms}$).

6.5 Discussions

To understand the physics behind the impaired Y and ε_y, the modified flow structure under the control schemes measured by flow visualization, PIV and LDA measurements were firstly examined. Without control, the Kármán vortex street is evident in Figure 6-11(a) and Figure 6-12(a). The solid square in the figures corresponds to the cylinder position. Once a control scheme is deployed, vortex shedding from the cylinder and the normalized maximum spanwise vorticity, $|\omega^*_{z\max}| = |\omega_{z\max}|h/U_\infty$, are weakened to various degrees, depending on the schemes used, as evident in Figures 6-11(b)-(f) and Figures 6-12(b)-(f); vortices appear breaking up, showing considerably less coherence and weaker strength. The most significant alteration to the flow is obtained when the two two-element control schemes are applied (Figures 6-11(e)-(f) and Figures 6-12(e)-(f)). For u + Y_Control scheme, the vortex street is almost completely destroyed; the corresponding $|\omega^*_{z\max}|$ and circulation (Γ) decreases by 60% and 85%, respectively. Γ around a vortex is estimated by Eq.(3-1).

Figure 6-13 exhibits the modification of the cross flow distributions of the mean velocity $\overline{U}^*$, normalized by U_∞, and Reynolds stresses $\overline{u^2}^*$, $\overline{v^2}^*$ and $\overline{uv}^*$, normalized by U_∞^2, measured by LDA at $x/h = 3$ under the u + Y_Control scheme. In the range

of $y / h = -1.4 \sim 1.4$, the maximum $\overline{U}^*$, $\overline{u^2}^*$ and $\overline{v^2}^*$ decline considerably, up to 14%, 19%, 19%, respectively, compared with those unperturbed. On the other hand, $\overline{uv}^*$ decreases by about 21%. The increased mean velocity deficit is related to the decreased entrainment of high speed fluid from the free-stream under the action of the weakened vortices (Warui & Fujisawa, 1996). Evidently, the weakened vortices are responsible for the decrease in $\overline{u^2}^*$ and $\overline{v^2}^*$, and accordingly the increased $\overline{uv}^*$ since $\overline{uv}^*$ is largely associated with the incoherent motion, residing in the saddle region between two consecutive vortices (Zhou & Antonia, 1994b). Note that $\overline{U}^*$, $\overline{u^2}^*$ and $\overline{v^2}^*$ remain reasonably symmetric and $\overline{uv}^*$ is anti-symmetric about the centerline although the perturbation was imposed only on the upper side of the cylinder, in line with the flow patterns shown in Figure 6-11 and Figure 6-12.

The mean drag coefficient, $\overline{C}_D$, was calculated using Eq.(3-4) based on $\overline{U}^*$, $\overline{u^2}^*$ and $\overline{v^2}^*$. $\overline{C}_D$ was 2.09 for the uncontrolled case, agreeable with the previously reported range, 1.7 ~ 2.2 (Lee, 1975 ; Knisely, 1990; and Zhou & Antonia, 2002). Under u + Y_Control scheme, $\overline{C}_D$ dropped by 30%. Apparently, the weakened vortex shedding should correspond to an increased backpressure and subsequently reduced $\overline{C}_D$.

Again, insight into the physics behind the modified flow and structural vibration can be better gained by examining the spectral phase and coherence between the simultaneously measured Y and u_2, i.e. ϕ_{Yu_2} and Coh_{Yu_2} using Eqs.(3-3) and (3-2), respectively. As demonstrated in Section 3.5, ϕ_{Yu_2} was approximately equivalent to

the phase relationship between the lateral structural oscillating velocity, $\dot{Y}$, and the lateral velocity, v, of the flow around the cylinder. Hence ϕ_{Yu_2} = 0 and -π indicated the synchronized and opposite movements between $\dot{Y}$ and v, respectively. Without perturbation, ϕ_{Yu_2} was about zero near f_s^* = $f_n^{'*}$, $2f_s^*$ and $f_n^{''''*}$ (Figure 6-14(a)), that was, $\dot{Y}$ and v are synchronized at these frequencies. The plateaus around f_s^* (or $f_n^{'*}$), $2f_s^*$ and $f_n^{''''*}$ indicated that the synchronization occurred over a range of frequencies. However, ϕ_{Yu_2} at these frequencies was all changed from 0 to near -π under different control schemes (Figures 6-14(b)-(f)), suggesting that $\dot{Y}$ and v collided or acted against each other, resulting in impaired vortex shedding and cylinder vibration. This phase change was most extensive under the two-element schemes for $f_n^{'*}$, $2f_s^*$ and $f_n^{''''*}$, explaining its superior performance over the one-element schemes. Accordingly, Coh_{Yu_2} at f_s^* (or $f_n^{'*}$), $2f_s^*$ and $f_n^{''''*}$, receded greatly (Figure 6-15); for u + Y_Control (Figure 6-15(f)), it reduced by 74.2%, 67.0% and 83.2%, respectively, around the three frequencies, compared with the unperturbed case. The drastic reduction in Coh_{Yu_2} implied a nearly decoupled correlation between vortex shedding and structural vibration.

From a different perspective, the alteration in ϕ_{Yu_2} and reduction in Coh_{Yu_2} can also be related to a similar altered fluid-structure system damping as that in Section 4.5. The free vibration of a flexible structure consists of multiple modal oscillations and each of them corresponds to a different effective damping ratio. The same auto-regressive moving average (ARMA) technique used in Section 4.5 was used again to calculate the effective damping ratios, associated with $f_n^{'*}$ and $f_n^{''''*}$, i.e. $\zeta_{y,e}^{(k)}$ (k = 1,

3), from the measured time-domain Y signals. The ARMA model of an order of 190 and 70000 data points were presently used for calculation. Figure 6-16 shows the effective first- and third-mode damping ratios for different schemes. The corresponding structural damping ratios, $\zeta_{y,s}^{(k)}$, indicated by a dash line, were measured under no-flow condition with the cylinder excited by an electromechanical shaker. Without control, vortex shedding synchronized with the lateral structural vibration, and $\zeta_{y,e}^{(k)}$ was less than $\zeta_{y,s}^{(k)}$, albeit slightly, suggesting a negative fluid damping ratio $\zeta_{y,f}^{(k)}$ since $\zeta_{y,e}^{(k)} = \zeta_{y,s}^{(k)} + \zeta_{y,f}^{(k)}$. The negative $\zeta_{y,f}^{(k)}$ simply means that vortex shedding enhanced the structural vibration. $\zeta_{y,e}^{(k)}$ increased gradually following the ladder of $u\_$, $\varepsilon_{y}\_$, $Y\_$, $u + \varepsilon_{y}\_$ and $u + Y_$Control. The maximum damping ratio was obtained under $u + Y_$Control, in which $\zeta_{y,e}^{(1)}$ and $\zeta_{y,e}^{(3)}$ rose by 60% and 87%, respectively, compared with uncontrolled case. The variation in $\zeta_{y,e}^{(1)}$ and $\zeta_{y,e}^{(3)}$ was agreeable with the trend shown in Figures 6-3 to 6-5 and Figures 6-7 to 6-9, providing an explanation for the effectively attenuated structural oscillations.

The interpretation of the closed-loop control mechanism given in Chapter 4 seems to apply to the present case. Fluid excitations with a high energy concentration at f_s^* and $2f_s^*$ cause structure resonance at $f_n^{"*}$ and strong oscillations at $f_n^{""*}$. At these frequencies, the structural vibration is in-phase with the vortex shedding. The control effect successfully alters the nature of the fluid-structure interactions, changing the in-phased fluid-structure synchronization into anti-phased interactions. This leads to an effective impairment of vortex shedding and a great enhancement of

fluid-structure damping at the same time. As a result, the structural vibration is attenuated.

The one-element control schemes use either flow or structural response as feedback. The flow response u_2 contains only information on the flow excitation and nothing on the structural vibration. Thus, u_Control alters the flow excitation and therefore indirectly affects the structural vibration. On the other hand, both ε_y_ and Y_Control schemes use the structural vibration information, without the flow, for feedback, performing better in suppressing the vibration than u_Control scheme. Note that ε_y is a measure of the structural deformation, which indirectly reflects the vibration, while Y is a direct measure of the lateral structural movement, which is the direct agent to perturb the flow. Consequently, Y_Control performs better than ε_y_Control (Figures 6-4 to 6-12). Since the one-element schemes use signals from either flow or structural vibration, the information on the non-linear flow-structure interaction is not made use of. This information is however an important part of physics behind the vortex-induced vibrations. Therefore, the schemes cannot achieve the best performance. On the other hand, the two-element schemes utilize a combination of flow and structural vibration signals for feedback and reflect the interaction/coupling between flow and structural vibration, addressing the essence that governs both structural vibration and vortex shedding. As a result, the two-element schemes outperform the one-element scheme, even though the input energies to the actuators are appreciably lower. For the two two-element schemes, the better performance of u + Y_Control is due to the direct relationship of Y with the structural vibration on one hand, and with the perturbation to flow on the other hand.

6.6 Non-resonance Cases

Interests were also aroused to test the effectiveness of the closed-loop control on the flexible structural vibration (Y) under non-resonance conditions when the vortex shedding frequency (f_s) was set to be different from the natural frequencies of the cylinder. Compared with the resonance case, non-resonance vibration control in a cross flow has seldom been considered in the literature. Resonance vibration is usually dominated by one particular mode, whereas non-resonance vibrations usually involve responses from different modes. From the point of view of control, non-resonance control is therefore much more challenging.

The same experimental setup shown in Figure 6-2 was used again and the flow velocity, U_∞, was tuned to be 2.5 m/s (Re = 2800) and 7 m/s (Re = 8000), corresponding to f_s = 20.5 Hz and 57.5 Hz, respectively. In the first configuration, f_s was less than f_n' = 47.9 Hz while for the second, f_s lied between f_n' and f_n''' (= 164.2 Hz). Two control schemes, i.e. Y_Control and u + Y_Control, were considered, both having been found before to be the most performing one-element and two-element control schemes in resonance control. Experiments also followed the same procedure as described previously.

It was observed that similar control performances on both structural vibration and fluid field as resonance case were obtained. Table 6-3 tabulates a summary of the control results. Detailed experimental results, including the parameter optimisation of the controller, control performances and phase/coherence analyses are given in Appendix. Evidently, irrespective of Re and control scheme, the root mean square value of Y, ε_y and u_2, i.e. Y_{rms}, $\varepsilon_{y,\,\mathrm{rms}}$ and $u_{2,\,\mathrm{rms}}$, and Γ were all reduced to different

extent using relatively low perturbation voltage (V_p), suggesting the effectiveness of the control. The u + Y_Control outperforms Y_Control in every category, resulting in a higher reduction in Y_{rms}, $\varepsilon_{y,\,rms}$, $u_{2,\,rms}$ and Γ despite smaller root mean square value of V_p, i.e. $V_{p,\,rms}$. Analyses conducted for the resonance case were repeated for understanding the control effects under non-resonance case. Results showed similar alteration in phase shift and spectral coherence between structural vibration and flow, mainly centred at four different frequencies, i.e. f_s^*, $2f_s^*$, f_n^* and $f_n^{'''*}$.

It is concluded that the vortex-induced flexible structural vibration at occurrence of non-resonance can also be effectively suppressed using the proposed perturbation technique together with closed-loop control. For example, using u + Y_Control scheme, Y_{rms}, $\varepsilon_{y,\,rms}$, $u_{2,\,rms}$ and Γ at Re = 8000 were reduced by 58%, 52%, 53% and 88%, respectively, compared with their un-controlled counterparts. Closed-loop control successfully changed the phase shift between structural vibration and flow from in-phase to anti-phase, accompanied by a reduction in their spectral coherences and an enhancement of system damping. As a result, non-resonant structural vibration was attenuated.

6.7 Conclusions

Experimental investigation has been conducted to control the vortex-induced resonant vibration of a fix-supported flexible cylinder based on various feedback signals. Five control schemes are investigated depending on the feedback signal used. The three one-element schemes, namely u_, ε_y_ and Y_Control, deploy feedback signal either from flow or from cylinder vibration. Two two-element control schemes,

namely $u + \varepsilon_{y\_}$ and $u + Y_$Control, use a combination of both structural vibration and flow signals. The investigation leads to the following conclusions.

1) Both resonant and non-resonant flexural vibration of a flexible cylinder in a cross flow can be successfully controlled using the present perturbation technique. Under the control, the phase relationship between vortex shedding and structural displacement at dominant frequencies is changed from in-phase to anti-phase. This alters the synchronized motion between fluid and structure to collision between them, causing significantly increased modal damping ratios of the fluid-structure system. Consequently, vortex shedding is impeded and the structural vibration is effectively reduced.

2) A suitable choice of the feedback signal is crucial in determining the effectiveness of the control. The control performances in terms of suppressing structural vibration are gradually improved following the ladder of $u\_$, $\varepsilon_{y\_}$, $Y\_$, $u + \varepsilon_{y\_}$ and $u + Y_$Control. The two-element schemes perform much better than the one-element scheme, in terms of suppressing both vortex shedding and structural vibration. Furthermore the input energy required by the two-element schemes is minimum. The results are ascribed to its feedback signals, which reflect the interactions between fluid and structure. Among all schemes, $u+ Y_$Control performs best, resulting in a reduction by 71% in Y, 65% in ε_y, 63% in u_2, 85% in Γ and 30% in $\overline{C}_D$, compared with their uncontrolled counterparts.

Table 6-1 Optimal $\widetilde{P}_q$ and $\widetilde{\phi}_q$ (q represents u_1, ε_y or Y) under different control schemes.

Control Scheme / Optimal Parameter	u_Control	ε_y_Control	Y_Control	ε_y + Y_Control	u + Y_Control
$\widetilde{P}_{u_1}$	2			0.4	2
$\widetilde{\phi}_{u_1}$	108°			120°	85°
$\widetilde{P}_{\varepsilon_y}$		6		6	
$\widetilde{\phi}_{\varepsilon_y}$		72°		130°	
$\widetilde{P}_Y$			10		8
$\widetilde{\phi}_Y$			144°		160°

Table 6-2 Control voltage in r.m.s required by different control schemes.

Control Scheme	u_Control	ε_y_Control	Y_Control	u + ε_y_Control	u + Y_Control
$V_{p,\,\mathrm{rms}}$ (volts)	106	94	80	62	54

Table 6-3 Control performance of various control schemes under non-resonance case.

Control Scheme / Control Effect	Re = 2800		Re = 8000	
	Y_Control	$u + Y$_Control	Y_Control	$u + Y$_Control
Y_{rms}	24%↓	43%↓	37%↓	58%↓
$\varepsilon_{y,\,\mathrm{rms}}$	20%↓	39%↓	31%↓	52%↓
$u_{2,\,\mathrm{rms}}$	19%↓	42%↓	36%↓	53%↓
Γ	45%↓	79%↓	54%↓	88%↓
$V_{p,\,\mathrm{rms}}$	92 volts	60 volts	75 volts	55 volts

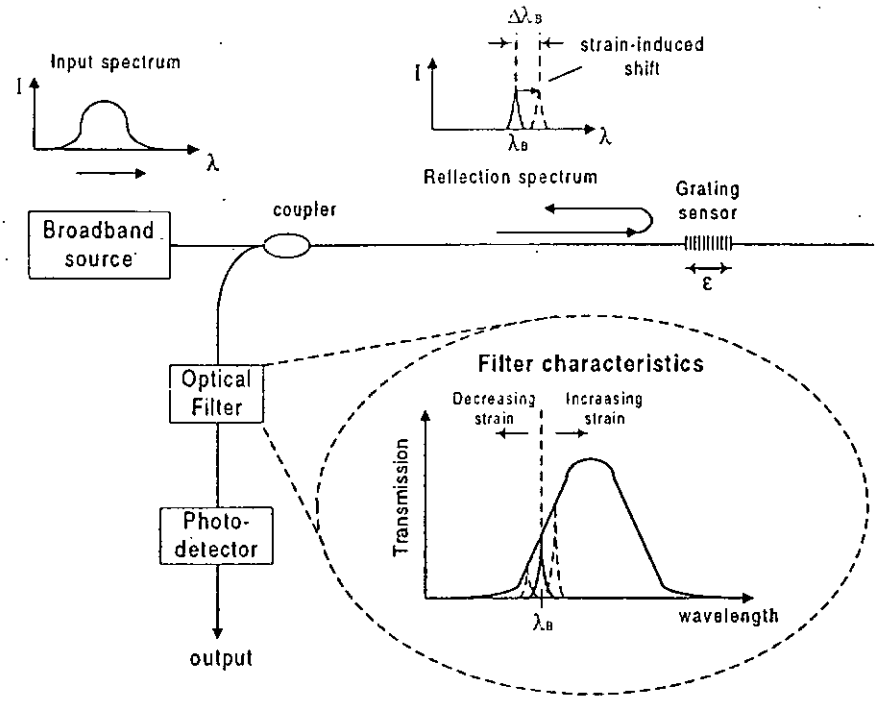

(a)

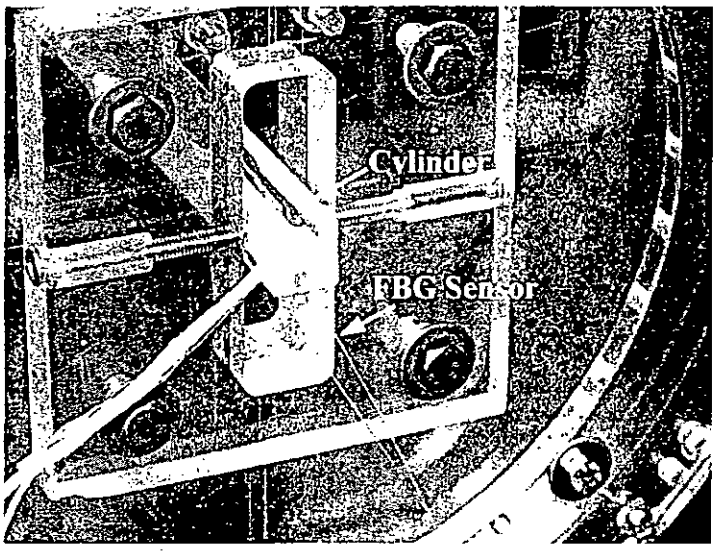

(b)

Figure 6-1 FBG strain sensing: (a) generic concept of Bragg grating strain sensing; (b) photo of the FBG sensor installed in the present experimental setup.

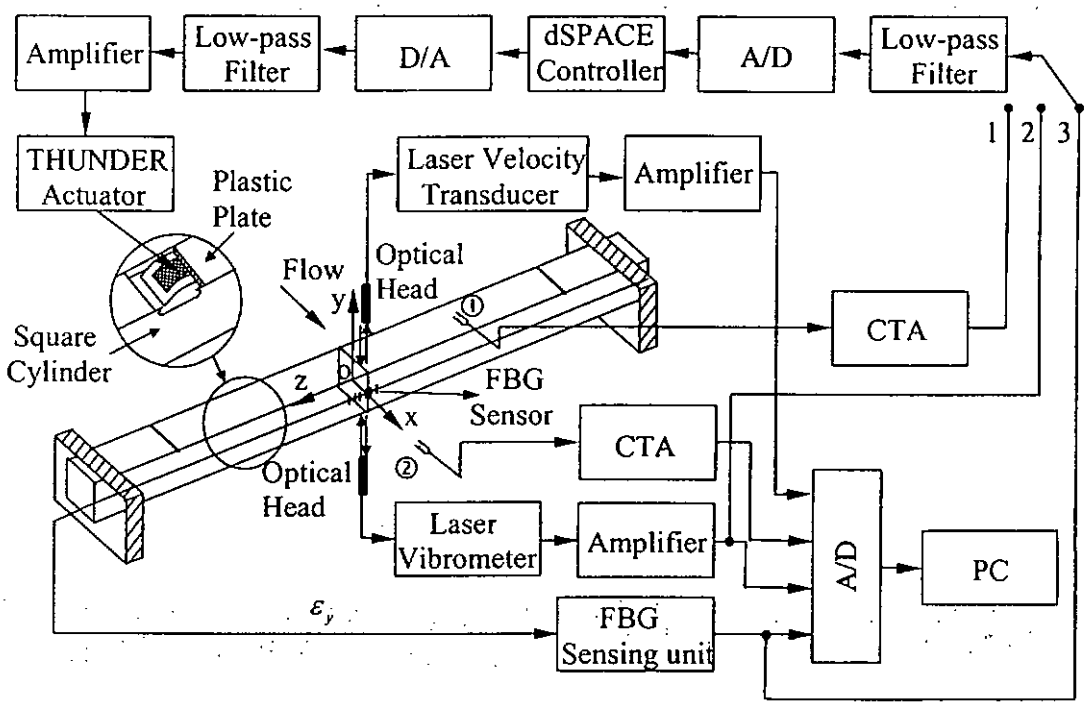

Figure 6-2 Experimental setup. ① Feedback hot wire was located at $x/h = 0$, $y/h = 1.5$, $z/h = 5$; ② Monitor hot wire was located at $x/h = 2$, $y/h = 1.5$, $z = 0$.

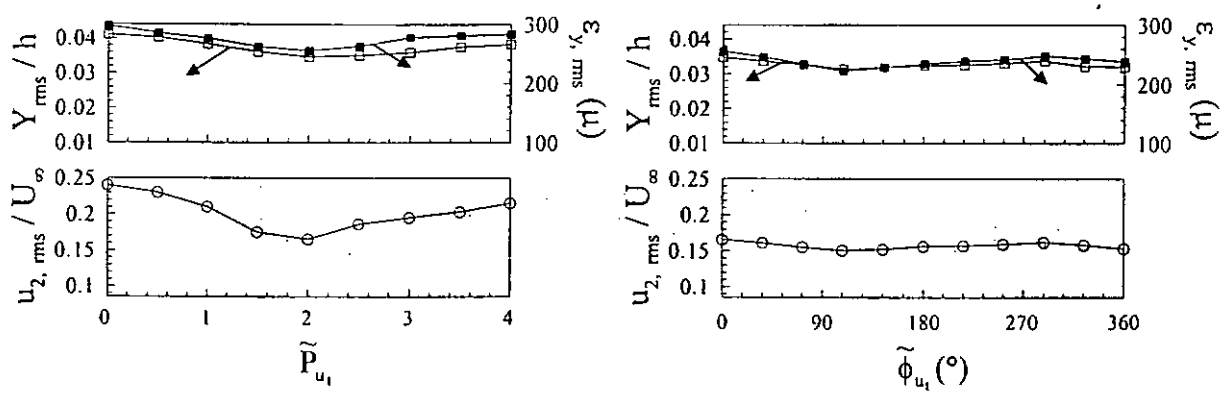

(a)

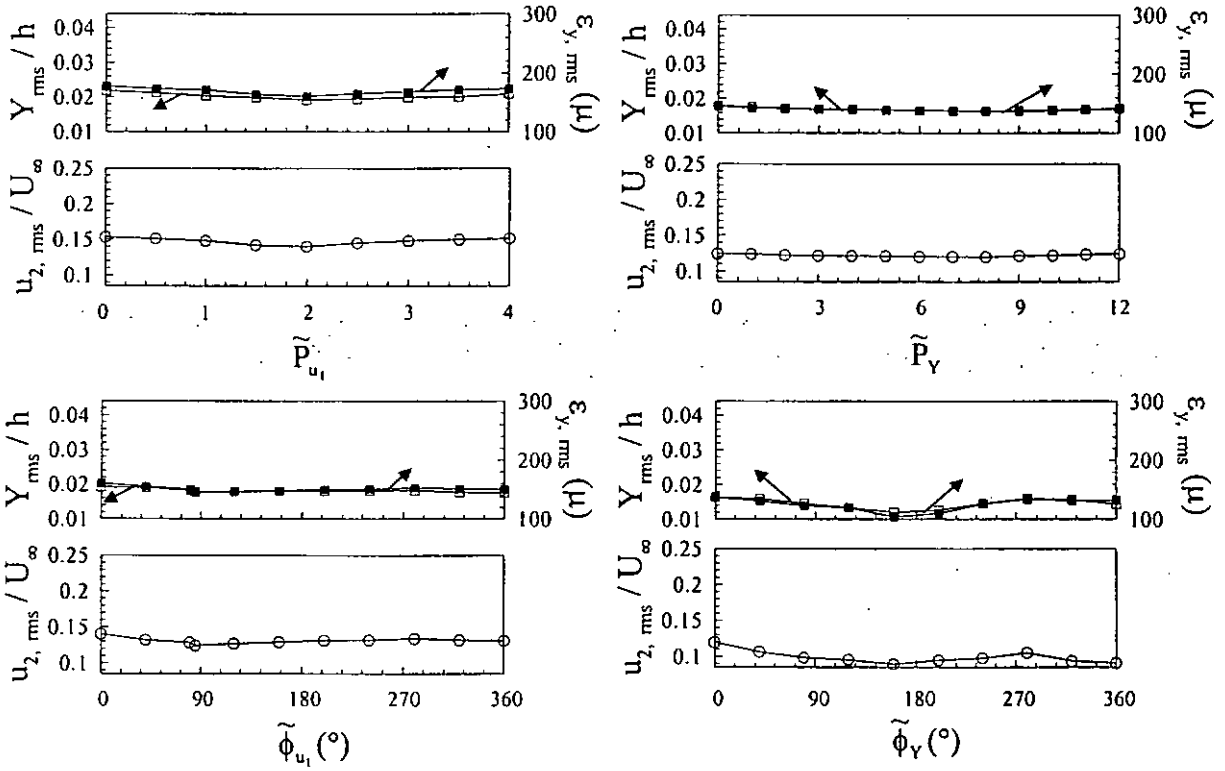

(b)

Figure 6-3 Typical closed-loop control response of normalized r.m.s. values of structural vibration (Y_{rms}), fluctuating streamwise flow velocity ($u_{2,\,rms}$), fluctuating strain in y, $\varepsilon_{y,\,rms}$ under different control schemes: (a) u_Control; (b) u + Y_Control. Re = 6700. Y_{rms} / h; $\varepsilon_{y,\,rms}$; $u_{2,\,rms}$ / U_∞.

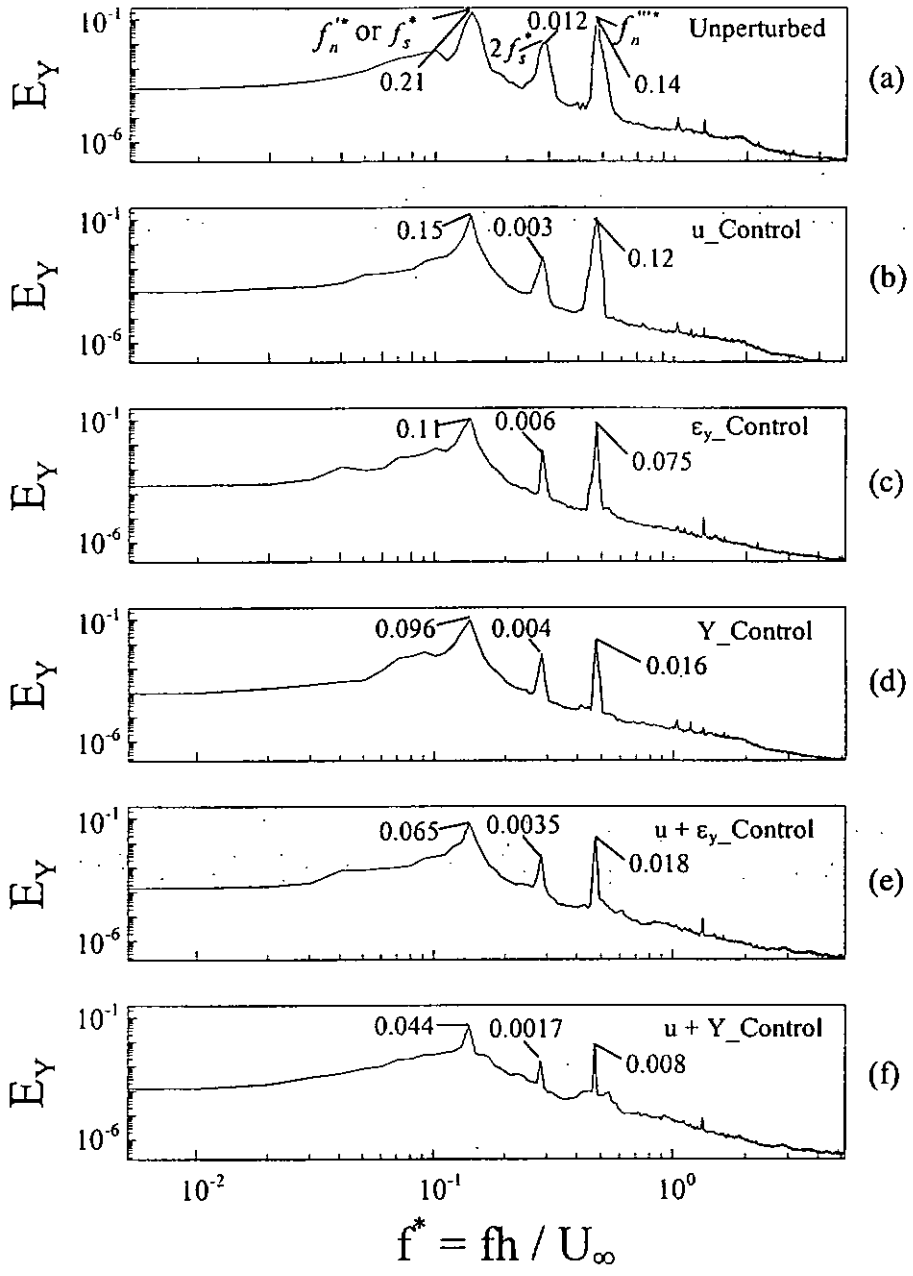

Figure 6-4 Effect on power spectrum of structural vibration (Y), E_Y, under different control schemes: (a) unperturbed; (b) u_Control; (c) ε_y_Control ; (d) Y_Control; (e) u + ε_y_Control; (f) u + Y_Control. Re = 6700.

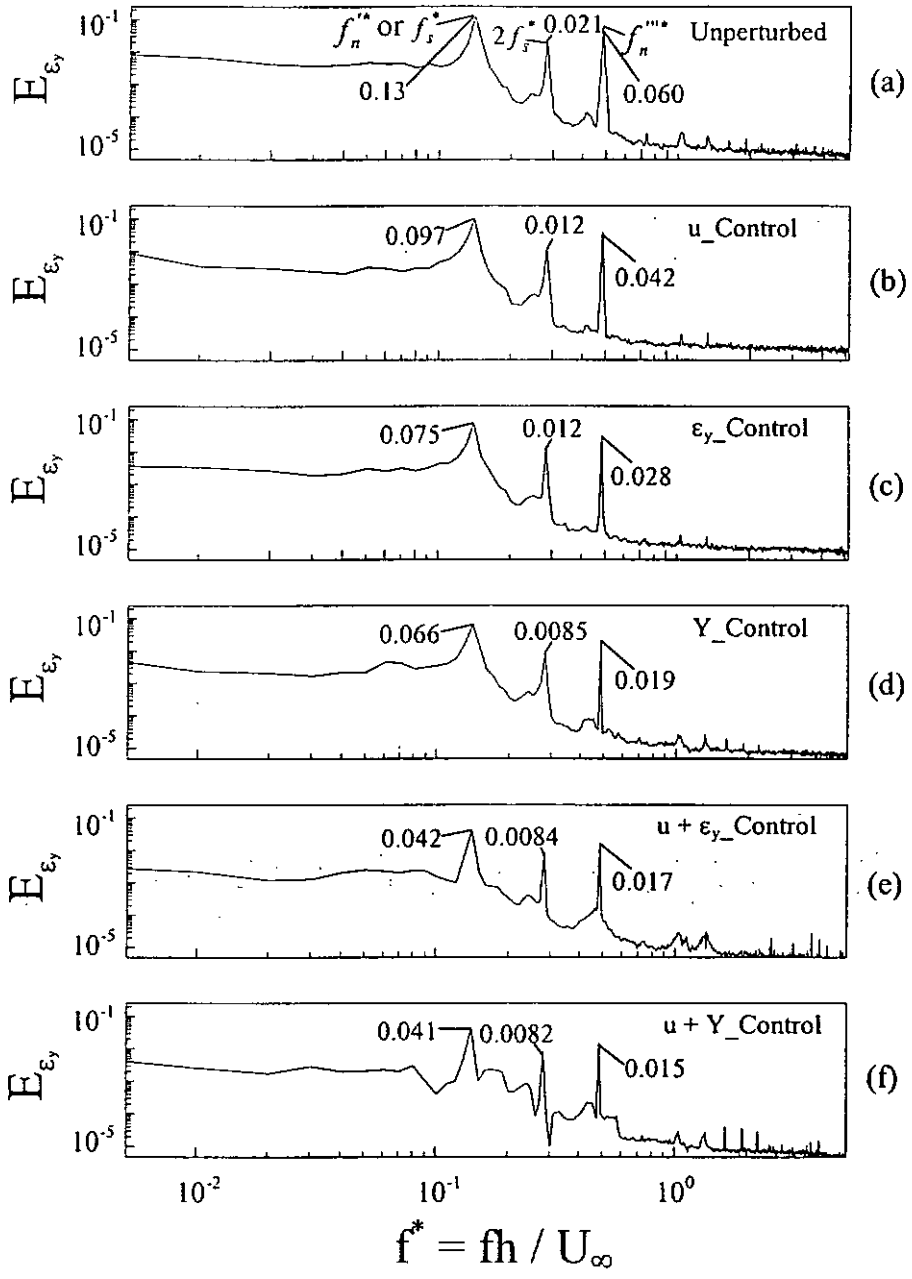

Figure 6-5 Effect on power spectrum of fluctuating strain in the y direction (ε_y), E_{ε_y}, under different control schemes: (a) unperturbed; (b) u_Control; (c) ε_y_Control ; (d) Y_Control; (e) u + ε_y_Control; (f) u + Y_Control. Re = 6700.

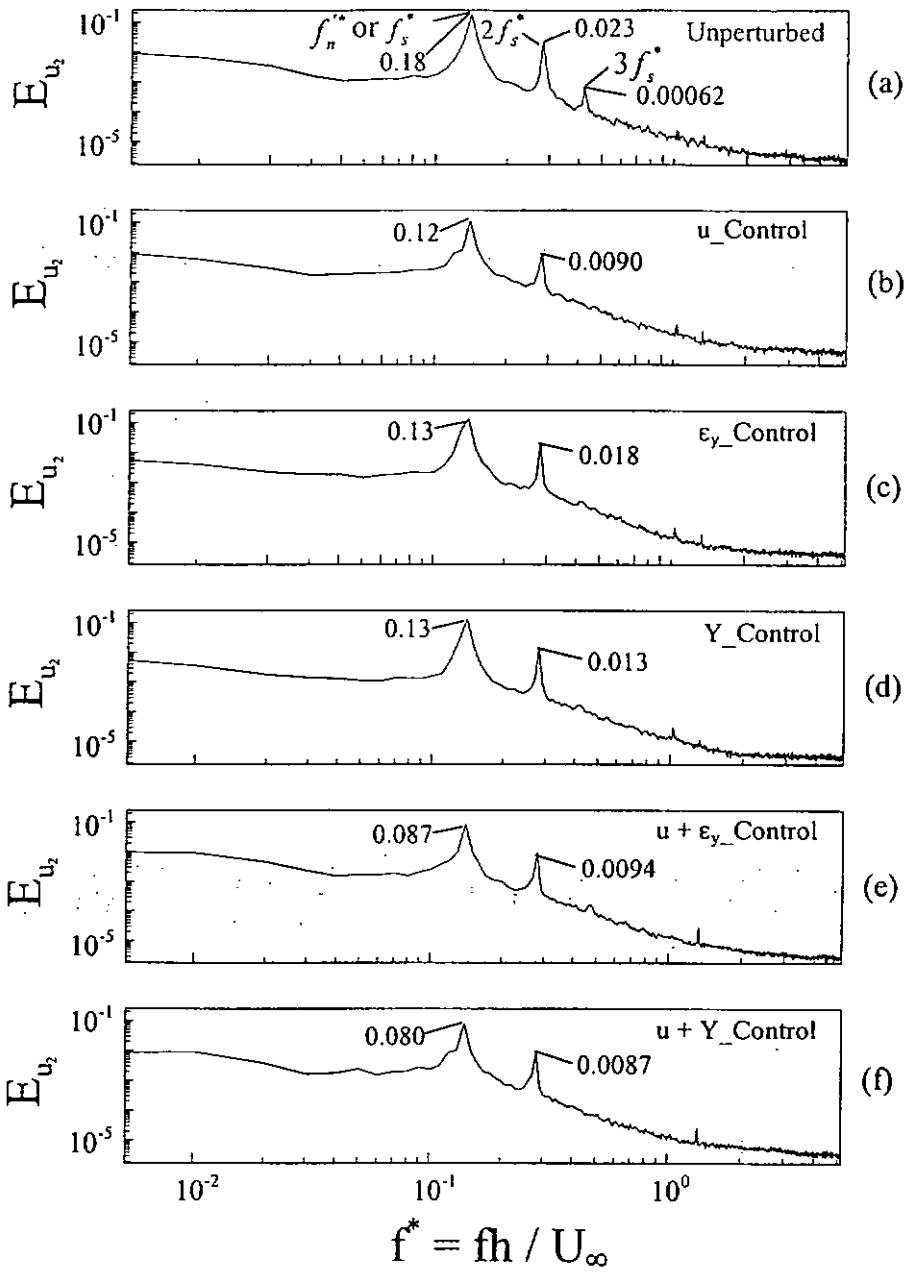

Figure 6-6 Effect on power spectrum of streamwise flow velocity (u_2), E_{u_2}, under different control schemes: (a) unperturbed; (b) u_Control; (c) ε_y_Control; (d) Y_Control; (e) $u + \varepsilon_y$_Control; (f) $u + Y$_Control. Re = 6700.

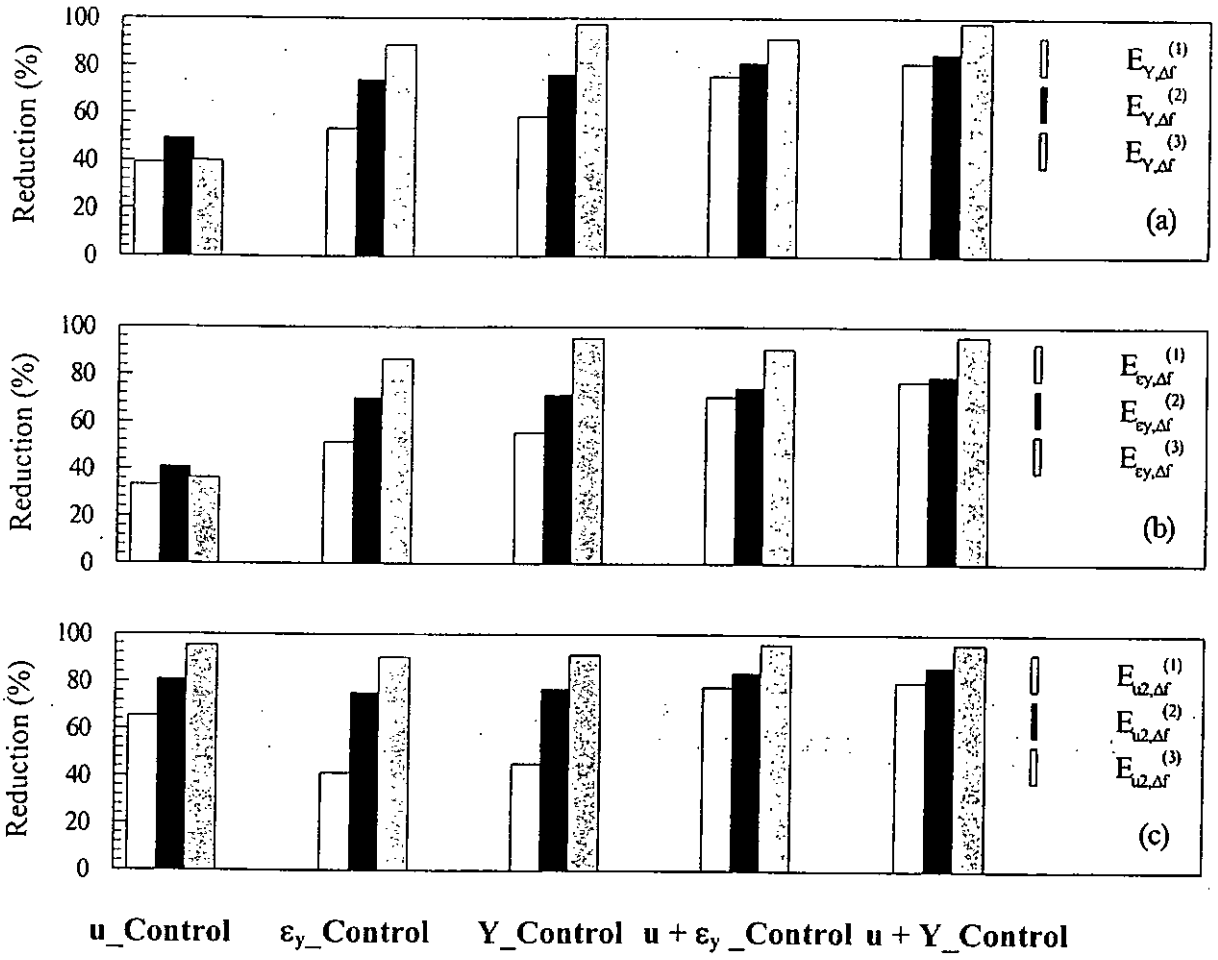

Figure 6-7 Reduction in $E_{Y,\Delta f}^{(n)}$, $E_{\varepsilon_y,\Delta f}^{(n)}$ and $E_{u_2,\Delta f}^{(n)}$ (n = 1, 2, 3). (a) Y, (b) ε_y and (c) u_2, respectively. Re = 6700.

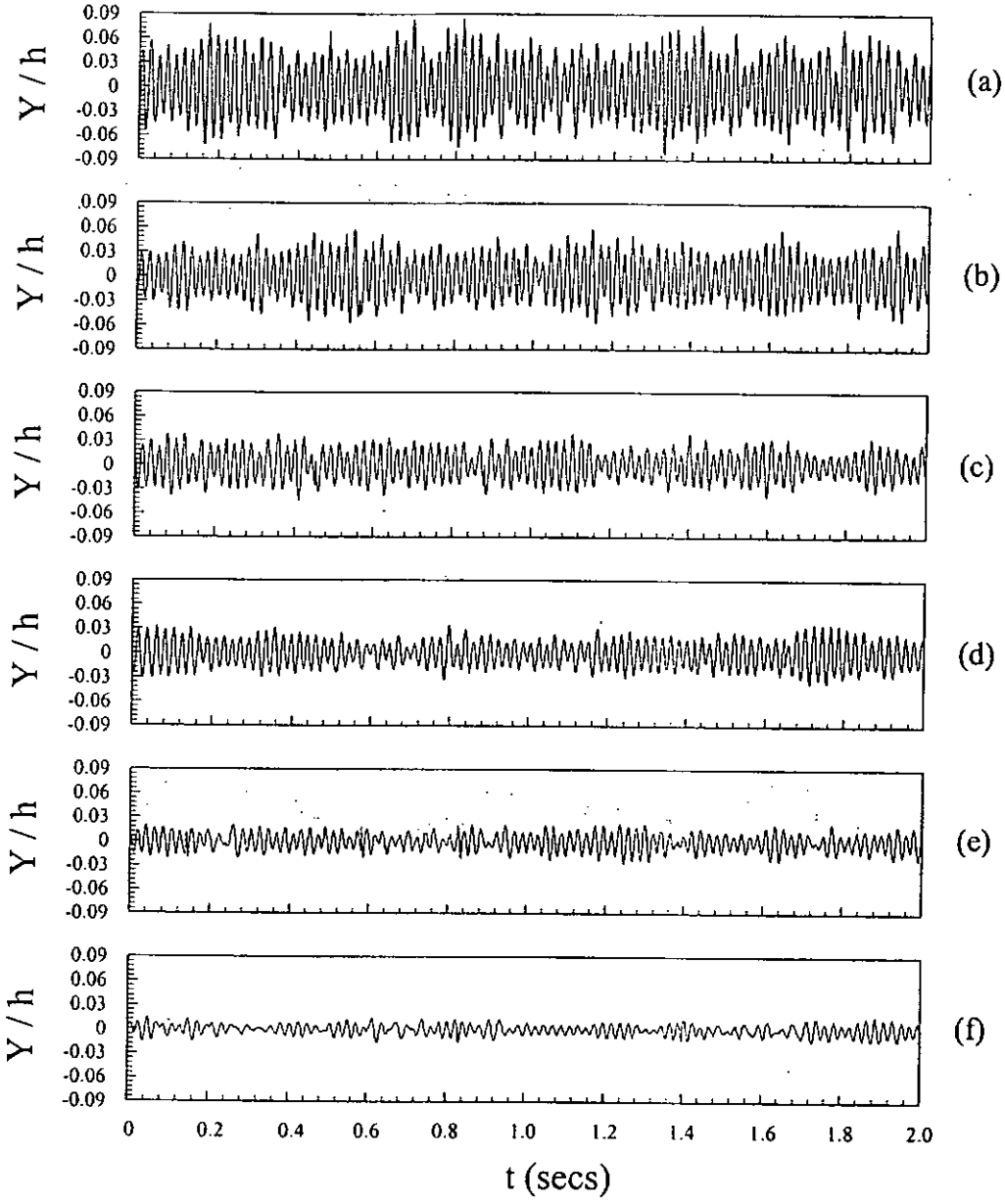

Figure 6-8 Typical time histories of structural vibration (Y) under different control schemes: (a) unperturbed; (b) u_Control; (c) ε_y_Control ; (d) Y_Control; (e) $u + \varepsilon_y$_Control; (f) $u + Y$_Control. Re = 6700. The time origin was arbitrary.

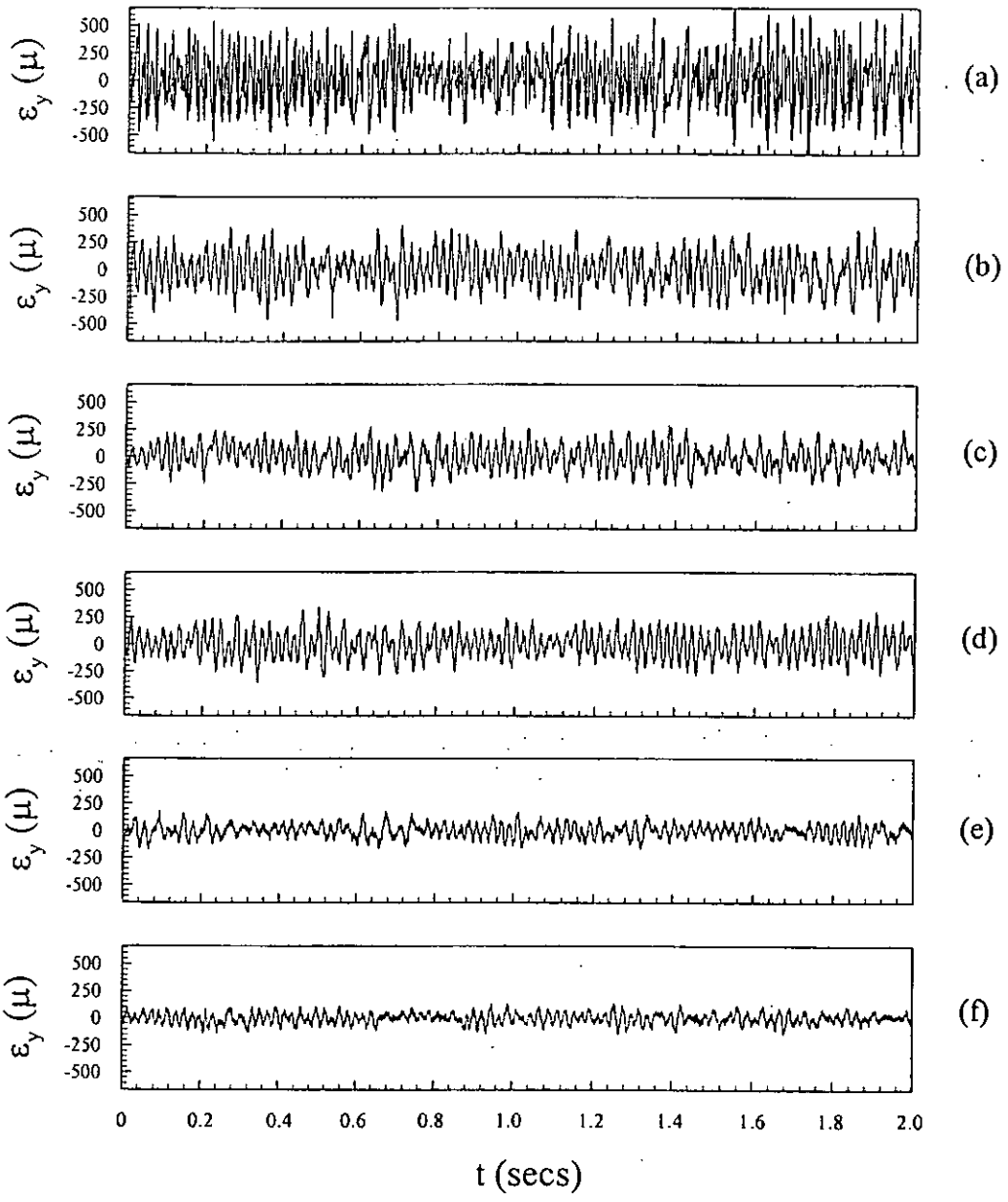

Figure 6-9 Typical time histories of fluctuating strain in the y direction (ε_y) under different control schemes: (a) unperturbed; (b) u_Control; (c) ε_y_Control ; (d) Y_Control; (e) u + ε_y_Control; (f) u + Y_Control. Re = 6700. The time origin was arbitrary.

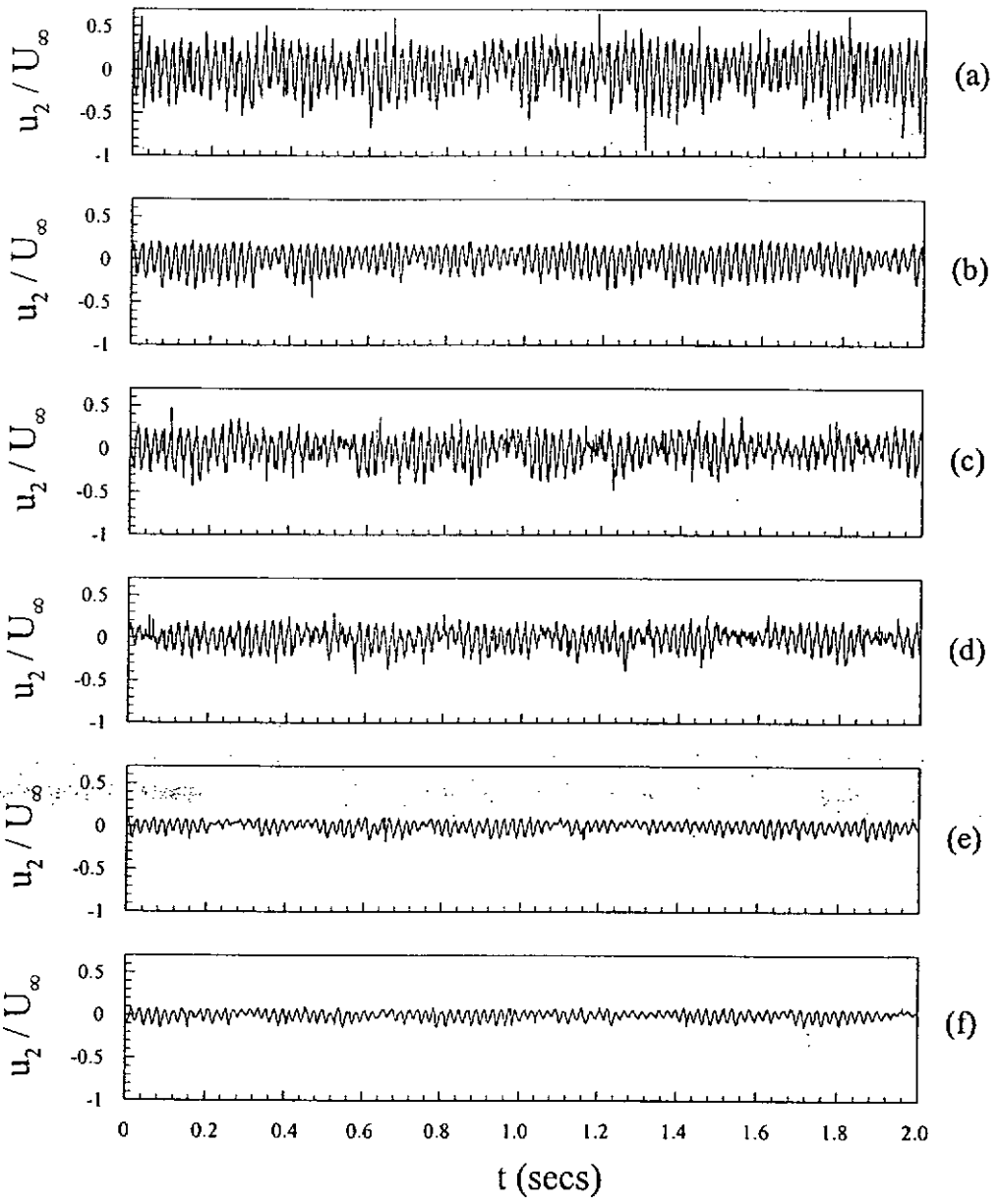

Figure 6-10 Typical time histories of streamwise flow velocity (u_2) under different control schemes: (a) unperturbed; (b) u_Control; (c) ε_y_Control ; (d) Y_Control; (e) u + ε_y_Control; (f) u + Y_Control. Re = 6700. The time origin was arbitrary.

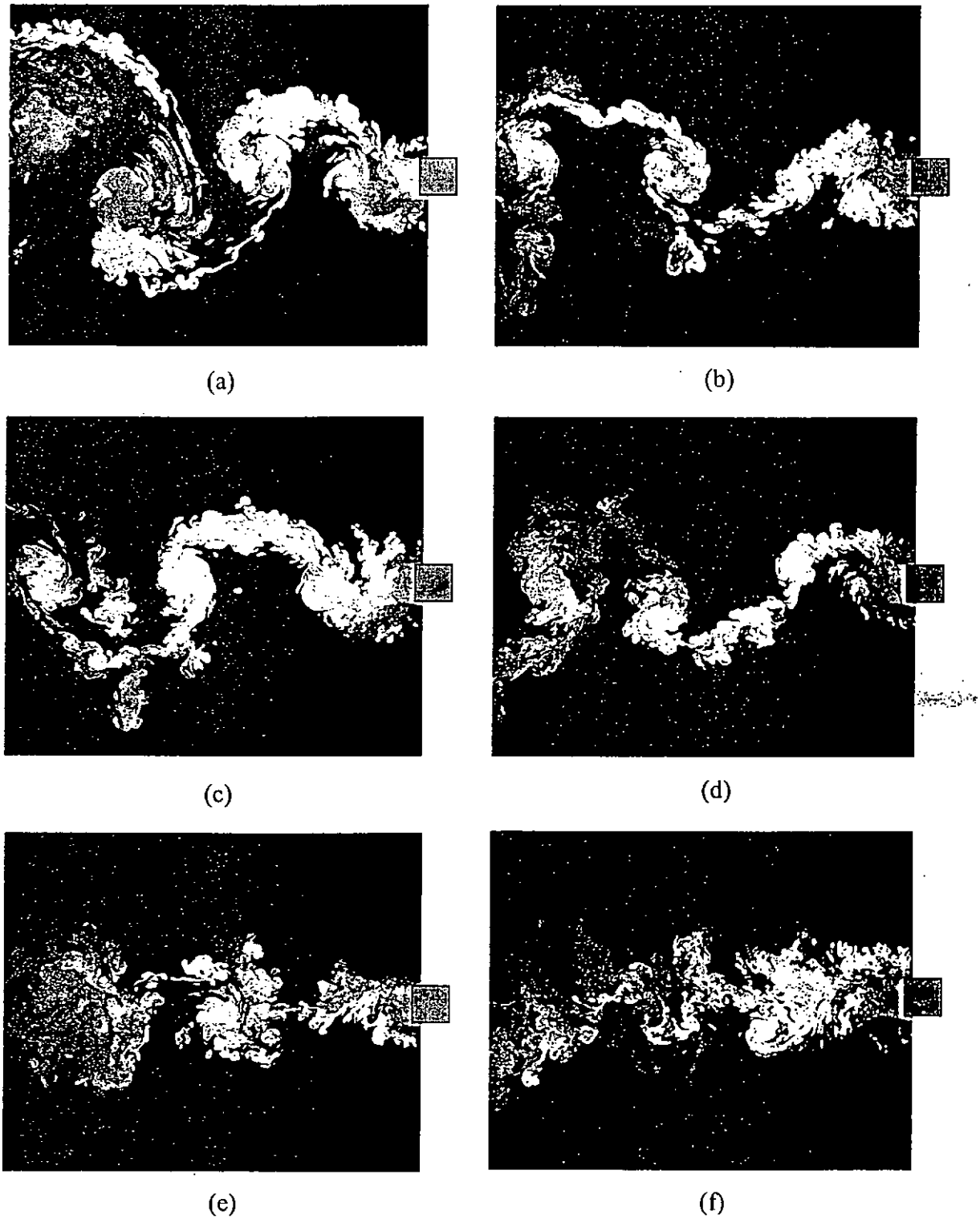

Figure 6-11 Typical photographs from flow visualization under different control schemes: (a) unperturbed; (b) u_Control; (c) ε_y_Control ; (d) Y_Control; (e) u + ε_y_Control; (f) u + Y_Control. Re = 6700.

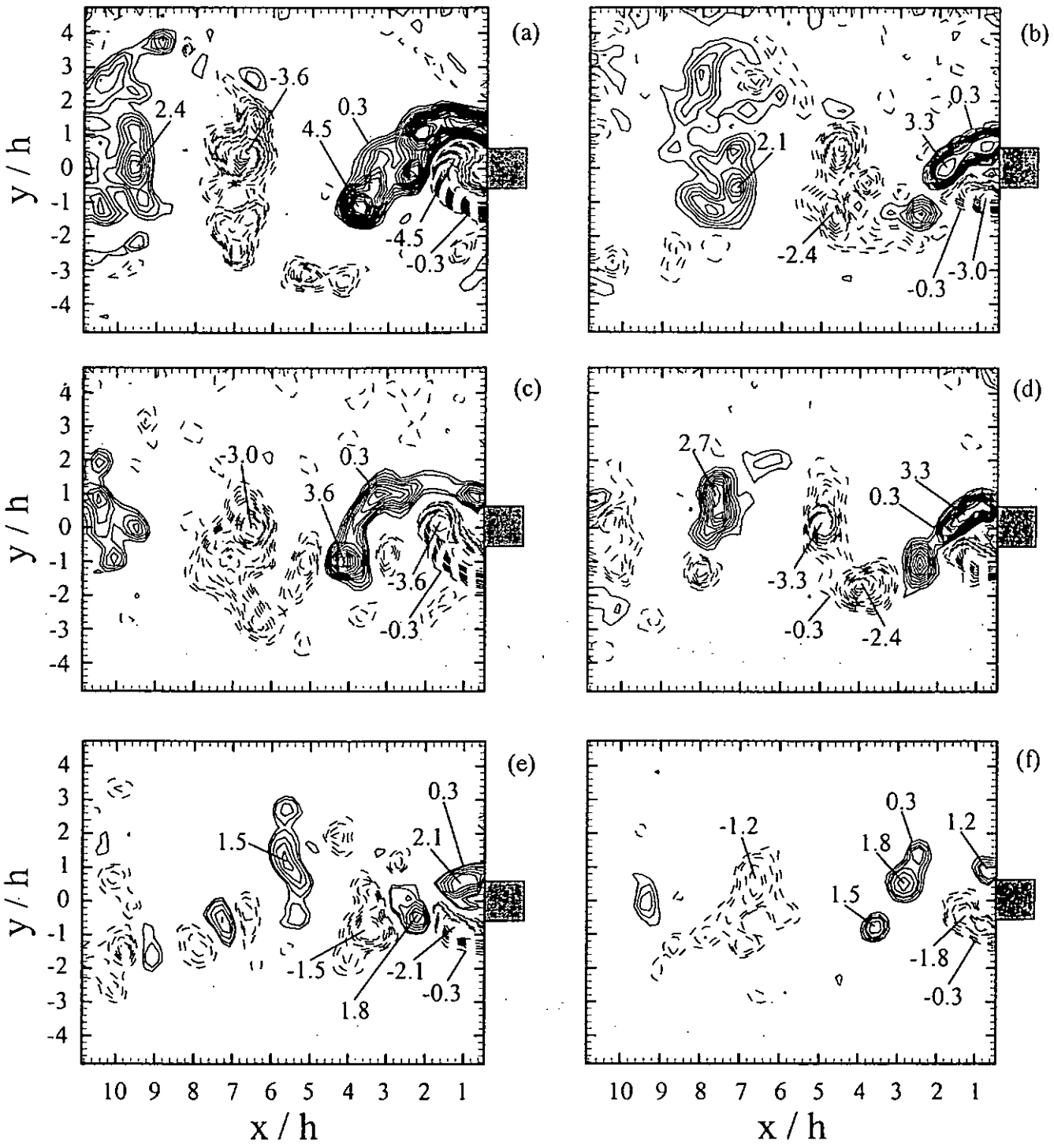

Figure 6-12 PIV measured iso-contours of spanwise vorticity $\omega_z^* = \omega_z h / U_\infty$ under different control schemes: (a) unperturbed; (b) u_Control; (c) ε_y_Control ; (d) Y_Control; (e) u + ε_y_Control; (f) u + Y_Control. Re = 6700.

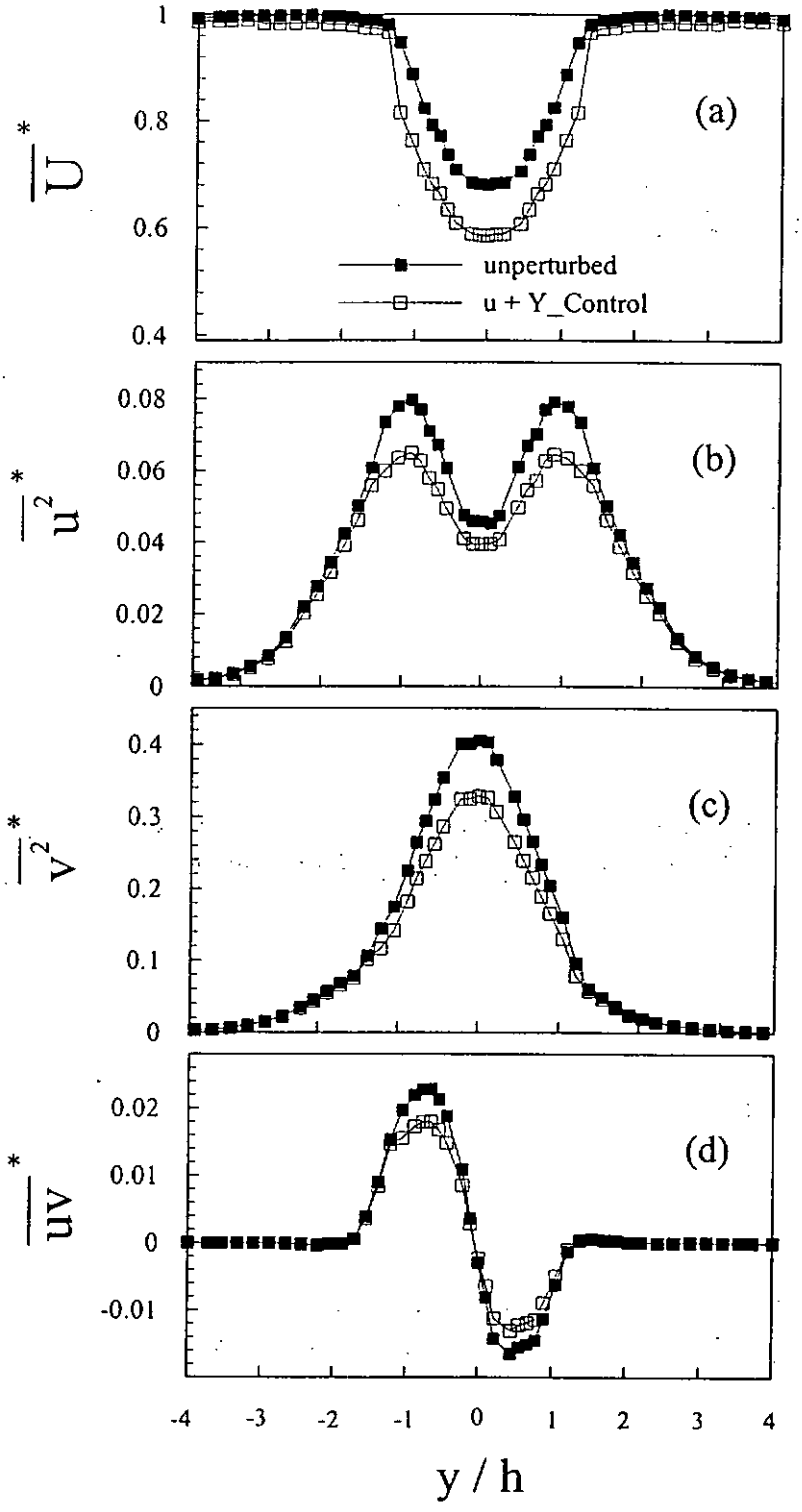

Figure 6-13 Cross-flow distribution of mean velocity and Reynolds stresses at $x/h = 3$ with and without control: (a) $\overline{U}^*$, (b) $\overline{u^2}^*$, (c) $\overline{v^2}^*$, (d) $\overline{uv}^*$. Re = 6700.

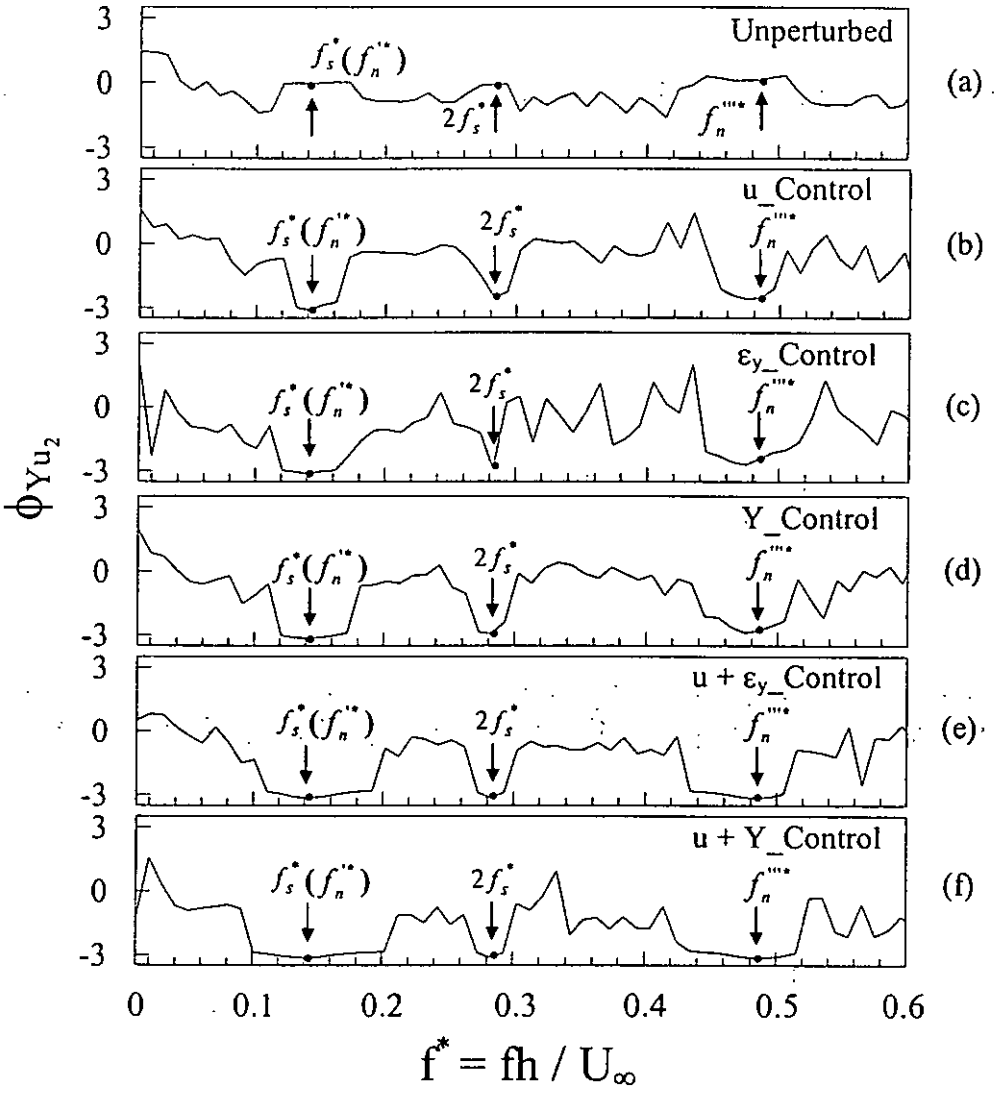

Figure 6-14 Phase shift ϕ_{Yu_2} between structural vibration (Y) and fluctuating streamwise flow velocity (u_2) under different control schemes. Re = 6700.

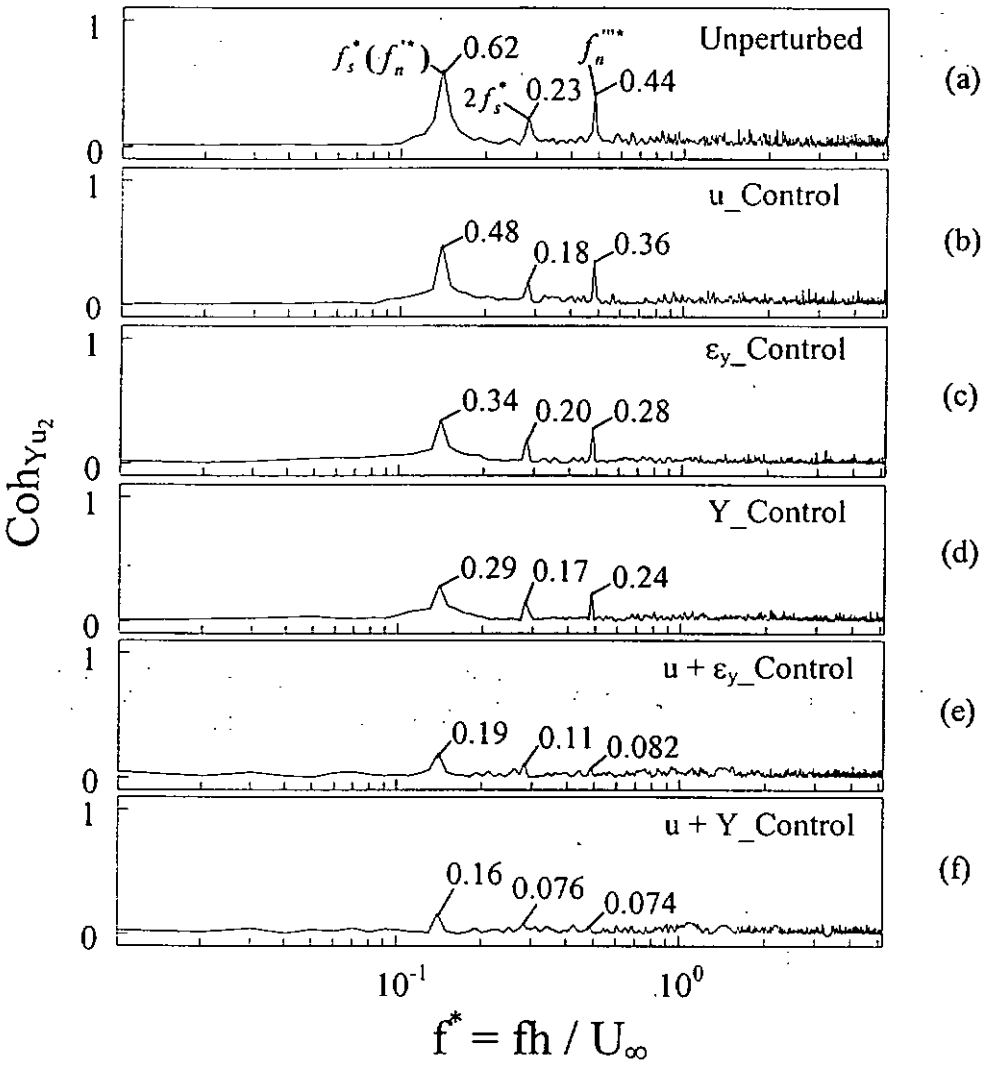

Figure 6-15 Spectra coherence (Coh_{Yu_2}) between structural vibration (Y) and fluctuating streamwise flow velocity (u_2) under different control schemes. Re = 6700.

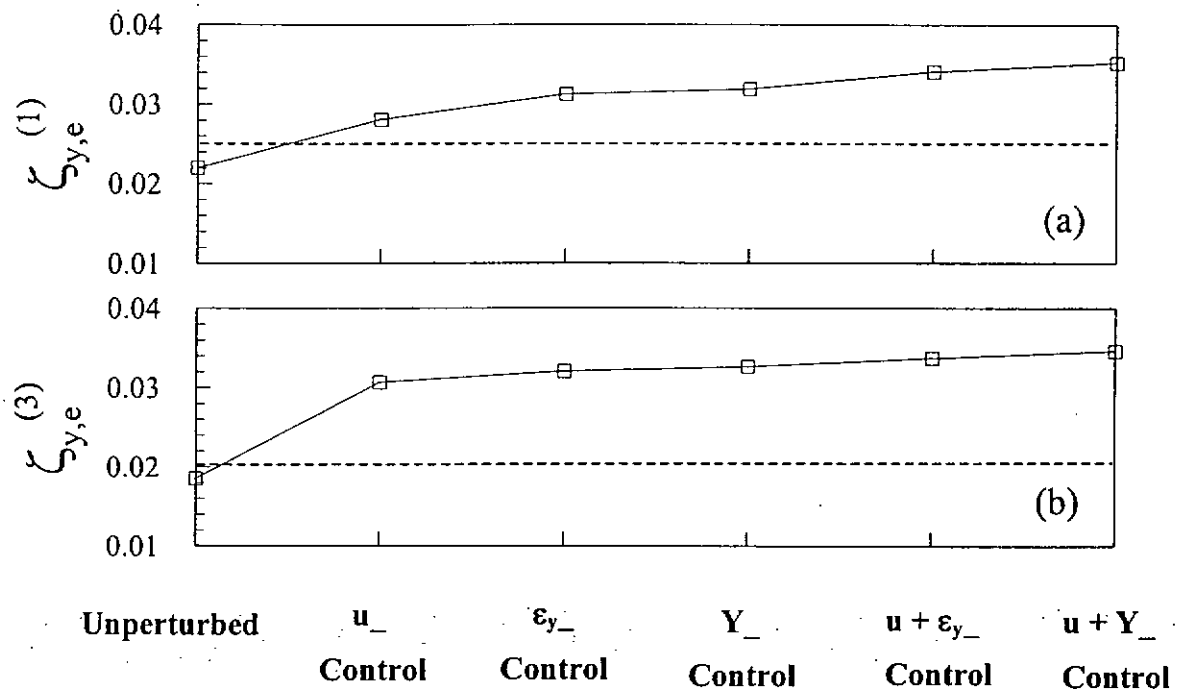

Figure 6-16 Effect of closed-loop control on the effective damping ratios in the y direction associated the first and third modal oscillation frequencies: (a) $\zeta_{y,e}^{(1)}$; (b) $\zeta_{y,e}^{(3)}$. The dash line denotes the structural damping ratio $\zeta_{y,s}^{(k)}$ measured without flow. Re = 6700.

CHAPTER 7

CONCLUSIONS AND RECOMMENDATIONS

7.1 General Conclusions

When a two-dimensional bluff body is subject to a cross flow, vortex shedding from the structures creates fluid excitation forces, which in turn causes the structure to vibrate. The resultant structural motion influences the flow field, giving rise to nonlinear fluid-structure coupling. In practice, people often pursue desired changes in vortex shedding or vortex-induced structural vibration to satisfy the actual requirement of engineering. Literature review shows a need of fundamental research in several aspects, such as a simultaneous control of both flow and flow-induced structural vibration, control of flexible structure vibrations in cross flow, investigations on various sensing schemes and feasibility of using advanced smart sensors/actuators. These issues motivated the present research, in which the active control of fluid-structure interaction on square cylinders in a cross flow has been experimentally investigated. The whole work underwent five stages.

1). A novel technique, referred to as perturbation technique, was established. The perturbed action to flow was based on an advanced piezoceramic THUNDER actuator. The superiority of THUNDER over conventional piezoelectric actuators was

discussed and its installation method was described. Major experimental facilities used through the thesis, such as PIV and LDA, were briefed for those unfamiliar.

2). The open-loop control of the resonant fluid-structure interaction on a flexible-supported rigid cylinder in a cross flow was experimentally studied using the proposed perturbation technique. Activated by a sinusoidal wave with controllable frequency and amplitude, three THUNDER actuators, embedded underneath the surface of the cylinder, produced a periodic perturbation on the cylinder surface and thus the fluid field, which altered the interactions between synchronizing cylinder motions and vortex shedding. Subsequently, both vortex shedding and its induced cylinder vibration were modified simultaneously. The perturbation effect on structural vibration and vortex strength was shown using several techniques including flow visualization, PIV, laser vibrometer and hot wire, to measure. The perturbed fluid-structure interaction was investigated based on a simultaneous measurement of flow and structural vibration using laser vibrometer and hot wire. Meanwhile, the variation in the cross flow distribution of Reynolds stresses was also measured using a two-component LDA system.

3). To further improve the control performance obtained in the open-loop control and reveal the underlying physics of flow-structure interaction under external perturbation, a closed-loop control system based on a PID controller was implemented. Three control schemes, utilizing feedback signals from flow, from the structural vibration or a combination of both, were considered and compared. To understand the underlying physics, changes in spectral phase and coherence between flow and structural vibration due to the deployment of the control were investigated, along with the varying fluid damping of the fluid-structure system, which was

evaluated from structural oscillation signals using an auto-regressive moving average (ARMA) technique.

4). In order to understand the intrinsic relation between the perturbation and flow field, the closed-loop manipulation of wake from a fix-supported rigid cylinder was experimentally investigated. A closed-loop control system deploying a simplified PID controller was implemented. Tuned at one Re, the effectiveness of the controller was assessed in a range of Re to examine its robustness. The fluctuating lift and drag forces on the cylinder were measured using load cells. Together with the measurement of the perturbation movement, the relationship between the perturbation and flow modification was examined in detail.

5). The closed-loop control technique was finally extended to a fix-supported flexible cylinder under both the resonance and non-resonance conditions. Five control schemes were considered and compared, which utilized feedback signals from streamwise fluctuating flow velocity u, lateral structural vibration Y, dynamic strain ε_y caused by the vibration, or a combination of these responses. These signals were measured using a hot wire, a laser vibrometer and an optical fiber Bragg grating (FBG) sensor, respectively. The control performances on the structural oscillation were evaluated in both time and frequency domain of Y, ε_y and u. In order to understand the underlying physics, the flow behind the cylinder was documented using a number of techniques, including PIV, flow visualization and a two-component LDA. The spectral phase and coherence between u and Y, along with the varying damping of the fluid-structure system under the control, were discussed in detail.

Present work led to the following major conclusions:

1) The so-called perturbation technique proved to be very effective in controlling the vortex shedding and vortex induced vibration of a cylinder in a cross flow. The essence of the technique was to generate a local perturbation on the cylinder surface to perturb the interaction between the flow and structural vibration. The THUNDER actuator was found to perfectly fulfill the requirement, due to its appealing characteristics such as high displacement range, high load-bearing capacity and small dimensions. A proper installation was crucial to ensure a maximum performance of the actuators.

2) Both vortex shedding and vortex-induced vibration, irrespective of the stiffness, boundary conditions or vibration regime (resonance or non-resonance) of the cylinder, were successfully and simultaneously controlled using the perturbation technique along with an active control system.

In case of open-loop control, the resonant interactions between vortex shedding and structural vibration were sensitive to the perturbation frequency (f_p^*). As f_p^* fell within the synchronization range (0.11 ~ 0.26 or $0.8 f_n'$ ~ $2 f_n'$) of the fluid-cylinder system where $f_n' = f_s$, the spectral coherence at f_s, vortex strength and drag coefficient were substantially increased, especially at $f_p^* = 0.13$, showing the great enhancement of the synchronization. When f_p^* was outside the synchronization range, however, the three quantities and maximum structural displacement were subject to a significant decrease, especially at $f_p^* = 0.1$, indicating the effective impairment of the resonance. The perturbation effect persisted up to $x / h \approx 25$.

When the closed-loop control was deployed, a proper tuning of the controller parameters ensured a systematic suppression of vortex shedding and structural vibration. A suitable choice of the feedback signal was crucial in determining the effectiveness of the control. Comparing the one-element schemes using feedback signals from individual flow or structural vibration with two-element schemes using feedback signals from the combination of both, it was observed that two-element schemes reflected the non-linear fluid-structure interaction, therefore resulted in a maximum reduction in structural vibration, vortex strength and drag coefficient, although the least input energy was required.

3) The mechanism of the active control lied in a modification of the nature of fluid-structure interaction. Vortex-induced vibration originated from fluid excitation forces, which were created by vortex shedding from a bluff body. The forces caused the structure to vibrate. The resultant structural vibrations might in turn influence the flow field, giving rise to fluid-structure coupling. The proposed control technique effectively turned the in-phased vortex shedding and structural vibration into the anti-phased and subsequently their correlation was diminished. This phenomenon happened at all dominant frequencies, e.g. f_s^*, $2f_s^*$, $f_n'^*$, and $f_n''''^*$ with a resonant flexible cylinder. This was accompanied by a significant increase in the effective damping ratio of the flow-structure system, implying an enhanced dissipation of vortex shedding and structural vibration energies. As a result, both vortex strength and structural vibration amplitude were significantly reduced. From another point of view, the control induced by the perturbation technique also changed

the interrelationship between the surface perturbation force, F_p, and the force, F_f, of the cylinder acting on fluid that was associated with vortex shedding. When the two forces were anti-phased, vortex strength, fluctuating lift and drag coefficients and mean drag coefficient were greatly weakened. When they were in-phased, F_p and F_f re-enforced each other, which enhanced significantly the formation of vortex shedding.

4) The proposed technique, together with a PID controller, possessed a certain degree of robustness. Tuned under one Re, it was demonstrated to be effective over a range of Re.

7.2 Recommendations

This thesis points to a great potential of the perturbation technique for vortex shedding and vortex-induced vibration control in engineering applications. More specifically, the following areas are worthy investigating in the future:

1. Suppression of aerodynamic-borne noise from fluid-structure interaction, e.g. vortex shedding impinging on hard surfaces in cascade structures in flow.
2. Improvement of control performance using more advanced adaptive controllers, such as μ-synthesis and neural network.
3. A deeper understanding of the underlying physics through numerical simulations.
4. Implementation of the technique in real engineering products by investigating other types of actuators to make the whole system easier and less intrusive in its installation, and more reliable in its performance.

APPENDIX

EXPERIMENTAL RESULTS OF CLOSED-LOOP CONTROL OF VORTEX-INDUCED VIBRATION ON A FLEXIBLE CYLINDER AT OCURRENCE OF NON-RESONANCE CASE

Table A-1 Optimal $\widetilde{P}_q$ and $\widetilde{\phi}_q$ (q represents u_1 or Y) under different control schemes.

Control Scheme / Optimal Parameter	Re = 2800		Re = 8000	
	Y_Control	$u + Y$_Control	Y_Control	$u + Y$_Control
$\widetilde{P}_{u_1}$		3.5		4
$\widetilde{\phi}_{u_1}$		100°		120°
$\widetilde{P}_Y$	3	8	8	5
$\widetilde{\phi}_Y$	120°	95°	144°	80°

Table A-2 Reduction in percentage of Spectra coherence (Coh_{Yu_2}) between structural vibration (Y) and fluctuating streamwise flow velocity (u_2) for non-resonance case under Y_Control and u + Y_Control, respectively.

Re \ Control Scheme		Y_Control	u + Y_Control
Re = 2800	$f_n^{'*}$	33%↓	58%↓
	$f_n^{''''*}$	53%↓	73%↓
	$f_s^{'*}$	21%↓	54%↓
	$f_s^{''''*}$	24%↓	57%↓
Re = 8000	$f_n^{'*}$	41%↓	66%↓
	$f_n^{''''*}$	65%↓	74%↓
	$f_s^{'*}$	35%	52%
	$f_s^{''''*}$	28%↓	57%↓

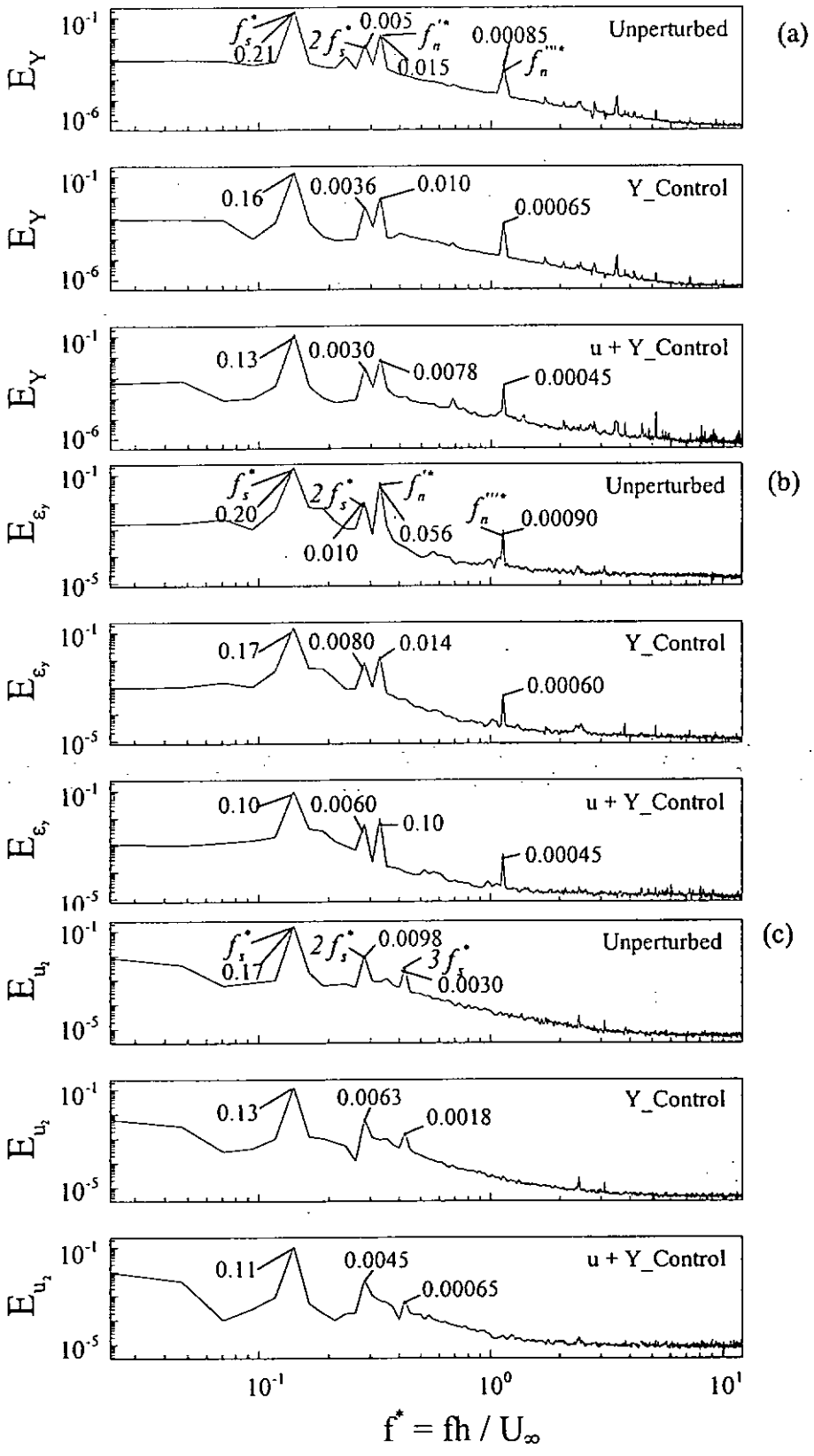

Figure A-1 Effect on power spectrum of: (a) Y, (b) ε_y, and (c) u_2 under the control schemes of Y_Control and u + Y_Control, respectively. Re = 2800.

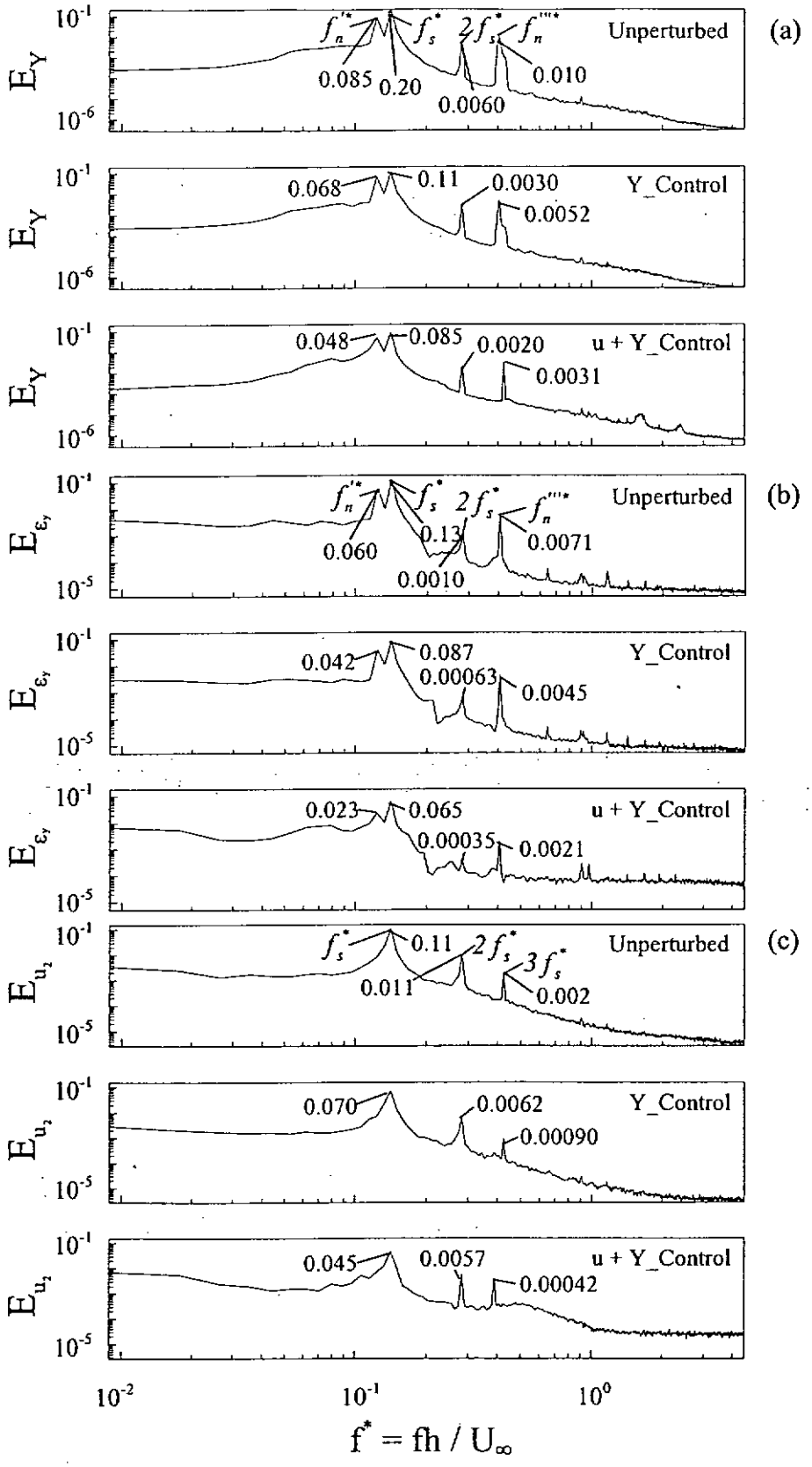

Figure A-2 Effect on power spectrum of: (a) Y, (b) ε_y, and (c) u_2 under the control schemes of Y_Control and u + Y_Control, respectively. Re = 8000.

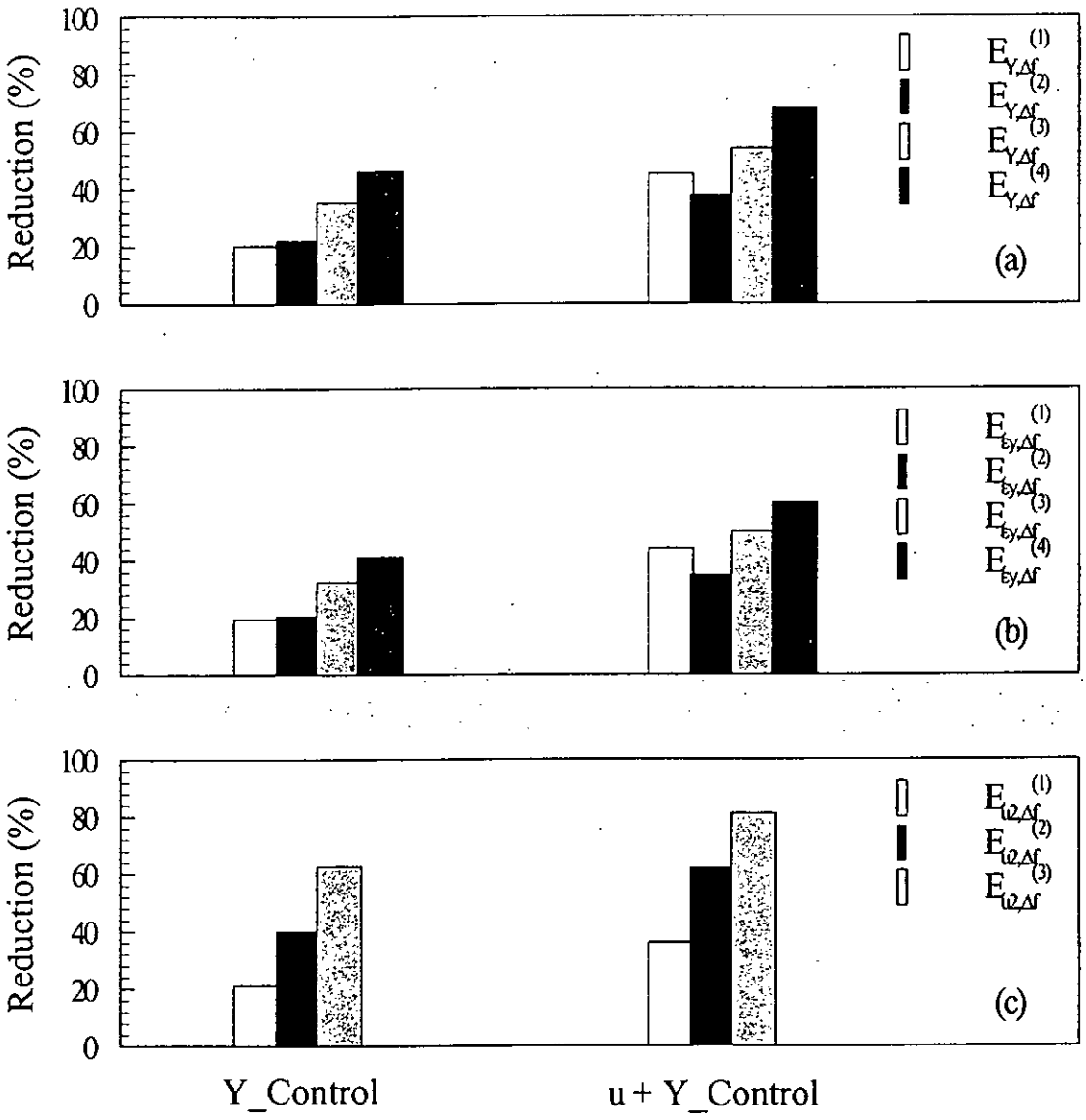

Figure A-3 Reduction in $E^{(n)}_{Y,\Delta f}$, $E^{(n)}_{\varepsilon_y,\Delta f}$ and $E^{(n)}_{u_2,\Delta f}$ (n = 1, 2, 3, 4). (a) Y; (b) ε_y; and (c) u_2. Re = 2800.

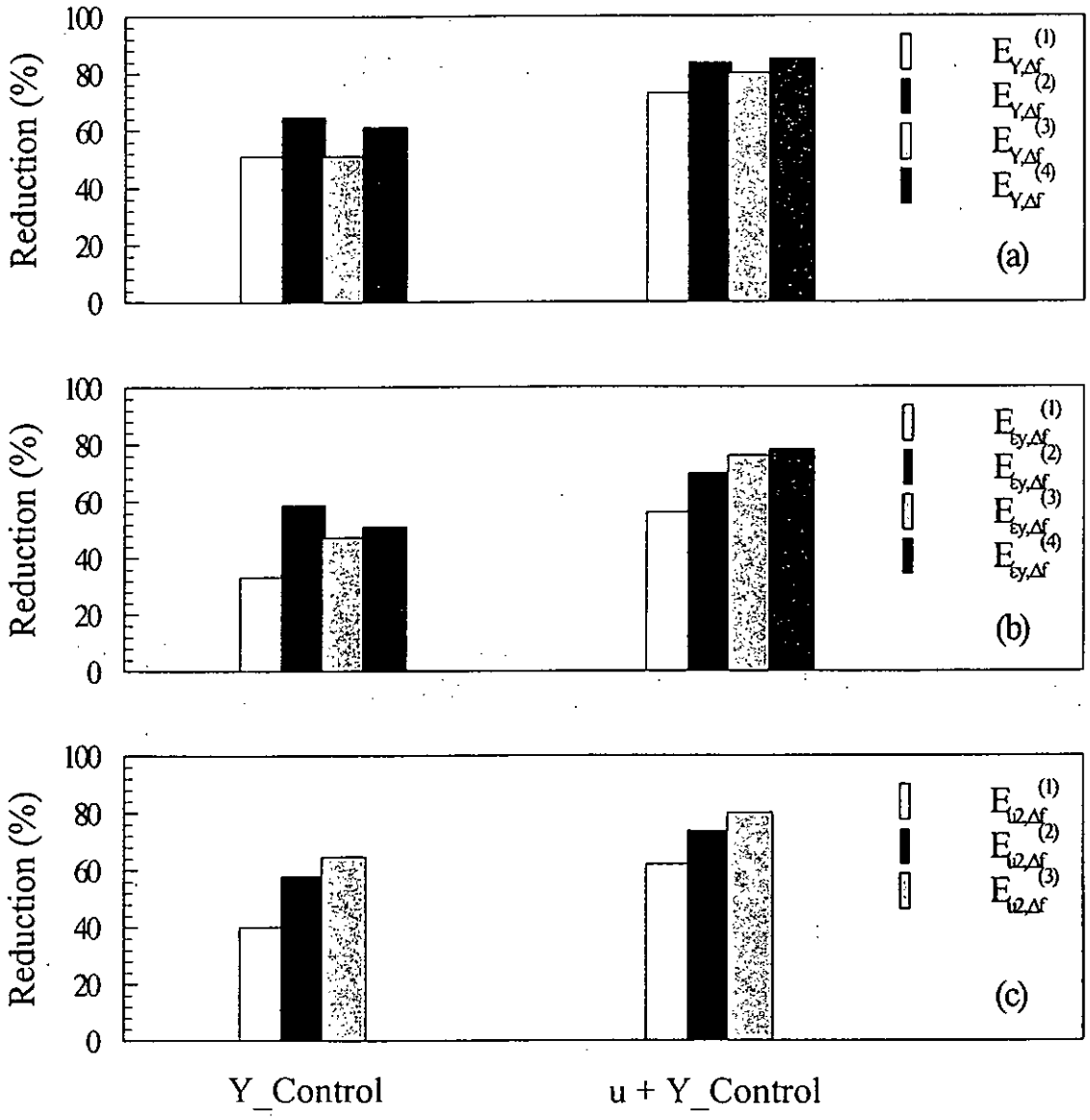

Figure A-4 Reduction in $E^{(n)}_{Y,\Delta f}$, $E^{(n)}_{\varepsilon_y,\Delta f}$ and $E^{(n)}_{u_2,\Delta f}$ (n = 1, 2, 3, 4). (a) Y; (b) ε_y; and (c) u_2. Re = 8000.

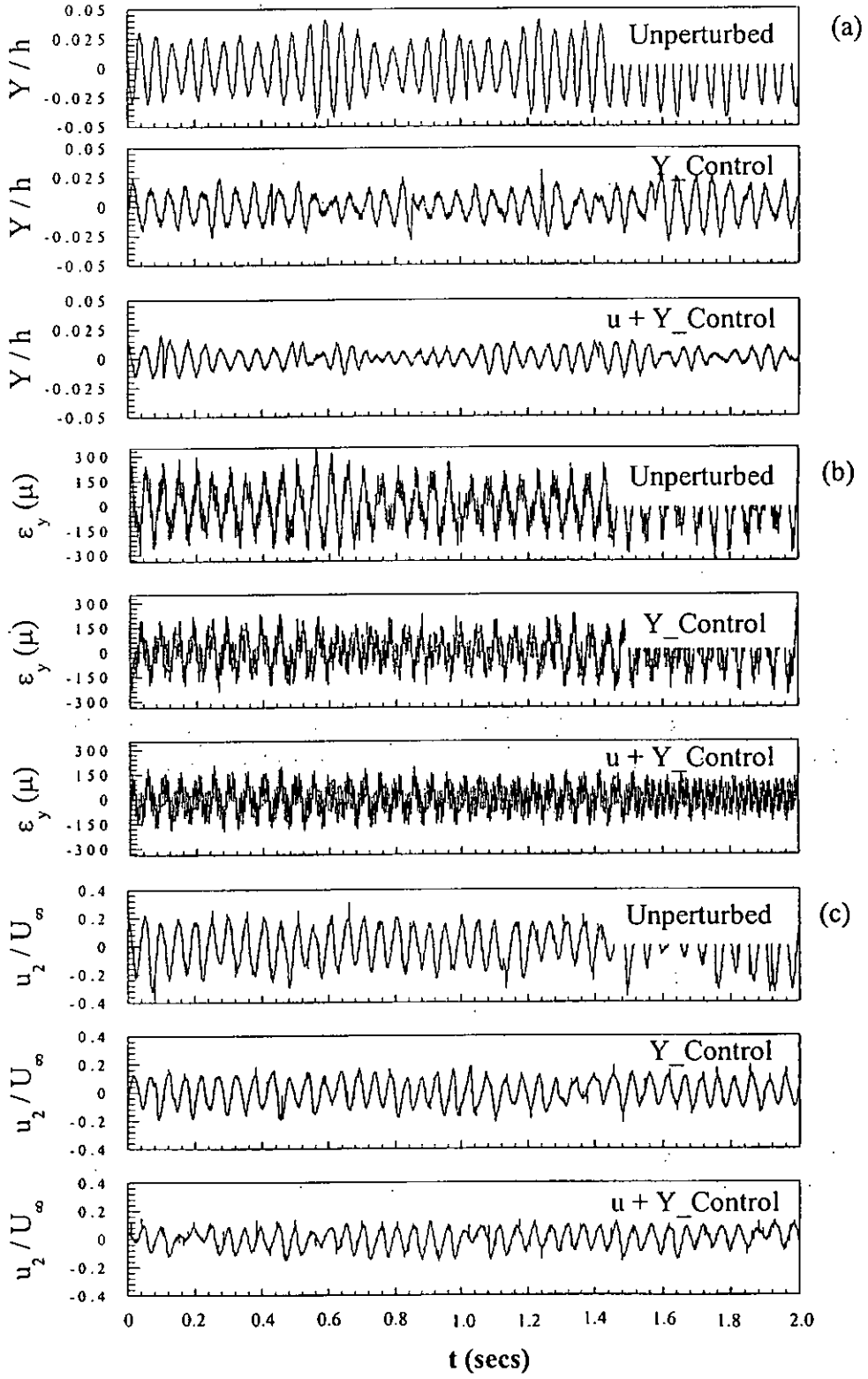

Figure A-5 Typical time histories under *Y*_Control and u + *Y*_Control, respectively: (a) Y; (b) ε_y; (c) u_2. Re = 2800. The time origin was arbitrary.

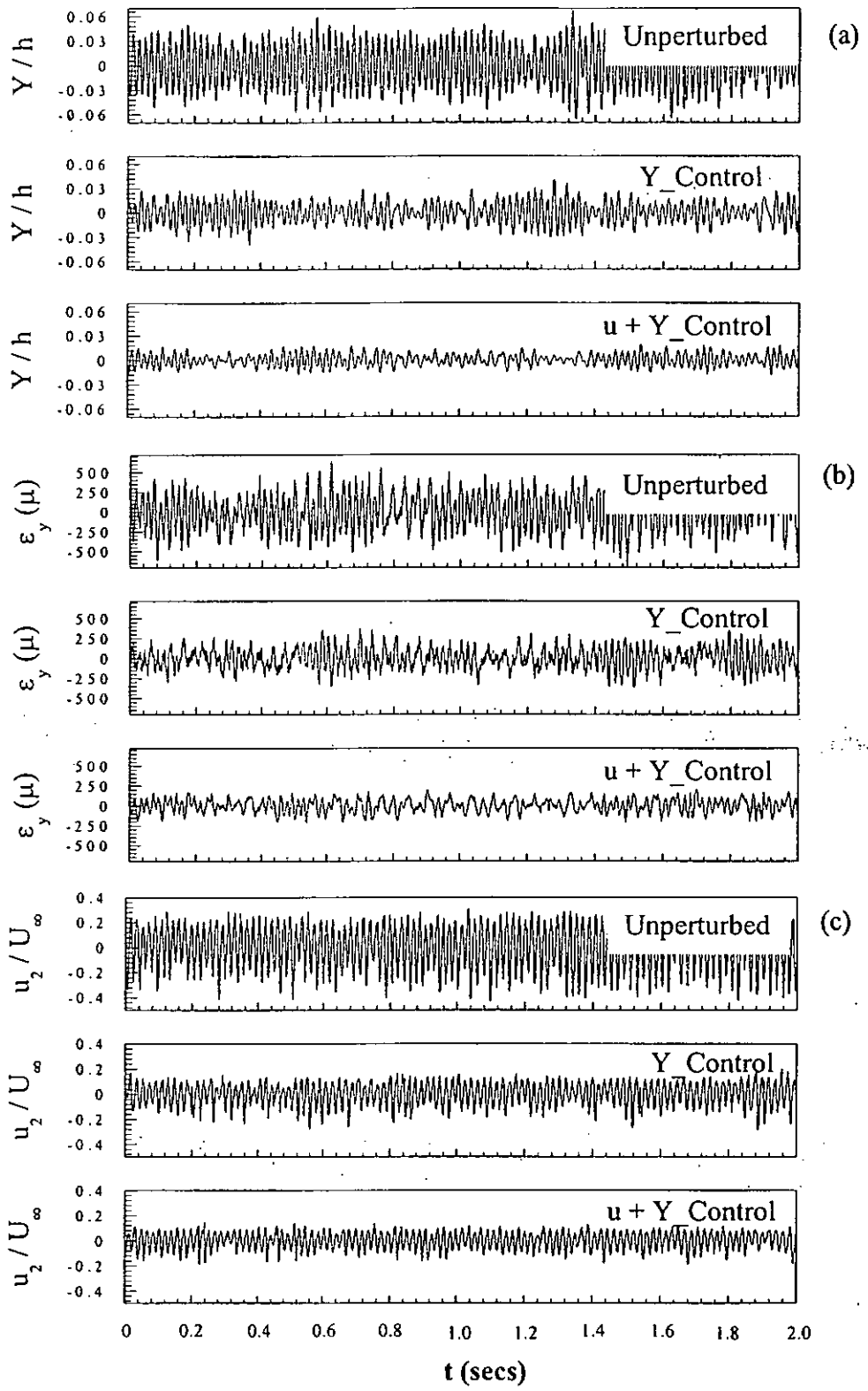

Figure A-6 Typical time histories *Y*_Control and u + *Y*_Control, respectively: (a) Y; (b) ε_y; (c) u_2. Re = 8000. The time origin was arbitrary.

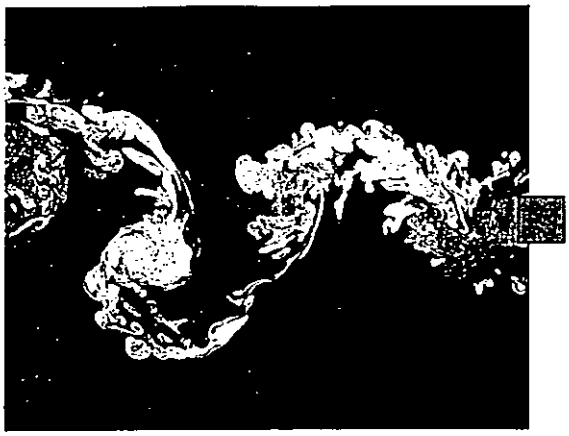

(a)

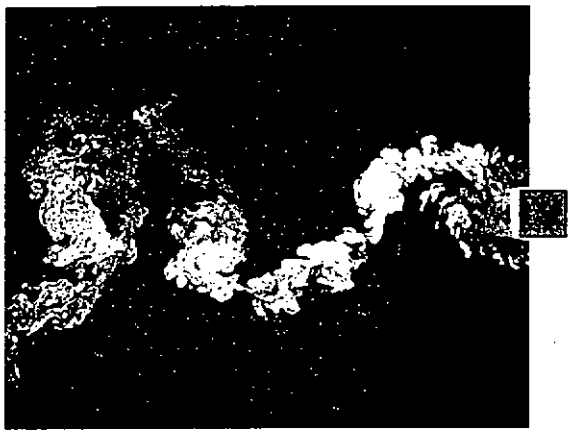

(b)

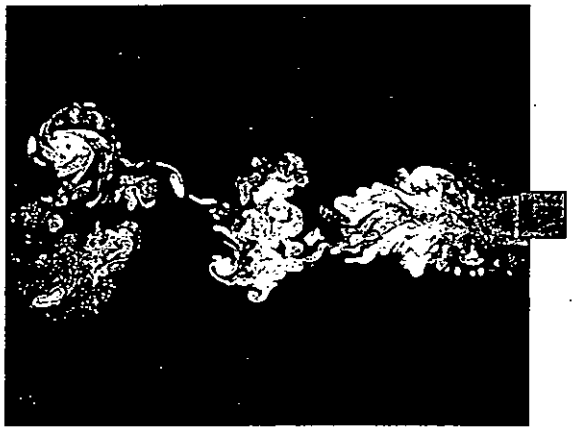

(c)

Figure A-7 Typical photographs from flow visualization with and without control: (a) unperturbed; (b) *Y*_Control; (c) u + *Y*_Control. Re = 2800.

(a)

(b)

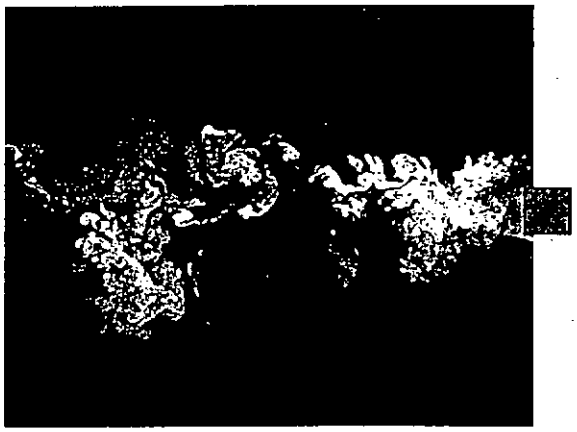

(c)

Figure A-8 Typical photographs from flow visualization with and without control: (a) unperturbed; (b) *Y*_Control; (c) *u* + *Y*_Control. Re = 8000.

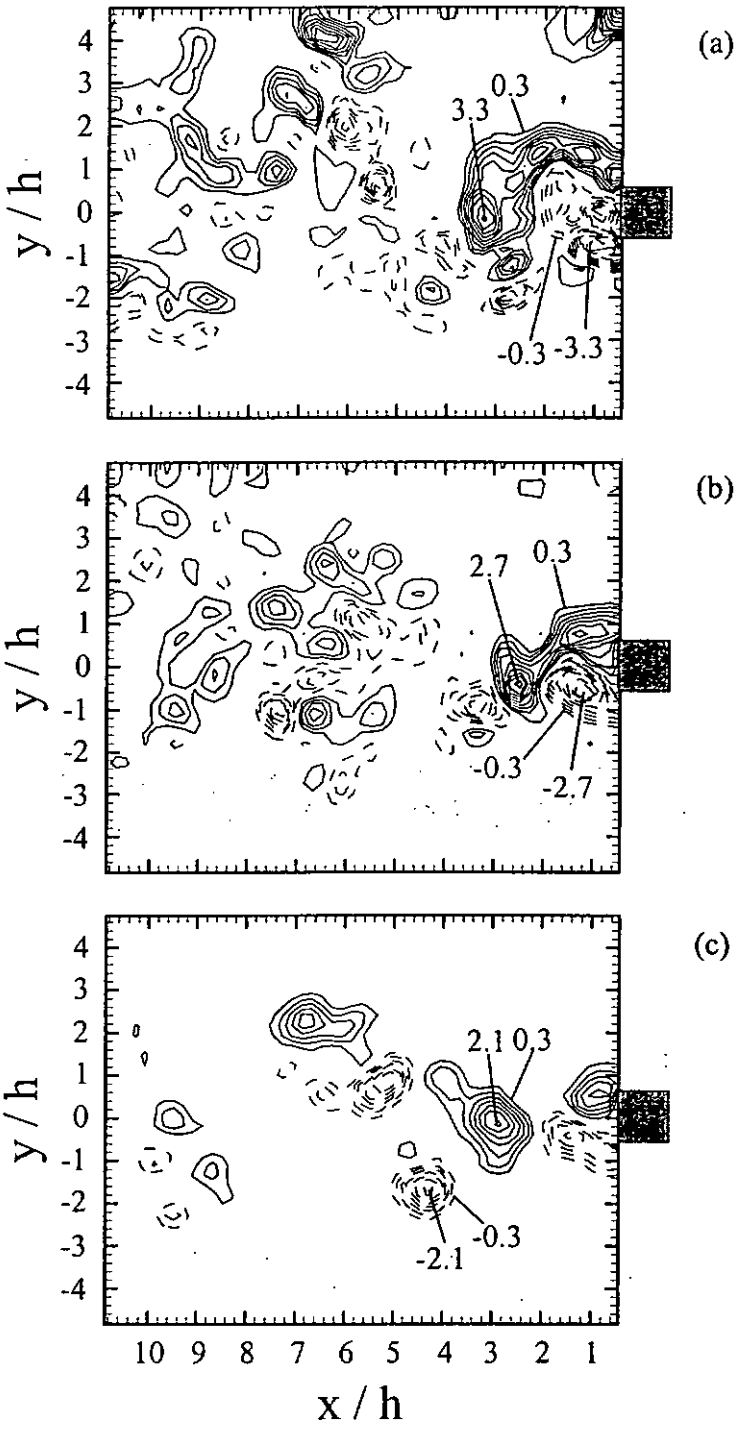

Figure A-9 PIV measured iso-contours of spanwise vorticity $\omega_z^* = \omega_z h / U_\infty$ with and without control: (a) unperturbed; (b) *Y*_Control; (c) *u* + *Y*_Control. Re = 2800.

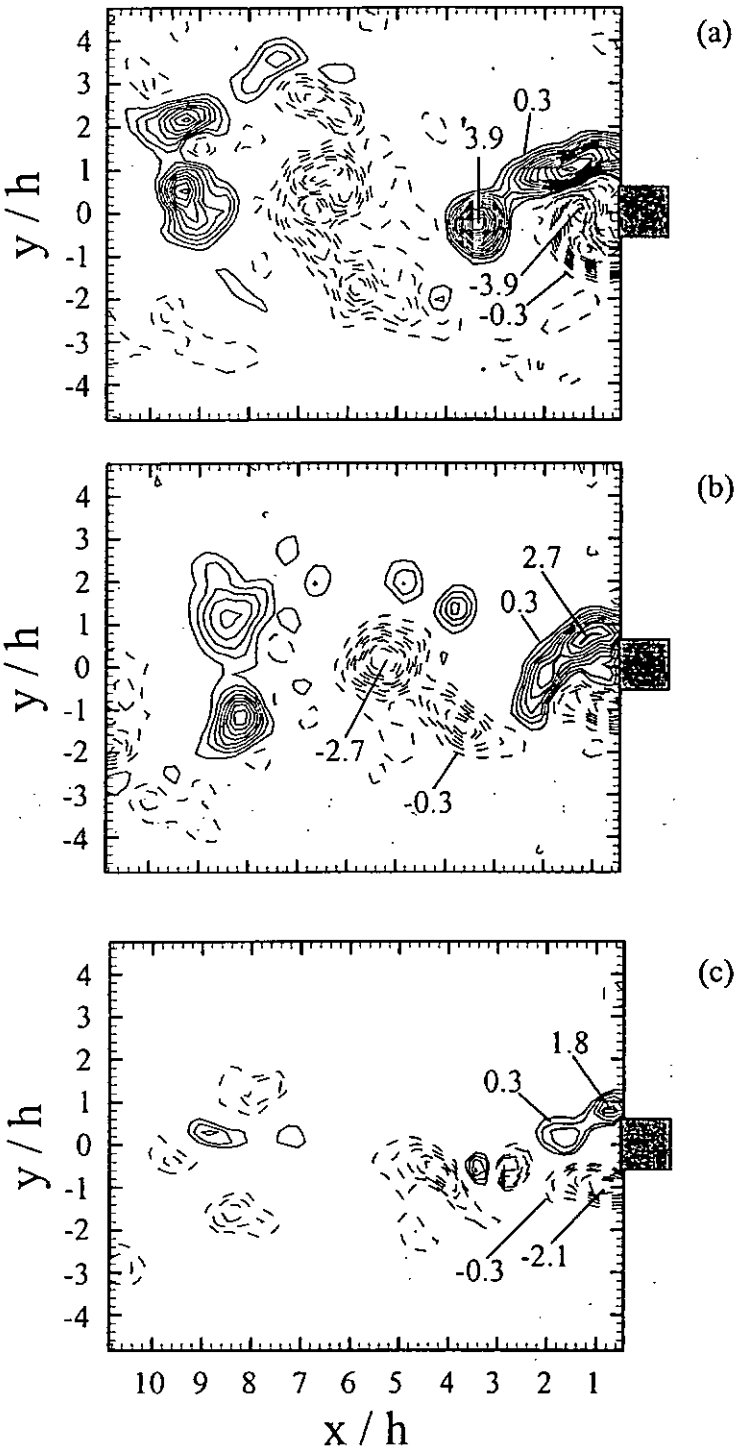

Figure A-10 PIV measured iso-contours of spanwise vorticity $\omega_z^* = \omega_z h / U_\infty$ with and without control: (a) unperturbed; (b) *Y*_Control; (c) *u* + *Y*_Control. Re = 8000.

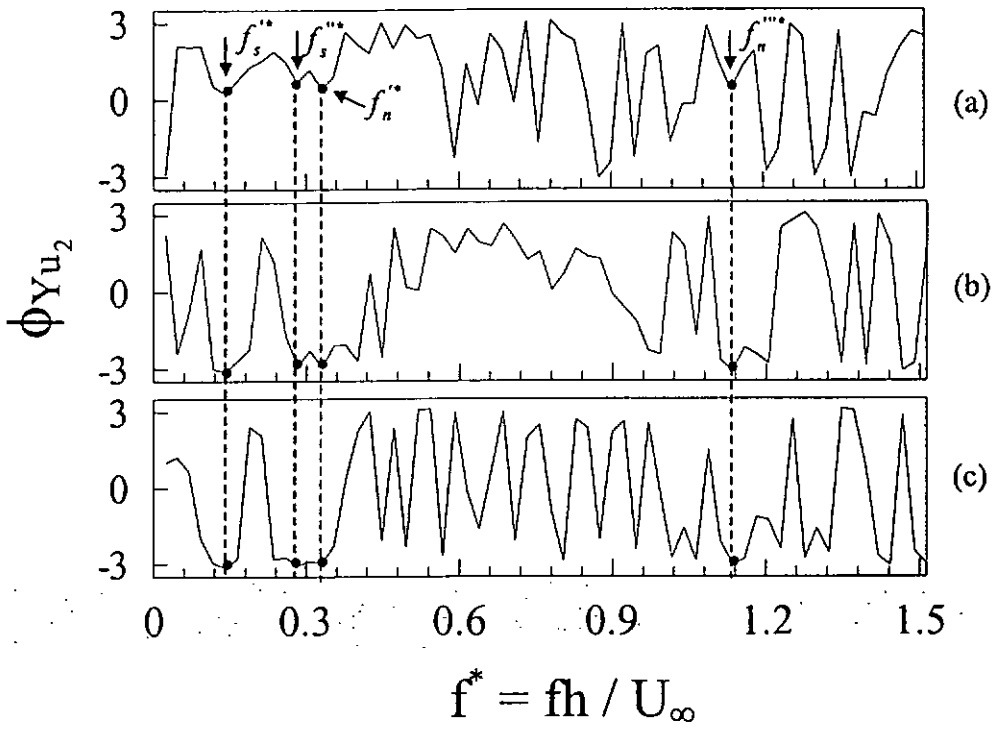

Figure A-11 Phase shift ϕ_{Yu_2} between structural vibration (Y) and fluctuating streamwise flow velocity (u_2) under different control schemes: (a) unperturbed; (b) Y_Control; (c) u + Y_Control. Re = 2800,

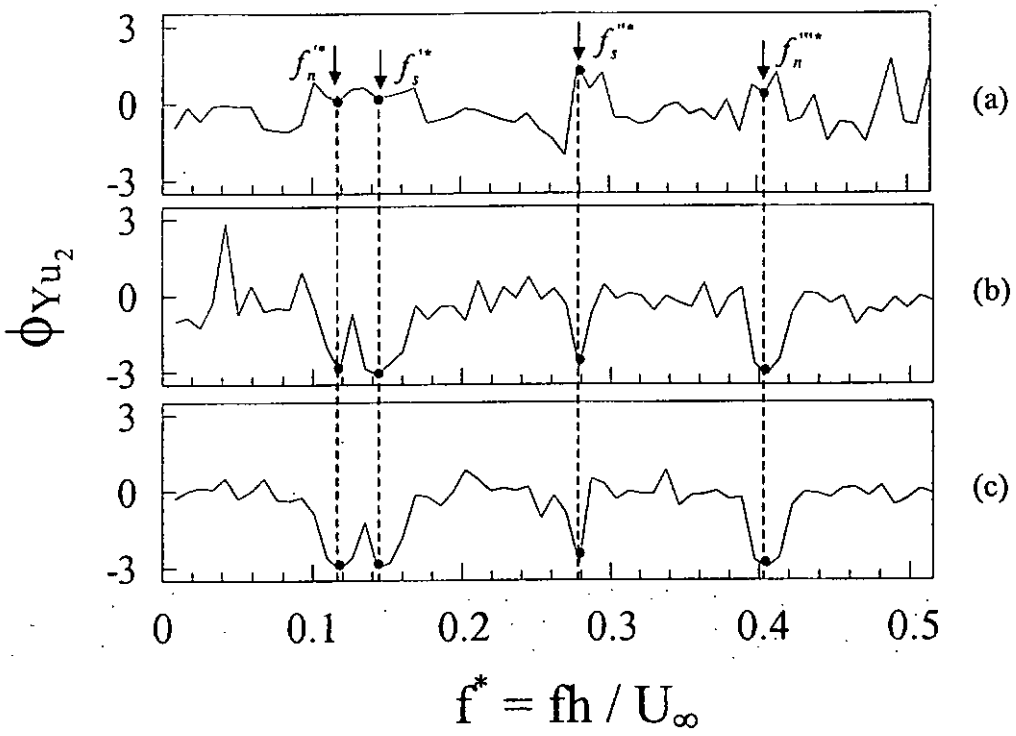

Figure A-12 Phase shift ϕ_{Yu_2} between structural vibration (Y) and fluctuating streamwise flow velocity (u_2) under different control schemes: (a) unperturbed; (b) Y_Control; (c) u + Y_Control. Re = 8000,

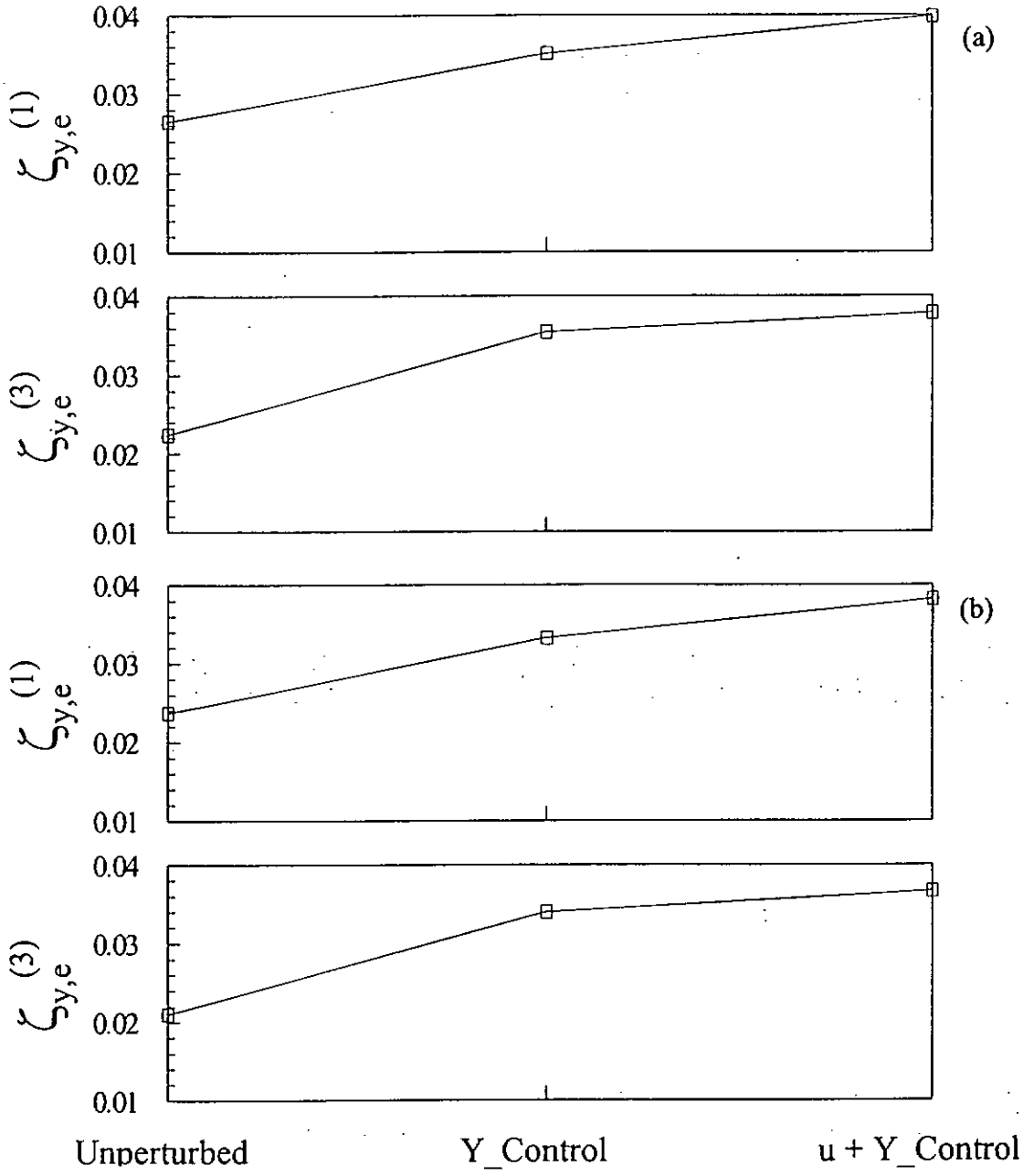

Figure A-13 Effect of closed-loop control on first and third mode cross flow effective damping ratios, i.e., $\zeta_{y,e}^{(1)}$ and $\zeta_{y,e}^{(3)}$: (a) Re = 2800; (b) Re = 8000.

References

Alam, M. M., Moriya, M., Takai, K. & Sakamoto, H. 2002 Suppression of fluid forces acting on two square prisms in a tandem arrangement by passive control of flow. *Journal of Fluids and Structures*, **16**, 1073-1086.

Antonia, R. A. & Rajagopalan, S. 1990 A comment on the determination of drag of a circular cylinder. *AIAA Journal*, **28**, 1833–1835.

Baz, A. & Ro, J. 1991 Active control of flow-induced vibrations of a flexible cylinder using direct velocity feedback. *Journal of Sound and Vibration*, **146**, 33-45.

Baz, A. & Kim, M. 1993 Active modal control of vortex-induced vibrations of a flexible cylinder, *Journal of Sound and Vibration*, **165**, 69-84.

Bearman, P. W. 1967 On vortex street wakes, *Journal of Fluid Mechanics*. **28**, 625-641.

Bearman, P. W. 1984 Vortex shedding from oscillating bluff bodies. *Annual Review of Fluid Mechanics*, **16**, 195-222.

Bera, J. C., Michard, M. & Sunyach, M. 2000 Changing lift and drag by jet oscillation: experiments on a circular cylinder with turbulent separation. *European Journal of Mechanics – B/Fluids*, **19**, 575-595.

Berger, E. 1967 Suppression of vortex shedding and turbulence behind oscillating cylinders. *Physics of Fluids*, **10**, 191-193.

Berger, E. & Wille, R. 1972 Periodic flow phenomena. *Annual Review of Fluid Mechanics*, **4**, 313-340.

Bishop, R. E. D. & Hassan, A. Y. 1964 The lift and drag forces on a circular cylinder in a flowing fluid. *Proceedings of the Royal Society Series A, London*, **277**, 51-75.

Blevins, R. D. 1985 The effect of sound on vortex shedding from cylinders. *Journal of Fluid Mechanics*, **161**, 217-237.

Blevins, R. D. 1990 *Flow-Induced Vibration*. Krieger Publishing Company, Malabar, Florida.

Bouak, F. & Lemay, J. 1998 Passive control of the aerodynamics forces acting on a circular cylinder. *Experimental Thermal and Fluid Science*, **16**, 112-121.

Brian, C. & Donald, C. 1983 An experimental study of entrainment and transport in the turbulent near wake of a circular cylinder. *Journal of Fluid Mechanics*, **136**, 321-374.

Cantwell, B. & Coles, D. 1983 An experimental study of entrainment and transport in the turbulent near wake of a circular cylinder. *Journal of Fluid Mechanics*, **136**, 321-374.

Chomaz, J. M., Huerre, P. & Redekopp, L. G. 1988 Bifurcations to local and global modes in spatially developing flows. *Physical Review Letters*, **60**, 25-28.

Copeland, B. M., Buckley, J. D., Bryant, R. G., Fox, R. L. & Hellbaum, R. F. 1999 THUNDER – an ultra-high displacement piezoelectric actuator. *NASA Langley Research Center*. Hampton, VA, 23681-0001.

Davies, M. E. 1976 A comparison of the wake structure of a stationary and oscillating bluff body, Using a conditional average technique. *Journal of Fluid Mechanics*, **75**, 209-231.

Den Hartog, J. P. 1947 *Mechanical Vibrations*. McGraw-Hill, New York.

Dorf, Richard C. & Bishop, Robert H. 1995 *Modern control systems*. Addison-Wesley Publishing Company, Inc., USA.

Every, M. J., King, R. & Weaver, D. S. 1982 Vortex-excited vibrations of cylinders and cables and their suppression. *Ocean Engineering*, **9**, 135-157.

Ffowcs Williams, J. E. & Zhao, B. C. 1989 The active control of vortex shedding. *Journal of Fluids and Structures*, **3**, 115-122.

Filler, J. R., Marston, P. L. & Mih, W. C. 1991 Response of the shear layers separating from the circular cylinder to small amplitude rotational oscillations. *Journal of Fluid Mechanics*, **231**, 481-499.

Franklin, G., Power, J. D. & Emami-Naeini Abbas 1991 *Feedback Control of Dynamics Systems*. Addison-Wesley Publication Company, California, USA, pp 107-147.

Franklin, G., Powell, J. D. & Workman, M. 1998 *Digital Control of Dynamics Systems*. Addison-Wesley Publication Company.

Fuchs, H. V., Mercker & Michel, U. 1979 Mode expansion of coherent structures in the wake of a circular disk. *Turbulent Shear Flows*, **2**, 282-296.

Fujisawa, N., Nakabayashi, T. 2002 Neural network control of vortex shedding from a circular cylinder using rotational feedback oscillations. *Journal of Fluids and Structures*, **16**,113-119.

Fujisawa, N. & Takeda, G. 2003 Flow control around a circular cylinder by internal acoustic excitation. *Journal of Fluids and Structures*, **17**, 903-913.

Gad-el-Hak, M. 2001 Flow control: The future. *Journal of aircraft*, **38**, 402-418.

Gau, C., Wu, J. M. & Liang, C. Y. 1999 Heat transfer enhancement and vortex flow structures over a heated cylinder oscillating in the crossflow direction. *Journal of heat transfer-transactions of the ASME*, **121**, 789-795.

Gerrard, J. H. 1966 Formation region of vortices behind bluff bodies. *Journal of Fluid Mechanics*, **25**, 401-413.

Ghee, T. A. & Leishman, J. G. 1992 Unsteady circulation control aerodynamics of a circular cylinder with periodic jet blowing. *AIAA journal*, **30**, 289-299.

Ghoniem, A. F. & Ng, K. K. 1987 Numerical study of the dynamics of a forced shear layer. *Physics of Fluids*, **30**, 706-721.

Goyder, H. G. D. 2002 Flow-induced vibration in heat exchangers. *Chemical Engineering Research and Design*, **80**, 226-232.

Gowda, B. H. L. 1975 Some measurements on the phenomenon of vortex shedding and induced vibrations of circular cylinders. *Deutsche Luft-und Raumfahrt Forschungsbericht*, No. 75-01.

Griffin, O. M. & Ramberg, S. E. 1975 On vortex strength and drag in bluff-body wakes. *Journal of Fluid Mechanics*, **69**, 721-728.

Griffin, O. M. & Ramberg, S. E. 1976 Vortex shedding from a cylinder vibrating in line with an incident uniform. *Journal of Fluid Mechanics*, **75**, 257-271.

Griffin, O. M. & Hall, M. S. 1991 Review-vortex shedding lock-on and flow control in bluff body wakes. *Journal of Fluids Engineering*, **113**, 526-536.

Guerout, F. M. & Fisher, N. J. 1999 Steam generator fretting-wear damage: A summary of recent findings. *Journal of Pressure Vessel Technology-Transactions of the ASME*, **121**, 304-310.

Gunzburger, M. D. & Lee, H. C. 1996 Feedback control of Kármán vortex shedding. *Journal of Applied Mechanics*, **63**, 828-835.

Henoch, C. W. & Stace, J. 1995 Experimental investigation of a salt water turbulent boundary layer modified by an applied streamwise magnetohydrodynamic body force. *Physics of Fluids*, 7, 1371-1383.

Horner, G. & Taleghani, B. 2001 Single axis piezoceramic gimbal. *Journal of Intelligent Material Systems and Structures*, **12**, 157-160.

Hsiao, F. B. & Shyu, J. Y. 1991 Influence of internal acoustic excitation upon flow passing a circular cylinder. *Journal of Fluids and Structures*, **5**, 427-442.

Hwang, J. J. & Chao, C. H. 2000 Passive control of convective transport phenomena utilizing an attached-detached rib-array. *Journal of Thermophysics and Heat Transfer*, **14**, 579-583.

Huang, X. Y. 1996 Feedback control of vortex shedding from a circular cylinder. *Experiments in Fluids*, **20**, 218-224.

Huerre, P. & Monkewitz, P. A. 1985 Absolute and convective instability in free shear layers. *Journal of Fluid Mechanics*, **159**, 151-168.

Huerre, P. & Monkewitz, P. A. 1990 Local and global instabilities in spatially developing flows. *Annual Review of Fluid Mechanics*, **22**, 473-537.

Hussain, A. K. M. F. & Hayakawa, M. 1987 Eduction of large-scale organized structures in a turbulent plane wake. *Journal of Fluid Mechanics*, **180**, 193-229.

Jaffe, B., Cook, W. R. & Jaffe, H. 1971 *Piezoelectric Ceramics*. Academic Press, New York.

James, S. W., Tatam, R. P., Fuller, S. R. & Crompton, C. 1999 Monitoring transient strains on a gun barrel using fibre Bragg-grating sensors. *Measurement Science & Technology*, **10**, 63-67.

Jayachandran, V., Meyer, N. E., Westervelt, M. A. & Sun, J. Q. 1999 Piezoelectrically driven speakers for active aircraft interior noise suppression. *Applied Acoustics*, **57**, 263-277.

Jin, W., Zhou, Y., Chan, P. K. C. & Xu, H. G. 2000 A fibre-optic grating sensor for the study of flow-induced vibrations. *Sensors and Actuators*, **79**, 36-45.

Kersey, A. D., Davis, M. A., Patric, H. J., LeBlanc, M., Koo, K. P., Askins, C. G., Putnam, M. A. & Friebele, E. J. 1997 Fiber grating sensors. *Journal of Lightwave Technology*, **15**, 1442-1462.

Kim, S. J. & Lee, C. M. 2000. Investigation of the flow around a circular cylinder under the influence of an electromagnetic field. *Experiment in Fluids*, **28**, 252-260.

Knisely, C. W. 1990 Strouhal numbers of rectangular cylinders at incidence – A review and new data. *Journal of Fluids and Structures*, **4**, 371–393.

Konstantinidis, E., Balabani, S. & Yianneskis, M. 2003 Relationship between vortex shedding lock-on and heat transfer-Implications for tube bundles in cross-flow. *Chemical Engineering Research and Design*, **81**, 695-699.

Koopman, G. H. 1967 The vortex wakes of vibrating cylinders at low Reynolds numbers. *Journal of Fluid Mechanics*, **28**, 501-512.

Lee, B. E. 1975 The effect of turbulence on the surface pressure field of a square prism. *Journal of Fluid Mechanics*, **69**, 263–282.

Lewit, M. 1992 Active control of dipole sound from cylinders. *Proceeding of DAGA '92*, Berlin, Germany.

Liepmann, H. W. & Nosenchuck, D. M. 1982 Active control of laminar-turbulent transition. *Journal of Fluid Mechanics*, **118**, 201-204.

Lyn, D. A. & Rodi, W. 1994 The flapping shear layer formed by flow separation from the forward corner of a square cylinder. *Journal of Fluid Mechanics*, **267**, 353-376.

Marouzé, J. P. & Cheng, L. 2002 A feasibility study of active vibration isolation using THUNDER actuators. *Smart Materials and Structures*, **11**, 854-862.

Min, C. H. & Choi, H. C. 1999 Suboptimal feedback control of vortex shedding at low Reynolds numbers. *Journal of Fluid Mechanics*, **401**, 123-156.

Mizrahi, V. & Sipe, J. E. 1993 Optical properties of photosensitive fibre phase gratings. *Journal of Lightwave Technology*, **11**, 1513-1517.

Morey, W. W., Ball, G. & Singh, H. 1996 Applications of fiber grating sensors, in: R.P. De Paula, J.W. Berthod III (Eds.), Fiber Optics and Laser Sensors XIV. *SPIE* **2839**, pp. 2-7.

Morgenthal, G. & McRobie, A. 2002 A comparative study of numerical methods for fluid structure interaction analysis in long-span bridge design. *Wind and Structures*, **5**, 101-114.

Naudascher, E. 1987 Flow-induced streamwise vibrations of structures. *Journal of Fluids and Structures*, **1**, 265-298.

Ongoren, A. & Rockwell, D. 1988 Flow structure from an oscillating cylinder. Part I. Mechanisms of phase shift and recovery in the near wake. *Journal of Fluid Mechanics*, **191**, 197-223.

Oster, D. & Wygnanski, I. 1982 The forced mixing layer between parallel streams. *Journal of Fluid Mechanics*, **123**, 91-130.

Ottino, J. M. 1989 *The kinematics of mixing: stretching, chaos, and transport*. Cambridge University Press, London.

Owen, J. C., Bearman, P. W. & Szewczyk, A. A. 2001 Passive control of viv with drag reduction. *Journal of Fluids and Structures*, **15**, 597-605.

Parker, R. 1966 Resonance effects in vortex shedding from parallel plates, some experimental observations. *Journal of Sound and Vibration*, **4**, 62-72.

Pettigrew, M. J. & Taylor, C. E. 2003 Vibration analysis of shell-and-tube heat exchangers: an overview - Part 1: flow, damping, fluidelastic instability. *Journal of Fluids and Structures*, **18**, 469-483.

Pinkerton, J. L. & Moses, R. W. 1997 A Feasibility study to control airfoil shape using THUNDER. *NASA Technical Memorandum* 4767.

Provansal, M., Mathis, C. & Boyer, L. 1987 Benard-von Kármán instability: transient and forced regimes. *Journal of Fluid Mechanics*, **182**, 1-22.

Protas, B. & Wesfreid, J. E. 2002 Drag force in the open-loop control of the cylinder wake in the laminar regime. *Physics of Fluids*, **14**, 810-826.

Ricciardelli, F. 2001 On the amount of tuned mass to be added for the reduction of the shedding-induced response of chimneys. *Journal of Wind Engineering and Industrial Aerodynamics*, **89**, 1539-1551.

Roussopoulos, K. 1993 Feedback control of vortex shedding at low Reynolds numbers. *Journal of Fluid Mechanics*, **248**, 267-296

Sakamoto, H., Haniu, H. & Kobayashi, Y. 1989 Fluctuating force acting on rectangular cylinders in uniform flow (on rectangular cylinders with fully separated flow). *Transactions of the Japan Society of Mechanical Engineers*, Series **B 55**, 2310-2317.

Sakamoto, H., Tan, K. & Haniu, H. 1991 An optimum suppression of fluid forces by controlling a shear layer separated from a square prism. *Journal of Fluid Engineering*, **113**, 183-189.

Sakamoto, H., Tan, K., Takeuchi, N. & Haniu, H. 1997 Suppression of fluid forces acting on a square prism by passive control. *Journal of Fluids Engineering-Transactions of the ASME*, **119**, 506-511.

Sarpkaya, T. 1979 Vortex-induced oscillations- A selected review. *Journal of Applied Mechanics*, **46**, 241-258.

Schumm, M. 1991 Experimentelle untersuchungen zum problem der absoluten und konvektiven instabilität in nachlauf zweidimensionaler stumpfer körper. Disseration T. U. Berlin(D 83) also Fortschrittsberichte VDI, Reihe 7, Strömungstechnik Nr. 196. VDI.

Sébastien, Caillaud, Emmanuel, de Langre & Franck, Baj 2003 Active vibration control for the measurement of fluidelastic effects. *Journal of Pressure Vessel Technology*, **125**, 165-170.

Shiels, D. & Leonard, A. 2001 Investigation of a drag reduction on a circular cylinder in rotary oscillation. *Journal of Fluid Mechanics*, **431**, 297–322.

Shimada, K. & Ishihara, T. 2002 Application of a modified k-ε model to the prediction of aerodynamics characteristics of rectangular cross-section cylinders. *Journal of Fluids and Structures*, **16**, 465-485.

Strommen, E. & Hjorth-Hansen, E. 2001 On the use of tuned mass dampers to suppress vortex shedding induced vibrations. *Wind and Structures*, **4**, 19-30.

Strykowsky, P. J. 1986 The control absolutely and convectively unstable shear flows. Ph.D. Thesis, Yale University, New Haven/U.S.A.

Sumner, D., Price, S. J. & Païdoussis, M. P. 2000 Flow-pattern identification for two staggered circular cylinders in cross-flow. *Journal of Fluid Mechanics*, **411**, 263-303.

Tani, J., Qiu, J. & Liu, Y. 1999 Robust control of vortex-induced vibration of a rigid cylinder supported by an elastic beam using μ-synthesis. *Journal of Fluids and Structures*, **13**, 865-875.

Tanida, Y., Okajima, A. & Watanabe, Y. 1973 Stability of a circular cylinder oscillating in a uniform flow or in a wake. *Journal of Fluid Mechanics*, **61**, 769-784.

Taylor, C. E. & Pettigrew, M. J. 2000 Random excitation forces in heat exchanger tube bundles. *Journal of Pressure Vessel Technology-Transactions of the ASME*, **122**, 509-514.

Tsutsui, T., Igarashi, T. & Nakamura, H. 2001 Drag reduction and heat transfer enhancement of a square prism. JSME International *Journal Series B-Fluids and Thermal Engineering*, **44**, 575-583.

Tokumaru, P. T. & Dimotakis, P. E. 1991 Rotary oscillation control of a cylinder wake. *Journal of Fluid Mechanics*, **224**, 77-90.

Unal, M. F. & Rockwell, D. 1988a On vortex formation for a cylinder. Part 1. The initial instability. *Journal of Fluid Mechanics* **190**, 491-512.

Unal, M. F. & Rockwell, D. 1988b On vortex formation from a cylinder. Part 2. Control by splitter plate interference. *Journal of Fluid Mechanics*, **190**, 513-529.

Valencia, A. & Paredes, R. 2003 Laminar flow and heat transfer in confined channel flow past square bars arranged side by side. *Heat and Mass Transfer*, **39**, 721-728.

Vickery, B. J. 1966 Fluctuating lift and drag on a long cylinder of square cross-section in a smooth and turbulent stream. *Journal of Fluid Mechanics*, **25**, 481-494.

Viswanath, P. R. 1996 Flow management techniques for base and afterbody drag reduction. *Progress in Aerospace Sciences*, **32**, 79-129.

Wang, Y., Haller, G., Banaszuk, A. & Tadmor, G. 2003 Closed-loop Lagrangian separation control in a bluff body shear flow model. *Physics of Fluids*, **15**, 2251-2266.

Ware, A. G. & Shah, V. N. 1988 Age-related degradation of boiling water-reactor vessel internals. *Nuclear Engineering and Design*, **133**, 49-62.

Warui, H. M. & Fujisawa, N.1996 Feedback control of vortex shedding from a circular cylinder by cross-flow cylinder oscillations. *Experiments in Fluids*, **21**, 49-56.

Williamson, C. H. K. & Roshko, A. 1988 Vortex formation in the wake of an oscillating cylinder. *Journal of Fluids and Structures*, **2**, 355-381.

Williams, David R., Mansy, Hussein & Amato, Cliff 1992 The response and symmetry properties of a cylinder wake subjected to localized surface excitation. *Journal of Fluid Mechanics*, **234**, 71-96.

Wilson, J. F. & Tinsley, J. C. 1989 Vortex load reduction: Experiments in optimal helical strake geometry for rigid cylinders. *ASME Journal of Energy Resources Technology*, **111**, 72-76.

Wolfe, D. & Ziada, S. 2003 Feedback control of vortex shedding from two tandem cylinders. *Journal of Fluids and Structures*, **17**, 579-592.

Wu, H. W. & Perng, S. W. 1999 Enhancement of heat transfer of mixed convection for heated blocks using vortex shedding generated by an oblique plate in a horizontal channel. *ACTA Mechanica*, **136**, 77-89.

Wygnanski, I., Oster, D., Fiedler, H. & Dziomba, B. 1979 On the perseverance of quasi-dimensional eddy-structure in a turbulent mixing layer. *Journal of Fluid Mechanics*, **93**, 325-335.

Yamane, T. & Orita, T. 1994 Relationship of pressure wave velocity to self-excited oscillation of collapsible-tube flow. *JSME International Journal Series A-Solid Mechanics and Material Engineering*, **37**, 71-78.

Yoon, K. J., Shin, S., Park, H. C. & Goo, N. S. 2002 Design and manufacture of a lightweight piezo-composite curved actuator. *Smart Materials and Structures*, **11**, 163-168.

Zdravkovich, M. M. 1981 Review and classification of various aerodynamic and hydrodynamic means for suppressing vortex shedding. *Journal of Wind Engineering and Industrial Aerodynamics*, **7**, 145-189.

Zhang, H. J., Zhou, Y. & Antonia, R. A. 2000 Longitudinal and spanwise structures in a turbulent wake. *Physics of Fluids*, **12**, 2954-2964.

Zhang, H. J., Zhou, Y., So, R. M. C., Mignolet, M. P. & Wang, Z. J. 2003 A note on the fluid damping of an elastic cylinder in a cross-flow. *Journal of Fluids and Structures* **17**, 479-483.

Zhou, C. Y., So, R. M. C. & Mignolet, M. P. 2000 Fluid damping of an elstric cylinder in a cross flow. *Journal of Fluids and Strctures* **14**, 303-322.

Zhou Y. & Antonia R. A. 1993 A study of turbulent vortices in the wake of a cylinder. *Journal of Fluid Mechanics*, **253**, 643-661.

Zhou, Y. & Antonia, R. A. 1994a Effect of Initial Conditions on Structures in a Turbulent Near-Wake. *AIAA Journal*, **32**, 1207–1213.

Zhou, Y. & Antonia, R.A. 1994b Critical Points in a Turbulent Near-Wake. *Journal of Fluid Mechanics*, **275**, 59-81.

Zhou, Y. & Antonia, R. A. 1995 Memory Effects in Turbulent Plane Wakes. *Experiments in Fluids*, **19**, 112-120.

Zhou, Y. & Antonia, R. A. 2002 Effect of Initial Conditions on Structures in a Turbulent Near-Wake. *AIAA Journal*, **32**, 1207–1213.

Zhou, Y., So, R. M. C., Jin, W., Xu, H. G. & Chan, P. K. C. 1999 Dynamic strain measurements of a circular cylinder in a cross flow using a fibre bragg grating sensor. *Experiments in Fluids*, **27**, 359–367.

Zhou, Y., Wang, Z. J., So, R. M. C., Xu, S. J. & Jin, W. 2001 Free vibrations of two side-by-side cylinders in a cross flow. *Journal of Fluid Mechanics*, **443**, 197-229.

Zhou, Y., Zhang, H. J. & Liu, M. W. 2002 The turbulent wake of two side-by-side circular cylinders. *Journal of Fluid Mechanics*, **458**, 303–332.